Effect of Superloads on Pavement Life

FINAL REPORT

December 2021

By (PI) Dr. Julie Vandenbossche, PE, PhD
University of Pittsburgh

COMMONWEALTH OF PENNSYLVANIA
DEPARTMENT OF TRANSPORTATION

CONTRACT 4400018535
WORK ORDER 19

1. Report No. FHWA-PA-2022-001-PITT WO 019	2. Government Accession No.	3. Recipient's Catalog No.
4. Title and Subtitle Effect of Superloads on Pavement Life (WO19)	**5. Report Date** December 2021
	6. Performing Organization Code
7. Author(s) J.M. Vandenbossche, C.A. Donnelly, N. Buettner, S. Sen, and Z. Brody	**8. Performing Organization Report No.**
9. Performing Organization Name and Address Department of Civil and Environmental Engineering University of Pittsburgh Benedum Hall 3700 O'Hara Street | Pittsburgh, PA 15261	**10. Work Unit No. (TRAIS)**
	11. Contract or Grant No. 4400018535
12. Sponsoring Agency Name and Address The Pennsylvania Department of Transportation Bureau of Planning and Research Commonwealth Keystone Building 400 North Street, 6th Floor Harrisburg, PA 17120-0064	**13. Type of Report and Period Covered**
	14. Sponsoring Agency Code

15. Supplementary Notes

PI contact info: 705 Benedum Hall, 3700 O'Hara Street, Pittsburgh, PA 15261 – jmv7@pitt.edu

16. Abstract

Superloads (SLs) are a class of vehicles that typically exceed both gross vehicle weight limits and axle load limits, in addition to occupying two or more lanes of traffic. In PA, SLs require special permits but their effect on pavement distresses have not been evaluated. In this study, lab and computational analyses were combined to quantify the effect of SLs on flexible and rigid pavements. In rigid pavements, SLs were found to disproportionately increase fatigue damage particularly under conditions of high positive temperature gradients. Laboratory testing also indicated that this damage increases non-linearly, so that it is higher for pavements that are already significantly damaged than those that are still relatively undamaged. Additionally, the heavy loads increased the dowel looseness developed at transverse joints, although this increase would require 1,000 of passes of a SL. A higher dowel looseness may potentially lead to higher faulting. Computational analysis found that this potential was enhanced when the slab experienced high temperature gradients, as would be the case in late spring and summer. Untied shoulders and poor aggregate interlock are also other factors that may cause an increase in looseness and hence faulting. For flexible pavements, the fatigue damage, rutting, and potential for shear failure were particularly high when the AC and base layers were thin and relatively less stiff. However, as in the rigid pavements case, a single pass of a SL truck does not cause any appreciable damage to the flexible pavement. Predictive models for damage caused to flexible and rigid pavements were developed and implemented into Excel workbooks.

17. Key Words Superloads, rigid pavements, flexible pavements, pavement performance prediction, dowel looseness	18. Distribution Statement No restrictions. This document is available from the National Technical Information Service, Springfield, VA 22161
19. Security Classif. (of this report) Unclassified	**20. Security Classif. (of this page)** Unclassified	**21. No. of Pages** 255	**22. Price**

Form DOT F 1700.7   **(8-72)**   **Reproduction of completed page authorize**

ACKNOWLEDGEMENT

DISCLAIMER

The contents of this report reflect the views of the authors who are responsible for the facts and the accuracy of the data presented herein. The contents do not necessarily reflect the official views or policies of the U.S. Department of Transportation, Federal Highway Administration, or the Commonwealth of Pennsylvania at the time of publication. This report does not constitute a standard, specification or regulation.

CONTENTS

1.0 INTRODUCTION TO SUPERLOADS

Superloaded vehicles, or Superloads (SLs) for short, are a class of vehicles that exceed the legally permitted gross vehicle weight of 200 kips, and typically also axle load limits (20 kips and 34 kips for single and tandem axles respectively). They are also usually much larger in size than typical vehicles, often occupying two or more lanes of traffic. Due to their unique configurations, SLs require special analysis and permitting before being allowed to drive on roads in all states, including PA. This report summarizes methods to analyze the effect of SLs on flexible and rigid pavements and guidelines that were developed to aid PennDOT in processing SL permits in a scientific manner.

First, a literature review was conducted to identify studies relevant to the effect of Superloads on the performance and cost of concrete and asphalt pavements. Current practices employed by highway agencies that pertain to Superload identification, permitting, and analysis were also reviewed. The scope of this task is summarized in the following main topics:

- Description of Superloads
- Pennsylvania Superload Vehicle Profile Development
- Development of Superload Weight Restrictions

Aside from the investigation of highway agency practices, this task consists of methodologies that can be used to develop a profile of superload vehicles in Pennsylvania from weigh-in-motion (WIM) and permit data. Additionally, literature that quantifies damage caused by the vehicles and the associated pavement cost were investigated. The findings of these tasks are discussed in the following sections. After that, laboratory and computational efforts conducted to quantify the damage and develop guidelines are discussed.

2.0 DESCRIPTION OF SUPERLOADS

Permitting procedures nationwide were investigated to develop a comprehensive description of superloads. The survey-based NCHRP study, *Practices for Permitting Superheavy Load Movements on Highway Pavements,* summarizes the policies employed state-to-state for the evaluation and issuance of superheavy commercial vehicle permits (Papagiannakis, 2015). It is evident from this review that the definition of superloads and permitting fees vary among jurisdictions.

2.1 Summary of State Superload Weight Restrictions

The federal government regulates the size and weight of vehicles on interstate highways, as over 80% of annual truck miles traveled occur on the National Highway System (FHWA & DOT, Pavement Comparative Analysis Technical Report, 2016). The federally mandated maximum allowable vehicle weights are stated in the Code of Federal Regulations as 80,000 pounds Gross Vehicle Weight (GVW), 20,000 pounds single axle weight, and 34,000 pounds tandem axle weight. (FHWA & DOT, US Code of Federal Regulations, Title 23, Part 658.17., 2018).

However, many states have exceptions to these limits for trucks transporting certain commodities to promote businesses and enable local economic growth. To accommodate these larger truck loads, weight restrictions for superload vehicles are controlled by individual states. Vehicles that surpass the maximum weight restrictions for annual permit holders are referred to as superloads throughout this report. Table 1 contains a summary of superload weight thresholds by state and any other pertinent details relating to these limits. It is evident that superload definitions vary among states. Some Jurisdictions define superloads based on GVW alone, while others are classified based on axle weights or a combinations of axle weights, tire weight limit, and GVW.

Table 1: Superload definition by state (Papagiannakis, 2015)

State	Superload GVW (kips)	Tire Weight Limit (lb/in.)	Permitted Axle Load Limits (kips) for single, tandem, tridem, and quad axles	Comments
Alabama	>150	700	22, 44, 66, 88	
Alaska	>150	700	30, 56, 70, 80	
Arizona	>250	-	-	

State				
Arkansas	-	-	20, 40, 60, 68	
California	-	620	Depends on axle spacing and route type	
Colorado	>200	-	27, 50, 65, 72	
Connecticut	>140	600	22.4, 40, 60, 80	
Delaware	>120	-	20, 40, 60, 80	
D.C.	>248	-	31, 62, 93, 124*	*Actual weight depends on spacing/ tire pressure
Florida	>199	550	-	
Georgia	>150	-	23, -, 60, 92	
Hawaii	-	-	-	Over legal weights require bridge analysis
Idaho	>200	600	Depends on route type	
Illinois	>187	-	29, 54, 75, 100	
Indiana	>120	800	28, 48, 60, 80	
Iowa	>156	-	20, 40, 60, 80	
Kansas	>150	-	24, 49, 60, 65	
Kentucky	>200	700	20, 48, 60, 80	
Louisiana	>254	700	24, 45, 60, 80	Analysis performed off highway system only
Maine	>150	600	*, 39.1, 62.1, 110	*Single axle weight limited by tire width
Maryland	>150	-	27, 52, 63, -	
Massachusetts	130 permit max	800	Depends on axle spacing	
Michigan	>164	700	Depends on route, vehicle width, and tire size	Unit tire pressures 525/450 for rig/flex under restrictions
Minnesota	>144	600	20, 40*, 60, 72	*46 with bridge check
Mississippi	>190	550	12, 48, 57/*63, 64/*72	*Axle weights on interstate/off interstate. AASHTO agreement for GVW < 120 kips

State				
Missouri	>160	-	20, 46, 60, 72	AASHTO agreement for GVW < 120 kips
Montana	126 permit max	500	22, 48, 51.75, 55.4	
Nebraska	>160	-	20, 34, 60	
Nevada	106 permit max	-	Depends on axle spacing and route type	
New Hampshire	-	-	27.5, 50, 67.5, 80	
New Jersey	-	800	Based on tire unit weight	
New Mexico	-	-	Depends on route	
New York	>199.9	-	Depends on route, axle spacing, and vehicle configuration	Engineering review for GVW > 140 kips
North Carolina	>132	-	25, 50, 60, 68	
North Dakota	>150	-	12*, 45, 60, 68	*Steer axle
Ohio	>120	-	29, 36/*50, 47/*60, 60/*80	*Spacing 4 ft/4 ft, 1 in.
Oklahoma	>150	-	-,40, 60, 65	
Oregon	>200	600	21.5/43/depends on spacing	
Pennsylvania	>201	800	27, 52, 63, 72	
Rhode Island	120 permit limit	-	Depends on route and vehicle configuration	
South Carolina	>130	-	20, 40, 60, 80	
South Dakota	>200	600	53.3% higher than bridge formula weight limits	
Tennessee	160 permit limit	-	20, 40, 60, 80	AASHTO agreement for GVW < 120 kips
Texas	>254.3	-	25, 46, 60, 70	Pavement analysis when GVW > 500 or tire weight > 6 kips
Utah	>125	600	29.5, 50, 61.75, Bridge formula	
Vermont	>150	600	Depends on tire size	
Virginia	>150	-	24, 44, 75/*54.5, 100/*64.5	*Interstate/ other
Washington	>200	500/600	22, 43, 65, 70	

West Virginia	120 permit limit	-	28, 45, 50, 55	
Wisconsin	191 permit limit	-	20, 60, 81, 90	
Wyoming	>150	-	25, 55, 65, 74	

Survey results from the NCHRP study are summarized in Figure 1. Superloads are most commonly defined by GVW. A GVW of 200 kips or more is most commonly used to define a superload, but these vehicles can range from 120 to 500 kips in weight. Load limits for superloads defined with GVW and axle loads had GVW ranging from 80 to 350 kips, with tandem axle weights from 34 to over 60 kips. "Other" superload definitions were found to be more specific, and relating to factors such as vehicle dimensions, approval from a bridge bureau, or limitations on tire weight limits only.
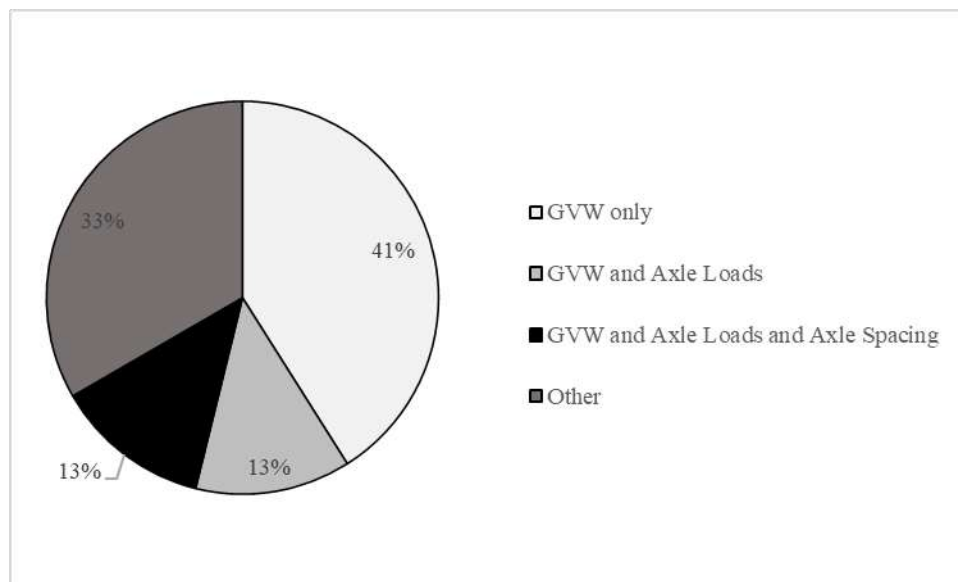
Figure 1: Superload definition by vehicle characteristics (Papagiannakis, 2015)

2.2 Summary of State Superload Permitting Fees

Like superload weight thresholds, superload single-trip permit fees vary among jurisdictions. Table 2 contains a summary of permit fees by state. Single-trip fees can be administered as a flat rate, as a function of weight-distance, in relation to GVW, or as a function of pavement cost recovery.

Table 2: Superload Single-trip Permit Fees by State (Papagiannakis, 2015)

State	Single-Trip "Superload" Permit Fees (GVW in kips)
Alabama	Permit fee: $100 for GVW > 150, additional fees decided on a case-by-case basis
Alaska	Permit fee: $20 for GVW > 150, additional fees decided on a case-by-case basis
Arizona	Single trip registration: $12/trip < 50 miles; $48/trip > 50 miles, Use fuel fee: $16/trip <50 miles; $65/ trip > 50 miles, Class "A" overweight permit fee: $75.
Arkansas	Permit fee: $17, Extra charges/ton: < 100 miles: $8, 101 to 150 miles: $10, 151 to 200 miles: $12, 201 to 250 miles: $14, >251 miles: $16
California	Permit fee: $16, Carrier pays cost of any infrastructure repairs
Colorado	Overweight (OW) fee: $10/ overweight axle, regardless of distance traveled
Connecticut	Permit fee: $23, additional fees decided on a case-by-case basis
Delaware	Permit fee: $10, Fees: $5 for each; no additional fees indicated
D.C.	Permit fee: $30; no additional fees indicated
Florida	GVW < 95: $0.27/mi GVW 95-112: $0.32/mi GVW 112-122: $0.36/mi GVW 132-142: $0.42/mi GVW 142-152: $0.45/mi GVW 152-162: $0.47/mi GVW 162-199: $0.003/1000 lb/mi GVW > 199: $0.003/1000 lb/mi
Georgia	GVW 150-180: $125 GVW > 180: $500 regardless of distance traveled
Hawaii	Permit fee: $5; no additional fee indicated
Idaho	Permit fee: $71; no additional fee indicated
Illinois	Permit fee: $50 Additional fees as a function of the number of axles, axle loads, GVW, and distance travelled for GVW < 120. Feed for GVW > 120 not indicated
Indiana	Permit fee: $42.50 Additional fee for GVW 108-150: $0.60/mi; for GVW>150 $1.0/mi
Iowa	Permit fee: $10; additional fees may be levied on a case-by-case basis
Kansas	Permit fee: $50 No specific additional fees indicated, but mover must pay all infrastructure damages
Kentucky	Permit fee: $60, Additional fee that depends on bridge analysis (i.e. number of axles, axle weight/ spacing)

Louisiana	Permit fee: $10, Additional fee for GVW > 254: $0.50/ton/mi of GVW > 80 plus fee for structural bridge analysis ($125-850)
Maine	Permit fee: -- Additional fees range from $6 to $27.50 depending on the amount by which the allowable 80 kip GVW is exceeded, regardless of distance traveled
Maryland	Permit fee: $50 Additional fees: $30 for the first 40 kips plus $5 for each additional ton, plus bridge analysis fees
Massachusetts	Permit fee: $350; additional fees may be decided on a case-by-case basis
Michigan	Permit fee: $50; additional fees decided on a case-by-case basis
Minnesota	Permit fee: $36 Additional fees based on damage assessment per mile (axle number and load)
Mississippi	Permit fee: -- Additional $0.05/mile/1000 lb
Missouri	Permit fee: $15 Additional $2/1000 lb in excess of legal GVW plus bridge analysis fee ($425 for 0-50 mi, 625 for 51-200 mi, and $925 for >200 mi move)
Montana	Permit fee: $10-$50 depending on miles driven Additional fee for GVW>100: $70 + $3.50/5000 lb on excess for each 25 miles driven
Nebraska	Permit fee: $20, additional fees decided on case-by-case basis
Nevada	$25 regardless of GVW and mileage
New Hampshire	GVW 80-90: $9.50 GVW 90-100: $10.50 GVW > 100: $2/each additional 10 kips regardless of distance traveled
New Jersey	$10 base fee + $5/ton in excess of 80k GVW + $5/ton on single/tandem axles > 22.4/24 kips
New Mexico	$25 + $0.025/mile/ton over 86.4 kips
New York	Permit fee: $40-$360 depending on commodity, plus analysis fee, plus bonding ($10k-$50k) depending on GVW
North Carolina	$12 + $3/1000 lb over 132 GVW regardless of mileage
North Dakota	GVW 150-160: $30 GVW 150-170: $40 GVW 170-180: $50 GVW 180-190: $60 GVW >190: $70 + $0.05/ton/mile on GVW > 200
Ohio	$135 flat rate + $0.04/ton/mile in excess of 120 kips GVW
Oklahoma	Special purpose overweight trip fee: $40 $10/1000 lb overweight (GVW > 150 with 8 axles)

Oregon	$8 fee + for GVW > 98k, $/mile that depends on GVW and number of axles ($0.01-$2.601/mi)
Pennsylvania	Permit fee: $25 or $50 + 0.03/ton/mile over carrier's registered weight
Rhode Island	Permit fee: $20 + for divisible loads: trailers $100, tractors $50/1000 lb over legal weight (max $1250); 2-, 3-, 4-axle trucks: $50/1000 lb over legal limit (max $1500) regardless of distance traveled
South Carolina	$3/ 1000 lb for GVW > 130 regardless of distance traveled
South Dakota	Permit fee: $20 + $0.02/ton/mile for GVW > 40 on 2 axles, GVW > 60 on 3, GVW > 80 on 4, GVW > 85 on 5 axles, GVW > 90 on 6 axles, GVW > 95 on 7 or more axles
Tennessee	Permit fee: $15 + bridge analysis fee ($100 to actual cost) + $0.05/ton/mile
Texas	Permit fee: $90 + fee depending on the number of counties traversed ($270-$1095) + maintenance fee for 200 < GVW < 254.3 ($375) + supervision fee for 200 < GVW < 254.3 ($35 for LOA > 95 ft, $500 for LOA < 95 ft)
Utah	Permit fee: $60 + fee ranging $65-$450 depending on GVW and distance traveled
Vermont	Permit fee: $35 + engineering inspection fees ranging from $800 to $10000 depending on GVW
Virginia	Permit fee: $30 + $0.1/mile/ton
Washington	Permit fee: $25 + $4.25/mmi + $0.50/5000 lb/mi for GVW in excess of 100 kips
West Virginia	Permit fee: $20 + $0.04/ton/mile of overweight
Wisconsin	Permit fee: $105 + $10/1000 lb for GVW > 150 kips regardless of distance traveled
Wyoming	Permit fee: $40 + $0.06/ton/mile traveled

As evident from Figure 2, permit fees charged as a function of weight distance, which is often regulated as $/ton/mile, are the most prevalent. The second most common type is a fee based on GVW or axle weight, for which distance traveled is not a consideration. Flat fees, making up 13% of the responding jurisdictions, are in the range of $5 to $550, and are independent of vehicle weight or distance traveled. A processing fee and an infrastructure usage fee specific to each superload case is charged for 12% of the jurisdictions, and 3% use a pavement damage cost recovery approach, requiring the shipper to pay for all infrastructure repairs.
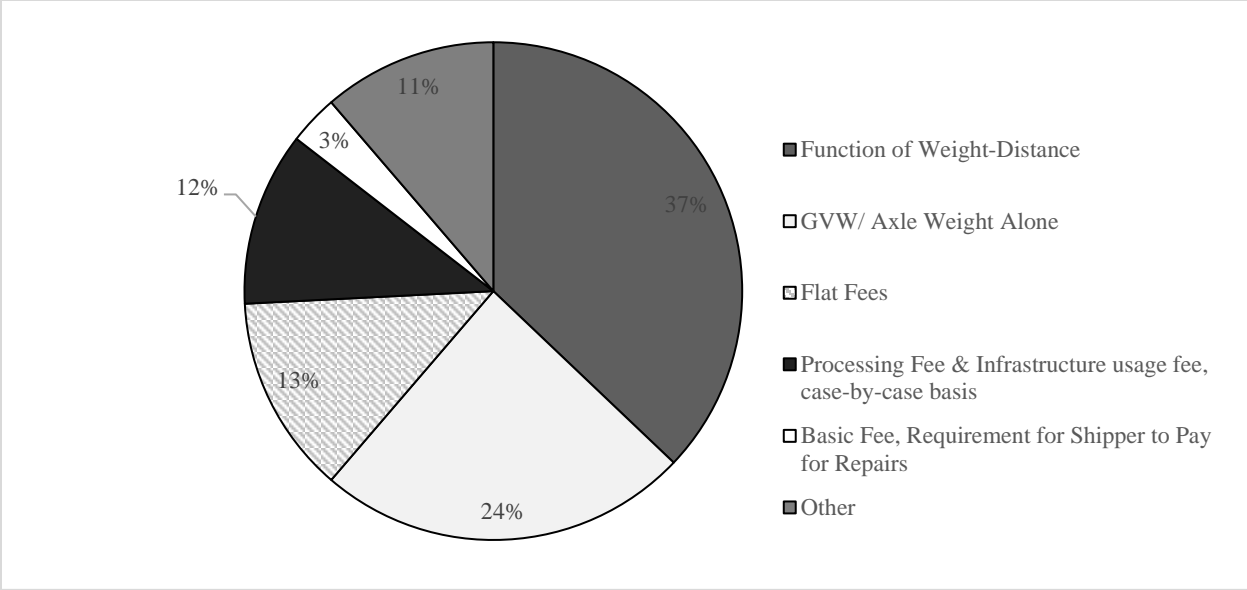
Figure 2: Variation of superload permit fee types among jurisdictions (Papagiannakis 2015)

3.0 SUPERLOAD VEHICLE PROFILE DEVELOPMENT

An accurate estimate of the number, axle configuration, gross vehicle weight, and individual axle weights of superload vehicles in Pennsylvania would aid in evaluating the effect of superloads on pavement life. Several methodologies to characterize vehicles of interest from WIM and permit data are available in existing literature. These studies are reviewed in the following sections.

3.1 WIM Data Based Profile Development

WIM technology, which allows for the automatic collection of traffic and vehicle weight data, can be used to populate a database of vehicles traveling on highways of interest. The data collected by WIM systems includes parameters such as gross vehicle weight, axle configuration, and axle weights. WIM data is widely prevalent and provides an unbiased sample of vehicle information since the locations of the systems are unknown to the public.

As previously mentioned, an accurate estimate of relevant vehicle characteristics is necessary to determine the extent superload vehicles are responsible for highway infrastructure damage in Pennsylvania. WIM data can be used to characterize superload vehicles, however WIM databases are very large and contain a considerable amount of irrelevant information. Several methods to extract relevant data from WIM databases are available in existing literature. Multiple studies have utilized WIM data to provide a statistical distribution of relevant vehicle characteristics (Miao & Chan, 2002; Mohammadi & Shah, 1992; OBrien, Enright, & Getachew, 2010). Other research has focused on classifying vehicles into different categories (Fiorillo & Ghosn, 2014). This section describes a selection of WIM data-based profile development methods established by various researchers.

Mohammadi and Shah (1992) determined the statistics of overload occurrence based on two sets of WIM data. One set of data was collected by the Illinois Department of Transportation (IDOT) and the other is a composite set of data acquired from the Federal Highway Administration (FHWA). Theoretical distribution models were developed for various vehicle load categories. Categories that had a significant number of overloaded vehicles revealed two distinct patterns separating the overloads from all other loads in the spectrum. A mixed distribution model, which combines two distribution functions, was selected to represent the entire data set. The probabilities

of overload occurrences were then calculated using the distribution models obtained for each vehicle load category.

Miao and Chan (2002) provided a statistical representation of gross vehicle weight, axle weight, and axle spacing based on ten years of Hong Kong WIM data. Since it is impossible to simulate such a large data set, sub-samples of recorded WIM data were compiled and simulated using the Kolmogorov-Smirnov (K-S) and Monte Carlo methods. The individual stochastic process that each vehicle characteristic of interest followed was identified and used to obtain the distribution parameters. These parameters were determined using the maximum likelihood estimation approach. Once the statistical parameters were established, the maximum gross vehicle weight and axle weight for the design life of a structure could then be calculated. Obtaining a mathematical distribution of relevant vehicle characteristics enables one to determine to what extent extremely heavy vehicles are present on highway infrastructure.

O'Brien et al. (2010) investigated the challenges of simulating traffic loading scenarios to estimate the effect of heavy traffic loads. Statistical distributions were fit to histograms of WIM data collected at two European sites. The collected traffic data included parameters such as the axle configuration, gross vehicle weight, and individual axle weights. Since the quality of the fit affects the accuracy of the results, the statistical distributions had to closely match the histograms of measured WIM data. Gross vehicle weight, which was selected to illustrate the difficulties associated with simulating traffic, was modeled using three different methods: parametric fitting, non-parametric fitting, and semi-parametric fitting.

Parametric fitting, which is a widely used approach, fits a histogram to a linear combination of normal distributions. Although this method provided a good fit for most of the range of values, it severely underestimated the probabilities in the upper tail where there is less data. Alternatively, non-parametric fitting directly uses a histogram to simulate traffic loading scenarios. This method was reasonable for the measured range of gross vehicle weight but could not accurately predict the probabilities in the upper region of the histogram. The proposed method, semi-parametric fitting, directly uses a histogram in the range where there is sufficient data and models the upper tail using parametric fitting. Semi-parametric fitting allowed for interpolation between data points, provided accurate predictions of probabilities in the upper tail region, and ensured non-zero probabilities of gross vehicle weight above the maximum value. The statistical distributions of gross vehicle

weight were then employed to simulate traffic loading scenarios using a Monte Carlo model for which characteristic heavy traffic load effects are estimated.

Fiorillo and Ghosn (2014) developed a procedure based on a data mining algorithm to segregate trucks in the New York State WIM database into permitted and illegal overweight vehicle categories. A set of data mining rules were first established based on the New York State Department of Transportation (NYSDOT) permit database, which includes the axle configuration, axle weights, and gross weight of each permitted truck. The data mining algorithm consisted of two parts. Pattern recognition was used to develop a matrix of trucks from the NYSDOT permit database to classify permit vehicles by comparing the axle configurations to those in the WIM database. The results were then improved by Bayesian updating, which statistically accounted for suspected illegal trucks that had axle configurations similar to those of permitted trucks.

The accuracy of the data mining procedure was confirmed by a survey conducted by the NYSDOT using a WIM system equipped with a camera. The results of the survey, which manually obtained the percentage of permitted and illegal overweight trucks, were consistent with the results of the data mining algorithm.

3.2 Permit Data Based Profile Development

Superload vehicle characteristics can also be determined from permit data. Overweight vehicle permits, which authorize the travel of overloaded vehicles, are issued by state agencies and contain relevant vehicle information, such as the gross vehicle weight, axle configuration, axle weights, and proposed route, of overweight vehicles. Very few studies regarding the characterization of superload vehicles from permit data are available for review.

(Correia & Branco, 2006) developed a procedure to check overweight vehicle permits based on the statistical analysis of a permit vehicle database. The analysis was performed to characterize vehicular overloads by vehicle type, transported material, origin and destination, transportation company, load, and vehicular overload design load for each vehicle type by gross weight range. Statistical distributions were fit to histograms of each vehicle characteristic. The probabilities of attribute occurrences were then calculated using the statistical distributions obtained for each vehicle characteristic. In addition, software was developed to evaluate the structural safety of bridges crossed by an overweight vehicle. The software also relates the vehicular overload database to a depiction of the traveled highways by a geographic information

system (GIS). This methodology enables state agencies to assess overload vehicle permits in an efficient manner.

3.3 Permit Data for Pennsylvania

A preliminary investigation of permit data was conducted to review characteristics of superloads in Pennsylvania. While superload permits can be issued due to length and width criteria in addition to weight, only permits for vehicles that exceeded a GVW of 200 kips were considered in this analysis. A total of 1616 superload permits issued from 2013 to 2015 were evaluated.

It was found that GVW does not necessarily increase with number of axles, and a linear trend between these parameters yields an R^2 value of 0.36, indicating variation in this data. This relationship is evident in Figure 3. The fact that the number of wheels per axle varies for these vehicles contributes to the variability observed in this figure.
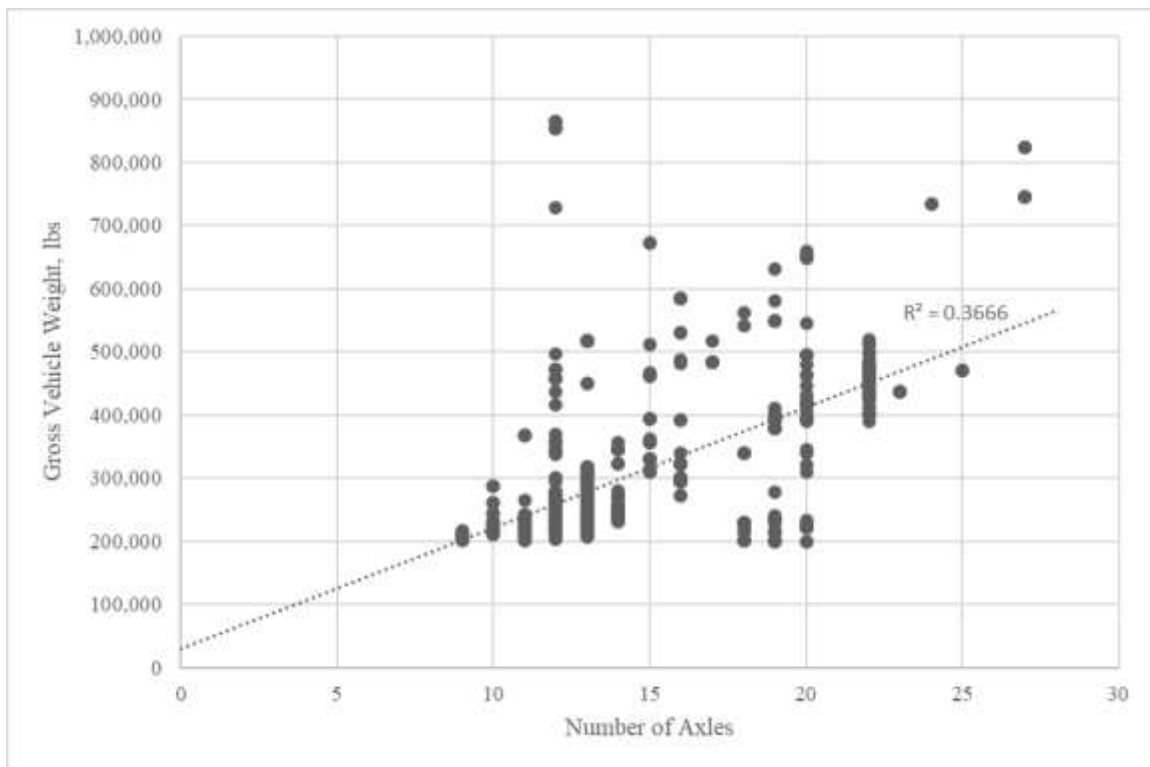
Figure 3: Pennsylvania superload gross vehicle weight vs. number of axles

The frequency of GVW and number of axles for the permitted superloads was determined. This analysis revealed that a GVW range of 235 to 270 kips was the most frequent, with 677

vehicles falling within this range during the years of interest. The next most frequent GVW ranging was 270 to 305 kips, followed by 200 to 235 kips, with 328 and 264 permits issued, respectively. It also is evident from this analysis that vehicles with 12-14 axles were the most common, with 1009 issued permits for superloads having this number of axles. The frequency distributions for this data can be found in Figure 4 and Figure 5.
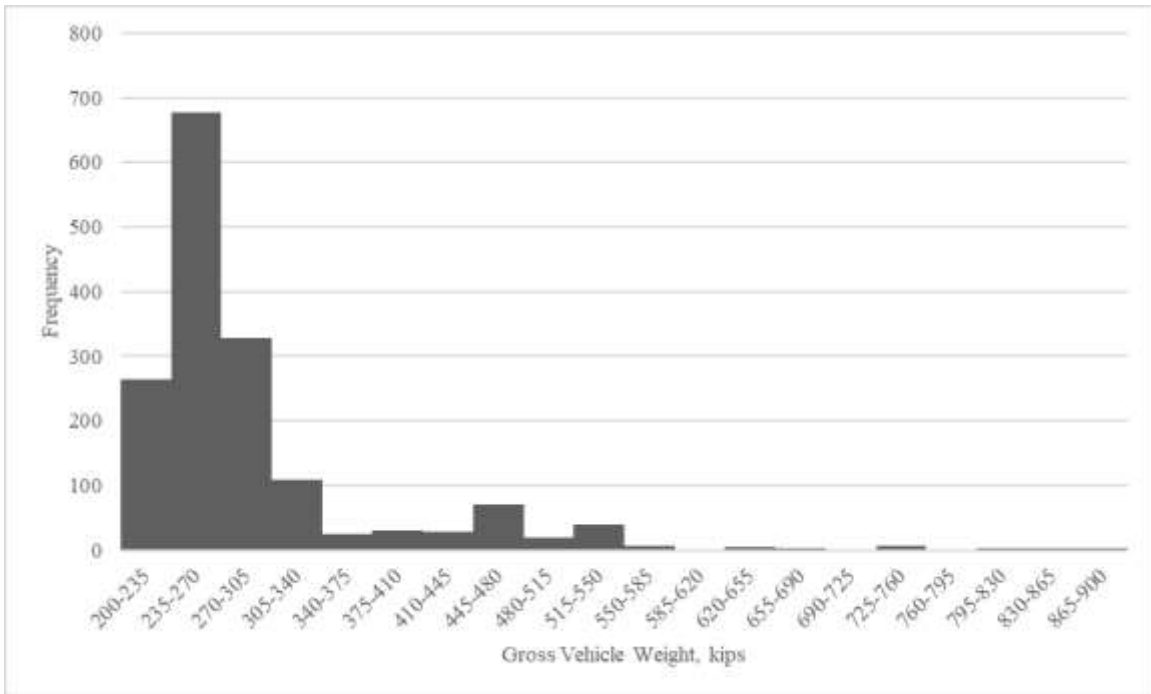
Figure 4: Frequency distribution of Pennsylvania superload GVW
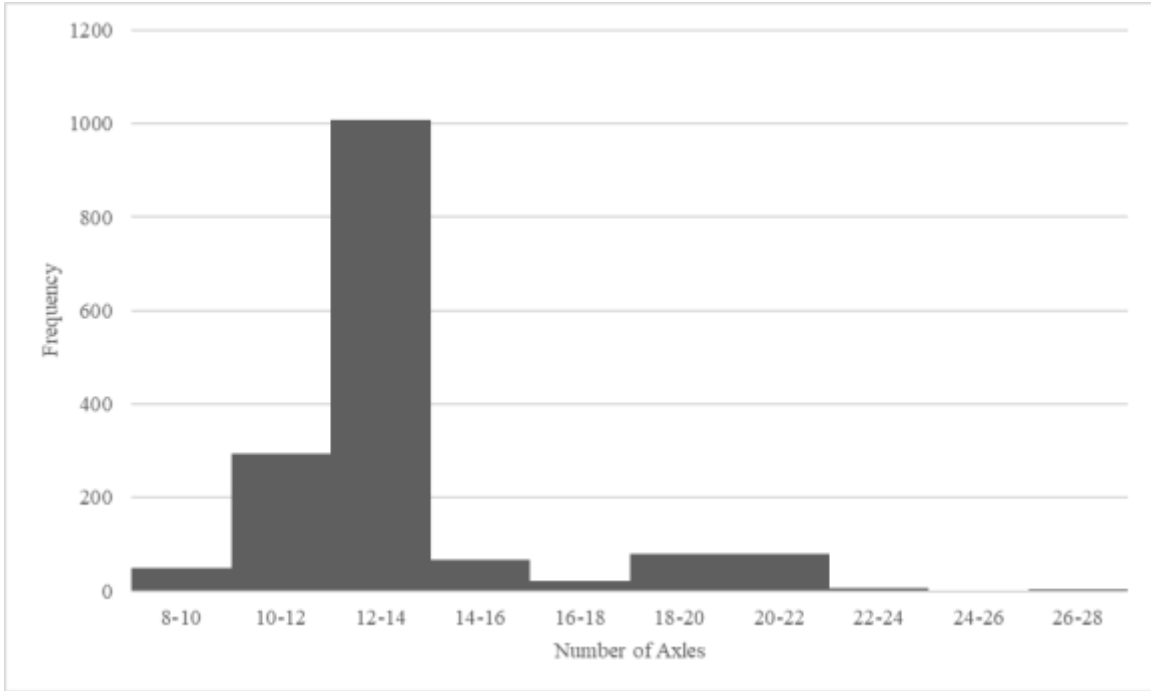
Figure 5: Frequency distribution of number of axles associated with Pennsylvania superloads

Further characterization of typical vehicles in Pennsylvania will result from additional analyses. Superloads will be categorized based on typical loads associated with axle configurations and spacing. The development of profiles for typical superloads will allow for the resulting pavement damage to be assessed using computational and laboratory analyses.

4.0 DEVELOPMENT OF SUPERLOAD WEIGHT RESTRICTIONS

Practices involved in the approval of superload permit applications vary among highway agencies. Depending on the proposed superload route, some jurisdictions only conduct bridge analyses during the review process, while others incorporate pavement analysis as well. These various policies are summarized in this section, along with studies that evaluate the effect of overloaded vehicles on pavement longevity using mechanistic analysis.

In addition to methods used to assess superload pavement damage, studies that aim to quantify the cost of pavement damage attributed to overloaded vehicles were also investigated. As evident from the review contained in Section 1.1.2, jurisdictions commonly issue single trip permit fees as a function of weight-distance (15%), or on the basis of infrastructure usage (15%). Methodologies that can be used to put a standardized monetary value on the infrastructure damage due to superloads are essential in the development of permit fees.

4.1 Assessment of Damage Caused by Superloads

A survey of superload permitting processes was administered to US and Canadian highway agencies during the NCHRP study (Papagiannakis, 2015). Forty highway agencies responded to the survey. It was found that during the superload permitting process, 15% of agencies always perform pavement analyses, while 40% sometimes do, and 45% never do.

Of the 22 responding agencies that perform a pavement analysis during the superload permitting process, 13% use industry-developed mechanistic methods such as those used by the Portland Cement Association (PCA) or the Asphalt Institute (AI), and 31% use methods from the AASHTO '93 guide (AASHTO, 1993). The remaining 56% use mechanistic-empirical methods developed in their state. their own in-state developed mechanistic-empirical method. None of the responding states use the Mechanistic Empirical Pavement Design Guide in the evaluation of superloads. This information is summarized in Figure 6.
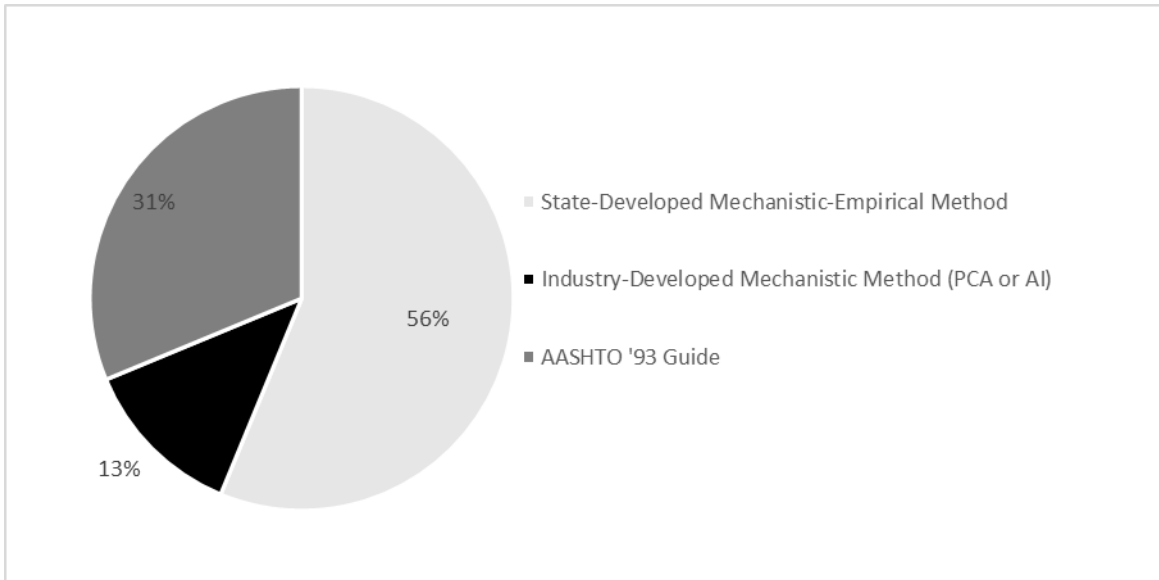
Figure 6: Type of superload pavement analyses among responding jurisdictions (Papagiannakis, 2015)

Some of the agencies that perform mechanistic-empirical pavement analyses during the issuance of superload permits were investigated further. Information about these policies was obtained from email correspondence with personnel responsible for superload permitting for their state DOTs.

In the state of Washington, superloads that are not permissible under the Revised Code of Washington, and pavement analysis is legally required during the permitting process. The weakest pavement structure on the proposed route undergoes engineering evaluation during the permitting process. A finite element analysis is performed to determine the critical strain induced by the maximum wheel load of the superload. This value is then compared to the critical strain resulting from the heaviest legally permitted standard steering axle in the state of Washington. If the critical strain exceeds the strain from the legally permitted axle, then it is recommended that the superload not be permitted for travel. These analyses are typically only required for flexible pavements because the rigid and composite pavements are commonly in areas of high ESALs and have a fairly large structural capacity. They are also commonly located in urban areas that are not along routes commonly loaded by superloads. However, due to stringent bridge analyses performed by WSDOT's Bridge and Structures office, superload applications are often rejected prior to any pavement analysis (personal communication).

In Minnesota, superloads are evaluated using a mechanistic-empirical computer program for the evaluation of flexible pavements called MnPAVE. Vehicle loads are simulated using a layered elastic analysis. The proposed load is then compared to the MnPAVE allowable stress criteria, which is intended to protect the aggregate base layer from failure during a single heavy load event (Minnesota Department of Transportation, 2012). If the superload exceeds the allowable stress criteria, it is likely that the superload will cause pavement failure (personal communication).

A number of studies have been conducted to evaluate the effect of superloads on pavement longevity using mechanistic analysis. This included a study conducted by (Chen, Fernando, & Murphy, 1996) during which the potential damage of superloads was evaluated with FWD tests and simulated using an elastic analysis. Other studies have resulted in the development of mechanistic-based methodologies for the evaluation of superheavy load movements on flexible pavements (Chen, Lambert, Tsai, & Zhang, 2013; Hajj, et al., 2018). In general, it is evident that mechanistic analysis methods often involve linear elastic analysis for the structural evaluation of flexible pavements, while finite element analysis is conducted for rigid pavements.

4.2 Quantifying Cost Associated with Superload Damage

Literature that pursues the cost quantification of the accelerated pavement damage caused by overloaded vehicles was reviewed. It was found that the most commonly used cost allocation technique is the incremental approach, during which the required increase in pavement thickness required to accommodate an increase in truck weight is calculated for a constant design life. Aside from the incremental approach, some studies factor in the cost of maintenance and rehabilitation (Ghosn, et al., 2015), IRI data (Rodriguez, Sinha, Labi, Tine, & Dutta, 2005), or PSR data (Bai, et al., 2010) to determine the cost implications of heavy vehicles.

At the forefront of this literature is the *Federal Highway Cost Allocation Study* (FHWA; DOT, 1998). The purpose of this study was to determine highway-related costs accredited to various truck types to evaluate the current federal highway user charges. This project involved the separation of federal highway costs into four categories; pavement cost, bridge cost, system enhancement cost, and other attributable costs. Required pavement thickness costs were attributed to vehicle classes according to Vehicle Miles Traveled (VMT). VMT were then weighted by a Passenger Car Equivalent (PCE) factor, which is used to compare the effect of different vehicle

types on pavement cost. The cost for any required additional pavement thickness for overloaded vehicles was then established using ESALS. Reconstruction, resurfacing, and rehabilitation cost was also assigned to vehicle classes based on their contribution to pavement damage. FHWA posted an addendum to this study in 2000, which assigned pavement damage cost to vehicle miles traveled for different vehicle classes, as evident in Table 3 (FHWA, 2000).

Table 3: Unit pavement cost for various vehicle classes on rural and urban interstates

Vehicle Class/ Interstate Class	Marginal Pavement Cost (Cents per mile)
40,000 4-axle Single Unit Truck/ Rural	1
40,000 4-axle Single Unit Truck/ Urban	3.1
60,000 4-axle Single Unit Truck/ Rural	5.6
60,000 4-axle Single Unit Truck/ Urban	18.1
60,000 5-axle Combination Truck/ Rural	3.3
60,000 5-axle Combination Truck/ Urban	10.5
80,000 5-axle Combination Truck/ Rural	12.7
80,000 5-axle Combination Truck/ Urban	40.9

Table 3 illustrates the increase in cost associated with a change in weight of vehicle classes. The incremental cost approach model used in this project is utilized by many other studies for highway cost allocation. It was applied to overload vehicles but not necessarily those classified as superloads.

A study was conducted for the Ohio Department of Transportation to determine the impact of permitted overweight trucks on Ohio's transportation system and economy (Campbell, et al., 2009). This study divided pavement designs and their associated costs into functional classes, and allocated costs to vehicles using VMT and ESALS via the incremental approach. Vehicle impact was quantified in two groups; over 80,000 lb and less than or equal to 80,000 lb Pavements were designed for each functional class with and without overweight vehicles using the AASHTO '93 Design Guide (AASHTO, 1993). It was found when overweight vehicles were removed from the WIM database, pavements were designed to be one inch thinner. The cost allocation portion of

this study revealed that overweight vehicles are responsible for 122 million dollars of damage per year for the concrete pavement systems in Ohio that were analyzed. Overall, this approach relates pavement design to the effect of overweight vehicles but neglects pavement maintenance cost.

A NYSDOT study goes a step further than the Ohio DOT study and quantifies cost as an increase in design thickness and maintenance that would be necessary for overweight vehicles (Ghosn, et al., 2015). This study allocated cost to divisible permit trucks, special hauling permit trucks, and illegally overweight trucks based on material cost and corrective maintenance interventions for asphalt and concrete pavements. This was determined using an amount of ESALS that exceed the most severe legal vehicle in each class/weight category. The total necessary number or corrective maintenance interventions required for a roadway to remain at an acceptable IRI was determined using a MEPDG approach. It was found that the cost attributed to overweight trucks on the NYSDOT pavement network is roughly 145 million dollars per year, with 22 million allocated to divisible permit trucks, 49 million for special hauling permit trucks, and 73 million for illegally overweight trucks.

A study performed for the Indiana DOT (Rodriguez, Sinha, Labi, Tine, & Dutta, 2005) developed a model for estimating the service life and cost of pavement preservation activities based on IRI data rather than VMT for vehicle classes. Unlike the NYSDOT study, this study only considers pavement maintenance activities and neglects new pavement construction costs. In the model, pavement preservation activities are divided between 'rehabilitation' and 'non-rehabilitation' categories, which encompass all maintenance and reconstruction required for the roadway. A correlation is used between time and number of lane-miles requiring rehabilitation. For the determination of overall pavement costs, the percent of the system requiring maintenance, along with the total system size and unit preservation costs were identified. Preservation costs were then determined for three classes of highways in Indiana. These classes included interstate roads, non-interstate roads in the national highway system, and state roads that are not in the national highway system. The annual pavement preservation cost was estimated to be approximately 404 million dollars a year in Indiana using the model. However, it should be noted that this study focuses on pavement costs not specific to overloaded vehicles.

Bai et al. from the University of Kansas investigated the cost of pavement damage due to meat industry-related transportation in a 2010 study. While this study integrates the incremental approach, it also incorporates the Present Serviceability Rating (PSR) to estimate maximum

pavement life. Annual ESALS for pavement sections were determined by multiplying VMT by truck ESALS. An acceptable decline in PSR values was determined for each road segment in the study. Then, average reconstruction costs per mile was multiplied by percent PSR loss due to traffic and then divided by ESAL lives of pavement segments to determine unit costs per ESAL. To determine damage cost for a highway section, ESALs were multiplied by unit cost per ESAL. It was estimated during this study that damage due to meat-industry related transportation alone amounted to over 3 million dollars annually in the state of Kansas. While this study did not investigate the impact of all overweight vehicles, it presents a unique method for quantifying cost.

A study performed for the Wisconsin DOT was aimed at determining the single-trip infrastructure impacts of over-size, over-weight loads (Adams, et al., 2013). This study included the examination of all overload operations, such as permit issuance, permit fees, agency costs, in addition to infrastructure impacts to assess the permit fee structure in various states. An infrastructure cost framework using the incremental approach was established in this study to accomplish this. First, truck configurations and corresponding ESALs per vehicle were identified. Then, incremental changes in ESALS by overloads were determined from permit information. The cost associated with additional ESAL miles traveled due to overloads was estimated, followed by a calculation of the change in pavement costs. The final step was to determine the agency costs attributed to the overloads. This study recommended that the results be validated with field data, because approaches developed to evaluate single-trip impacts are often not. After conducting interviews with several state DOTs, it was found that single trip permits often do not capture ongoing infrastructure damage due to overweight vehicles. It is evident from this review that the cost of pavement damage from overweight vehicles is substantial in comparison to vehicles below the overweight threshold.

5.0 PAVEMENT RESPONSE AND DAMAGE MODELS

Having examined SLs and permitting procedures, the next task was to assess pavement response and damage models. In general, existing models do not consider the effect of SLs, which has unique configurations and loads as compared to typical traffic. Therefore, a fresh assessment has to be performed for SLs. The following sections will provide guidance on:

1. Quantifying the development of dowel looseness from superloads
2. Quantifying the effects of superloads on concrete fatigue
3. Establishing extreme overload guidelines

Fatigue cracking and faulting are considered for concrete pavements, while bottom-up cracking and rutting in all layers are considered for asphalt pavements. For each pavement distress, structural response and damage prediction models are analyzed.

6.0 RIGID PAVEMENTS

6.1 Pavement Response

6.1.1 Fatigue Cracking

Fatigue cracking in Portland cement concrete (PCC) pavements is caused by vehicle loads, temperature gradients, moisture gradients, and uniform changes in temperature. Fatigue cracking can occur as bottom-up cracking or top-down cracking depending on the loading conditions and structural features of the pavement.

Bottom-up cracking occurs when there are significant tensile stresses at the bottom of the PCC slab. Bottom-up cracking is prevalent when the top of the PCC slab is warmer than the bottom. This positive temperature gradient causes the PCC slab to curl downward, as shown in Figure 7. This deformation is restrained by factors, such as self-weight, which results in the development of stresses at the bottom of the PCC slab. Bottom-up cracks propagate to the surface of the pavement as the number of load applications increases. The critical structural response for bottom-up cracking is the stress at the bottom of the PCC slab near the transverse center of the longitudinal edge/shoulder joint. The critical axle loading for bottom-up cracking is a single axle loaded in this location, as shown in Figure 8.
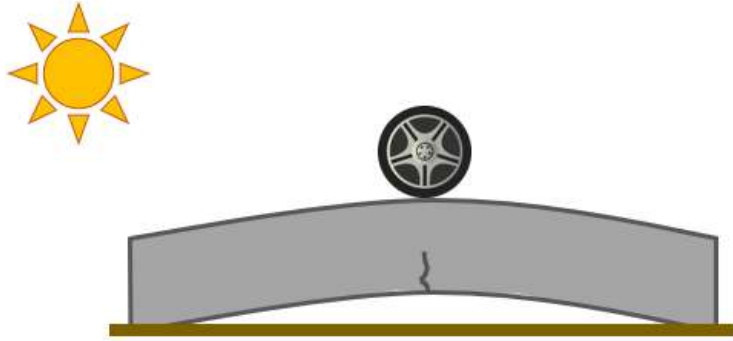
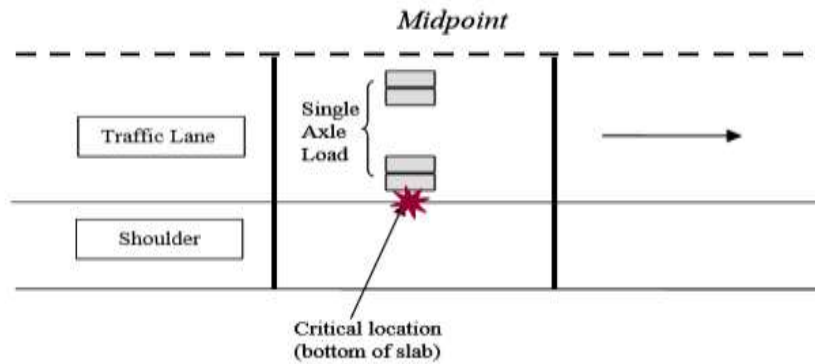Figure 7: PCC slab curl when a positive temperature gradient is present.

Figure 8: Critical loading position for the development of bottom-up cracking (Applied Research Associates (ARA), 2004).

Top-down cracking is primarily of concern when there is a negative temperature gradient in the PCC slab or positive differential shrinkage exists between the top and the bottom of PCC slab. This causes the PCC slab to curl up, as shown in Figure 9. In this distress mechanism, the crack initiates at the top of the pavement. The critical structural response for top-down cracking is the stress at the top of the PCC slab at midslab on the lane/shoulder joint. The critical loading position for top-down cracking is when truck axles are loaded at the opposite ends of the slab simultaneously, as shown in Figure 10.
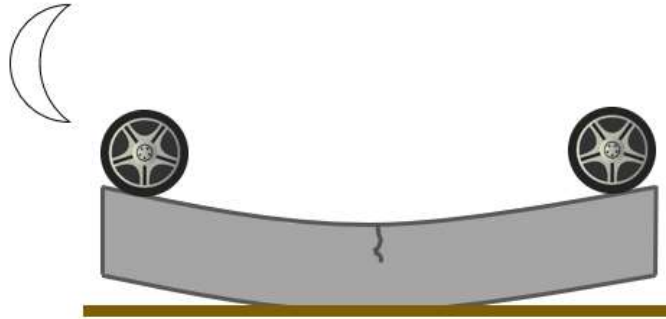
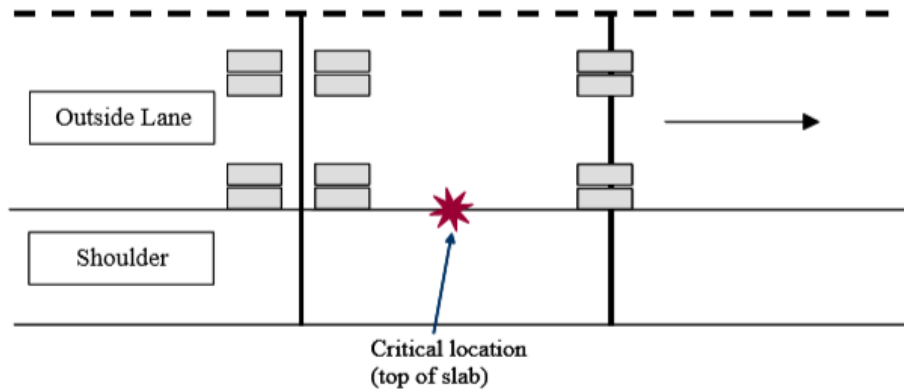Figure 9: PCC slab curl when a negative temperature gradient is present.

Figure 10: Critical loading position for the development of top-down cracking (Applied Research Associates (ARA), 2004).

A study conducted at Michigan State University analyzed the effect of multi-axle trucks on PCC pavement fatigue (Chatti, et al., 2009). The investigation involved an analysis of in-service pavement distress data, a mechanistic analysis, and a laboratory investigation. The results of this study indicate that multi-axles may be less damaging in fatigue than single and tandem axles. Further evaluation of this observation is necessary to determine the optimal axle configurations for superload vehicles to minimize the development of fatigue cracking.

Both the transient gradients and the built-in gradient must be considered when estimating stress in a pavement. The "built-in" gradient is typically define as the composite of the long-term drying shrinkage coupled with the temperature gradient at the time the concrete sets (i.e., at the zero-stress time). Pavement ME assumes the net effect of this to factors results in an equivalent temperature difference of -10°F. This gradient is considered in combination with the transient temperature and moisture gradients for design purposes and therefore increases the magnitude of top-down cracking and decreases the magnitude of bottom-up cracking.

6.1.2 Faulting

Faulting is defined as the difference in elevation between the approach, or unloaded, slab and the leave, or loaded, slab. Faulting occurs as a result of the pumping mechanism. Pumping occurs when free moisture underneath the PCC slab moves across the joint, carrying (or "pumping") loose fines in the base or subbase out of the joint and beneath the approach slab. This results in a void forming under the leave slab and a buildup of fines under the approach slab that cause a higher difference in elevation between the approach and leave slabs, as shown in Figure 11.
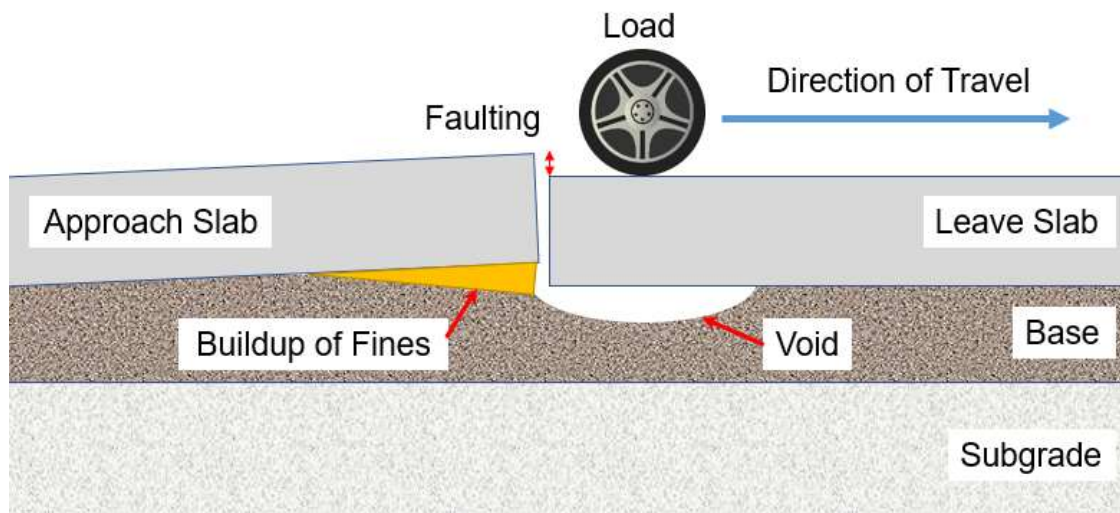

Figure 11: The pumping mechanism results in the formation of a buildup of fines and a void under the approach and leave slabs, respectively, and the development of faulting.

For pumping to occur, four factors must be present:

- Differential Deflections, which is defined as a difference in elevation between the approach and leave slabs.
- Unstabilized fines in the base or subbase that are free to move
- Free moisture underneath the PCC slab that assists in transporting fines across the joint.
- Vehicle loads

The effectiveness of load transfer mechanisms can be calculated using load transfer efficiency (LTE), shown in Equation 1.

$$LTE = \frac{\delta_{UL}}{\delta_L} * 100\% \tag{1}$$

where,

LTE is the load transfer efficiency of the joint, %

δ_{UL} is the corner deflection of the unloaded slab, in

δ_L is the corner deflection of the loaded slab, in

Over time, load transfer mechanisms in PCC pavements become less effective due to repeated traffic loads. Aggregate interlock decreases due to a reduction in the shear capacity of the joint because of repeated vehicle loads. Additionally, opening and closing of the joint due to temperature changes cause hourly variation in joint stiffness for undoweled pavements. The ability of the dowel to transfer load decreases due to socketing around the dowel. The socketing is a result of high contact stresses in the concrete surrounding concrete causing deterioration of the concrete.

Temperature and moisture gradients affect the performance of dowel bars that have socketing around them because the shape of the slab impacts the degree to which the dowel is in contact with the surrounding concrete. When the slab is curled due to a temperature or moisture gradient, the dowel comes into contact with the surrounding concrete and increases the load transfer potential, as seen in Figure 12. The critical condition for faulting, when the load transfer potential is the lowest, occurs when there is no temperature or moisture gradient, as the slab is flat with the dowel positioned with the least contact with the concrete (Alland, 2018).
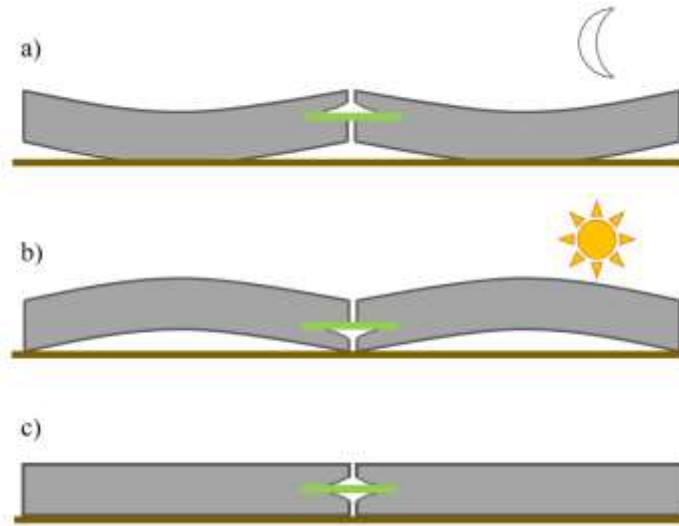
Figure 12: Effect of a) negative b) positive temperature and c) no gradient on the dowel.

6.1.3 Prediction of Critical Structural Response

The finite element method is commonly used to determine the structural responses (i.e., stresses and deflections) of PCC pavements. This can be accomplished using either a 2.5D analysis with pavement-specific programs such as ISLAB (Khazanovich, et al., 2000). Pavement-specific programs 3D FEM analysis programs, such as EverFE (Davids, 2003), or 3D general-purpose finite element software such, as ABAQUS (ABAQUS, 2011), are also available.

The pavement responses incorporated into the design process in Pavement ME for predicting distress in JPCP were determined using ISLAB (Applied Research Associates (ARA), 2004). ISLAB was selected due to is accuracy and computational efficiency (Applied Research Associates (ARA), 2004). Moreover, numerous models can be batched and processed very efficiently in ISLAB. Therefore, ISLAB was selected for determining the tensile stresses at the top and bottom of PCC slabs for analyzing the effects of superloads.

EverFE allows users to model dowels by specifying a stiffness representing the interaction between the dowel and the concrete or by specifically selecting the looseness of the dowel. In addition, the model outputs the estimated dowel deflection and contact stress between the dowel and concrete, which can then be used to estimate the potential for increased dowel looseness. Unlike EverFE, ISLAB models joint load transfer using spring elements so stresses and deflections in the dowels cannot be determined. EverFE was also chosen over other general purpose finite element programs due to its computational efficiency.

6.2 Prediction of PCC Pavement Fatigue Damage

6.2.1 PavementME Fatigue Cracking Model

Fatigue cracking prediction in PavementME involves the following steps (Applied Research Associates (ARA), 2004):

    1. Define climatic and traffic conditions

    2. Calculate stress

    3. Calculate fatigue damage

    4. Determine percent slabs cracked

Once the climatic and traffic data is processed and stress is calculated, fatigue damage is accumulated in a linear fashion using Miner's damage hypothesis (Miner, 1945):

$$FD = \Sigma \frac{n_{i,j,k,l,m,n}}{N_{i,j,k,l,m,n}} \tag{2}$$

where,

    $FD =$ total fatigue damage (top-down or bottom-up), fraction

    $n_{i,j,k,l,m,n} =$ applied number of load applications at condition i, j, k, l, m, n

    $N_{i,j,k,l,m,n} =$ allowable number of load applications at condition i, j, k, l, m, n

    $i =$ age

    $j =$ month

    $k =$ axle type (single, tandem, and tridem for bottom-up cracking; short, medium, and long wheelbase for top-down cracking)

    $l =$ load level

    $m =$ temperature difference

    $n =$ traffic path

The number of applications until failure are predicted based on the following field calibrated model:

$$\log(N_{i,j,k,l,m,n}) = C_1 \left(\frac{MR_i}{\sigma_{i,j,k,l,m,n}}\right)^{C_2} + 0.4371 \tag{3}$$

where,

$N_{i,j,k,l,m,n}$ = allowable number of load applications at condition i, j, k, l, m, n

MR_i = PCC modulus of rupture at age i, psi

$\sigma_{i,j,k,l,m,n}$ = applied stress at condition i, j, k, l, m, n, psi

C_1, C_2 = calibration constants (for global model, $C_1 = 2.0$; $C_2 = 1.22$)

A traffic wander analysis is incorporated into the fatigue damage summation to account for variation in lateral wheel position. To relate fatigue damage to cracking, a model was fit to 242 cracking observations (Sachs, Vandenbossche, & Snyder, 2015). This field calibrated transfer function relates fatigue damage to cracking:

$$CRK = \frac{1}{1+0.52FD^{-2.17}} \tag{4}$$

where,

CRK = predicted amount of bottom-up or top-down cracking, fraction

FD = total top-down or bottom-up fatigue damage, fraction

The current mechanistic-empirical design guide assumes that a slab may crack from either bottom-up or top-down, but not both simultaneously. The following equation determines the total amount of cracking:

$$TCRACK = \left(CRK_{Bottom-up} + CRK_{Top-down} - CRK_{Bottom-up} \cdot CRK_{Top-down}\right) \cdot 100\% \tag{5}$$

where,

$TCRACK$ = total cracking, %

$CRK_{Bottom-up}$ = predicted amount of bottom-up cracking, fraction

$CRK_{Top-down}$ = predicted amount of bottom-up cracking, fraction

6.2.2 Other Fatigue Life Prediction Models

To calculate fatigue damage, the number of applications until failure must be predicted. In the literature, there are many fatigue life prediction models that are derived from different data sets (i.e., laboratory specimens or field sections) and that are of different mathematical forms (e.g., logarithmic, exponential, etc.). Most models, such as the PavementME fatigue life prediction model, predict the number of applications until failure for concrete based on stress ratio. Stress ratio is defined as:

$$SR = \frac{\sigma}{MR} \tag{6}$$

where,

SR = stress ratio

σ = total tensile stress due to traffic and curling at slab edge, psi

MR = modulus of rupture, psi

Other fatigue life prediction models consider factors such as stress range and stress reversals. Since the minimum stresses in a PCC pavement are rarely zero due to environmental conditions, a stress range approach may be able to give a more accurate depiction of the fatigue damage in the pavement. The Aas-Jakobsen fatigue life prediction model, which was developed for concrete beams, incorporates a factor to account for stress range effects (Aas-Jakobsen, 1970). Several researchers adapted the Aas-Jakobsen model for fatigue life assessment of plain concrete beams (Tepfers, 1979; Zhang, Phillips, & Wu, 1996) and PCC pavements (Domenichini & Marchionna, 1981; Hiller & Roesler, 2005). The stress range is not currently accounted for in the fatigue damage calculation in PavementME. For this to be done, the environmental stresses throughout the life of each calibration section would need to be known.

Several studies have shown that alternating tension-compression cycles, or stress reversals, have a negative impact on the fatigue life of concrete (Cornelissen, 1984; Zhang, Phillips, & Wu, 1996). The fatigue life prediction models developed in these studies consider both the tensile and compressive behavior of concrete. The fatigue life prediction model developed by Zhang et al. for plain concrete accounts for stress reversals along with loading frequency. In preliminary finite

element analyses of superload vehicles on PCC pavements, it is observed that superload vehicles can induce stress reversals (albeit at low stress states).

Many fatigue life prediction models are derived from laboratory beam or slab fatigue tests. In laboratory tests, concrete specimens can be forced to fail at a desired location. In the field, PCC pavements exhibit fatigue failure at a variety of different locations due to environmental and support conditions. Moreover, as exhibited by Roesler and Barenberg, the flexural strength of fully supported concrete slabs is larger than the modulus of rupture of a concrete beam (Roesler & Barenberg, 1999). This is known as the "size effect". For these reasons, it is important to use fatigue life prediction models for the prediction of concrete pavements with caution when they were developed based on data from beam laboratory specimens.

In Table 4, a summary of concrete fatigue life prediction models available in the literature is shown.

Table 4: Summary of Concrete Fatigue Life Prediction Models in Literature

Fatigue Model	Data Source	Equation	Comments
ARA 2004 (PavementME Fatigue Model)	JPCP Field Sections	$\log(N_{i,j,k,l,m,n}) = C_1 \left(\dfrac{MR_i}{\sigma_{i,j,k,l,m,n}} \right)^{C_2} + 0.4371$	Failure corresponds to 50% slab cracking
Packard and Tayabji 1985 (PCA Fatigue Model)	Laboratory Beams	$\log(N) = 11.737 - 12.077SR$ $for\ SR \geq 0.55$ $N = \left[\dfrac{4.2577}{SR - 0.4325} \right]^{3.268}\ for\ 0.45 < SR < 0.55$ $N = Unlimited\ for\ SR \leq 0.45$	
Darter 1977 (Zero-Maintenance Fatigue Model)	Laboratory Beams	$\log(N) = 17.61 - 17.61SR$ $\log(N) = 16.61 - 17.61SR$	50% Probability of Failure 24% Probability of Failure
Darter et al. 1993 (Calibrated Mechanistic Design Fatigue Model)	AASHO Road Test Field Sections	$\log(N) = \left[\dfrac{-SR^{-5.367}\log(1-P)}{0.0032} \right]^{0.2276}$	P = Probability of Failure
Darter et al. 1988 (ERES/COE Fatigue Model)	Corp of Engineers Field Sections	$\log(N) = 2.13SR^{-1.2}$	
Treybig et al. 1977 (ARE Fatigue Model)	AASHO Road Test Field Sections	$N = 23{,}440SR^{-3.21}$	
Majidzadeh and Ilves 1983 (RISC Distress Function)	AASHO Road Test Field Sections	$N = 22{,}209SR^{-4.29}$	
Foxworthy 1985 (Foxworthy Field Fatigue Model)	Corp of Engineers Field Sections	$\log(N) = 1.323\dfrac{1}{SR} + 0.588$	

Roesler 1998	Laboratory Slabs	$N = \left[\dfrac{1.2968}{SR}\right]^{32.57}$	
Aas-Jakobsen 1970	Laboratory Beams	$SR = 1 - \beta(1-R)\log(N)$	β = Material Parameter R = Ratio of Minimum Applied Stress to Maximum Applied Stress
Tepfers 1979	Laboratory Beams	$SR = 1 - \beta(1-R)\log(N)$	Adjusted Aas-Jakobsen 1970 β to $\beta = 0.0685$ for concrete
Domenichini and Marchionna 1981	Laboratory Beams	$SR = 1 - \beta(1-R)\log(N)$	Adjusted Tepfers 1979 $\beta = 0.0685$ to $\beta = 0.0954$ to account for field factors and material property variation
Cornelissen 1984 (Flexural Stress Reversals)	Laboratory Beams	$\log(N) = 9.91 - 7.45\dfrac{\sigma_{max}}{MR} + 1.93\dfrac{\sigma_{min}}{f'c}$	σ_{max} = Maximum Flexural Stress σ_{min} = Minimum Compressive Stress $f'c$ = Compressive Strength
Zhang et al. 1996 (Flexural Stress Reversals)	Laboratory Beams	$\dfrac{\sigma_{max}}{f_c} = C_f[1 - (1 - R')\beta\log(N)]$	σ_{max} = Maximum Stress σ_{min} = Minimum Stress f_c = Relevant Static Strength (Tensile or Compressive) C_f = Frequency Influence Coefficient $R' = \dfrac{\sigma_{min}}{\sigma_{max}}\dfrac{MR}{f'c}$ β = Material Parameter (0.0685 for concrete)

6.3 Additional Considerations for Fatigue Cracking

6.3.1 Limitations of Miner's Linear Damage Hypothesis

In most pavement design procedures, including the PavementME design procedure, damage is assumed to accumulate linearly in accordance with Miner's Hypothesis (Miner, 1945). However, several studies have demonstrated that concrete accumulates damage nonlinearly (Holmen, 1982; Oh, 1991a). Concrete damage accumulation has been shown to occur in three distinct stages: a decelerating accumulation stage, a linear accumulation stage, and an accelerating accumulation stage (Vega, Bhatti, & Nixon, 1995). Therefore, if a superload is applied to a pavement during the accelerating accumulation stage, the damage may be more significant than when applied in the linear stage. Miner's hypothesis does not account for the damaged stress state of the concrete caused by traffic loadings accumulated prior to the application of the superload. Pavement age may be an influential factor when characterizing damage caused by superloads since these vehicles can travel on older roads.

6.3.2 Fracture Mechanics

Fracture mechanics approaches are often used to explain mechanisms of fatigue damage accumulation that are not directly shown by S-N curves and Miner's damage hypothesis (Kolluru, O'Neil, Popovics, & Shah, 2000; Sain & Kishen, 2008; Gaedicke, Roesler, & Shah, 2009). Fracture mechanics models are based on crack propagation. In concrete analyzed by these models, an initial crack is specified at a desired location and a critical crack length is defined as failure. As cyclic loading is applied, the initial crack grows at a decelerating rate. Eventually, the crack begins to grow at an accelerating rate until it reaches the critical crack length (Kolluru, O'Neil, Popovics, & Shah, 2000).

Fracture mechanics is a tool for mechanistic assessment of fatigue crack growth in concrete. However, there are difficulties in implementing fracture mechanics to model fatigue damage in PCC pavements. In the field, a crack can initiate at various locations depending on the fluctuating environmental conditions. Additionally, it is difficult to determine i) an initial crack length and ii) a critical crack length to define as failure. Lastly, the interaction between cracks in PCC pavements (e.g., between bottom-up and top-down cracks) is not fully understood.

6.3.3 Damage Mechanics

Damage mechanics can be used to model the evolution of internal damage in concrete during cyclic loading (Alliche, 2004; Vega, Bhatti, & Nixon, 1995) in lieu of S-N curves and Miner's damage hypothesis. Damage mechanics is a useful tool for mechanistic assessment of the degradation of concrete. However, similar to fracture mechanics, there are difficulties in implementing damage mechanics to model damage in PCC pavements. The variables commonly chosen to represent damage in damage mechanics models (e.g., strain) are difficult to measure for the entire lifetime of a PCC pavement. Additionally, the applicability of many damage mechanics models for concrete would be affected by environmental considerations.

6.4 Prediction of PCC Pavement Faulting

6.4.1 PavementME Faulting Model

Pavement ME determines the faulting accumulation for a pavement structure on a monthly basis through the following steps (Applied Research Associates (ARA), 2004):

1. Define climatic and traffic conditions

2. Calculate deflections

3. Calculate initial maximum faulting

4. Establish joint LTE for the incremental period

5. Establish joint LTE for the incremental period

6. Establish joint LTE for the incremental period

To account for monthly variation in temperature and moisture, the Enhanced Integrated Climatic Model (EICM) is used to calculate values to be used in the faulting equations, such as the freezing ratio (FR) and average annual days with rainfall (WetDays). In addition, the EICM generates hourly temperature profiles of the pavement structure to be used to determine the curling of the slab due to temperature gradients.

The PavementME faulting model incorporates the differential energy concept, which can be calculated with Equation (7).

$$DE = \frac{k}{2}(\delta_L + \delta_U)\frac{1-\frac{LTE}{100}}{1+\frac{LTE}{100}} \tag{7}$$

where,

DE = differential energy of the system, psi

k = modulus of subgrade reaction, psi/in

δ_L = corner deflection under the loaded slab, in

δ_{UL} = corner deflection under the loaded slab, in

LTE = load transfer efficiency of the joint, %

The differential energy of the system is significantly influenced by the LTE of the system. The total LTE is function of three mechanisms of load transfer, which are individually determined and adjusted monthly:

$$LTE = 100[1 - \left(1 - \frac{LTE_{dowel}}{100}\right)\left(1 - \frac{LTE_{agg}}{100}\right)\left(1 - \frac{LTE_{base}}{100}\right)] \tag{8}$$

where,

LTE = joint load transfer efficiency, %

LTE_{dowel} = load transfer efficiency if only the dowel contributes, %

LTE_{agg} = load transfer efficiency if only aggregate interlock contributes, %

LTE_{base} = load transfer efficiency if only the base contributes, %

1. Calculate incremental change in faulting for given month

Using the calculated joint LTE, the maximum mean transverse faulting and incremental change in faulting for a given month is determined with Equations (9 - 13). The model then calculates the loss of load transfer capacity for each of the three mechanisms of LTE (aggregate interlock, dowels, and base).

$$\Delta Fault_i = C_{34} * (FAULTMAX_{i-1} - \Delta Fault_{i-1})^2 \qquad (9)$$

$$FAULTMAX_i = FAULTMAX_0 + C_7 * \sum_{j=0}^{m} DE_j * \text{Log}(1 + C_5 * 5.0^{EROD})^{C_6} \qquad (10)$$

$$FAULTMAX_0 = C_{12} * \delta_{curl} * \left[\text{Log}(1 + C_5 * 5.0^{EROD}) * \text{Log}\left(\frac{P_{200}*\text{WetDays}}{p_s}\right) \right]^{C_6} \qquad (11)$$

where,

$\Delta Fault_i$ = incremental change in mean transverse joint faulting for month i (current month), in

$FAULTMAX_i$ = maximum mean transverse joint faulting for month i (current month) , in

$FAULTMAX_0$ = initial maximum mean transverse joint faulting, in

$EROD$ = base-subbase erodibility factor, which is a function of base type

DE_i = sum of the deformation energy in month i (current month), psi/in

δ_{curl} = maximum mean monthly slab corner deflection due to curling and warping, in

p_s = overburden on subgrade, lb

P_{200} = percent subgrade material passing the #200 sieve, %

WetDays = average annual days of rainfall (greater than 0.1 in. rainfall)

$C_1, C_2, \dots C_7$ = calibration coefficients.

$$C_{12} = C_1 + C_2 * FR^{0.25} \tag{12}$$

$$C_{34} = C_3 + C_4 * FR^{0.25} \tag{13}$$

2. Calculate cumulative faulting

The total faulting can be calculated with Equation (14). Steps 4 through 6 are repeated each month up to the end of the last month of the design life of the pavement.

$$Fault_m = \sum_{i=1}^{m} \Delta Fault_i \tag{14}$$

where,

$Fault_m$ = total faulting after m number of months, in

$\Delta Fault_i$ = each monthly change in mean transverse joint faulting, in

As seen in this series of equations used for predicting the development of faulting, there are seven coefficients that must be defined through a calibration process (C8 is defined through the optimization process during calibration). These coefficients have been defined through a national calibration process that included faulting data from 397 JPCP projects and are listed in Table 5 (Sachs, Vandenbossche, & Snyder, 2015).

Table 5: Coefficients from the latest national calibration (Sachs et al. 2015).

Calibration Coefficient	Value
C_1	0.595
C_2	1.636
C_3	0.00217
C_4	0.00444
C_5	250
C_6	0.47
C_7	7.3
C_8	400

6.4.2 Other Faulting Prediction Models

The Portland Cement Association (PCA) developed a faulting model using Miner's linear cumulative damage concept (Wu, Mack, Okamoto, & Packard, 1993). This model does not account

for seasonal variation and assumes linear accumulation of damage. Laboratory studies concluded that damage initially accumulates rapidly before plateauing (Teller & Cashell, 1959; Marcus H. , 1951). The assumption of linear damage accumulation does not account for prior damage at the joint.

Several other models have been developed to predict the development of faulting. As a part of the Strategic Highway Program Project, Simpson et al. used Long Term Pavement Performance (LTPP) data to develop separate faulting models for doweled and undoweled pavements. In these models, faulting is calculated as a function of cumulative 18-kip equivalent single axle loads (ESAL), joint spacing, average modulus of subgrade reaction, pavement age, support conditions, and drainage parameters (Simpson, et al., 1994). These models incorporate climatic conditions through inputs of mean annual precipitation and mean freezing index. Similarly, Yu et al. developed models for doweled and undoweled pavement faulting as part of a Federal Highway Administration (FHWA) Rigid Pavement Performance and Rehabilitation (RPPR) project (Yu, Darter, Smith, Jiang, & and Khazanovich, 1996). Faulting is defined with the same set of parameters as Simpson et al., with the inclusion of the input of the mean number of days with maximum temperature above 90 degrees Fahrenheit. These early faulting models predict faulting in a simplistic manner and are often limited to the dataset with which these models were developed.

Other faulting models used Miner's hypothesis to determine faulting as a function of the ratio of applied ESALs to allowable ESALs. This approach was taken in a recalibration of the 1979 National Pavement Cost Model (NAPCOM) performed with LTPP data by Titus-Glover et. al. (Titus-Glover, Owusu-Antwi, & M.I, 1999) and for models developed by Yu et al. (Yu, Khazanovich, Rao, Darter, & Von Quintus, 1998). Although this approach estimates faulting at various points throughout the life of the pavement, it assumes that the damage accumulation is linear. This approach also does not take into account climatic conditions that vary throughout the year.

6.5 Additional Considerations for Faulting

6.5.1 Damage Accumulation Based on Axle Type

A study was performed at Michigan State University to determine the effect of multi-axle vehicles on the development of faulting through a laboratory study and mechanistic analysis (Chatti, et al., 2009). The laboratory experiment to study joint faulting under multiple axle loadings was

inconclusive due to a lack of significant deterioration despite a large number of load repetitions. While it was determined that multi-axle configurations induce higher damage, there were discrepancies with the results from tandem axle vehicles.

6.5.2 Ultimate Failure

Since superload axle configurations have a high concentration of weight over a given area, there is potential for a single load application to induce failure. The American Concrete Institute published Equation (15) to define the maximum allowable bearing stress as a function of dowel diameter and concrete compressive strength. Even though this relationship is thought to be very conservative, preliminary finite element analyses indicate that several superloads produce bearing stresses that exceed the limits determined using this equation (ACI Committee 325, 1956).

$$\sigma_{allowable} = f'_c \left(\frac{4-d}{3} \right) \tag{15}$$

where,

$\sigma_{allowable}$ = maximum allowable bearing stress between the dowel and the concrete, psi

f'_c = compressive strength of the concrete, psi

d = diameter of the dowel, in

6.5.3 Dowel Looseness Models

To better account for the development of dowel looseness, Buch performed a laboratory investigation to develop a predictive looseness model. In addition to accounting for load magnitude and number of applications, this model takes into account the presence of SiO_2 in the aggregate to estimate the abrasiveness of the concrete. This model has limitations due to the dependence on a non-dimensional parameter that is difficult to directly estimate (Buch & Zollinger, 1996).

7.0 FLEXIBLE PAVEMENTS

7.1 Pavement Response

7.1.1 Fatigue Cracking

Fatigue cracking is a load-related distress that occurs in HMA (hot-mixed asphalt) pavements. The loading conditions on the pavement structure and the thickness of the pavement determine whether the cracking is bottom-up or top-down. Bottom-up cracking is caused by repeated traffic loadings that result in tensile stresses and strains at the bottom of the asphalt layer. This results in the fatigue cracking initiating at the bottom of the asphalt layer, as shown in Figure 13. If the pavement structure has a stabilized base, fatigue cracking will initiate at the bottom of the base.
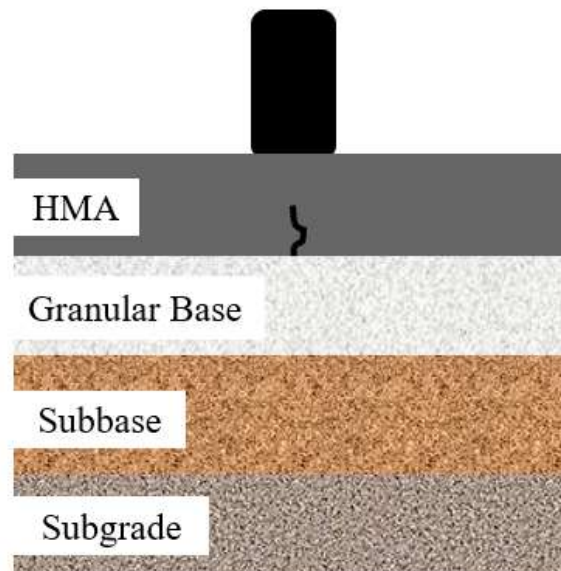
Figure 13: Bottom-Up Cracking in HMA Pavement

The degree of fatigue cracking in HMA pavements has been shown to be affected by the material properties of the asphalt (i.e., dynamic modulus, asphalt content in binder, air content) (Asphalt Institute, 1982). The critical response location longitudinally and transversely for fatigue cracking in HMA pavements is dependent on the structural properties of the pavement structure and the axle configurations in the traffic stream. A detailed analysis is typically needed to determine this location.

7.1.2 Rutting

Rutting, also known as permanent deformation, is a load-related distress that occurs in HMA pavements as a result of vertical compressive strains from an axle load. Factors contributing to the development of rutting in the asphalt layer include overloads, loading during extreme heat, mix instability, and temperature susceptibility. Rutting can also develop in the unbound supporting layers based on the layer properties and thicknesses in the structure. Typically, rutting occurs in the unbound supporting layers because the pavement structure is thin, unstable, or not sufficiently stiff. PavementME assumes that no permanent deformation occurs in chemically stabilized layers (Applied Research Associates (ARA), 2004).

The critical structural response for rutting is vertical strain. The location of the critical strain will vary with each layer. For asphalt and base layers, the critical vertical strains are commonly evaluated at mid-depth of each layer (or each sublayer if defined). For the subgrade, the critical vertical strain is commonly evaluated at the top of the layer.

On the surface of the asphalt, rutting is present as longitudinal depressions. These depressions commonly occur in the wheelpath and can lead to hydroplaning as it affects the surface drainage of the road. The depressions are typically broader if the permanent deformation developed in the lower layers of the pavement structure. The permanent deformation from all layers is accumulated to predict the magnitude of rutting exhibited on the surface of the asphalt.

7.1.3 Prediction of Critical Structural Response

The critical structural response for bottom-up cracking is the horizontal tensile strain at the bottom of the stabilized layer. The critical structure response for rutting is the vertical strain at the specified location previously defined in the layer or sublayer of interest. To determine these strains, HMA pavements are commonly modeled using linear elastic analysis or finite element analysis. Linear elastic analysis is a computationally efficient tool used to calculate the stresses, strains, and displacements in a pavement structure. The pavement models created in layered elastic analysis software are significantly simplified. Some of the assumptions of layered elastic analysis include (Burmister, 1945):

- All layers are linear elastic, isotropic, homogenous
- Pavement layers are infinite in the horizontal direction
- There are no discontinuities (unless specified at the layer surface)

- There are no body forces or initial stresses and strains

Thickness, elastic modulus, and Poisson's ratio are used to define the layer material properties. The interface between layers can be modeled as fully bonded or unbonded. In most layered elastic analysis programs, the contact area of the tire is modeled as a circular footprint. Layered elastic analyses are static analyses; however, the asphalt elastic modulus can be defined to represent a dynamic response along with the layer temperature. Some well-known layered elastic analysis programs include:

- MnLayer (Khazanovich & Wang, 2007)
- LEAF (Hayhoe, 2002)
- JULEA, which is incorporated into Pavement ME (Uzan, 1994)
- WESLEA (Van Cauwelaert, Alexander, White, & Barker, 1989)
- KenLAYER (Huang, 2004)
- BISAR (De Jong, Peutz, & Korswagen, 1979)

LEAF, which is currently used by the FAA for airfield pavements, offers a user-friendly way to manually define the loading configuration applied to the pavement. This is of interest for this superload analysis given the nontraditional axle configurations of these vehicles.

HMA pavements can also be modeled using 2D pavement-specific finite element analysis programs such as ILLI-PAVE (Raad & Figueroa, 1980) and MICH-PAVE (Harichandran, Yeh, & Baladi, 1990) or in 3D using general purpose finite element software packages such as ABAQUS (ABAQUS, 2011). The analysis of HMA pavements using 3D finite element models of often take significantly more time to develop and run than layered elastic analyses or 2D finite element models. However, 3D finite element analysis offers significant potential to model the dynamic interaction of axle loads on the pavement structure. A combination of visco-elastic layered analysis and 3D finite element analysis is currently being used by Khazanovich to assess the impacts of husbandry on HMA pavements (Khazanovich, 2018). A similar approach could be effective for quantifying damage caused by superloads.

7.2 Prediction of HMA Pavement Fatigue Damage

7.2.1 Pavement ME Bottom-Up Fatigue Cracking Model
Like the Pavement ME fatigue cracking model for PCC pavements, fatigue cracking damage is accumulated using a form of Miner's hypothesis (Applied Research Associates (ARA), 2004; Miner, 1945):

$$D = \sum_{i=1}^{T} \frac{n_i}{N_i} \tag{16}$$

where,

        D = damage, fraction

        T = total number of periods

        n_i = actual traffic repetitions for period i

        N_i = allowable failure repetitions under conditions prevailing in period i

The number of applications until failure is predicted using a modified form of the Asphalt Institute fatigue model (Applied Research Associates (ARA), 2004; Asphalt Institute, 1982):

$$N_f = 0.00432 * C\beta_{f1}k_1 \left(\frac{1}{\varepsilon_1}\right)^{k_2\beta_{f2}} \left(\frac{1}{E}\right)^{k_3\beta_{f3}} \tag{17}$$

$$C = 10^M \text{ (Correction term for effective binder content)} \tag{18}$$

$$M = 4.84 \left(\frac{V_b}{V_a+V_b} - 0.69\right) \tag{19}$$

where,

        N_f = allowable number of applications until failure

        V_b = effective asphalt content by volume, %

        V_a = air voids in asphalt mixture, %

        ε_1 = tensile strain at critical location (determined from structural response model)

        E = dynamic modulus of the asphalt, psi

        k_1, k_2, k_3 = global calibration factors (for global model, k_1 = 3.75; k_2 = 2.87; k_3 = 1.46)

β_{f1}, β_{f2}, β_{f3} = local calibration factors (for global model, β_{f1} determined as function of thickness; β_{f2} = 1.38; β_{f3} = 0.88)

This field calibrated transfer function relates fatigue damage to bottom-up cracking (AASHTO, 2008). A total of 405 distress observations were used to perform the calibration.:

$$FC = \left(\frac{6000}{1+e^{(C_1 * C_1' + C_2 * C_2' \log_{10}(D*100))}}\right) * \left(\frac{1}{60}\right) \qquad (20)$$

$$C_2' = -2.40874 - 39.748 * (1 + h_{ac})^{-2.856} \qquad (21)$$

$$C_1' = -2 * C_2' \qquad (22)$$

where,

D = fatigue damage, fraction

C_1, C_2 = local calibration factors (for global model, C_1 = 1.31; C_2 determined as function of thickness)

While this is a sophisticated approach for predicting fatigue cracking, the correlation coefficient between the predicted and observed percent fatigue cracking is only 0.275.

7.2.2 Other Fatigue Life Prediction Models

The number of applications until failure for a given HMA pavement is commonly predicted based on the critical tensile strain at the bottom of the asphalt and the dynamic modulus. Asphalt fatigue prediction models are either derived from laboratory tests or field sections. For the models developed based on laboratory data, tests are performed under either under constant strain or constant stress loading conditions. Constant strain conditions represent thin asphalt layers while constant stress conditions represent thick asphalt layers.

In the NCHRP 1-10 report, Finn et al. developed a field-calibrated model to predict the number of applications until failure. Failure is defined as 10% and 45% cracking using Equations 23 and 24, respectfully, (Finn, et al., 1977):

$$\log N_f = 15.947 - 3.281 * \log\left(\frac{\varepsilon_t}{1*10^{-6}}\right) - 0.854 * \log\left(\frac{E^*}{1*10^3}\right) \qquad (23)$$

$$\log N_f = 16.086 - 3.281 * \log\left(\frac{\varepsilon_t}{1*10^{-6}}\right) - 0.854 * \log(\frac{E^*}{1*10^3}) \tag{24}$$

where,

$N_{f(10)}$ = allowable number of applications to 10% fatigue cracking

$N_{f(10)}$ = allowable number of applications to 10% fatigue cracking

ε_t = critical tensile strain at the bottom of the asphalt layer, in/in

E^* = dynamic modulus of the asphalt, psi

Shell International developed the Shell-Oil Model as a function of same parameters using a wide range of asphalt mixtures and 20% fatigue cracking as failure (Claessen, Edwards, Sommer, & Uge, 1977):

$$N_f = 0.0685(\varepsilon_t)^{-5.671}(E)^{-2.363} \tag{25}$$

The Shell International model was modified to create separate models for constant strain and constant stress conditions (Bonnaure, Gravois, & Udron, 1980). The penetration index and amount of binder content were incorporated into these models.

The Asphalt Institute predicted the number of applications until failure (defined as 20% cracking in the wheelpath) for asphalt based on the critical tensile strain at the bottom of the asphalt layer, the dynamic modulus of the asphalt, and mixture properties (Asphalt Institute, 1982):

$$N_f = 0.0796C(\varepsilon_t)^{-3.291}(E)^{-0.854} \tag{26}$$

$$C = 10^M \tag{27}$$

$$M = 4.84(\frac{V_b}{V_a+V_b} - 0.69) \tag{28}$$

A modified version of this model was incorporated into Pavement ME. Several other bottom-up fatigue cracking models include:

- MichPave (Baladi, 1989)
- SHRP (Lytton, 1993)

- MnPAVE (Tanquist, 2012)

Prediction of HMA Pavement Rutting

7.3.1 PavementME Rutting Models

Asphalt Permanent Deformation

The asphalt permanent deformation model incorporated into Pavement ME defines permanent deformation as a function of the temperature and thickness of the asphalt, number of load repetitions and depth of the analysis point (Applied Research Associates (ARA), 2004).

$$\frac{\varepsilon_p}{\varepsilon_r} = k_z \beta_{r1} 10^{k_1} T^{k_2 \beta_{r2}} N^{k_3 \beta_{r3}} \tag{29}$$

$$k_z = (C_1 + C_2 * depth) * 0.328196^{depth} \tag{30}$$

$$C_1 = -0.1039 * H_\alpha^2 + 2.4868 * H_\alpha - 17.342 \tag{31}$$

$$C_2 = 0.0172 * H_\alpha^2 - 1.7331 * H_\alpha + 27.428 \tag{32}$$

where,

ε_p = plastic strain, in/in

ε_r = resilient strain, in/in

T = layer temperature, °F

N = number of load repetitions

H_{ac} = total asphalt thickness, in

$depth$ = depth of evaluation, in

k_1, k_2, k_3 = global calibration factors (for global model, k_1 = -2.45, k_2 = -3.01, k_3 = 0.22)

$\beta_{r1}, \beta_{r2}, \beta_{r3}$ = local calibration factors (for global model, β_{r1} = 0.40, β_{r2} = 0.52, β_{r3} = 1.36)

Unbound Layers Permanent Deformation

It is assumed in Pavement ME that only the asphalt surface layer as well as unbound layers are susceptible to permanent deformation, and not deformation that might develop within a stabilized

base layer. The permanent deformation caused in unbound layers and the subgrade are estimated in Pavement ME using the following equation:

$$\delta_a(N) = \beta_{s_1} k_1 \varepsilon_v h \left(\frac{\varepsilon_0}{\varepsilon_r}\right) |e^{-(\frac{\rho}{N})^{\beta}} \tag{33}$$

where,

δ_a = permanent deformation for the layer/sublayer, in

N = number of load repetitions

ε_0, β, and ρ = material parameters based on laboratory tests

ε_r = resilient strain imposed in laboratory test to obtain material parameters, in/in

ε_v = average vertical strain in the layer/sublayer, in/in

h = thickness of the layer/sublayer, in

k_1 = global calibration factor (0.965 for base, 0.675 for subgrade)

β_{s1} = local calibration factor (1 for base, 1 for subgrade)

Total Permanent Deformation

In Pavement ME the total permanent deformation that develops at the pavement surface is estimated based on the summation of the deformation accumulated in each layer using the following:

$$PD = \sum_{i=1}^{nsublayers} \varepsilon_p^i h^i \tag{34}$$

where,

PD = pavement permanent deformation, in

$nsublayers$ = number of sublayers

ε_p^i = total plastic strain in sublayer i, in/in

h_i = thickness of sublayer, in

7.3.2 Other Rutting Prediction Models

Rutting prediction models are available for each individual layer as well as models that predict total pavement rutting. Models, such as the ones incorporated in Pavement ME, account for rutting in the asphalt and unbound layers individually.

Asphalt Permanent Deformation

Asphalt rutting prediction models are commonly developed by relating the ratio of accumulated permanent strain over the vertical compressive strain to the asphalt temperature and the number of load applications. The asphalt rutting prediction models developed by Leahy (Leahy, 1989), Ayres (Applied Research Associates (ARA), 2004), and Kaloush and Witczak (Applied Research Associates (ARA), 2004) were of this form. The equation used in Pavement ME was developed based on the Kaloush and Witczak model shown in the following two equations:

$$\frac{\varepsilon_p}{\varepsilon_v} = 10^{-3.15552} N^{0.39937} T^{1.734} \tag{35}$$

$$\varepsilon_v = \frac{1}{|E^*|}(\sigma_z + \mu\sigma_x - \mu\sigma_y) \tag{36}$$

where,

ε_p = accumulated permanent strain, in/in

ε_v = vertical compressive strain, in/in

N = number of load repetitions

T = pavement temperature, °F

σ_z = stress in z-direction, psi

σ_x = stress in x-direction, psi

σ_y = stress in y-direction, psi

$|E^*|$ = dynamic modulus of asphalt, psi

μ = Poisson's ratio

In addition to Leahy, Ayres, and Kaloush and Witzcak, the Asphalt Institute developed a predictive equation for the permanent deformation of asphalt (Asphalt Institute, 1982).

Unbound Layers Permanent Deformation

The basis for predicting permanent deformation in unbound layers was developed by Tseng and Lytton (Tseng & Lytton, 1989):

$$\delta_a(N) = \beta_1 \left(\frac{\varepsilon_0}{\varepsilon_r}\right) e^{-\left(\frac{\rho}{N}\right)^\beta} \varepsilon_v h \qquad (37)$$

where,

δ_a = permanent deformation for the layer/sublayer, in

N = number of load repetitions

ε_0, β, and ρ = material parameters based on laboratory tests

ε_r = resilient strain imposed in laboratory test to obtain material parameters, in/in

ε_v = average vertical strain in the layer/sublayer, in/in

h = thickness of the layer/sublayer, in

β_1 = calibration factor for unbound materials

To predict $\varepsilon_0/\varepsilon_r$ and the material properties, Tseng and Lytton created predictive equations based on water content of the layer, the deviator stress, the bulk stress, and the resilient modulus of the layer/sublayer (Tseng & Lytton, 1989). Ayres modified these models to account for inconsistences and to condense the granular and subgrade predictions into one set of equations. The final form of the Pavement ME predictive equation was based on adjustments and calibration of the models developed by Ayres (Applied Research Associates (ARA), 2004).

Other unbound layer rutting prediction models available in the literature include:

- Shell International Model (Claessen, Edwards, Sommer, & Uge, 1977) (Subgrade)
- Asphalt Institute (Asphalt Institute, 1982) (Subgrade)
- PAVRUT (Allen & Deen, 1986)
- MnPAVE (Tanquist, 2012)

Models that predict the overall rutting in an entire pavement structure include:

- MICH-PAVE (Baladi, 1989)
- Modified VESYS Model (Ali & Tayabji, 2000)

7.4 Additional Considerations for HMA Pavement Analysis

7.4.1 Limitations of Miner's Linear Damage Hypothesis

Miner's linear damage hypothesis is used in Pavement ME for bottom-up cracking damage accumulation. Like concrete, fatigue damage accumulates nonlinearly in asphalt. If a superload is applied to a HMA pavement late in the service life, the damage may be more significant than if applied earlier in the service life. Pavement age may be important to consider in the evaluation of damage caused by superloads.

7.4.2 University of Nevada-Reno

The damaged state of each layer (i.e., the degraded stiffness) in a HMA pavement can be determined using FWD backcalculation. In the study on FWHA superheavy vehicle study conducted by Hajj et al., this was completed to aid the deflection-based service limit analysis of superheavy vehicles (Hajj, et al., 2018). The approach of using FWD backcalculation for bottom-up cracking damage assessment of damaged pavements may also be of value for superload analysis.

Additionally, in a study conducted by Batioja-Alvarez et al., the pavement damage-associated costs for Nevada HMA pavements were estimated (Batioja-Alvarez, Kazemi, Hajj, Siddharthan, & Hand, 2018). In this study, a damage equivalency between overweight vehicle damage and standard traffic damage was used to determine the reduction in pavement life caused by overweight vehicle passes. This was completed using the calibrated mechanistic-empirical Nevada pavement damage models. Although this study assumed Miner's linear hypothesis for damage equivalency, it provides a framework for evaluating the damage and associated costs caused by overweight vehicles.

As a result of the FWHA study, 3D-Move ENHANCED was developed to statically and dynamically analyze superheavy vehicles. Some of the features of this program include the analysis of nonuniform tire footprints, asphalt layer temperature, and vehicle movement at low speeds (Hajj, et al., 2018). It was noted in this study that the low speeds commonly traveled by superheavy vehicles are critical to model due to the viscoelastic response of the asphalt. However, this program is still in development and is not commercially available yet.

8.0 SUMMARY OF PAVEMENT RESPONSE AND DAMAGE MODELS

Models developed to predict the development of fatigue cracking and faulting in PCC pavements and fatigue cracking and rutting in HMA pavements were assessed with regards to their applicability to superloads. It is evident that the prediction of structural responses for PCC pavement fatigue cracking and faulting can be effectively evaluated in pavement-specific programs such as ISLAB and EverFE. For an accurate prediction of the structural response of an HMA pavement, the time and temperature dependent behavior of the asphalt must be considered. While layered elastic analysis programs offer a computational efficient method of structural response calculation, 3D finite analysis or a visco-elastic layered analysis may be necessary to capture this behavior.

For both PCC and HMA pavements, a number of prediction models have been developed to identify damage induced by environmental and vehicle loadings. For charactering the damage induced by superloads, it is essential to use a damage model that is calibrated with field data to ensure that the predicted damage represents the damage occurring in the field. The damage models incorporated into Pavement ME design are the most promising for analyzing superloads. Pavement ME itself cannot be used to assess damage caused by superloads because it is not capable of evaluating non-standard axle configurations. The next step in this study is to investigate the damage induced by the superloads. This will include investigating the stresses and strains induced into the pavement for both asphalt and concrete pavements. Next, the damage models incorporated into Pavement ME will be used to quantify the percent life consumed by each pass of typical superloads. The applicable of these pavement response and damage prediction models can then be assessed.

9.0 QUANTIFYING THE DEVELOPMENT OF DOWEL LOOSENESS

The purpose of this task is to establish the relationship between the damage to the concrete surrounding dowels in concrete pavements and applied superloads. A computational study was performed to identify critical superload configurations. The study established the amount of contact stress between the dowel and surrounding concrete, which was subsequently used to design a laboratory beam test. The experimental design for the beam test was developed using critical parameters identified from previous dowel studies reported in the literature. The results from the lab tests are presented here and will be used to assess the potential for damage when superloads are applied.

9.1 Dowel Looseness

The use of dowel bars has been shown to be highly effective in mitigating the development of faulting in concrete pavements, but the long-term effectiveness of dowels can be reduced due the accumulation of damage to the concrete surrounding the dowel. This accumulation of damage, which is referred to as dowel looseness, results in a loss joint performance.

Previous studies have been performed to evaluate the development of damage in the concrete surrounding the dowels (Friberg, 1938; Ciolko, Nussbaum, & Colley, 1979; Marcus H. , 1951; Teller & Cashell, 1959). It was shown that increase in looseness results in decreased joint load transfer efficiency (LTE) (Teller & Cashell, 1959). Through these past studies, dowel diameter, pavement depth, joint width, concrete strength, and axle load were identified as the significant parameters affecting the development of dowel looseness.

To date, there has not been a study to evaluate the effect of oversized and overloaded vehicles (referred to as superloads or SLs) on dowel looseness, however, previous studies have developed the methodology for quantifying looseness for typical vehicular loads. To quantify looseness in a doweled joint, a load is applied on one side of the joint. As the load is applied, deflections at the face of both the loaded and unloaded joints are measured. These measurements are used to calculate the differential deflection (DD) of the joint at progressively increasing loads, as shown in the following equation.

$$DD = \delta_L - \delta_{UL} \tag{38}$$

59

where,

DD = Differential deflection, mils;

δ_L = deflection at the loaded face of the joint, mils; and

δ_{UL} = deflection at the unloaded face of the joint, mils

To determine looseness, DD is plotted against applied load. If looseness is present, the DD and load will display a bilinear relationship. At low load magnitudes, there is a rapid rate of increase in DD with load, resulting in a steep slope. The slope of this relationship decreases at an inflection point, and subsequent increases in load cause smaller increases in DD. Looseness is estimated by estimating the intercept of the best fit line of the data after the inflection point. This is shown in Figure 14, where the total DD data is separated into two sections with DD prior to the inflection point shown in blue and DD after the inflection point shown in orange. Looseness was estimated as 2 mils using the portion of the dataset in orange.
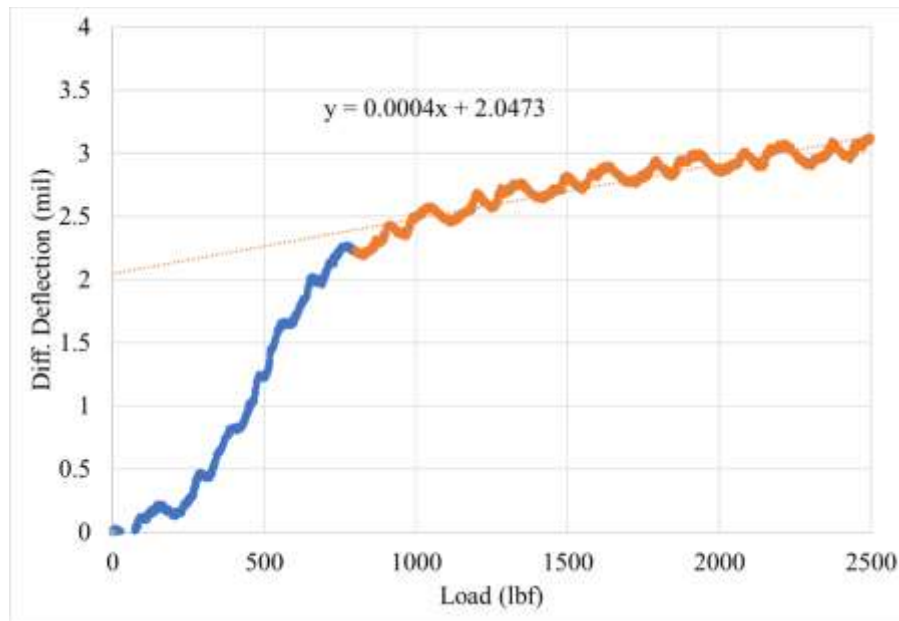
Figure 14: Example looseness plot, where looseness is estimated at approximately 2 mils. The blue portion of the curve is DD prior to the inflection point and the orange portion is DD after the inflection point.

9.2 Computational Analysis

Looseness is generated by the high contact stresses between the dowel and the surrounding concrete, which are referred to as bearing stresses (Friberg, 1938; Marcus, 1951). Therefore, it is

critical that laboratory specimens and loading conditions are designed to generate stresses are representative of those induced by traffic loads. To design the beam test setup accordingly, a series of finite element analyses were performed using the general purpose finite element software ABAQUS™ and the concrete pavement specific software EverFE (Davids, 2003; Inc, A, 2013).

First, EverFE was used to identify bearing stresses and pavement deflections under critical loading cases through a series of six-slab JPCP models, referred to as "full slab" models. A series of analyses was performed to identify the critical dowel bearing stresses under various loading conditions based on a set of typical SL permits provided by the Pennsylvania Department of Transportation (PennDOT). Through this analysis, it was determined that tandem axles are the critical axle configuration for the development of bearing stress. Additionally, the effect of spacing between tandem axle groupings was not significant. The critical tandem axle was the axle with an approximately 46-kip load. The critical loading scenario was when the axle was positioned so that the outermost wheel was directly over the outermost dowel, as shown in Figure 15a. In all cases, the axle was placed adjacent to the outer edge of the slab, which is the critical condition.

A series of ABAQUS™ models were developed to design the small-scale beam test, referred to as the "beam models". An example of a beam model is shown in Figure 15b. Restraint conditions and applied loads were adjusted until bearing stresses calculated in the beam model replicated bearing stresses calculated in the full slab model. It was critical not only to match maximum bearing stress, but also the profile of bearing stress along the length of the dowel. An example of the bearing stress profiles matched between the slab and beam models is shown in Figure 16.
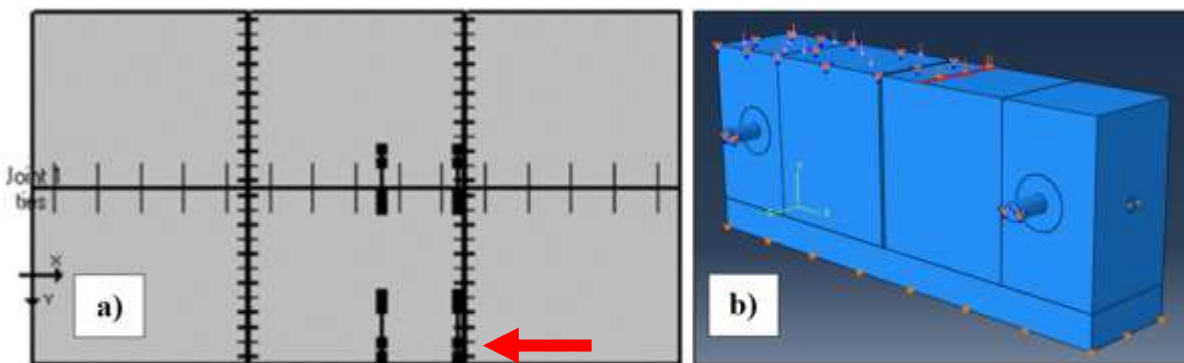
Figure 15: a) Plan view of slab model generated to evaluate critical SL tandem axle, with the critical dowel identified with the red arrow; and b) beam model developed to develop a representative beam specimen testing apparatus.
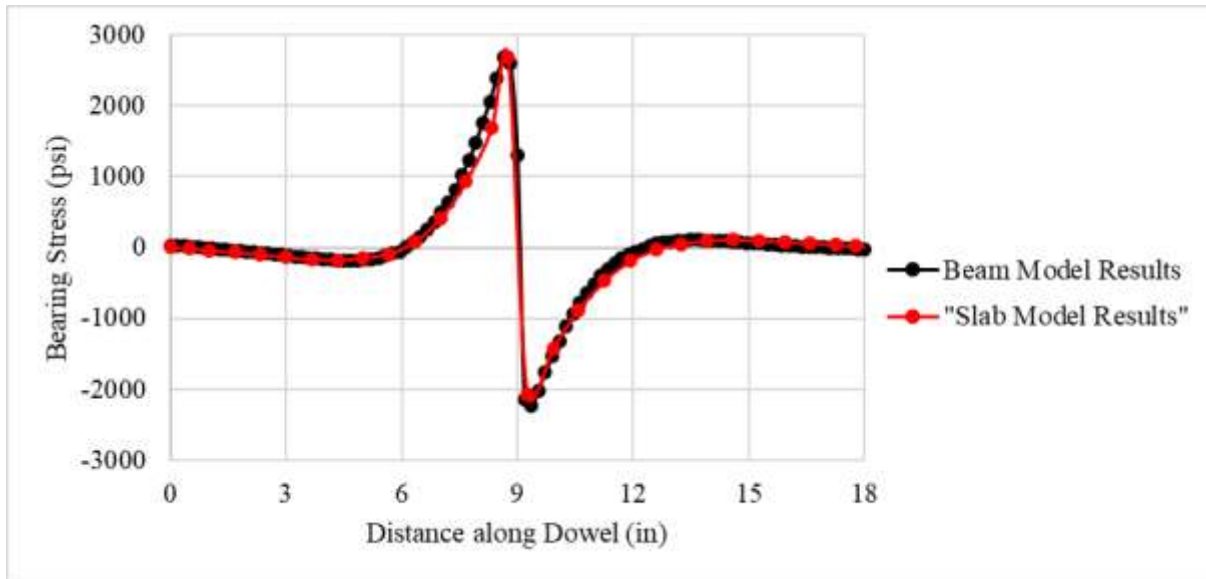
Figure 16: Example of matched bearing stress profiles between the beam and slab models.

9.3 Laboratory Study

9.3.1 Experimental Design

An experimental design was created to capture the effects of critical factors on the development of dowel looseness. Critical factors were identified through previous dowel studies and the computational analysis, and consisted of pavement thickness, load magnitude, concrete strength, and dowel diameter. The three load magnitudes that were tested were representative of an 18-kip standard single axle, 36-kip standard tandem axle, and the critical 46-kip superload tandem axle and are denoted as Low, Medium, and High, respectively. The complete experimental design is shown in Table 6.

Table 6: Experimental Design, where X represents combinations considered, and grayed cells represent unrealistic combinations of dowel diameter and pavement thickness that were not included in the design.

Pavement Thickness (in)	Load	Dowel Diameter (in)		
		1	1.25	1.5
6	Low			(gray)
	Medium	X	X	(gray)
	High			(gray)
8	Low		X	(gray)
	Medium		X	(gray)
	High		X	(gray)
10	Low	(gray)		
	Medium	(gray)	X	X
	High	(gray)	X	X

9.3.2 Test Configuration and Specimen Preparation

The computational analysis was used to design the laboratory setup for the beam test, which is shown in Figure 17. The bearings, vertical restraint, and subgrade were designed to ensure that the beam approximately replicated deflections determined in the computational analysis.
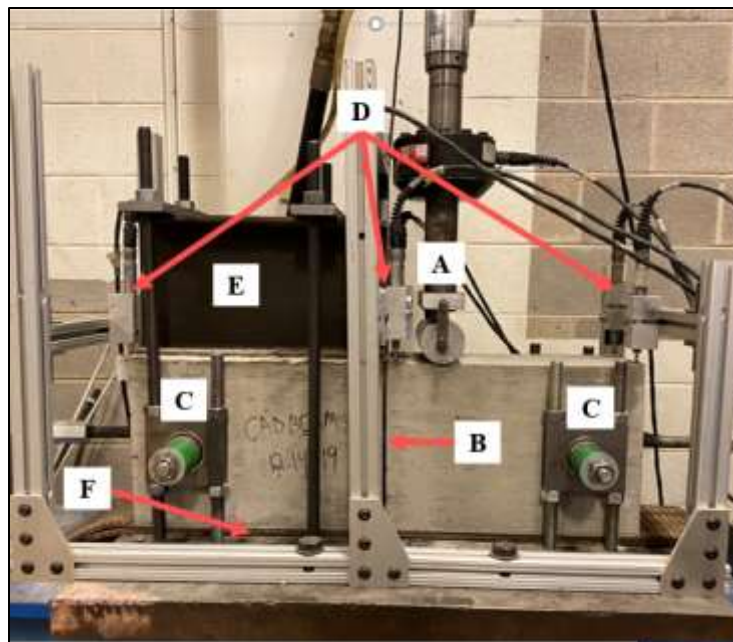
Figure 17: Example beam specimen in the loading frame where A: loading head, B: simulated joint, c) bearings, d) sensors, e) vertical restraint, and f) subgrade.

The sensor frame shown in Figure 17 held seven linear variable differential transformer (LVDT) sensors, which were used to measure the deflection of the surface of the beam with a high degree of precision. The layout of the LVDT sensors is shown in Figure *18*. Deflection measurements from sensors 1 and 2 were averaged to determined δ_L, and sensors 3 and 4 were averaged to determine δ_{UL}. Sensors 5 – 7 were used to verify the desired rotation of the beam under loading was being achieved.
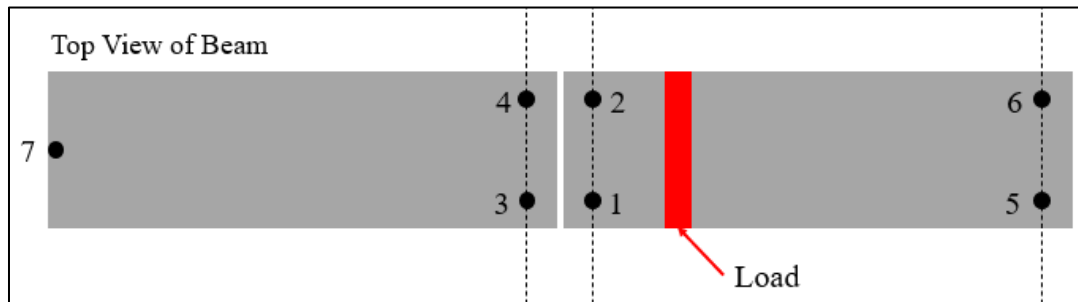
Figure 18: Plan view of beam test sensor layout.

Dowels were positioned mid-depth in each specimen. Each beam was cast with companion cylinders to determine the compressive strength and elastic modulus of the concrete at the time of testing.

9.3.3 Test Procedure

Specimens were subjected to two types of loading sequences during testing. The first consists of loads applied at a frequency of 5 Hz, which are referred to as cyclic loads. The cyclic loads were designed to replicate vehicles traveling across a joint so as to damage to the concrete surrounding the dowel. The frequency of 5 Hz was selected to minimize testing time while ensuring adequate time for the beam to rebound between loads. At specific intervals, cyclic loading was interrupted by a series of static loads. Static loads consisted of 10 loads applied at 0.1 Hz, with 15 seconds of rest between each load application. Data was recorded at 1024 Hz during the static load applications to capture the level of damage at regular intervals. The magnitude of the applied load for both cyclic and static loading was determined through the computational analysis to replicate axle loads. Cyclic and static load sequences are shown in Figure 19a and Figure 19b, respectively.
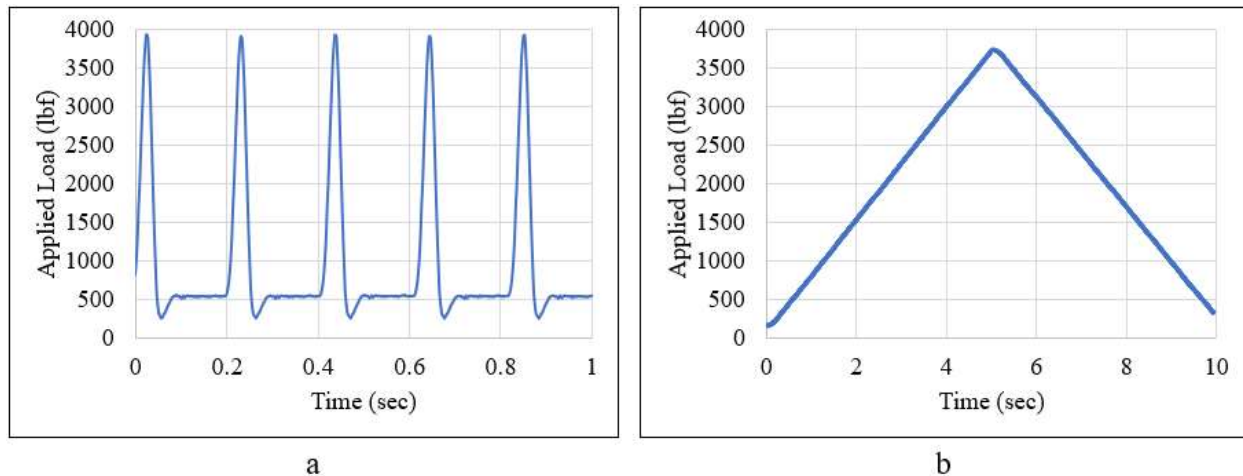
Figure 19: a) Cyclic loading sequence and b) static loading sequence.

Preliminary tests indicated negligible increase in looseness after 1,000,000 to 2,000,000 load cycles. Therefore, cyclic loads were applied for 2,000,000 load cycles, with static load readings taken at specific intervals in between. Previous studies identified that the majority of looseness develops within the first 500,000 cycles, and so more frequent readings were taken in the early stages of the test. Each test took approximately 118 hours to complete.

Upon completion of a test, the data was processed to determine the accumulation of damage. It was observed that all specimen exhibited some looseness prior to the application of a single load cycle. Deflection measurements began to increase with additional loads after 1,000 cycles. As such, the first 1,000 cycles were treated as seating loads and the initial baseline was established at 1,000 cycles. Therefore, all results are reported with respect to the conditions present at 1,000 cycles.

9.3.4 Dowel Looseness Results

The measured deflection and calculated looseness were normalized to the respective values obtained after 1,000 cycles. Summarized laboratory results are presented in Table 7. Each specimen is coded using the following convention: dowel diameter, beam thickness, load level. The low-, medium-, and high-load levels are abbreviated as LL, ML, and HL, respectively. In the case of the 1.25-in dia. dowel, 8-in beam, ML specimen, three replicates were tested. Each replicate is appended with "_a", "_b", or "_c".

Table 7: Summary of normalized beam test results. Each specimen is designated by its dowel diameter, beam thickness, and the load level (LL = low load, ML = medium load, and HL = high load). Replicates are denoted as a, b, and c. f_c' is the compressive strength of the concrete.

Specimen	Avg. f_c' (psi)	Max δ_L (mils)	Max δ_{UL} (mils)	Max DD (mils)	Max Looseness (mils)
1", 6", ML	5,816	41.52	24.23	7.00	5.16
1.25", 6", ML	5,856	27.06	25.33	0.56	1.00
1.25", 8", LL	5,881	12.79	12.45	0.12	0.12
1.25", 8", ML_a	4,715	28.34	20.06	6.34	5.63
1.25", 8", ML_b	6,141	24.49	23.97	0.18	0.20
1.25" 8", ML_c	5,575	31.10	20.92	2.71	2.99
1.25", 8", HL	5,089	36.86	28.11	4.47	3.69
1.25" 10", ML	7,051	20.21	16.77	1.37	0.84
1.25", 10", HL	6,911	37.35	34.51	1.61	1.38
1.5", 10", ML	5,554	16.94	16.09	0.24	0.34
1.5" 10", HL	6,966	23.70	22.10	0.30	0.70

The maximum deflection of the unloaded portion of the beam (δ_{UL}) appears to be most impacted by beam size. However, the deflection of the loaded portion of the beam (δ_L) varies with dowel diameter, concrete strength, and load level. As a result, the differential deflections vary with these parameters. Additionally, test results indicate that looseness is related to differential deflection, which will be discussed in greater detail later.

Average normalized looseness was calculated for each specimen at specific intervals and presented in Figure 20. Error bars indicate the standard deviation of the 10 readings taken at the end of each interval.
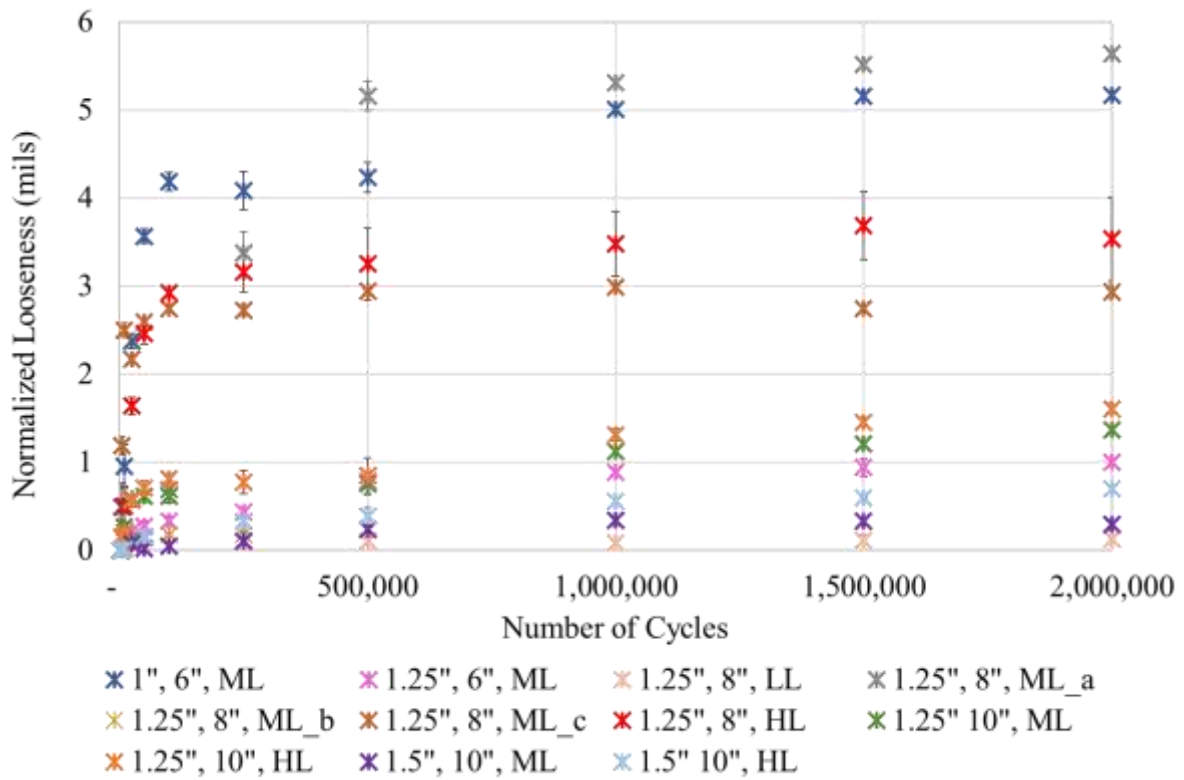
Figure 20: Normalized looseness for all specimens over cyclic load cycles.

The beam test results indicate that the majority of looseness develops early on after a low number of load cycles are applied, specifically within the first 100,000 load cycles, and additional loads after 1,000,000 induce minimal increases in looseness. Results were evaluated on a semi-log plot, as shown in Figure 21.
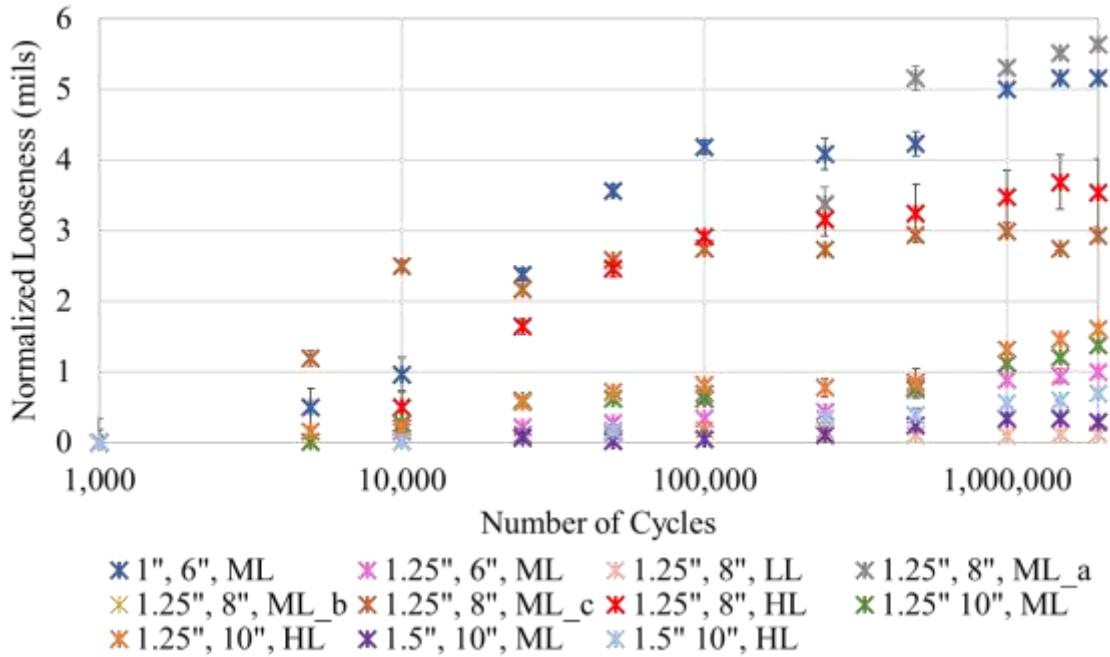
Figure 21: Normalized looseness development for all specimens shown on a semi-log plot.

The results were grouped together based on various factors to enable comparison. These are presented in the following sections.

9.3.4.1 Effect of Beam Size

Average normalized looseness is plotted against the number of load cycles grouped by beam size in the following plots. Figure 22 shows looseness development for 6-in beam specimens with 1-in and 1.25-in dia. dowels subjected to the same load level. As expected, looseness was significantly lower in the 1.25-in dowel specimen as compared to the 1-in dowel specimen, indicating dowel diameter is critical for the mitigation of damage.
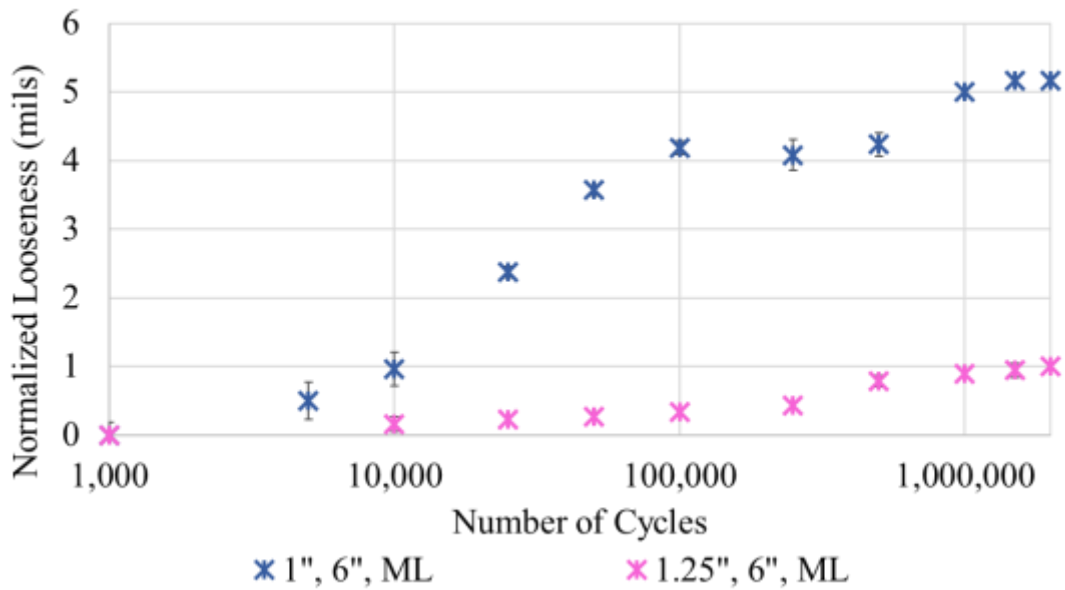
Figure 22: Normalized looseness development for a 6-in beam.

Results from the 8-in beam specimens are presented in Figure 23. Looseness varied with concrete strength and load level. As such, these factors need to be further analyzed independently.

Results from the 10-in beam specimens are presented in Figure 24. It was observed that both DD and looseness were lower for the 10-in beams as compared to the 8-in beams. Additionally, both 1.5-in dia. dowel specimens generated lower looseness as compared to the 1.25-in dowel specimens. Lastly, the high load specimens generated higher looseness for both the 1.25-in and 1.5-in dowel cases. Overall, the looseness measured for these specimens were extremely low, indicating that thicker pavement structures with larger diameter dowels are effective at mitigating the development of looseness.
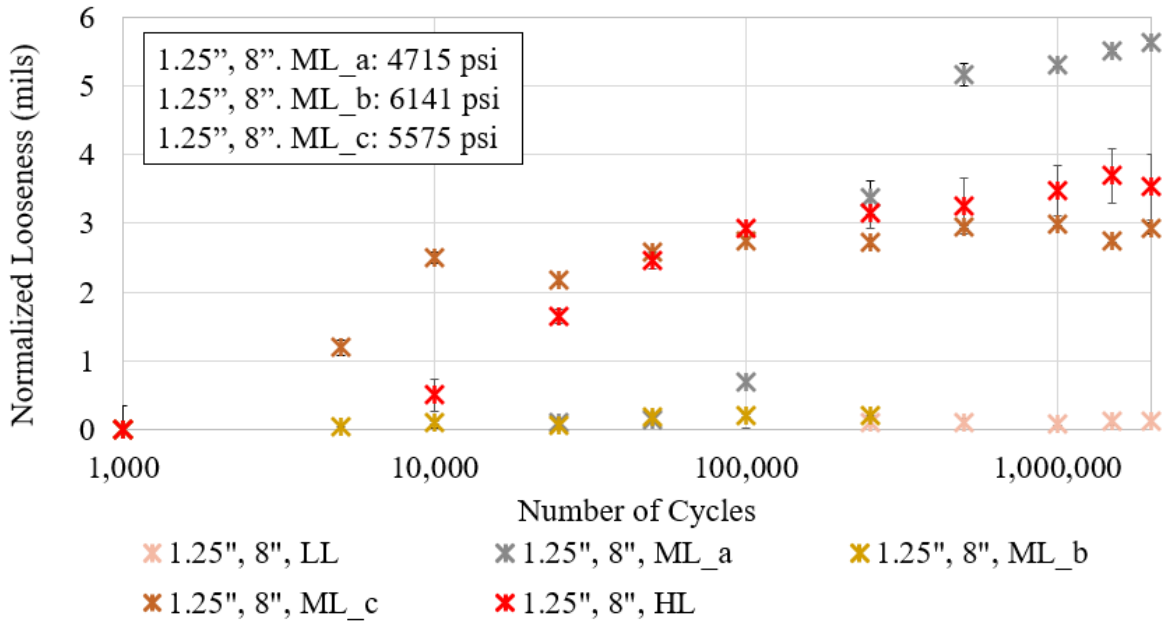
Figure 23: Normalized looseness development for an 8-in beam.
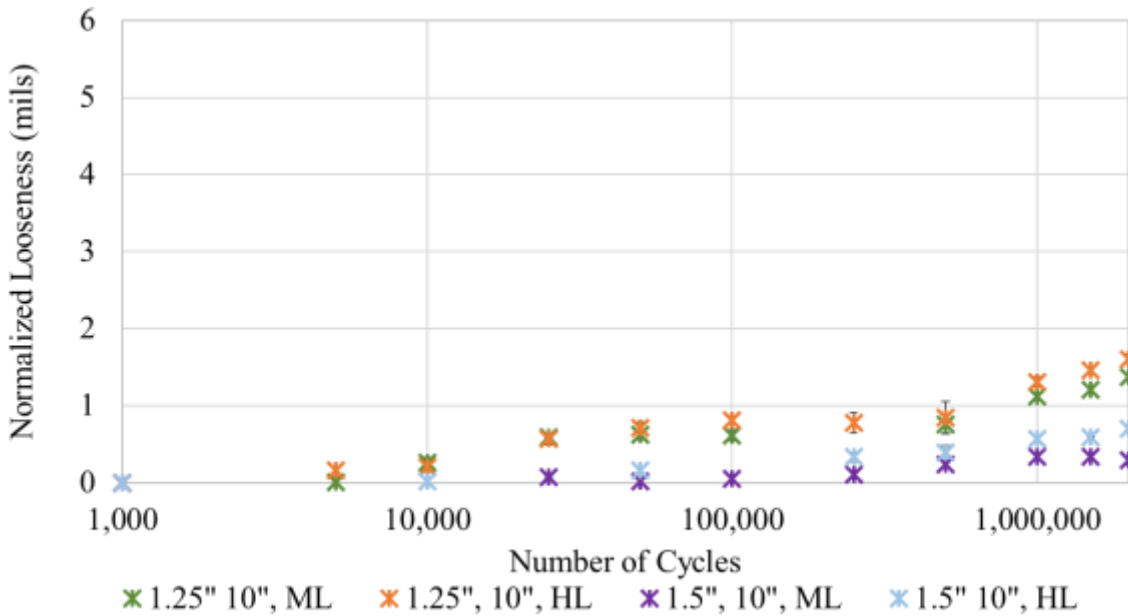
Figure 24: Normalized looseness development for a 10-in beam.

9.3.4.2 Effect of Concrete Strength

Initial tests indicated that strength was a dominating factor which affected the development of looseness. This is seen in the three replicates of the 1.25-in dowel, 8-in beam, ML specimen.

Specimens had average compressive strengths of 4715, 6141, and 5575 psi for specimen ML_a, ML_b, and ML_c, respectively. As shown in Figure 25, the low strength specimen (ML_a) generated significantly higher looseness over 2,000,000 load cycles compared to the medium strength specimen (ML_c) over the same number of load cycles. The high strength specimen (ML_b) generated negligible looseness after 250,000 load cycles.
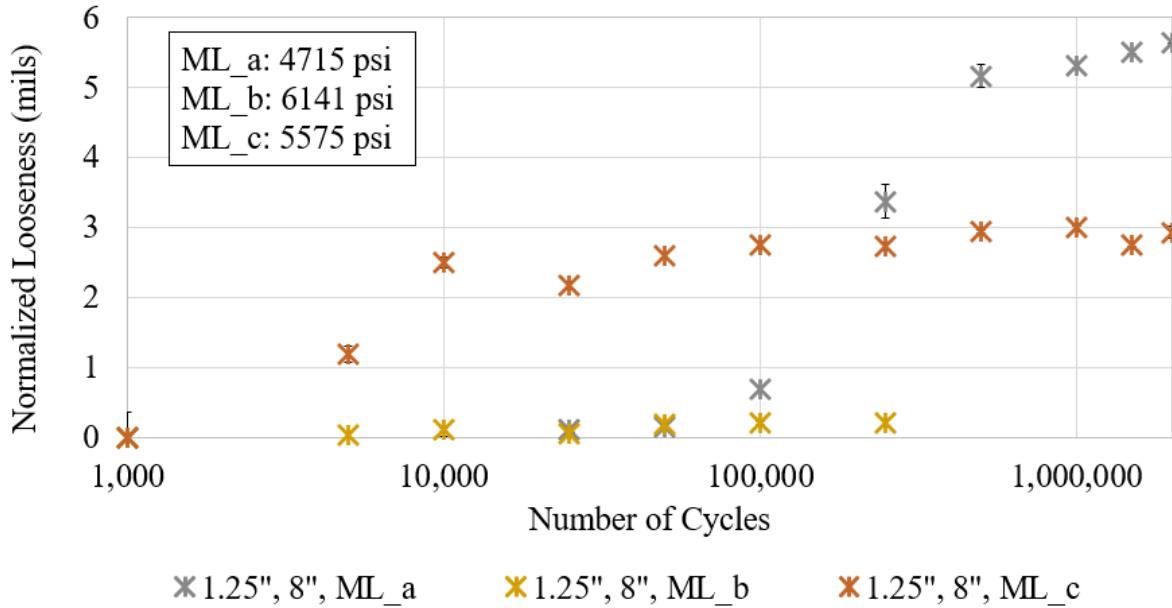
Figure 25: Comparison between three replicates of 1.25 in dowel, 8 in beam with different concrete strengths and a medium load.

9.3.4.3 Effect of Load

The effect of load on looseness development is shown in Figure 26, where 1.25-in doweled specimens in 8-in beams with comparable concrete strengths were subjected to different load levels. The specimen subjected to the low load, representative of an 18-kip single axle, developed minimal looseness over 2,000,000 load cycles. Specimens subjected to both medium and high loads displayed significantly higher levels of looseness. The specimen tested under high loading, representative of the superload vehicle, had the highest looseness after 2,000,000 load cycles. Additionally, it was observed that the medium load specimen had a lower rate of development of looseness. These results indicate that the magnitude of applied load affects the damage experienced by the concrete over a high number of load applications. Similar trends are observed in the 10-in beam specimens shown in Figure 23, where specimens subjected to high loads generate measurably higher levels of looseness compared to those tested at medium load levels.
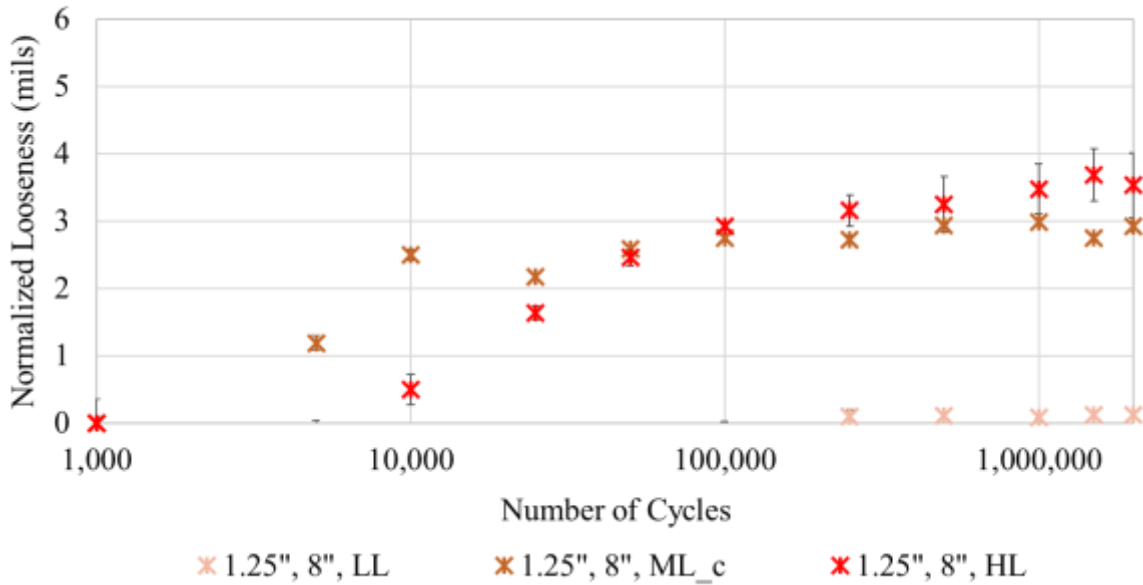
Figure 26: Comparison between 1.25-in dia. dowel, 8-in beam at low, medium, and high loads.

9.3.4.3 Looseness vs. Differential Deflection

It was observed that specimens with measurable differential deflections also displayed a highly linear relationship with measurable looseness values. The relationship between looseness and differential deflection is illustrated in Figure 27. This would suggest that differential deflections develop only if the concrete medium surrounding the dowel has been damaged.
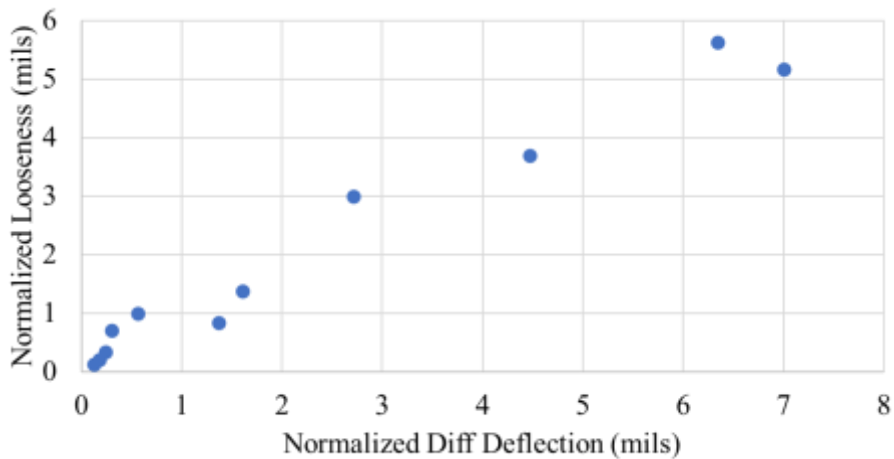
Figure 27: Relationship between looseness and differential deflection.

9.4 Summary of Dowel Looseness

The results from the beam tests indicate several critical findings regarding the development of dowel looseness over a high number of load applications:

- All specimens with measurable differential deflections produced measurable looseness. This indicates that a primary mechanism for development of differential deflection is damage to the concrete medium surrounding the dowel bar.

- The strong linear relationship exists between looseness and differential. Increase in the damage of a specimen manifested itself in proportionately greater differential deflections.

- Deflections on the unloaded portion of the beam were similar between specimens of the same beam thickness. Deflections on the loaded portion of the beam varied by beam thickness, concrete strength, and applied load.

- Looseness development is a non-linear behavior with respect to number of applied loads. This was illustrated in the series of semi-log plots presented.

- For a given beam thickness, an increase in the dowel diameter resulted in a decrease in both looseness and differential deflection.

- Concrete strength has a significant effect on looseness. High strength specimens displayed significantly lower deflections and looseness when compared to lower strength specimens at the end of 2,000,000 load cycles.

- The magnitude of applied load affects the magnitude of looseness developed in a specimen. While these loads are applied over two million load cycles, the higher bearing stresses generated by superloads induces higher damage compared to those induced by typical vehicles, which manifests itself as a higher looseness. A substantial number of loadings are required for this damage to develop.

10.0 SUPERLOAD STRESS ANALYSIS ON JPCP

The purpose of this study is to evaluate the effects of superloads on the fatigue performance of JPCPs. By conducting this analysis, the critical loading conditions and pavement features for superload damage analysis were determined. This section first presents the identification of the critical environmental conditions (i.e., peak temperature gradients) present in typical Pennsylvania JPCPs. Then, the process to characterize Pennsylvania superload axle configurations is discussed. Following this, the approach used to identify the critical positions of superload axle configurations on JPCPs is introduced. Lastly, the maximum tensile stresses caused by superload axle configurations on JPCPs of various designs are presented, with the impact of these stresses on the fatigue life of JPCPs emphasized.

10.1 Environmental Conditions

Before the maximum tensile stress caused by superload axle configurations can be quantified, it is essential to identify the critical environmental conditions that develop in Pennsylvania JPCPs. To do this, the Enhanced Integrated Climatic Model (EICM) was utilized to numerically evaluate hourly temperature profiles through the JPCP over its service life (Larson & Dempsey, 2003). By utilizing the capabilities of the EICM, the peak temperature gradients can be identified and related to the critical times of a day when a superload might be applied to a JPCP.

A concrete pavement design, selected to be representative of a typical Pennsylvania interstate JPCP (Pennsylvania Department of Transportation,, 2020a; 2020b), was developed for the EICM analysis. The pavement structure consists of a concrete slab, an asphalt treated permeable base (ATPB) layer, an A-1-a crushed gravel subbase layer, and A-2-6 subgrade. North American Regional Reanalysis (NARR) climate data was used, and Pittsburgh, Pennsylvania was defined as the climate station. Figure 28 shows the layers of the pavement structure and Table 8 provides the inputs assumed for the EICM analysis. From the predicted temperature distributions, the equivalent linear temperature gradients were then evaluated.
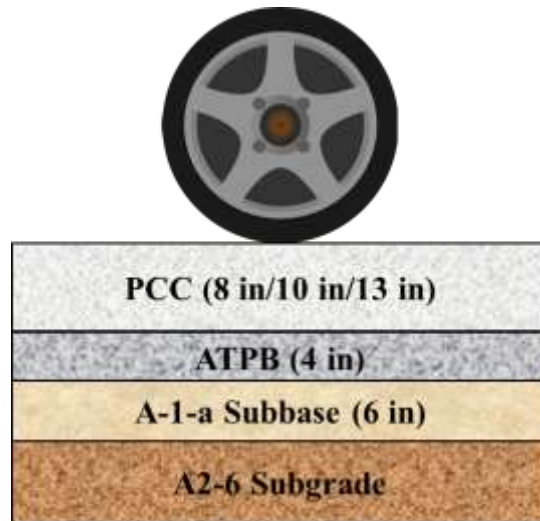
Figure 28: Representative Pennsylvania JPCP design for EICM analysis.

Table 8: Inputs for EICM analysis.

Type of Pavement	New Rigid
Climate Station/Data	Pittsburgh (NARR)
Groundwater Table Depth	10 ft
Surface Shortwave Absorptivity	0.85
Shoulder Type	Concrete
Concrete Layer Thicknesses	8/10/13 in
Concrete Unit Weight	146 pcf
Concrete Thermal Conductivity	1.25 BTU/hr-ft-°F
Concrete Heat Capacity	0.28 BTU/lb-°F
ATPB Layer Thickness	4 in
ATPB Unit Weight	150 pcf
ATPB Thermal Conductivity	0.67 BTU/hr-ft-°F
ATPB Heat Capacity	0.23 BTU/lb-°F
Subbase Soil Classification	A-1-a
Subbase Layer Thickness	6 in
Subgrade Soil Classification	A2-6

Note: Materials properties recommended in Pavement ME for A-1-a and A2-6 were adopted for the EICM analysis (ARA 2004).

The frequency distribution of linear temperature gradients present in JPCPs in Pennsylvania is shown in Figure 29. As shown, concrete slabs of all thicknesses are subjected to temperature gradients between -2.5 °F/in and 3 °F/in for the majority of the design life. Moreover, 8-in concrete slabs are subjected to temperature gradients outside this range for less than 3% of

the design life while 10-in and 13-in concrete slabs are subjected to temperature gradients outside this range for less than 1% of the design life. Therefore, linear temperature gradients of -2.5 °F/in, 0 °F/in, and 3 °F/in were considered for the superload finite element analysis. It should be noted that a built-in temperature gradient and an equivalent linear temperature gradient representing the irreversible moisture gradient were not accounted for in this analysis but would result in an increase in the magnitude of the negative temperature gradient and a decrease in the positive temperature gradient (Nassiri & Vandenbossche, 2012).

(a)

(b)

76
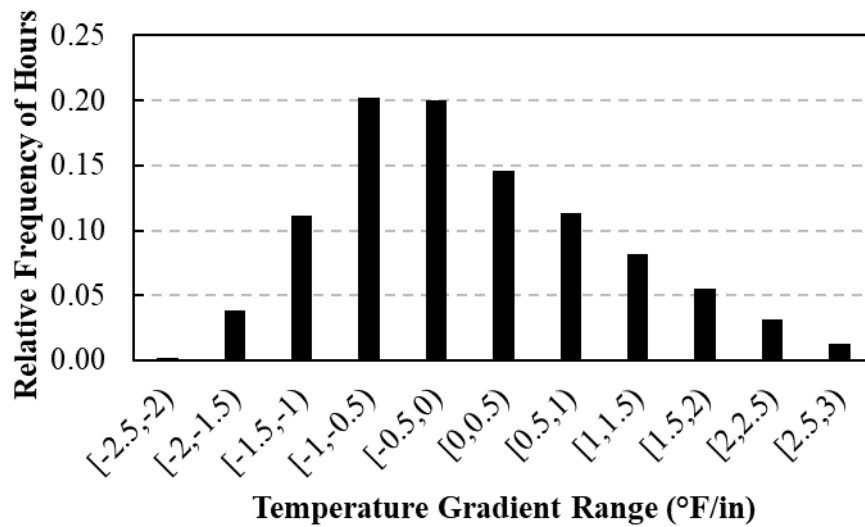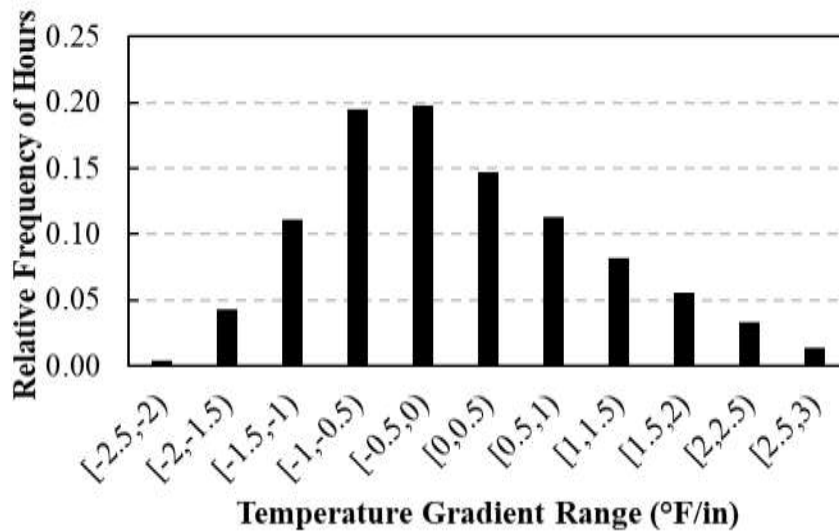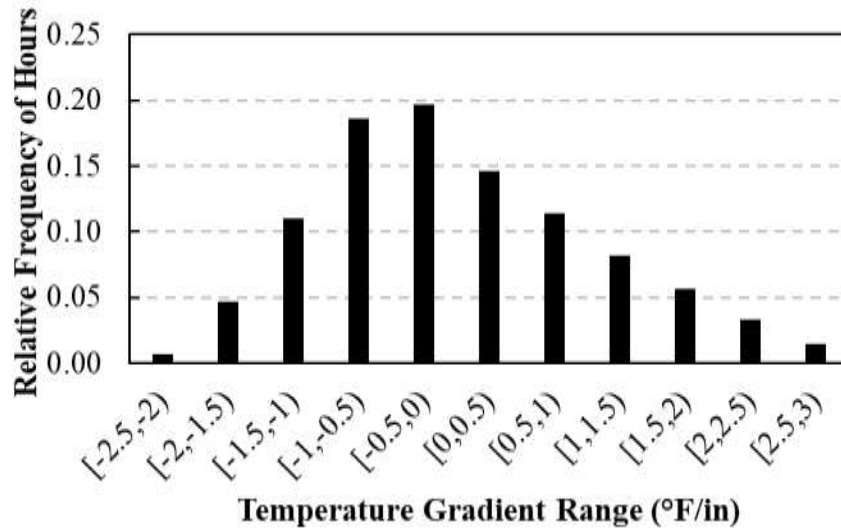
(c)

Figure 29: Relative frequency of temperature gradients for a (a) 8-in slab, (b) 10-in slab, and (c) 13-in slab in Pittsburgh, Pennsylvania.

10.2 Axle Configurations

To estimate the critical stresses caused by superloads during peak environmental conditions, the axle configurations on superload vehicles must be established. Of the ten superload vehicle profiles provided by PennDOT (Table 9), five unique axle configurations were identified. These axle configurations were detailed with the critical axle spacings and load magnitudes for the development of bottom-up and top-down cracking and were included in the finite element analysis, as shown in Figure 30. Incomplete pull truck details were given for SL1 and SL2 so the analysis was restricted to only the trailer portion of these superload vehicles.

Table 9: Characteristics of Pennsylvania superloads (information provided by PennDOT).

Vehicle	Gross Vehicle Weight, lb	Description
SL1	516,616	Pull Truck: 1 single axle and 1 tandem axle, spaced 14.3 ft apart, 18,000 lb/single axle and 40,000 lb/tandem axle, 2 tires/single axle and 8 tires/tandem axle Trailer: 20 single axles, spaced 9.1 ft apart, 22,932 lb/single axle, 4 tires/single axle
SL2	865,444	Pull Truck: Information not provided Trailer: 24 single axles, spaced 4.9 ft, 18,032 lb/single axle, 4 tires/single axle

77

SL3	580,000	Pull Truck: 1 single axle and 1 tridem axle, spaced 13.0 ft apart, 20,000 lb/single axle and 54,000 lb/tridem axle, 2 tires/single axle and 12 tires/tridem axle Trailer: 12 tandem axles, spaced between 12.3-12.5 ft apart, 37,250 lb/tandem axle, 8 tires/tandem axle Push Truck: 1 single axle and 1 tandem axle, spaced 19.2 ft apart, 19,000 lb/single axle and 40,000 lb/tandem axle, 2 tires/single axle and 12 tires/tandem axle
SL4	530,024	Push/Pull Truck: 1 single axle and 1 tridem axle, spaced 13.2 ft apart, 20,000 lb/single axle and 60,000 lb/tridem axle, 2 tires/single axle and 12 tires/tridem axle Trailer: 8 tandem axles, spaced 14.1 ft apart, 46,253 lb/tandem axle, 8 tires/tandem axle
SL5	530,000	Pull Truck: 1 single axle and 1 tridem axle, spaced 14.1 ft apart, 18,000 lb/single axle and 72,000 lb/tridem axle, 2 tires/single axle and 12 tires/tridem axle Trailer: 8 tandem axles, spaced 14.5 ft apart, 44,500 lb/tandem axle, 8 tires/tandem axle Push Truck: 1 single axle and 1 tridem axle, spaced 12.1 ft apart, 15,900 lb/single axle and 68,100 lb/tridem axle, 2 tires/single axle and 12 tires/tridem axle
SL6	463,000	Pull Truck: 1 single axle and 1 tridem axle, spacing information not provided, 16,000 lb/single axle) and 63,000 lb/tridem axle, 2 tires/single axle and 12 tires/tridem axle Trailer: 8 tandem axles, spacing information not provided, 42,000 lb/tandem axle, 8 tires/tandem axle Push Truck: 1 single axle and 1 tandem axle, spacing information not provided, 14,000 lb/single axle and 40,000 lb/tandem axle, 2 tires/single axle and 8 tires/tandem axle
SL7	854,316	Pull Truck: N/A Trailer: 24 single axles, spaced 4.9 ft, 17,800 lb/single axle, 4 tires/single axle
SL8	450,070	Pull Truck: 1 single axle and 1 tandem axle, spaced 19.3 ft apart, 18,000 lb/single axle and 40,000 lb/tandem axle, 2 tires/single axle and 8 tires/tandem axle Trailer: 20 single axles, spaced 9.1 ft apart, 19.604 lb/single axle, 4 tires/single axle
SL9	N/A	Pull Truck: 1 single axle and 1 tridem axle, spaced 16.5 ft apart, no load information provided, no tire information provided Trailer: 8 tandem axles, spaced 16 ft apart, no load information provided, 8 tires/tandem axle Push Truck: 1 single axle and 1 tandem axle, spaced 20 ft apart, no load information provided, tire information for single axle not provided and 8 tires/tandem axle

		Pull Truck: 2 single axles and 2 tandem axles, spaced 14.3 ft and 5 ft apart, 20,000 lb/single axle and 35,000 lb/tridem axle, 2 tires/first single axle, 4 tires/second single axle and 8 tires/tandem axle
SL10	436,550	
		Trailer: 8 tandem axles, spaced 16.1 ft apart, 46,300-49,350 lb/tandem axle, 8 tires/tandem axle
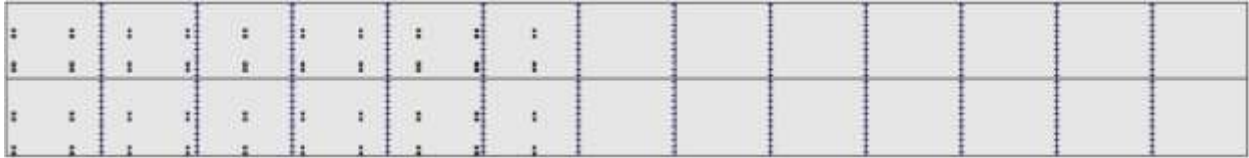
SL1 – Trailer Only
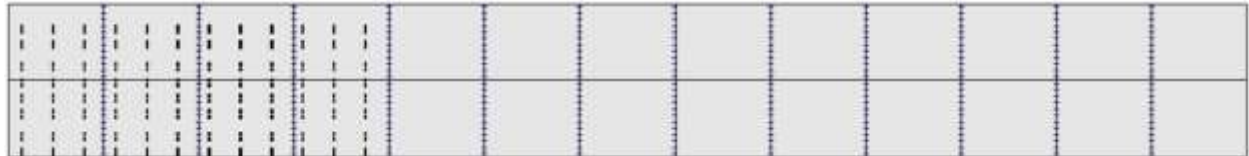
SL2 – Trailer Only
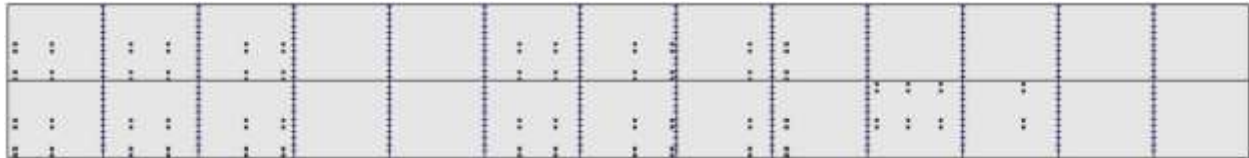
SL3 – Pull Truck and Trailer
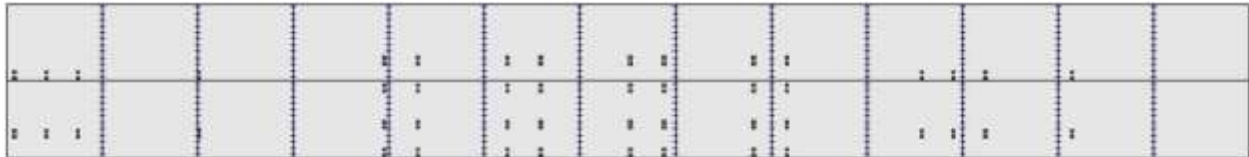
SL4 – Pull Truck, Push Truck, and Trailer
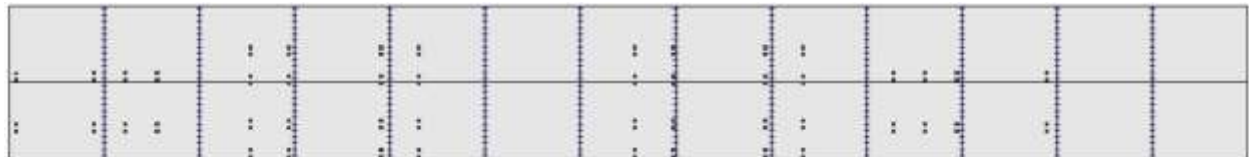
SL5 – Pull Truck, Push Truck, and Trailer

Figure 30: Pennsylvania superload axle configurations (13 15-ft slabs in each of the 2 12-ft lanes).

10.3 Finite Element Analysis

10.3.1 Model Development

With the peak environmental conditions and superload axle configurations established, the next step was to identify the critical axle position on the concrete slab for each axle configuration. Knowledge of this position is necessary to quantify the maximum tensile stresses that can occur as a result of the superload application. Using the pavement finite element modeling software ISLAB (Khazanovich, et al., 2000), the five superload axle configurations were each generated on a 40-ft by 195-ft JPCP model with the parameters outlined in Table 10. As indicated in Table 10, three concrete slab thicknesses (8 in, 10 in, and 13 in) and three temperature gradients (-2.5 °F/in, 3.0 °F/in, and 0 °F/in) were considered. JPCPs with 8-in and 10-in concrete slabs were modeled with asphalt and concrete shoulders. JPCPs with 13-in concrete slabs were only modeled with concrete shoulders.

Using a mesh size of 6 in by 6 in (established based on a separate convergence study), a series of finite element analyses were conducted for each superload axle configuration as the vehicle was moved incrementally down the roadway (i.e., at 15, 1-ft increments in the longitudinal direction along the roadway), as demonstrated in Figure 31. The outer wheels of each superload axle configuration were placed along the lane/shoulder joint during the movement as this was determined to be the critical path of movement for fatigue damage. Once the critical superload position for each loading condition was identified, the maximum tensile stress magnitude and its corresponding location were determined.

To compare the stresses caused by superloads to a design load, finite element analysis of the JPCP model was also conducted with an 18-kip single axle design load placed at midslab. The 18-kip single axle had four tires with each set of dual tires 5-ft apart. Each set of dual tires was specified to have a tire width of 8 in, center to center tire spacing of 12 in, and a tire pressure of 90 psi.

Table 10: ISLAB input parameters for finite element analysis.

Geometry	
Joint Spacing	15 ft
Shoulder Width	0/8 ft
Lane Width (Two Lanes)	12 ft
Slab Thickness	8/10/13 in
Concrete Properties	
Poisson Ratio	0.18
Elastic Modulus	4.6×10^6 psi
Coefficient of Thermal Expansion Coefficient	4.5×10^{-6} in/in/°F
Unit Weight	150 pcf
Subgrade Properties	
Modulus of Subgrade Reaction	200 pci
Joint Properties	
Longitudinal Joint LTE	0.9
Transverse Joint	Doweled
Dowel Properties	
Outside Diameter	1.25/1.5 in
Inside Diameter	0 in
Joint Width	0.1 in
Elastic Modulus	1.50×10^7 psi
Poisson Ratio	0.2
Modulus of Dowel Support	5.0×10^5 psi/in
Dowel Length	9 in
Dowel Spacing	12 in
Temperature	
Gradient	0/-2.5/3 °F/in

Note: Asphalt shoulders are represented in ISLAB by inputting zero for shoulder width; 1.25-in dowel diameter was only an input when 8-in concrete slabs were modeled.
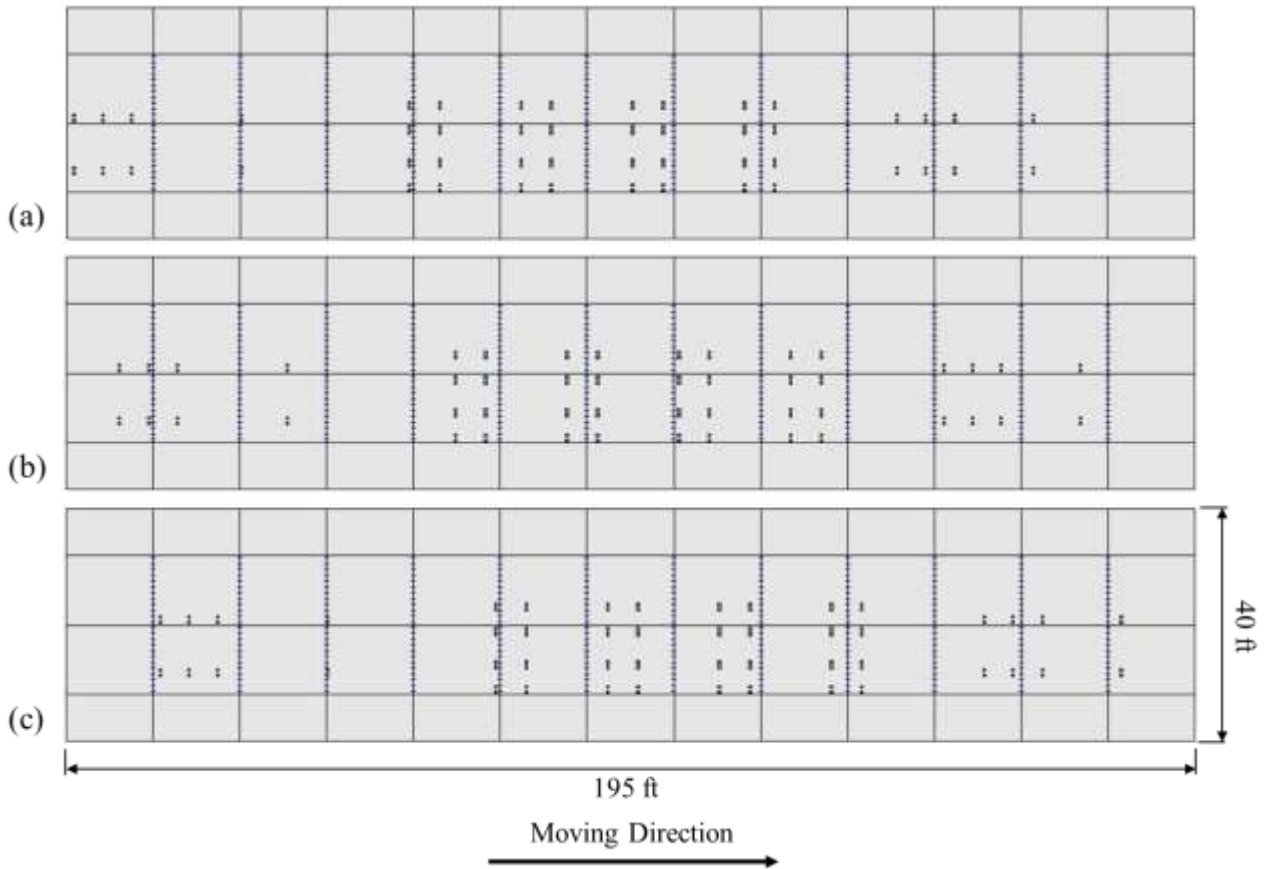
Figure 31: Finite element model of JPCP with superload (SL4) placed at (a) initial position (b) middle position (c) final position.

10.3.2 Finite Element Analysis Results

Figure 32 depicts the process of identifying the maximum tensile stress caused by superloads. For JPCPs with the peak positive temperature gradient and no temperature gradient, the maximum tensile stress occurred at the bottom of the concrete slab for each run. For JPCPs with the peak negative temperature gradient, the maximum tensile stress typically occurred at the top of the concrete slab between the application of consecutive axle loads, as would be expected.
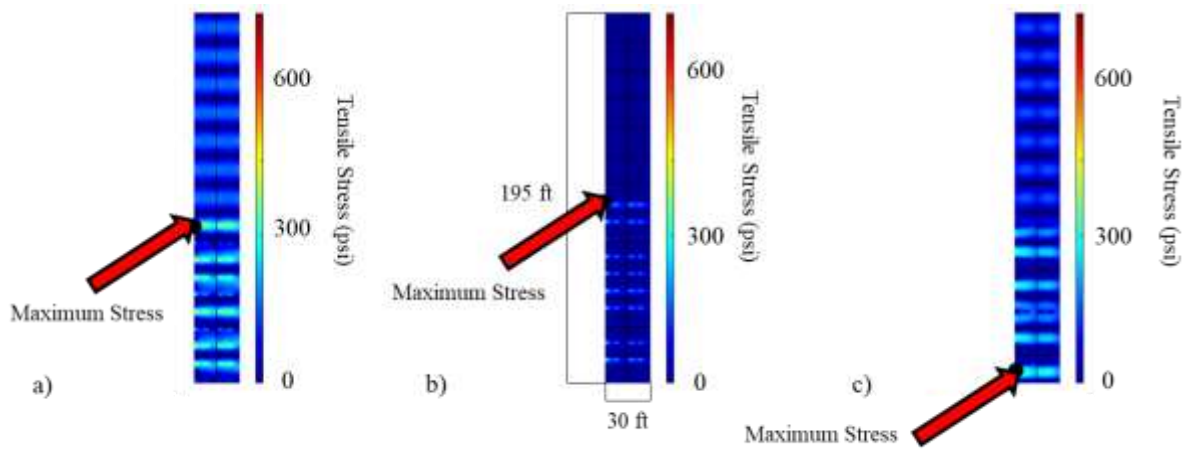
Figure 32: Identification of maximum tensile stress caused by SL1 at critical axle positions for (a) 8-in concrete slab, peak positive temperature gradient, asphalt shoulder (b) 8-in concrete slab, zero temperature gradient, asphalt shoulder (c) 8-in concrete slab, peak negative temperature gradient, asphalt shoulder.

Table 11 shows the maximum tensile stresses caused by each superload axle configuration along with the corresponding fatigue performance prediction of superload axle configurations. Superload vehicles SL1, SL4, and SL5 have axle configurations that cause significantly higher stresses than a design single axle load. SL1 consists of 10 continuous axle loads of approximately 23,000 lb each, spaced 9.1 ft apart. This configuration caused the largest tensile stress regardless of the temperature gradient present. The tensile stresses caused by SL4 were comparable to those of SL1. SL4 consists of a pull truck, push truck, and trailer with four tandem axle loads of approximately 46,000 lb, spaced 14.1 ft apart. The tensile stresses for SL5 were slightly less than those from SL1 and SL4. SL5 consists of a pull truck, push truck, and trailer with 4 tandem axle loads of approximately 44,500 lb, spaced 14.5 ft apart. From the axle configurations evaluated, it is observed that the heavily loaded single and tandem axles on the trailers of these superload vehicles result in significant tensile stresses in JPCPs.

Table 11: Results of superload finite element analysis and fatigue performance prediction.

Load Case	Positive Temperature Gradient			Negative Temperature Gradient			Zero Temperature Gradient		
	Tensile Stress, psi	N_f	% Life Consumed from One Passing	Tensile Stress, psi	N_f	% Life Consumed from One Passing	Tensile Stress, psi	N_f	% Life Consumed from One Passing
SA_8_A	526	92	1.1	146	Unlimited	-	310	3,100,000	<0.0
SA_10_A	429	5,800	<0.0	126	Unlimited	-	228	Unlimited	-
SA_8_C	424	7,300	<0.0	151	Unlimited	-	212	Unlimited	-
SA_10_C	350	180,000	<0.0	129	Unlimited	-	158	Unlimited	-
SA_13_C	256	Unlimited	-	100	Unlimited	-	110	Unlimited	-
SL1_8_A	606	3	100	387	36,000	<0.0	417	9,700	0.1
SL1_10_A	479	700	1.4	318	1,300,000	<0.0	289	Unlimited	-
SL1_8_C	493	380	3.0	298	16,000,000	<0.0	292	Unlimited	-
SL1_10_C	397	23,000	<0.0	256	Unlimited	-	207	Unlimited	-
SL1_13_C	287	Unlimited	-	191	Unlimited	-	137	Unlimited	-
SL2_8_A	502	260	4.6	305	5,600,000	<0.0	311	2,700,000	<0.0
SL2_10_A	424	7,300	0.2	278	Unlimited	-	228	Unlimited	-
SL2_8_C	460	1,600	0.8	290	Unlimited	-	267	Unlimited	-
SL2_10_C	393	27,000	<0.0	265	Unlimited	-	197	Unlimited	-
SL2_13_C	306	4,800,000	<0.0	177	Unlimited	-	136	Unlimited	-
SL3_8_A	518	130	4.6	344	240,000	<0.0	320	1,100,000	<0.0
SL3_10_A	431	3300	0.2	318	1,300,000	<0.0	237	Unlimited	-
SL3_8_C	442	5300	0.1	284	Unlimited	-	237	Unlimited	-
SL3_10_C	370	74,000	<0.0	264	Unlimited	-	177	Unlimited	-
SL3_13_C	278	Unlimited	-	212	Unlimited	-	125	Unlimited	-
SL4_8_A	592	5	80	371	70,000	<0.0	399	21,000	<0.0
SL4_10_A	496	330	1.2	369	77,000	<0.0	303	7,900,000	<0.0
SL4_8_C	485	530	0.8	315	1,900,000	<0.0	285	Unlimited	-
SL4_10_C	406	15,000	<0.0	312	2,500,000	<0.0	215	Unlimited	-
SL4_13_C	310	2,900,000	<0.0	264	Unlimited	-	153	Unlimited	-
SL5_8_A	547	37	11	342	260,000	<0.0	354	150,000	<0.0
SL5_10_A	458	1,700	0.2	341	280,000	<0.0	263	Unlimited	-
SL5_8_C	451	2,300	0.2	292	Unlimited	-	251	Unlimited	-
SL5_10_C	378	52,000	0.0077	289	Unlimited	-	188	Unlimited	-
SL5_13_C	285	Unlimited	-	244	Unlimited	-	134	Unlimited	-

Note: "Load Case" is constructed as follows: Superload Vehicle (SL) or Standard Axle (SA)_Slab Thickness (in)_Shoulder Type (C=Portland Cement Concrete and A=Asphalt Concrete)

To estimate the damage that could be attributed to the maximum tensile stress identified, the number of allowable applications before fatigue failure would occur was estimated using the PCA fatigue equation, shown in Equation 39 (Packard & Tayabji, 1985). The modulus of rupture of the concrete was assumed to be 650 psi:

$$\log(N_f) = 11.737 - 12.077 SR \; for \; SR \geq 0.55 \tag{39}$$

$$N_f = \left[\frac{4.2577}{SR - 0.4325}\right]^{3.268} \; for \; 0.45 < SR < 0.55 \tag{40}$$

$$N_f = Unlimited \; for \; SR \; \leq 0.45 \qquad (41)$$

where,

N_f = the number of maximum tensile stress applications until failure

SR = the ratio between critical stress and modulus of rupture of the concrete.

The fatigue life consumed was calculated for each load case based on the fatigue performance estimated using the PCA fatigue equation, as shown in Equation 40.

$$\% \; Fatigue \; Life \; Consumed = \frac{n_i}{N_f} \times 100\% \qquad (42)$$

where,

n_i = the number of maximum tensile stress applications per one superload vehicle passing

N_f = the number of maximum tensile stress applications until failure.

The fatigue performance and fatigue life consumed results are shown in Table 11. The stresses caused by superloads are observed to have a significant impact on the fatigue life of 8-in and 10-in concrete slabs when a large positive temperature gradient is present. Minor or insignificant damage occurred, regardless of slab thickness, when large negative temperature gradients or no temperature gradient is present. Concrete slabs that are 13-in thick are shown to experience very little fatigue damage when a large positive temperature gradient is in the slab and no fatigue damage when a large negative temperature gradient or no temperature gradient is present. Additionally, as shown in Table 11, pavement structures with concrete shoulders are shown to experience much less fatigue damage than pavement structures with asphalt shoulders, as the concrete shoulder is effective in reducing edge stresses.

To investigate how the critical stresses caused by superloads affect the thinner slabs with the peak positive temperature gradient, the locations of the critical stresses with respect to the midslab were determined. In Figure 33, it is observed that the maximum stress location for all of the superload axle configurations is at midslab near the longitudinal edge/shoulder joint (i.e., at

the Pavement ME critical stress response location (Applied Research Associates (ARA), 2004)). Therefore, all will contribute to the development of bottom-up cracking.
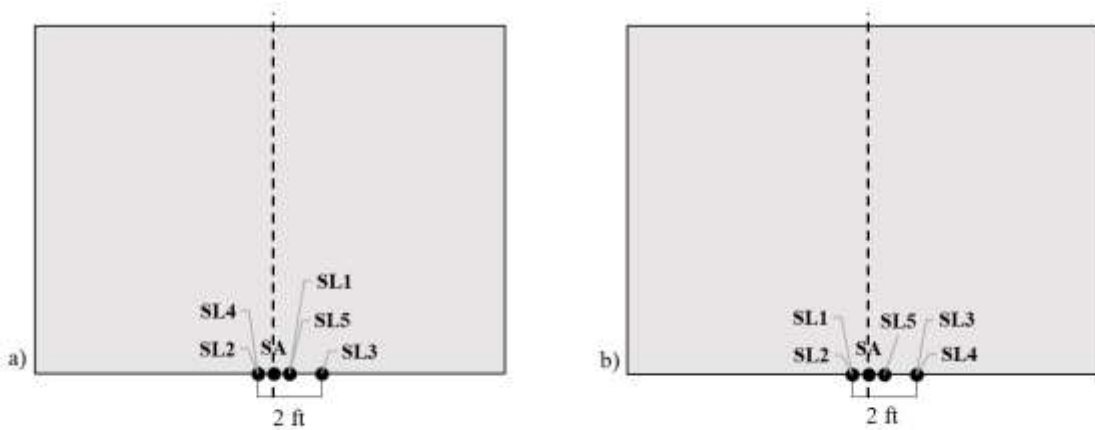
Figure 33: Maximum tensile stress locations on 12-ft by 15-ft concrete slab for (a) 8-in concrete slab with the peak positive temperature gradient and (b) 10-in concrete slab with the peak positive temperature gradient.

10.4 Stress Pulses

The maximum stresses determined in the finite element analysis were used to predict the fatigue life consumed by a superload application. The stresses generated by superloads were further investigated in regards to the stress range between pulses, the stress range between the maximum stress and the curling stress, and stress reversals. As previously shown, the thinner slabs were observed to exhibit significant tensile stresses when the peak positive temperature gradient was present. The fatigue damage corresponding to these stresses would be mitigated to some degree depending on the curling stress present in the JPCP. Additionally, the JPCPs with zero temperature gradient may be subjected to stress reversals, which are known to decrease the fatigue life of concrete (Cornelissen, 1984; Zhang, Phillips, & Wu, 1996). To explore both stress range and stress reversals, the variation in stress at the critical stress response location (i.e., mid-slab at lane/shoulder joint) as each superload moved along the JPCP was quantified. The focus of this analysis was on the 8-in JPCPs, and the movement, identified critical response location, and corresponding stresses are shown in Figure 34-Figure 38.

(a)
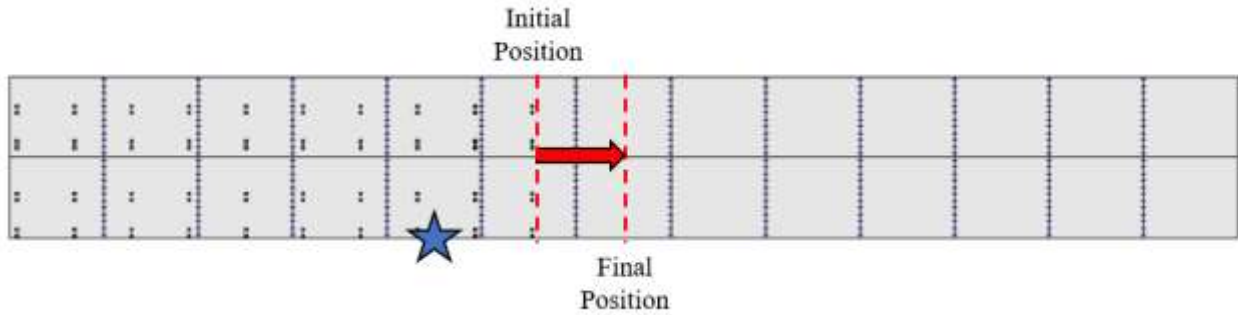
(b)
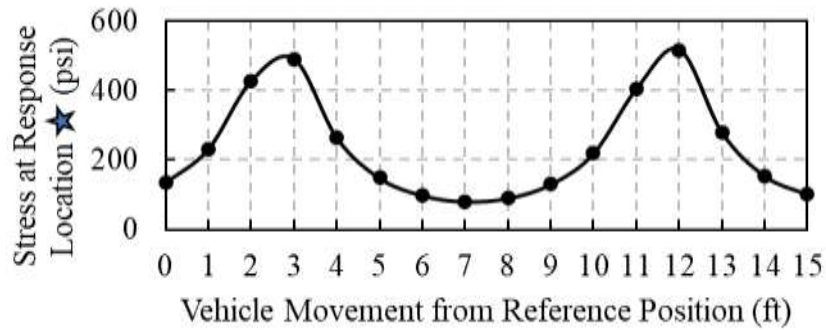
(c)
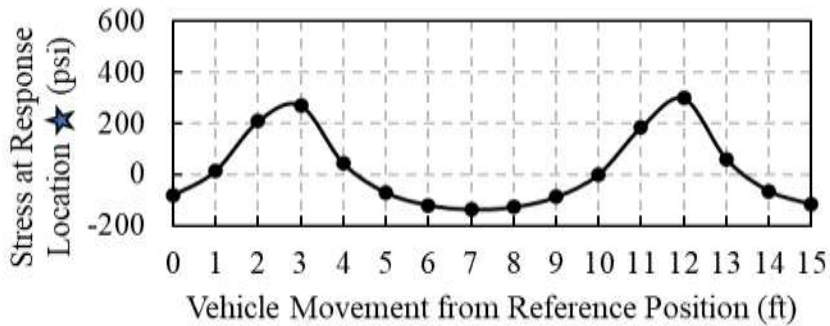
Figure 34: Stress pulse analysis where (a) depicts the superload movement of SL1 (b) depicts stress profile caused by SL1 at the critical stress response location for peak positive temperature gradient and (c) depicts the stress profile caused by SL1 at the critical stress response location for a zero temperature gradient.

(a)
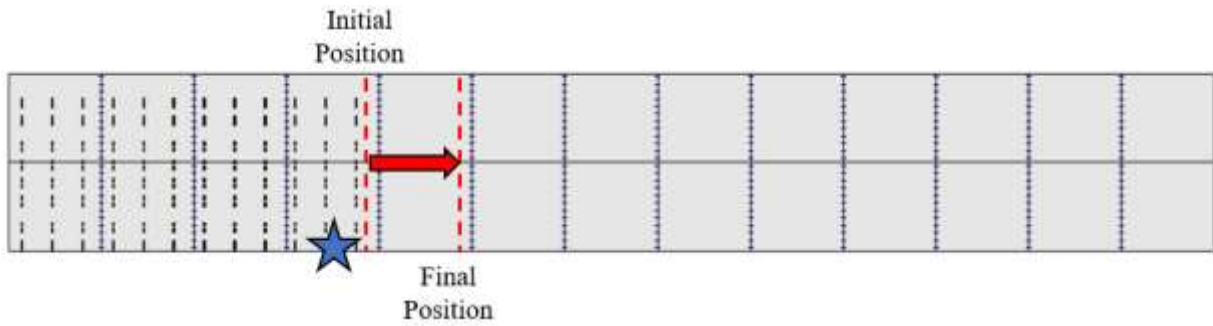
(b)
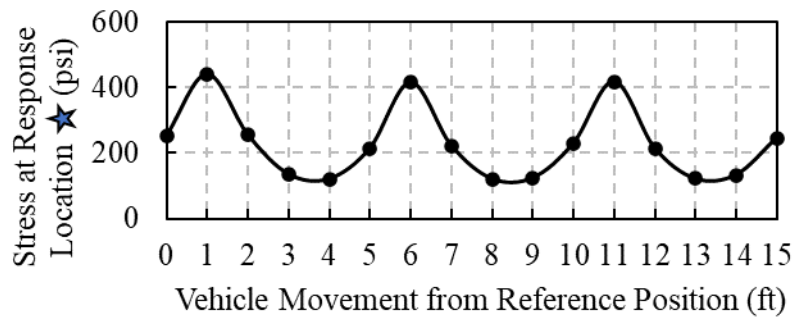
(c)
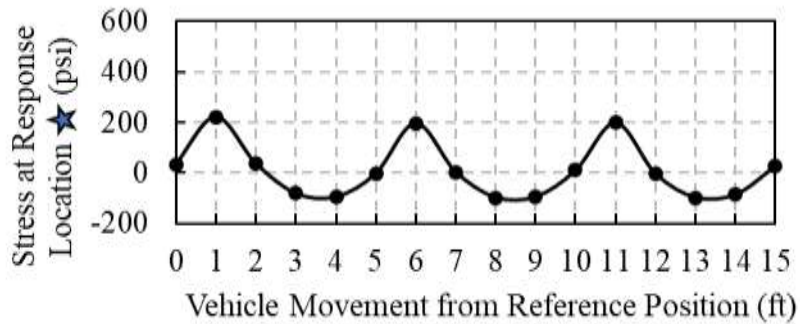
Figure 35: Stress pulse analysis where (a) depicts the superload movement of SL2 (b) depicts the stress profile caused by SL2 at the critical stress response location for peak positive temperature gradient and (c) depicts the stress profile caused by SL2 at the critical stress response location for zero temperature gradient.

(a)
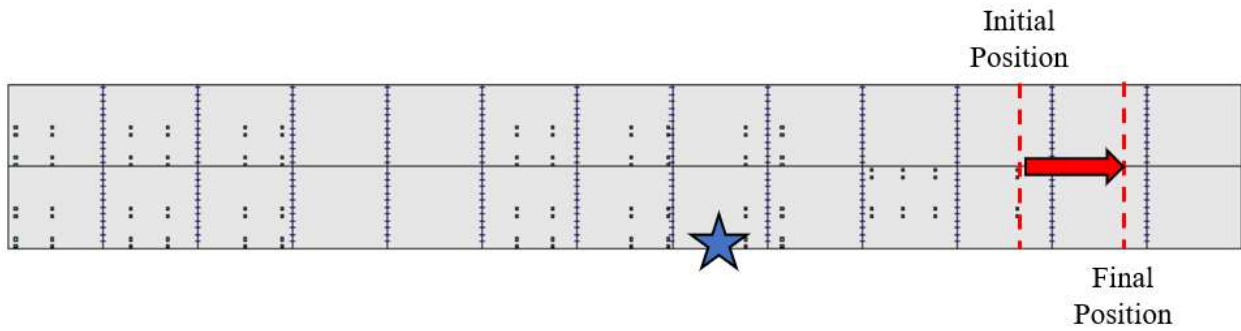
(b)
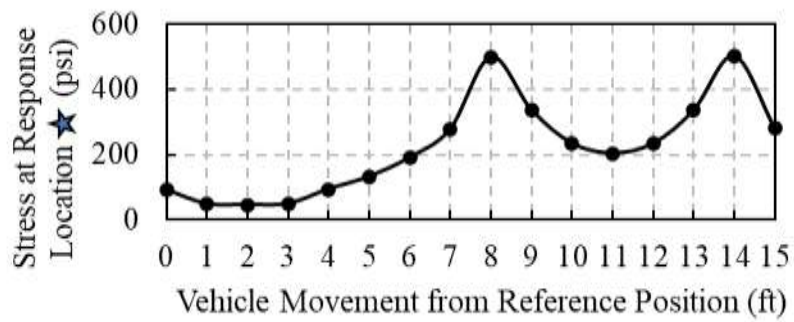
(c)
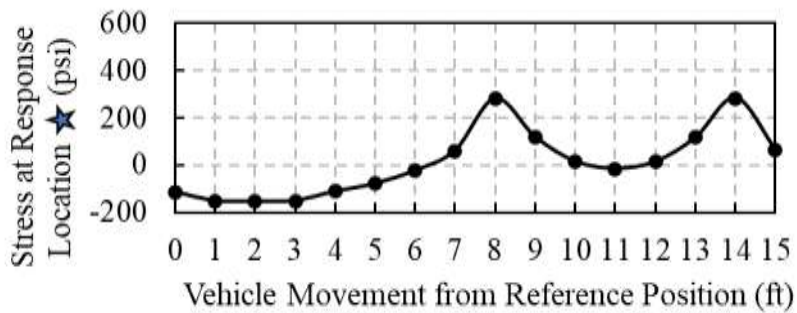
Figure 36: Stress pulse analysis where (a) depicts the superload movement of SL3 (b) depicts the stress profile caused by SL3 at the critical stress response location for peak positive temperature gradient and (c) depicts the stress profile caused by SL3 at the critical stress response location for zero temperature gradient.

(a)
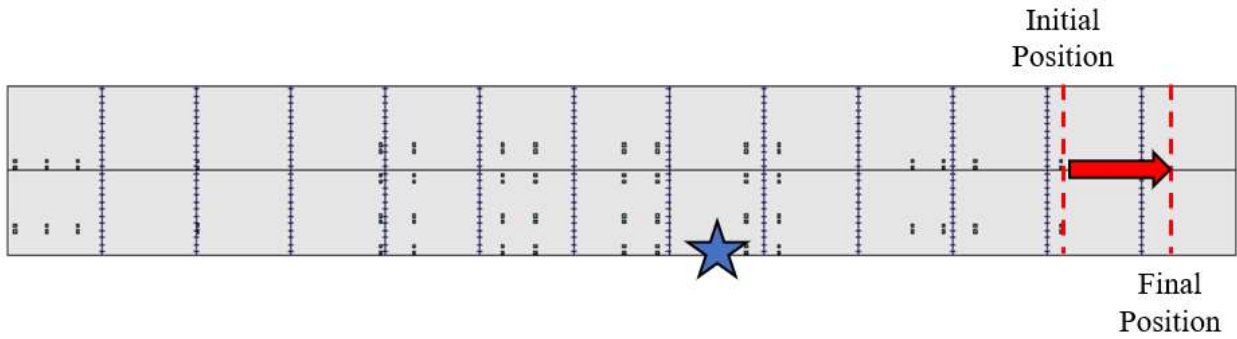
(b)
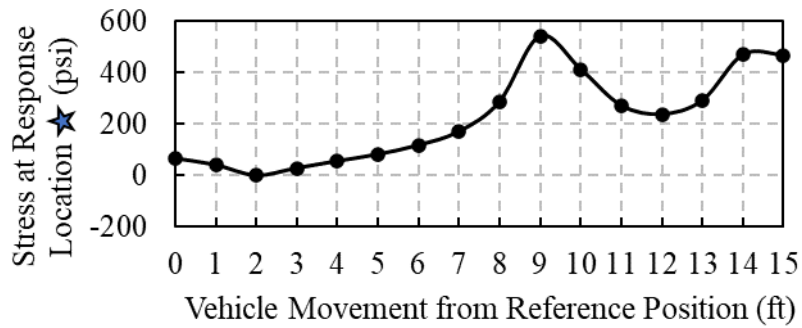
(c)
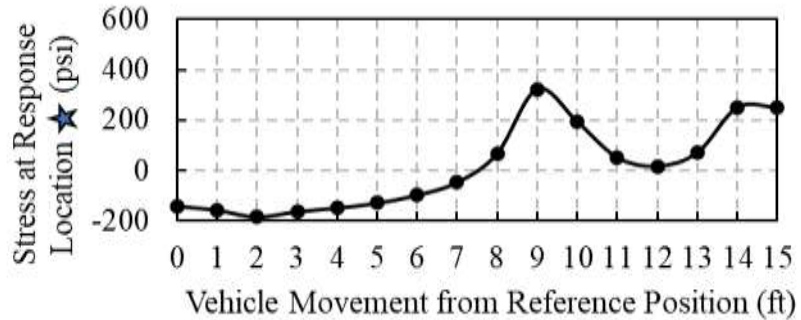
Figure 37: Stress pulse analysis where (a) depicts the superload movement of SL4 (b) depicts the stress profile caused by SL4 at the critical stress response location for peak positive temperature gradient and (c) depicts the stress profile caused by SL4 at the critical stress response location for zero temperature gradient.

Initial
Position

Final
Position
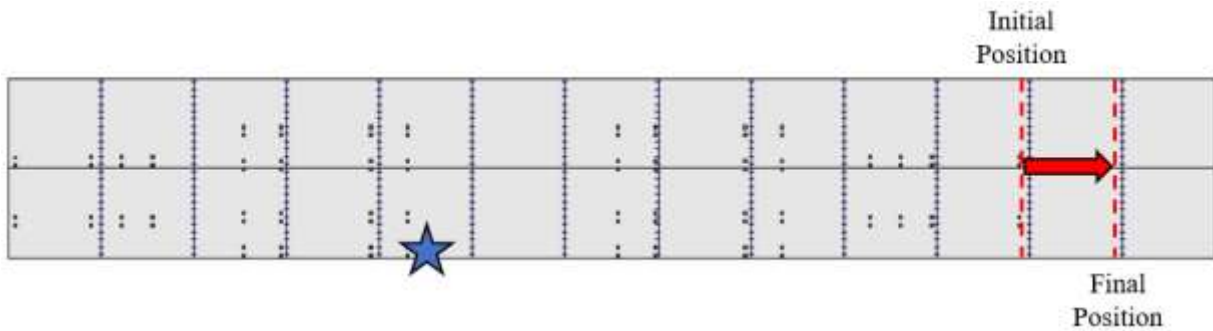
(b)
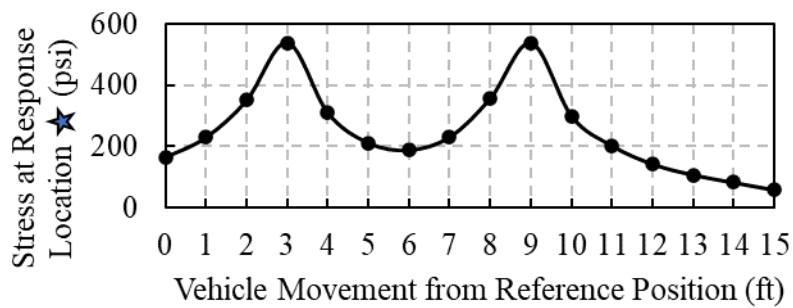
(c)
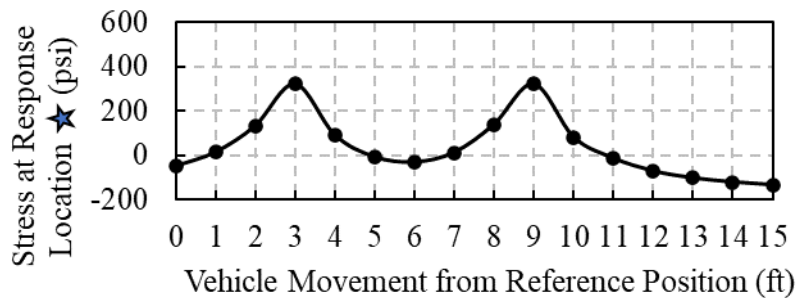
Figure 38: Stress pulse analysis where (a) depicts the superload movement of SL5 (b) depicts the stress profile caused by SL5 at the critical stress response location for peak positive temperature gradient and (c) depicts the stress profile caused by SL5 at the critical stress response location for zero temperature gradient.

Consider the stress pulses generated by superload application on concrete slabs with a peak positive temperature gradient (Figure 34b-Figure 38b). The stress between fatigue cycles for SL1 is approximately 100 psi, which is about 400 psi less than the maximum stress. For SL2, the minimum stress between fatigue cycles is also approximately 100 psi, which is 350 psi less than

the maximum stress. For SL3, SL4, and SL5 (i.e., the tandem axle superloads), the stress between peaks is approximately 300 psi less than the maximum stress.

Next, consider the stress pulses generated by superload application on concrete slabs with no temperature gradient present. As shown in Figure 34c-Figure 38c, the stress at the critical stress response location is shown to reverse between tension and compression. The stress pulses from the single axle superloads undergo about 100 psi in compression in between single axle fatigue cycles. The stress pulses from the tandem axle superloads exhibit stress reversals (up to 150-200 psi in magnitude) between tandem axle fatigue cycles. By comparing these results to those from Zhang *et al*. (Zhang, Phillips, & Wu, 1996), the fatigue life of the concrete would only be slightly decreased by these magnitudes of stress reversal.

To investigate the effects of the stress range between the maximum stress and the curling stress, the fatigue damage predicted through the PCA equation was compared to the fatigue damage predicted using a stress range damage model. The damage model developed by Tepfers for concrete beams (Tepfers, 1979) accounts for stress range. This was adapted by Domenichini and Marchionna (Domenichini & Marchionna, 1981) for concrete pavement damage analysis as follows:

$$SR = 1 - \beta(1-R)\log(N_f) \tag{43}$$

Where,

SR = the ratio between critical stress and modulus of rupture of the concrete

β = the coefficient to account for field and material variation (determined by Domenichini and Marchionna to be 0.0954)

$R = \dfrac{\sigma_{min}}{\sigma_{max}}$

N_f = the number of stress applications until failure.

This damage model was used in this analysis to study the effects of stress range on the damage caused by superloads. The damage in JPCPs with an 8-in slab and asphalt shoulder, 8-in slab and concrete shoulder, and 10-in slab with asphalt shoulder were studied. The maximum curling stresses in these three pavement designs were observed to be approximately 175 psi, 175 psi, and 150 psi, respectively. These stresses were each input as the minimum stress in the

stress range equation. The minimum stress is assumed to be 0 psi for all cases when no temperature gradient is present. Table 12 shows the comparison in fatigue damage prediction between the PCA damage model and the damage model considering stress range.

As shown in Table 12, by considering stress range, the predicted fatigue damage in the JPCPs with the peak positive temperature gradient decreases significantly. For instance, consider the case when SL1 is applied to the 8-in JPCPs with the peak positive temperature gradient. Using the PCA equation, the predicted fatigue life consumed is approximately 3% and 5% for JPCPs with a concrete and asphalt shoulder, respectively. When using the Domenichini and Marchionna damage model, the predicted fatigue life consumed is approximately 0.12% (concrete shoulder) and 0.26% (asphalt shoulder). This result indicates that the maximum stresses determined in the finite element analysis may not be as damaging as predicted by the PCA equation. It is important to note that there is some inherent variability between models due to how they were developed. The PCA equation was developed from concrete beam test data and the Domenichini and Marchionna damage model was developed from American Association of State Highway Officials (AASHO) road test data. Regardless of this difference, stress range is observed to be a consideration in the damage analysis for superloads.

Table 12: Fatigue damage prediction from PCA damage model (Packard & Tayabji, 1985) and damage model presented by Domenichini and Marchionna (Domenichini & Marchionna, 1981).

Load Case	Positive Temperature Gradient					Zero Temperature Gradient				
	Tensile Stress, psi	N_f (PCA)	% Fatigue Life Consumed from One Passing	N_f (D/M)	% Fatigue Life Consumed from One Passing	Tensile Stress, psi	N_f (PCA)	% Fatigue Life Consumed from One Passing	N_f (D/M)	% Fatigue Life Consumed from One Passing
SL1_8_A	606	3	100	10	100	417	9,700	0.1	5,700	<0.12
SL1_10_A	479	700	1.4	11,000	0.1	289	Unlimited	-	680,000	<0.0
SL1_8_C	493	380	3.0	8,500	0.1	292	Unlimited	-	590,000	<0.0
SL2_8_A	502	260	4.6	4,600	0.3	311	2,700,000	<0.0	290,000	<0.0
SL2_10_A	424	7,300	0.2	440,000	<0.0	228	Unlimited	-	6,500,000	<0.0
SL2_8_C	460	1,600	0.8	89,000	<0.0	267	Unlimited	-	1,500,000	<0.0
SL3_8_A	518	130	4.6	1,700	0.4	320	1,100,000	<0.0	210,000	<0.0
SL3_10_A	431	3,300	0.2	260,000	<0.0	237	Unlimited	-	4,600,000	<0.0
SL3_8_C	442	5,300	0.1	340,000	<0.0	237	Unlimited	-	4,500,000	<0.0
SL4_8_A	592	5	80	21	19	399	21,000	<0.0	11,000	<0.0
SL4_10_A	496	330	1.2	3,600	0.1	303	7,900,000	<0.0	400,000	<0.0
SL4_8_C	485	530	0.8	14,000	<0.0	285	Unlimited	-	770,000	<0.0
SL5_8_A	547	37	11	270	1	354	150,000	<0.0	60,000	<0.0
SL5_10_A	458	1,700	0.2	41,000	<0.0	263	Unlimited	-	1,700,000	<0.0
SL5_8_C	451	2,300	0.2	180,000	<0.0	251	Unlimited	-	2,700,000	<0.0

10.5 Summary of Superload Pulse Analysis

In this study, the maximum tensile stresses caused by superload axle configurations on JPCPs were determined for various concrete slab thicknesses and shoulder types using finite element analysis. The impact of this stress on the fatigue life of these JPCPs was estimated using the PCA fatigue damage model. The single and tandem axles that were heavily loaded in the trailer portion of the superload were observed to cause significant fatigue damage in 8-in and 10-in concrete slabs when large positive temperature gradients were present. Superloads did not greatly impact the fatigue lives of 13-in concrete slabs under any temperature gradient condition and of 8-in and 10-in concrete slabs when a negative temperature gradient or no temperature gradient was present. The presence of tied concrete shoulders significantly reduced the fatigue damage in JPCPs caused by superloads. As shown in the stress pulse analysis, by accounting for stress range, the fatigue life consumed from superloads is predicted to decrease. Stress reversals were shown to not be a large concern for superload damage analysis.

Through this computational analysis, the design features of JPCPs that are susceptible to significant fatigue damage from application of a superload were identified. Specifically, 8-in and 10-in JPCPs with asphalt shoulders are observed to be of primary concern. Moreover, this analysis showed that the damage imposed by superloads is greatly influenced by the temperature gradient in the concrete slab and thus, the time of day that the load is applied. With these numerical findings, a laboratory study was developed to evaluate the effects of overloads on damaged JPCPs, as discussed in Section 12.

11.0 DEVELOPMENT OF LABORATORY STUDY FOR FATIGUE IN JPCP

This section covers the development of the laboratory study that was performed to evaluate the effect of overloads on damaged JPCPs. First, the test set-up for the laboratory study is presented. Then, the experimental design, covering the range of parameters and the testing procedures included in the laboratory study, is discussed.

11.1 Test Setup

11.1.1 Loading Type

To determine the loading type for the laboratory study, the mechanism of fatigue damage in JPCPs is considered. Fatigue damage occurs at the top and bottom of a concrete slab from repeated tensile stress applications. The fatigue performance of concrete in tension has been commonly studied in the laboratory through concrete beam fatigue tests (Murdock & Kesler, 1958; Hilsdorf & Kesler, 1966; Raithby, 1979; Oh, 1986; Oh, 1991a; Chatti, et al., 2009; Roesler, 1998). As shown in Figure 39, concrete beams can be loaded in three-point and four-point bending to induce tensile stress. Four-point bending is preferred over three-point bending because the peak tensile stress is applied over a region rather than a localized point. This reduces the probability of overestimating the fatigue strength of the concrete, given that a larger area is scanned for defects. Concrete beams can also be simply supported or fully supported. Fully supported concrete beams carry load after cracking, which replicates the behavior of a JPCP. Thus, fully supported concrete beams have a greater flexural strength than simply supported concrete beams (Roesler, 1998). However, tensile stress and cracking can be directed to a specific region by using simply supported concrete beams, which makes it easier to analyze the progression of fatigue damage in concrete.
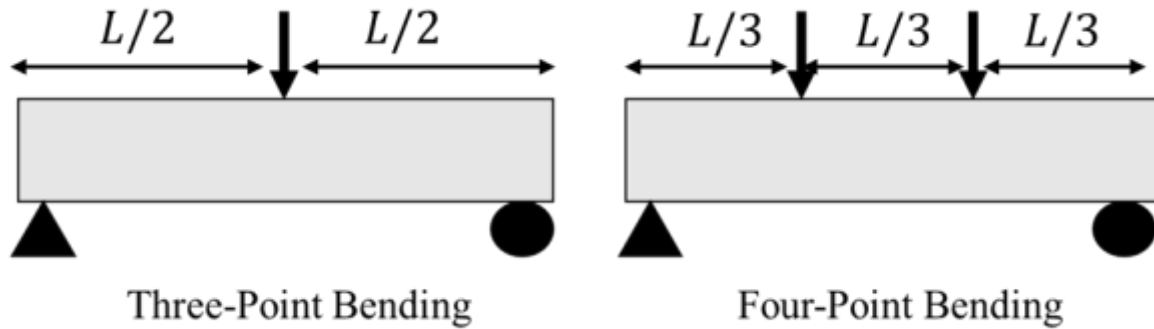
Figure 39: Loading types for concrete beam fatigue studies (L refers to the beam span).

The fatigue of concrete slabs can also be studied in the laboratory, as shown by Roesler and Gaedicke *et al.* (Gaedicke, Roesler, & Shah, 2009; Roesler, 1998). Concrete slabs have greater fatigue resistance than concrete beams due to specimen size and support conditions (Roesler, 2006; Roesler, 1998). While more representative of field conditions, concrete slabs are difficult to cast and test.

To meet the goals of this research, the four-point bending fatigue testing was performed on simply supported concrete beams. Through this approach, the effects of overloads can be directly and consistently quantified as a function of existing damage.

11.1.2 Specimen Size

The next step in the development of the laboratory study was to choose a concrete beam size. In the literature, several concrete beam sizes have been fatigued in four-point bending, as summarized in Table 13. For this study, it was essential to choose a concrete beam size that allows for analysis of the fatigue damage of concrete in flexural tension. In the multi-axle truck study conducted by Chatti *et al.*, a 4-in by 4-in by 24-in concrete beam size was chosen so that the fatigue of concrete was imposed in flexural tension only (i.e., not in flexural tension and shear). The following criteria was followed (Chatti, et al., 2009):

- The flexural capacity is less than shear capacity
- The slenderness ratio of the beam is at least three
- The flexural deformations are two to three times the shear deformations

To meet the goals of this research, the same concrete beam dimensions as used by Chatti *et al.* were chosen. These dimensions allow for the effective analysis of overloads on the fatigue life of concrete and are sufficiently small so that many concrete beams can be cast at once. The four-point bending configuration used for this concrete beam size is shown in Figure 40.

Table 13: Summary of concrete beam fatigue studies.

Study	Loading	Concrete Beam Size
Murdock and Kesler 1958	Four-Point Bending	6 in by 6 in by 60 in
Hilsdorf and Kesler 1966	Four-Point Bending	6 in by 6 in by 60 in
Raithby 1979	Four-Point Bending	4 in by 4 in by 20 in
Oh 1986	Four-Point Bending	4 in by 4 in by 20 in
Oh 1991a	Four-Point Bending	4 in by 4 in by 20 in
Oh 1991b	Four-Point Bending	4 in by 4 in by 20 in
Shi *et al.* 1993	Four-Point Bending	4 in by 4 in by 20 in
Zhang *et al.* 1996	Four-Point Bending	4 in by 4 in by 20 in
Zhang *et al.* 1997	Four-Point Bending	4 in by 4 in by 20 in
Roesler 1998	Four-Point Bending	6 in by 6 in by 21 in
Suh *et al.* 2005	Four-Point Bending	6 in by 6 in by 36 in
Chatti *et al.* 2009	Four-Point Bending	4 in by 4 in by 24 in
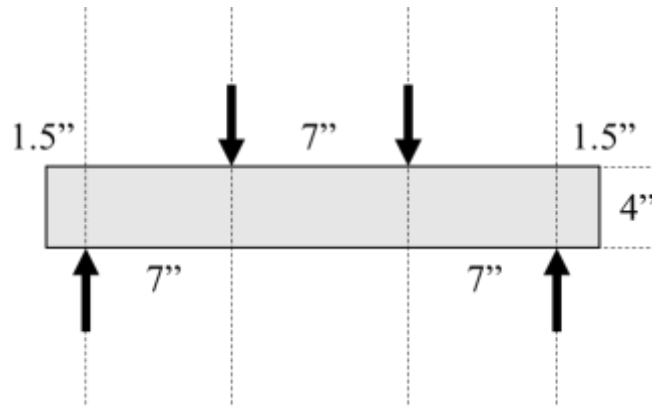
Figure 40: Four-point bending configuration used for 4-in x 4-in x 24-in concrete beam size.

11.1.3 Testing System

An MTS load frame equipped with a 5.5-kip, 6-in stroke hydraulic actuator and a 2.5-metric ton load cell was used to conduct the fatigue testing. The closed-loop hydraulic system was powered by a 2.6-gpm, 3000-psi hydraulic supply. The fatigue testing was controlled by an MTS® FlexTest 40 controller equipped with MTS® Station Manager and TestSuite Multipurpose Elite software.

The concrete beams analyzed in this study were instrumented with linear variable differential transformers (LVDTs) (TE Connectivity) in the layout depicted in Figure 41. Several concrete beams were also instrumented with 120-ohm strain gages (Texas Measurements) on the surface of the beam. The instrumentation was incorporated to ensure that the testing system functioned properly and to evaluate the progression of damage in the concrete.

The LVDTs measured neutral axis deflection and were positioned on the neutral axis of each concrete beam with a harness (pictured in Figure 42). The harness is fixed to the beam at mid-depth directly over the supports. This device allowed the LVDTs to stay in position on the beam as the load was applied. Three LVDTs were located on both sides of the concrete beam: one at midspan and one at each end of the middle third of the span, as shown in Figure 41. The MTS® FlexTest 40 controller sampled the deflection from the LVDTs at a frequency of 1024 Hz and recorded a cycle of deflection data every 16 cycles. The maximum and minimum deflection was also recorded for every cycle.
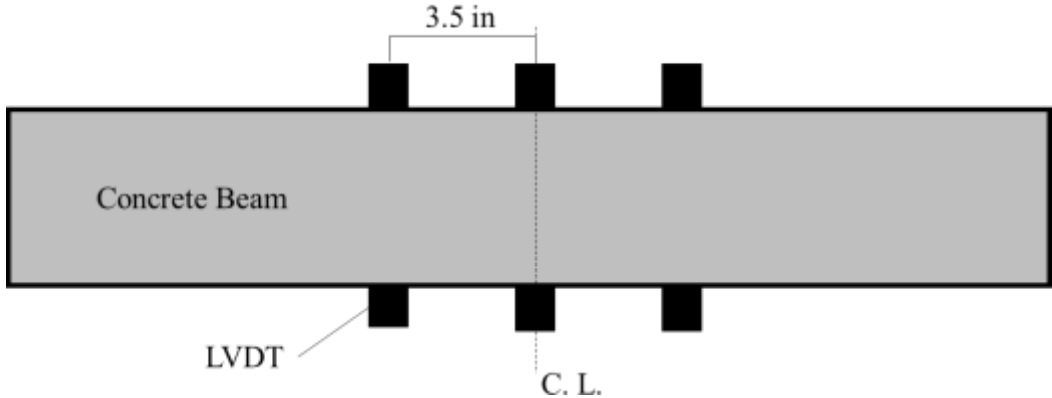
Figure 41: Top view of the LVDT layout.
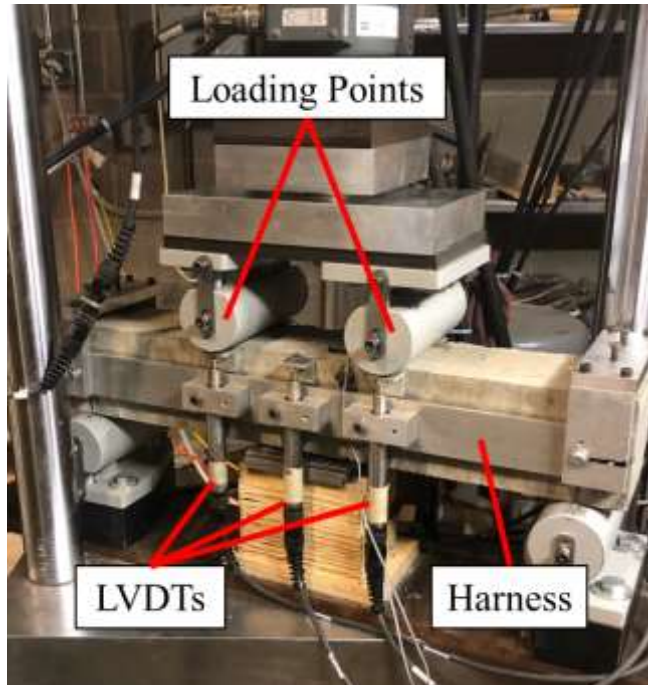
Figure 42: Harness for LVDTs affixed to concrete beam during fatigue testing.

Strain gages were equipped at the center of the top and bottom face on each concrete beam instrumented to measure bending strain. A "half-bridge" Wheatstone bridge circuit was configured with the two resistors having a resistance of 120 ohms. A Campbell Scientific CR1000X datalogger sampled and recorded the bending strain at a frequency of 250 Hz. Initial tests were performed the ensure that this frequency was sufficient for data collection.

11.1.4 Concrete Mixture Design

The concrete mixture design utilized in this study is presented in Table 14. This mixture follows the guidelines of a Class AA paving concrete in Pennsylvania (Pennsylvania Department of Transportation, 2020b). Two coarse aggregates (AASHTO No. 67 and AASHTO No. 8 limestone from Bryan Materials Group), fine aggregate (ordinary sand from Bryan Materials Group), and Type I/II HA cement (Kosmos Cement) are among the core components of the concrete mixture. The specific gravities of the No. 67 coarse aggregate, No. 8 coarse aggregate, and fine aggregate are 2.60, 2.70, and 2.62, respectively. The gradations of the three aggregates are shown in Figure 43. An air entrainer (Sika Air 360) and a superplasticizer (Sikament SPMN) were incorporated during mixing. The actual amount of water added was modified based on the measured aggregate moisture contents on the day of casting to reach the target water content.

Table 14: Concrete mixture design.

Water-to-Cement Ratio	0.44
No. 67 Coarse Aggregate (lb/yd^3)	1,450
No. 8 Coarse Aggregate (lb/yd^3)	300
Fine Aggregate (lb/yd^3)	1,346
Cement (lb/yd^3)	575
Water (lb/yd^3)	254
Sika Air 360 Air Entrainer (oz/100 lb cement)	1.5
Sikament SPMN Superplasticizer (oz/100 lb cement)	3.2
Target Air Content (%)	5
Target Slump (in)	2.0 +/- 0.5
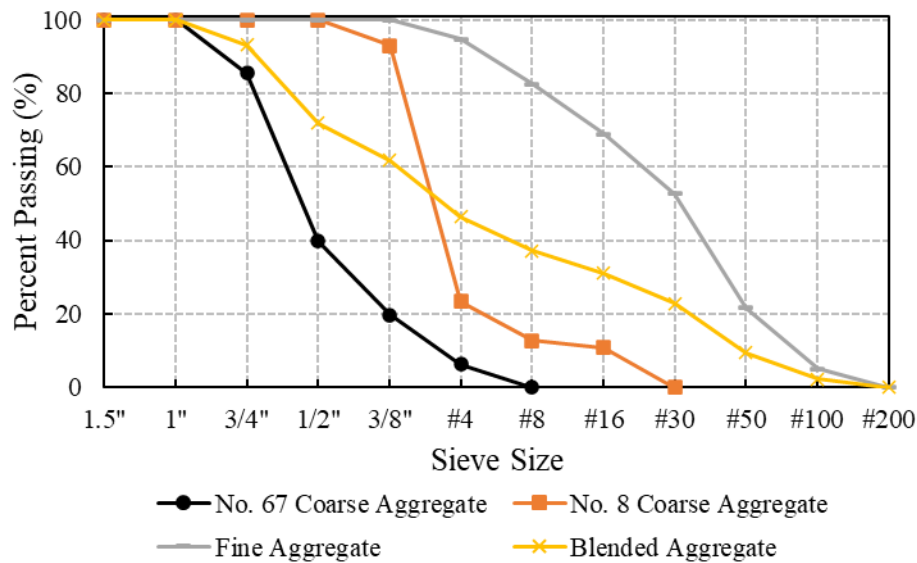
Figure 43: Percent passing for No. 67 coarse aggregate, No. 8 coarse aggregate, fine aggregate, and combined blended aggregate.

11.1.5 Specimen Preparation

All concrete specimens were made and cured in accordance to ASTM C192 (C192/C192M-21, 2019). Concrete beams were made for flexural strength testing and fatigue testing and companion concrete cylinders were made for compressive strength and elastic modulus testing. The flexural strength beams were used to define the stress ratio for fatigue testing, so the beams were 4-in by 4-in by 24-in like the fatigue beams. The compressive strength and elastic modulus cylinders were used to evaluate the strength of the concrete mixture as a function of age and were 4-in by 8-in based on the aggregate top size of the concrete mixture. The cylinders were tested in accordance

with ASTM C39 and C469 (C39/C39M-21, 2021; C469/C469M-14, 2014). All specimens were moist cured until testing except for a short duration for instrumentation, and all cylinders were sulfur capped before testing (C617/C617M-15, 2015).

11.2 Experimental Design

An experimental design was developed to evaluate the effects of overloads on damaged JPCPs. The experimental design consists of two programs: constant amplitude fatigue testing and damaged concrete fatigue testing. The constant amplitude fatigue testing program was designed to establish nonlinear damage curves for superload stresses. The damaged concrete fatigue testing was designed to quantify the damaging effects of an overload as a function of the percent life consumed in the concrete. The test setup outlined in Section 12.1 was used to conduct the fatigue testing.

11.2.1 Stress Profiles

The first step in the experimental design was to determine the stress profiles to be simulated in the fatigue testing. The computational results shown in Section 1 were used as guidance for the development of the stress profiles. Single axle and tandem axle waveforms were considered, since these are the axle types on superload trailers. Several other parameters, such as peak stress, minimum stress, and loading frequency (pictured in Figure 44) had to be established. Details regarding each parameter are discussed herein.
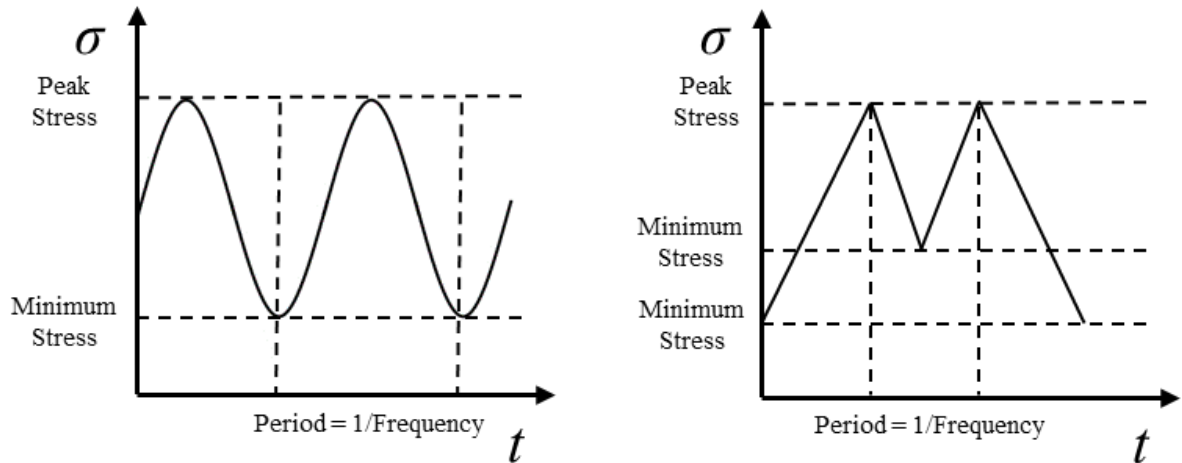
Figure 44: Single axle and tandem stress profiles with unknown parameters labeled.

Peak Stress

As shown in the stress analysis performed in Section 11.3.2, the peak stresses resulting from the superloads ranged between 100 and 600 psi. For instance, JPCPs with an 8-in thickness, a positive equivalent linear temperature gradient of 3 °F/in, and an asphalt shoulder can be subjected to stresses as high as 606 psi. The fatigue analysis presented in Section 11.3.2 showed that significant damage can occur for stress ratios above 0.7. For superloads that apply a stress ratio below 0.7 to a JPCP, the imposed damage is not expected to be very significant. Therefore, for this laboratory study stress ratios of 0.7, 0.8, and 0.9 were chosen. This is equivalent to a peak stress of 455 psi, 520 psi and 585 psi if the anticipated flexural strength of the concrete is 650 psi, for instance.

Minimum Load

A minimum seating load is required so that the loading head maintains constant contact with the concrete beam. A seating load of 10-20% of the maximum load is commonly used for this type of testing (Murdock & Kesler, 1958; Hilsdorf & Kesler, 1966; Roesler, 1998). For this study, the seating load resulting in 100 psi of stress was adopted. This is equivalent to the curling stress caused by a high positive temperature gradient. The load corresponding to a stress of 100 psi is 15-20% of the maximum load.

A load must be specified to define the stress that develops in between the two peak stresses produced by a tandem axle. From the stress pulses developed for SL3, SL4, and SL5 in Section 1.4, this stress was observed to be about 200 psi for a stress ratio of 0.9. For stress ratios of 0.7 and 0.8, this stress is closer to 100 psi. Since 100 psi is the stress corresponding to the seating load, the tandem axle waveform would not be significantly different than the stress profile for a single axle at these two stress ratios. Therefore, it was determined that the tandem axle waveform will only be analyzed at a stress ratio of 0.9 and that a stress magnitude of 200 psi would be applied in between the two peak stresses.

Loading Frequency

Loading frequency is known to have an effect on the fatigue life of concrete, primarily at high stress ratios (Hsu, 1981; Zhang, Phillips, & Wu, 1996). However, this impact is difficult to quantify for fatigue lives from 1,000 to 10,000,000 cycles (Hsu, 1981). In the literature, concrete fatigue testing commonly performed at a loading frequency between 3 Hz and 8 Hz.

It is critical to select a loading frequency that replicates the behavior of superloads, which can have high stress ratios that are applied very slowly. For instance, consider the Yankee Dryer superload trip that occurred in December of 2019 in Pennsylvania. Speeds as low as 15 mph were noted by PennDOT.

For this study, when a single axle loading pulse is applied at a stress ratio of 0.8 or 0.9, a loading frequency of 3 Hz was selected. This represents the movement of SL1 (from Section 11) at a speed of 15 mph. When a tandem axle loading pulse is applied at a stress ratio of 0.9, the loading frequency was 1 Hz. This represents the movement of SL4 (from Section 11) at a speed of 15 mph. When a single axle loading pulse was applied at a stress ratio of 0.7, the loading frequency was 8 Hz. An increase in the loading frequency for this stress ratio to decrease testing time was deemed acceptable since its less sensitive to loading frequency (Hsu, 1981) and commonly tested at higher loading frequencies than stress ratios of 0.8 and 0.9 (Shi, Fwa, & Tan, 1993; Zhang, Phillips, & Wu, 1996).

Stress Profiles

A total of four stress profiles were included in this study, as shown in Figure 45. Single axle stress profiles were generated with peak maximum stress ratios of 0.7, 0.8, and 0.9 using a

sinusoidal wave function, as seen in Figure 45a-c. For the tandem axle stress profile, only a stress ratio of 0.9 was considered using a custom waveform that ramped directly to the target values, as shown in Figure 45d.
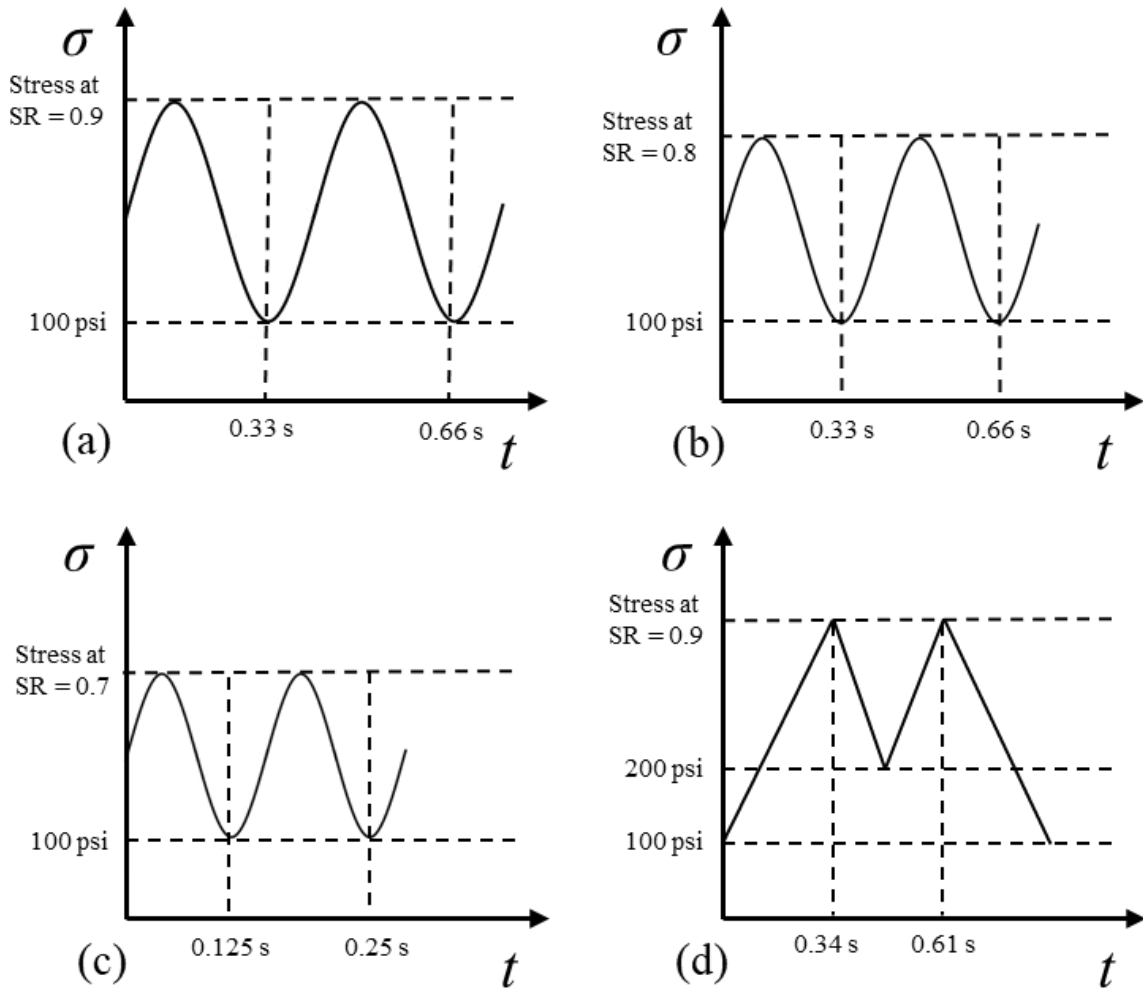
Figure 45: Stress profiles of (a) single axle at a stress ratio = 0.9, (b) single axle at a stress ratio of 0.8, (c) single axle at stress ratio = 0.7, and (d) tandem axle at a stress ratio of 0.9.

The stress profiles were generated by the testing system by specifying the target loads in the MTS® Multipurpose Elite software. To do this, concrete beams are tested statically to determine the average flexural strength, as calculated with Equation 42 (C39/C39M-21, 2021):

$$f_r = \frac{PL}{bh^2} \tag{44}$$

where,

f_r = the flexural strength of the beam, psi

P = the peak load applied by the testing machine, lb

L = the span length, in

b = the width of the beam at fracture, in

h = the depth of the beam at fracture, in

Then, to determine the load input at each stress ratio (i.e., 0.7, 0.8, 0.9), Equation 43 is used:

$$\sigma_{app} = SR\, f_r = \frac{P_{app}L}{bh^2} \tag{45}$$

where,

σ_{app} = the applied stress, psi

SR = the stress ratio

f_r = the average flexural strength of the concrete beams on the testing day, psi

P_{app} = the load corresponding to the applied stress, lb

L = the span length, in

b = the width of the beam, in

h = the depth of the beam, in

11.2.2 Flexural Strengths

To examine the influence of strength on the fatigue life of concrete beams subjected to the stress profiles depicted in Figure 44, fatigue beams were tested at two levels of concrete strength: "new pavement" and "old pavement". The new pavement condition was defined as having a modulus of rupture between 500 and 600 psi. The old pavement condition was defined as having a modulus of rupture between 700 and 800 psi.

Flexural strength tests of 4-in by 4-in x 24-in concrete beams were used to establish the stress ratios for the fatigue testing. The flexural strengths of concrete beams of this size were observed to be greater than that of conventional modulus of rupture beams (illustrated in Section

13). Instead of casting additional 6-in by 6-in by 21-in concrete beams, compressive strength testing was conducted on 4-in by 8-in cylinders and subsequent results were used to determine the strength conditions. The following relationship (Equation 44) was used to correlate compressive strength to modulus of rupture, as suggested by the American Concrete Pavement Association (ACI, 2008):

$$MOR = 2.3 \, f_c'^{\,2/3} \tag{46}$$

where,

MOR = the modulus of rupture, psi

f_c' = the compressive strength, psi

On average, new pavement strength was achieved after 3 days to 6-7 days of curing, and old pavement strength was reached after 14 days to 28 days of curing for the concrete mixture design used in this study. By testing at two levels of strength without altering the mixture design, a more direct comparison of the effects of flexural strength and age on the fatigue life of the concrete can be made.

11.2.3 Fatigue Testing

This laboratory study consisted of a constant amplitude test program and a damaged concrete test program. The constant amplitude test program enables an analysis of the effect of superload stresses on the fatigue life of concrete and provides a basis for the damaged concrete test program. The damaged concrete test program quantifies the effect of overloads on the fatigue life of concrete beams as a function of the percent life consumed in the concrete.

Constant Amplitude Test Program

In the constant amplitude fatigue tests, a load input, corresponding to one of the four stress profiles, was applied cyclically to a concrete beam until failure. Each of the four stress profiles (Section 12.2.1) were evaluated for each of the strength conditions (Section 12.2.2). Failure was defined as complete fracture of the beam. To estimate the load input for constant amplitude fatigue tests in the new pavement condition, the flexural strength was established by testing at least two concrete beams on the day the fatigue testing was performed. Since flexural strength gain occurred

slowly beyond 14 days of moist curing, flexural strength testing was conducted within two days of constant amplitude fatigue testing in the old pavement condition to identify the load input.

Damaged Concrete Test Program

In the damaged concrete tests, concrete beams were first fatigued to a target damage state using the load input corresponding to the single axle stress profile with a stress ratio of 0.7. Once the target damage state was achieved, the concrete beams were overloaded with ten fatigue cycles at a stress ratio of 0.8 or 0.9. Lastly, the stress ratio was returned back to 0.7 and applied cyclically until failure. The damaged concrete test program was structured in this manner to evaluate the effects of the overloads as a function of percent life consumed.

Damage states representing 15%, 50%, and 85% life consumed were chosen for this analysis to represent the different stages of nonlinear damage accumulation. Mindful consideration was given on how to achieve the damage states representing each percent life consumed. Given that fatigue test data can be quite variable, the damage states were not imposed by the predicting the number of fatigue cycles required at a stress ratio of 0.7. Instead, the nonlinear damage parameter of normalized compliance, representing the reduction of stiffness in the concrete, was used. Normalized compliance was related to the percent life consumed in the concrete using a relationship developed from the constant amplitude test results. More about the development and predictability of this relationship is discussed in Section 3.

To reach a target normalized compliance in a given test, a set number of fatigue cycles, ranging from 500-30,000 depending on the anticipated progression of damage in the beam, were applied. Then, the compliance was calculated for every subsequent cycle using Equation 45:

$$C_i = \frac{\delta_{i,max} - \delta_{i,min}}{P_{i,max} - P_{i,min}} \tag{47}$$

where,

C_i = compliance for cycle i, in/lb

$\delta_{i,max}$ = the maximum deflection for cycle i, in

$\delta_{i,min}$ = the minimum deflection for cycle i, in

$P_{i,max}$ = the maximum load for cycle i, lb

$P_{i,min}$ = the minimum load for cycle i, lb

The compliance for each fatigue cycle was normalized to the initial compliance to account for inherent differences (e.g., specimen size) between specimens, as shown in Equation 46:

$$C_i^{norm} = \frac{C_i}{C_0} \tag{48}$$

where,

      C_i^{norm} = the normalized compliance for cycle i

      C_0 = the initial compliance, in/lb

The normalized compliance for consecutive fatigue cycles at a loading frequency of 8 Hz would vary some. Therefore, the average normalized compliance over the most recent 16 cycles (i.e., 2 seconds) was compared to the target normalized compliance. If the target normalized compliance was approximately reached (i.e., at target C_i^{norm} +/- 0.01 for percent life consumed = 15%, 50% and C_i^{norm} +/- 0.02 for percent life consumed = 85%), ten overload cycles (i.e., single axle at a stress ratio of 0.8 or single axle at a stress ratio of 0.9) were applied, and the beam was loaded again at a stress ratio of 0.7 until failure. If the target normalized compliance was not approximately reached, more fatigue cycles were applied at a stress ratio of 0.7 until necessary.

The damaged concrete test program included analyses of concrete beams of both strength conditions. To estimate the load input for damaged concrete fatigue tests in the new pavement condition, at least two beams were tested in flexure on the day of testing. Since flexural strength gain occurred slowly beyond 14 days of moist curing, flexural strength testing was conducted within two days of damaged concrete fatigue testing in the old pavement condition to identify the load input.

11.2.4 Experimental Design

Table 15-Table 16 shows the experimental design matrix for the constant amplitude test program and damaged concrete test program, respectively. The number of concrete beams tested for each combination of parameters was chosen based on the variability observed in the laboratory.

Table 15: Experimental design matrix for the constant amplitude test program, with the number of replicates shown for each combination of parameters.

		Loading Cases			
		Single Axle			Tandem Axle
		SR = 0.7	SR = 0.8	SR = 0.9	SR = 0.9
Flexural Strength	New Pavement (500-600 psi)	4	4	4	4
	Old Pavement (700-800 psi)	3	3	4	3

Table 16: Experimental design matrix for the damaged concrete test program, with the number of replicates shown for each combination of parameters.

		Single Axle Loading Cases					
		Stress Ratio = 0.8			Stress Ratio = 0.9		
		Damage Level = 0.15	Damage Level = 0.50	Damage Level = 0.85	Damage Level = 0.15	Damage Level = 0.50	Damage Level = 0.85
Flexural Strength	New Pavement (500-600 psi)	3	3	3	3	3	3
	Old Pavement (700-800 psi)	3	3	3	3	3	3

12.0 LABORATORY RESULTS AND ANALYSIS

12.1 Cast Summary

A total of 64 beams were cast for performing fatigue testing, 130 4-in by 8-in cylinders were cast for characterizing the compressive strength and elastic modulus, and 99 beams were cast for characterizing the flexural strength. These specimens were made from nine different casts. In

Table 17, a summary of the fresh concrete properties and aggregate moisture contents for each cast is provided. The target slump and air content were 2 inches and 5%, respectively. After casting all specimens were cured in accordance with ASTM C192 until the time of testing (C192/C192M-21, 2019).

Table 17: Fresh concrete properties and aggregate moisture contents.

Cast	Slump (in)	Air Content (%)	Moisture Content of Coarse Aggregate (%)	Moisture Content of Fine Aggregate (%)
1	1.5	4.5	0.06	0.12
2	1	5.0	0.08	0.06
3	1.5	5.5	0.11	0.12
4	1	5.0	0.26	0.22
5	1	5.5	0.05	0.29
6	1	4.5	0.09	0.18
7	1	4.0	0.06	0.18
8	1.5	4.5	0.05	0.20
9	3	5.0	0.04	0.13

12.2 Material Properties

12.2.1 Compressive Strength

For Casts 1-6, compressive strength testing was conducted weekly for up to 28 days after casting. For Casts 7-9, compressive strengths were measured only up to 8 days after casting since fatigue testing was not conducted for strengths representative of that of an older pavement with the specimens from these casts. A complete summary of all concrete cylinders cast for this study is in the Task 4 Appendix A (Table A1). All the cylinders failed in cone and shear.

Figure 46-Figure 48 show the compressive strength gain curves for each cast. A similar trend for strength gain is observed for all casts. The compressive strength increases significantly (i.e., to between a mean of 3,000 psi and 4,000 psi) during the first few days of moist curing. Then, the compressive strength increases by about 1,000 psi from 3 to 7 days. After 7 days, the

compressive strength gain rate starts to decrease. From 14 to 28 days, the compressive strength gain curve flattens. The mean 28-day compressive strength was typically about 6,000 psi. The compressive strength gain curves are best fit with a logarithmic or power function. The coefficients of determination for the fitted logarithmic and power curves were between 0.84 and 0.98, indicating a very good fit.
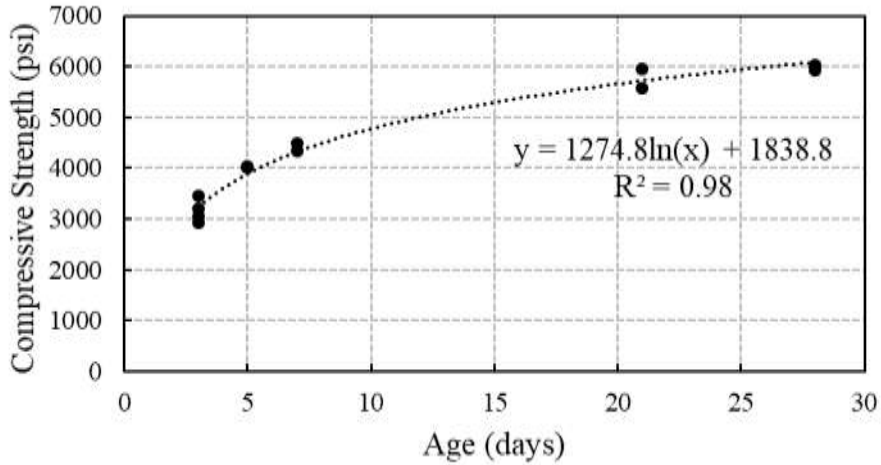
(a)
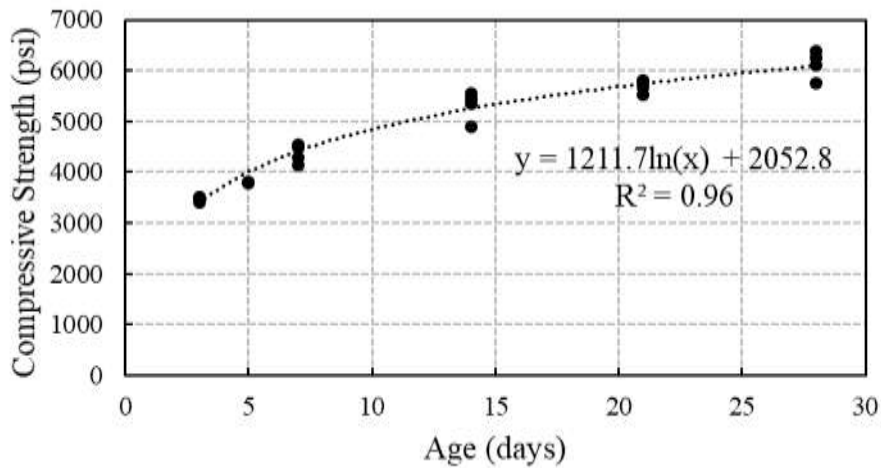
(b)
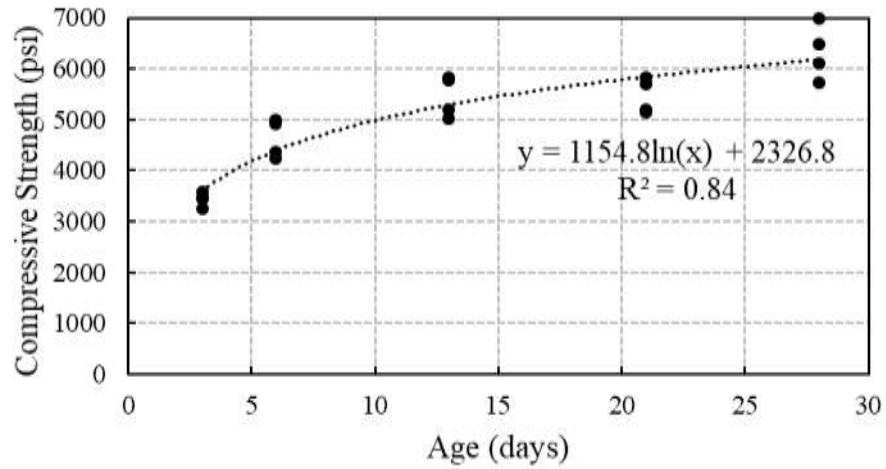
(c)

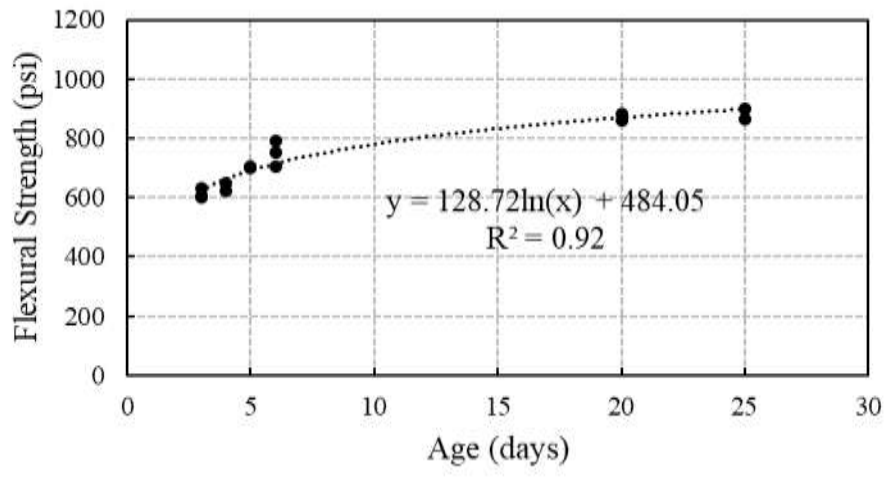Figure 46: Compressive strength gain curves for (a) Cast 1 (b) Cast 2 and (c) Cast 3.
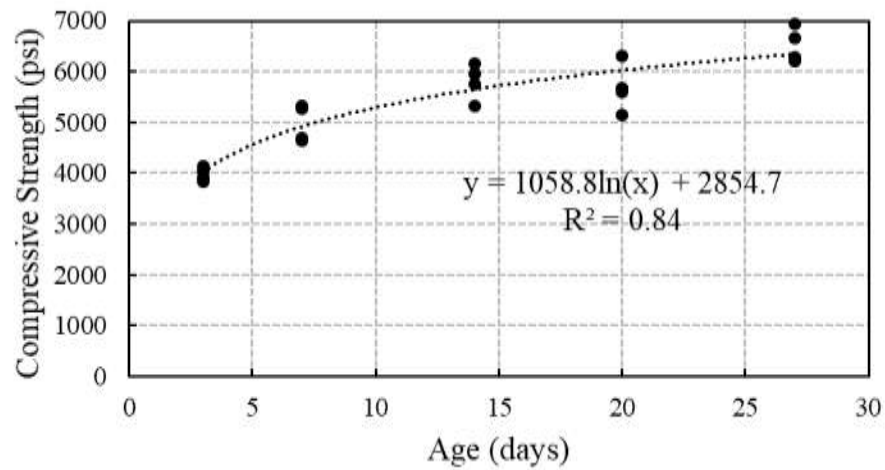
(a)
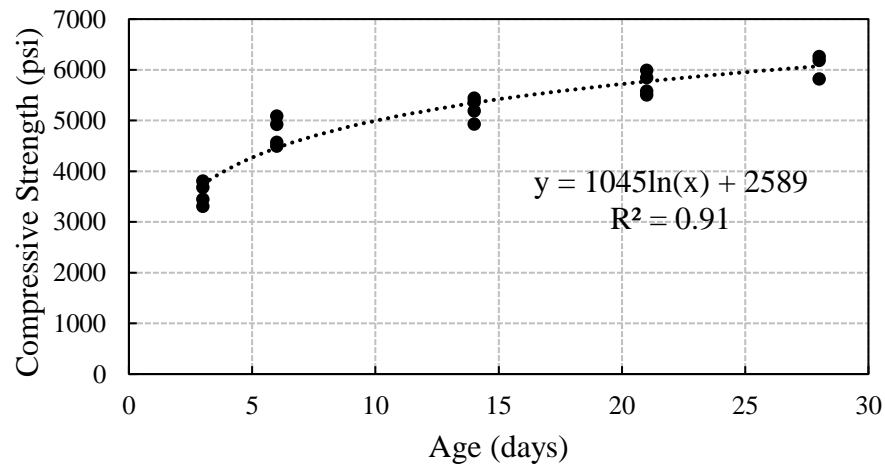
(b)
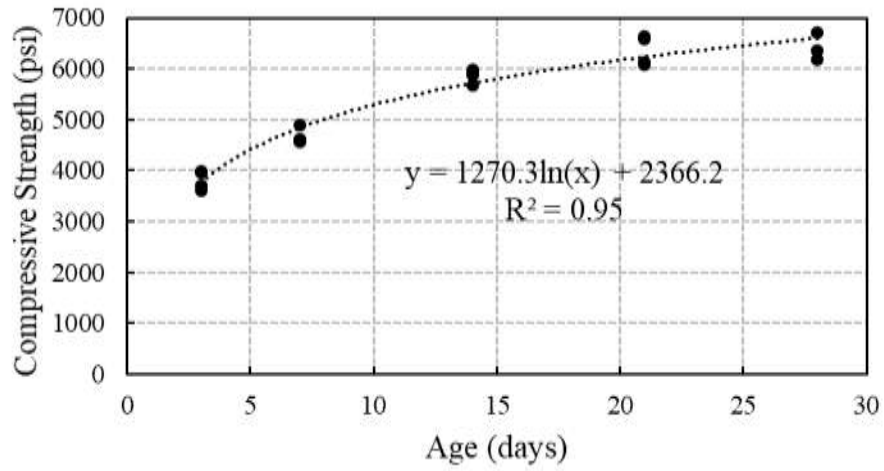
(c)

Figure 47: Compressive strength gain curves for (a) Cast 4 (b) Cast 5 and (c) Cast 6.
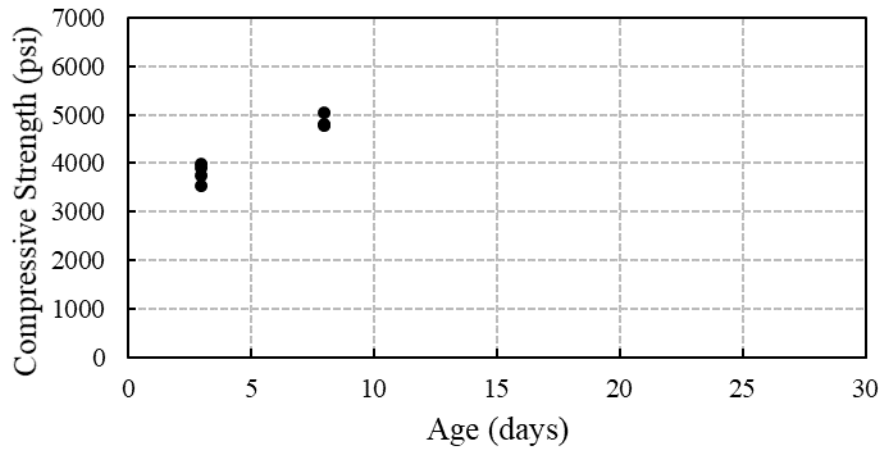
(a)
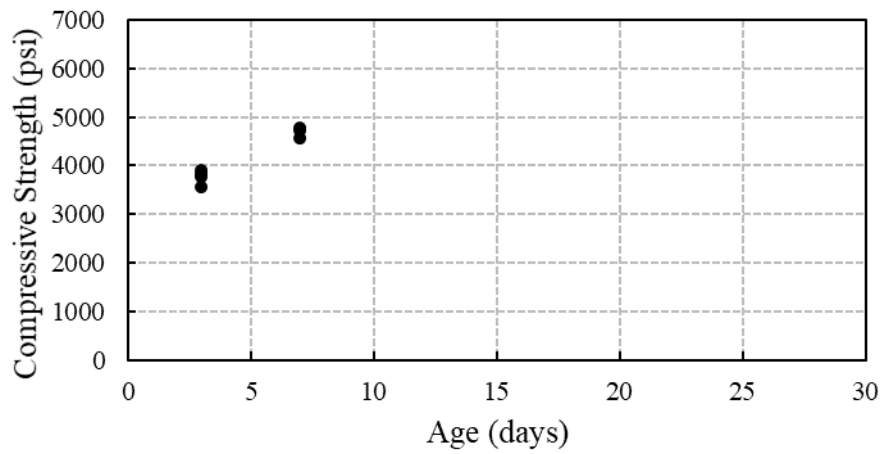
(b)
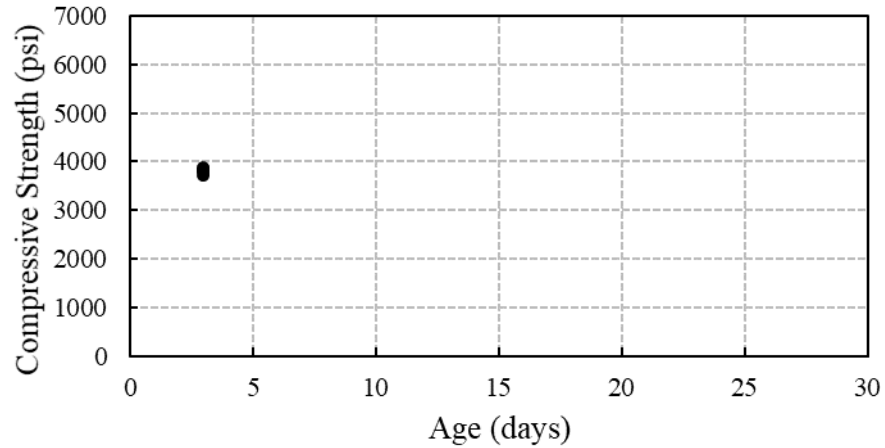
(c)

Figure 48: Compressive strength gain curves for (a) Cast 7 (b) Cast 8 and (c)
Cast 9.

Correlated Flexural Strength

The ACPA compressive strength to modulus of rupture correlation (Equation 44) was applied to each compressive strength. The target compressive strength representing that of a new pavement was 3,200 to 4,200 psi. The target compressive strength representing that of an old pavement was 5,300 to 6,500 psi. The new pavement target compressive strength equating to a modulus of rupture of 500 to 600 psi was achieved at between 3 to 6 or 7 days. The old pavement target compressive strength equating to a modulus of rupture of 700 to 800 psi was achieved at between 14 and 28 days.

12.2.3 Elastic Modulus

For Casts 1-6, elastic modulus testing was conducted weekly until 28 days of moist curing was reached. For Casts 7-9, elastic modulus tests were only conducted at three and seven to eight days after casting since this concrete was only used for casting the new pavement strength fatigue beams. Elastic modulus results are included in Task 4 Table A1 of Appendix A.

Figure 49-Figure 51 show the development of the stiffness of the concrete for each cast. A similar trend in the development of stiffness is observed for the concrete from all casts. The mean elastic modulus of the concrete is typically between 2,500,000 psi and 3,000,000 psi after 3 days of moist curing. After 7 days, the elastic modulus of the concrete surpasses 3,000,000 psi. Then, the concrete gains stiffness at a decreasing rate until the curve flattens at approximately 28 days. The mean 28-day elastic modulus was commonly between 3,300,000 and 3,700,000 psi. The

elastic modulus vs. time relationship is best defined with a logarithmic function. The coefficients of determination for the fitted logarithmic curves were between 0.70 and 0.91, indicating a good to very good fit.

(a)

(b)

(c)
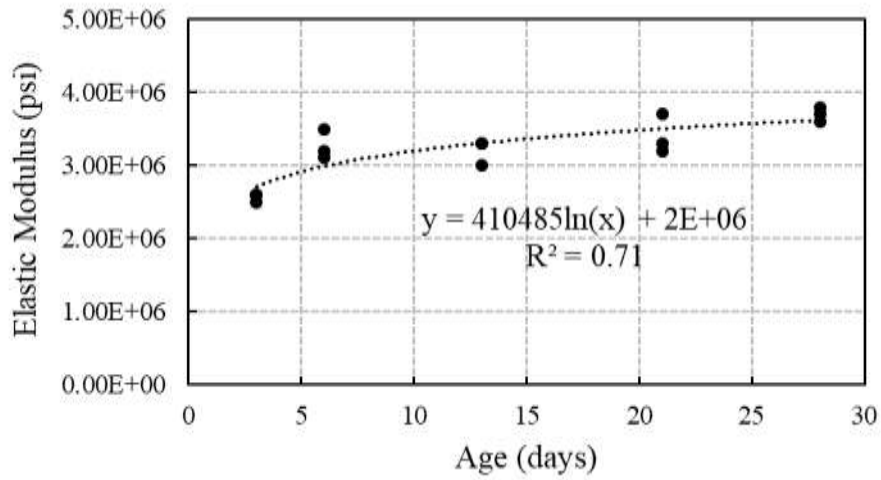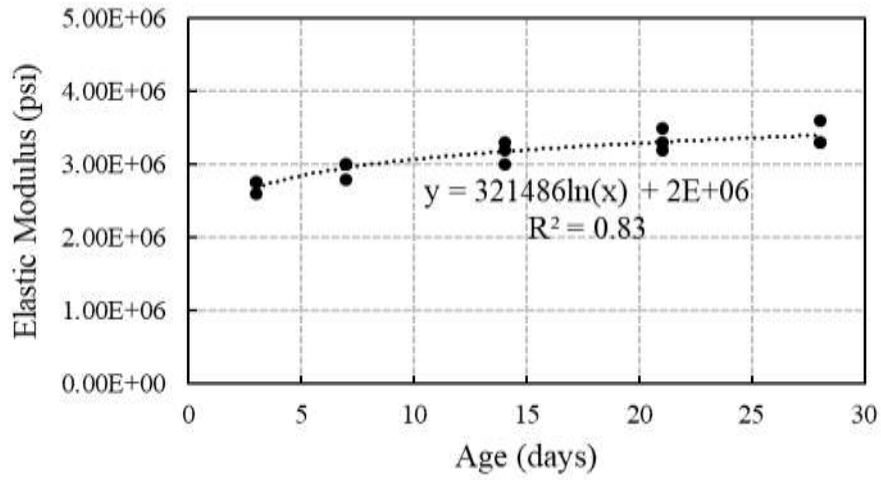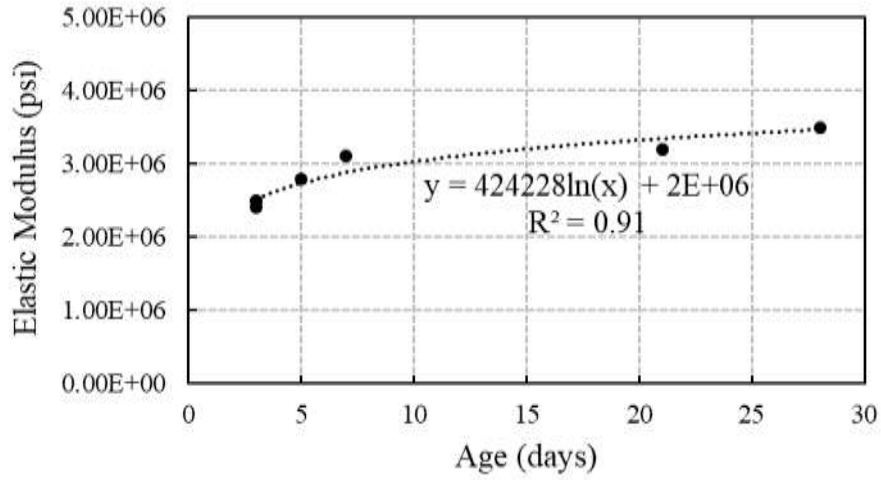
Figure 49: Elastic modulus gain curves for (a) Cast 1 (b) Cast 2 and (c) Cast 3.

(a)

(b)

(c)
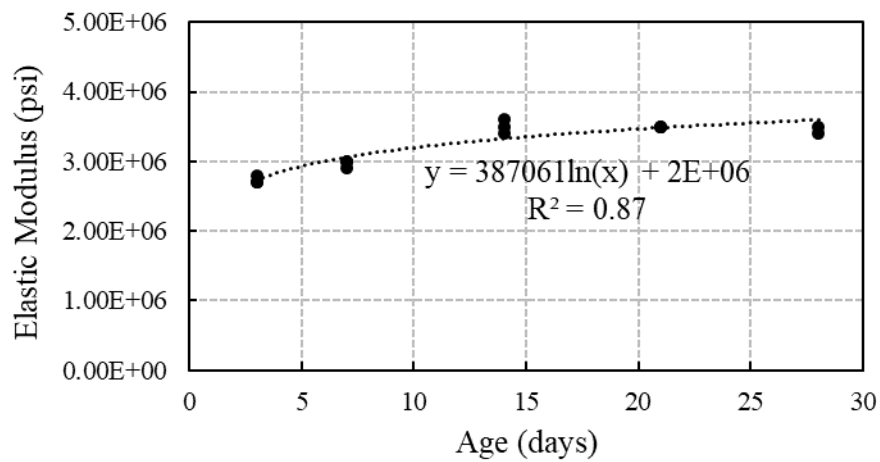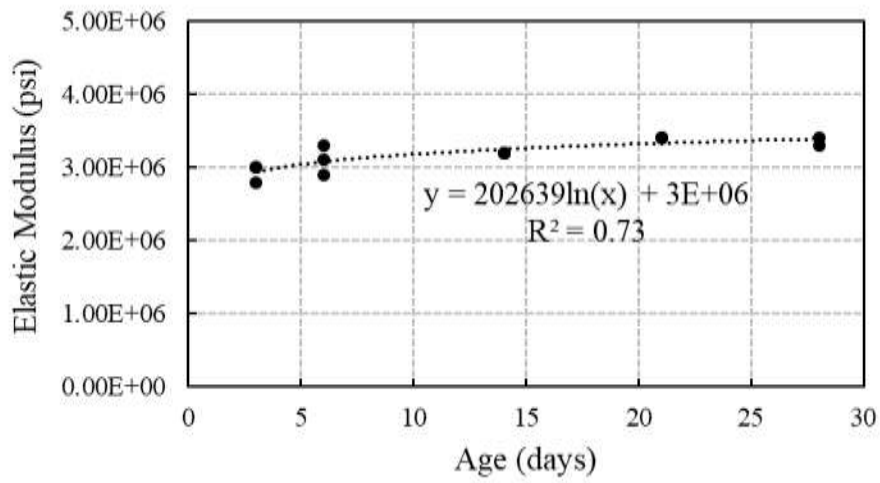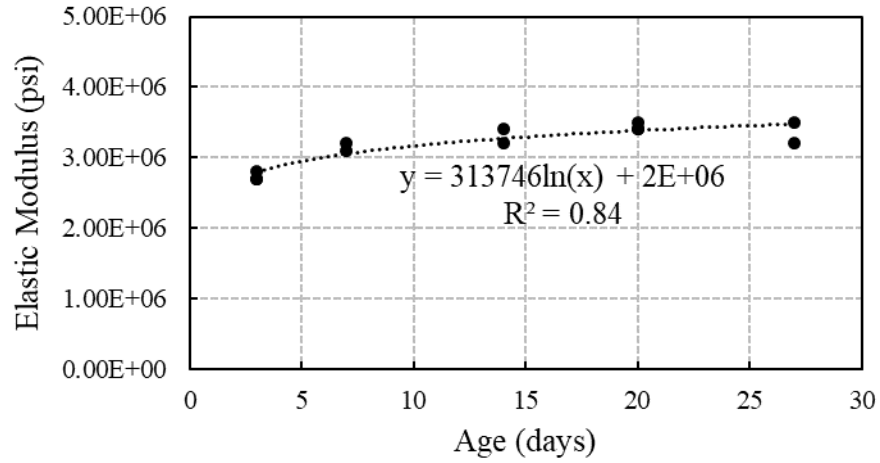
Figure 50: Elastic modulus gain curves for (a) Cast 4 (b) Cast 5 and (c) Cast 6.
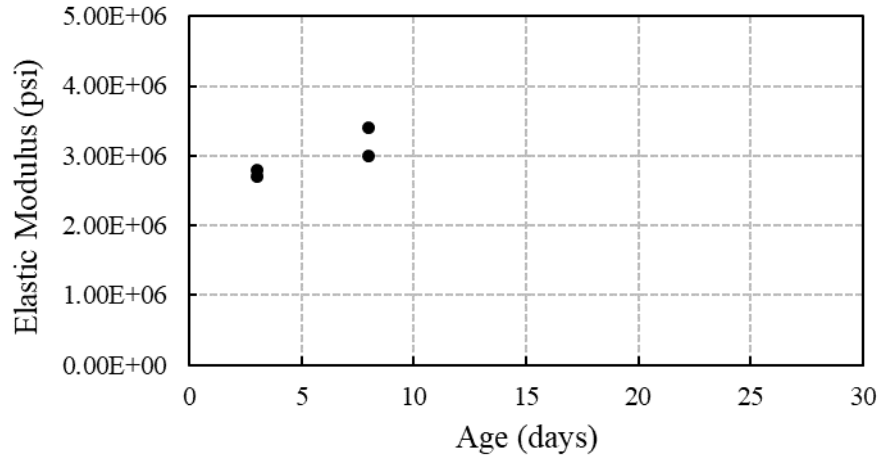
(a)
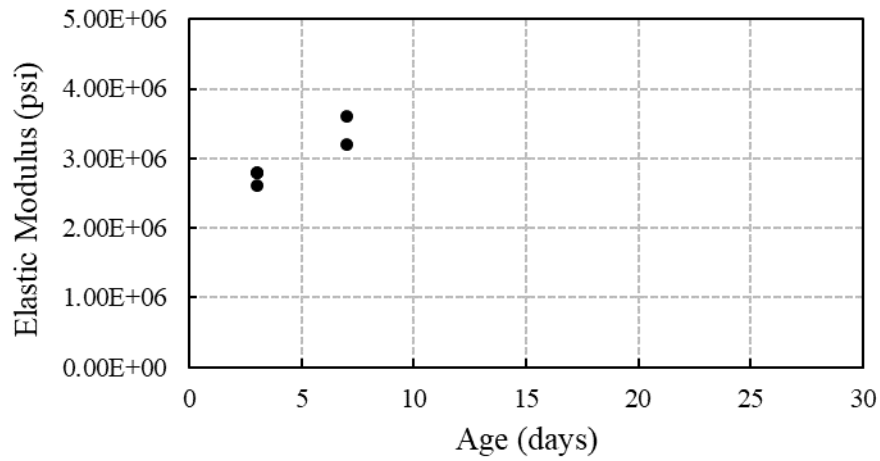
(b)
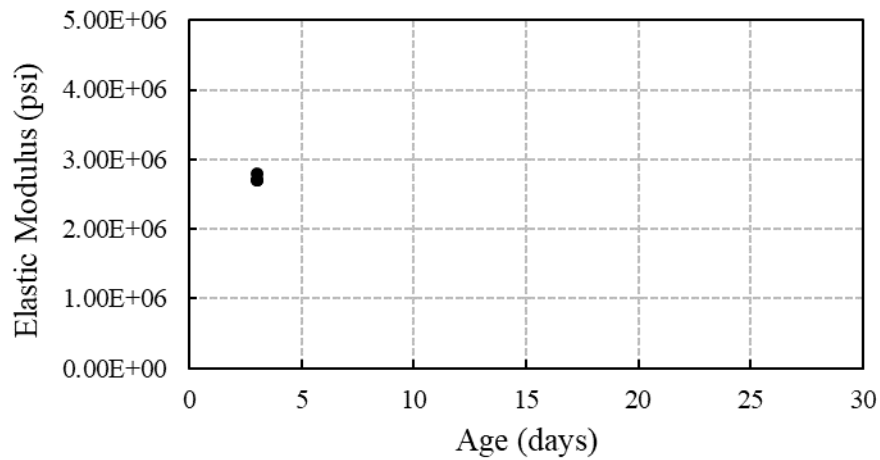
(c)

Figure 51: Elastic modulus gain curves for (a) Cast 7 (b) Cast 8 and (c) Cast 9.

12.2.3 Flexural Strength

Flexural strength testing was conducted on the 4-in by 4-in by 24-in concrete beams to establish the 28-day flexural strength gain curve. This allowed the flexural strength to be quantified

for the same smaller beam size that was used when performing the fatigue testing. Specimens from Cast 1 were used for this purpose. The flexural strength of the 4-in by 4-in by 24-in beams was also measured to establish the stress ratios for the fatigue testing, as stated in Section 12. A complete summary of the flexural strengths for this beam size is provided in the Task 4 Appendix A (Table A2). The flexural strengths of the smaller beams were observed to be about 20% greater than the flexural strengths estimated using the compressive strengths (Section 13.2.1), most likely indicating a size effect.

Concrete beams tested after 3 to 7 days failed either mostly around the aggregate or through and around the aggregate. Concrete beams tested between 14 and 28 days failed either through and around the aggregate or mostly through the aggregate. The failure developed in the region between the two loading lines for each test performed. Figure 52 depicts examples of typical cracking at failure.


(a)

(b)

(c)
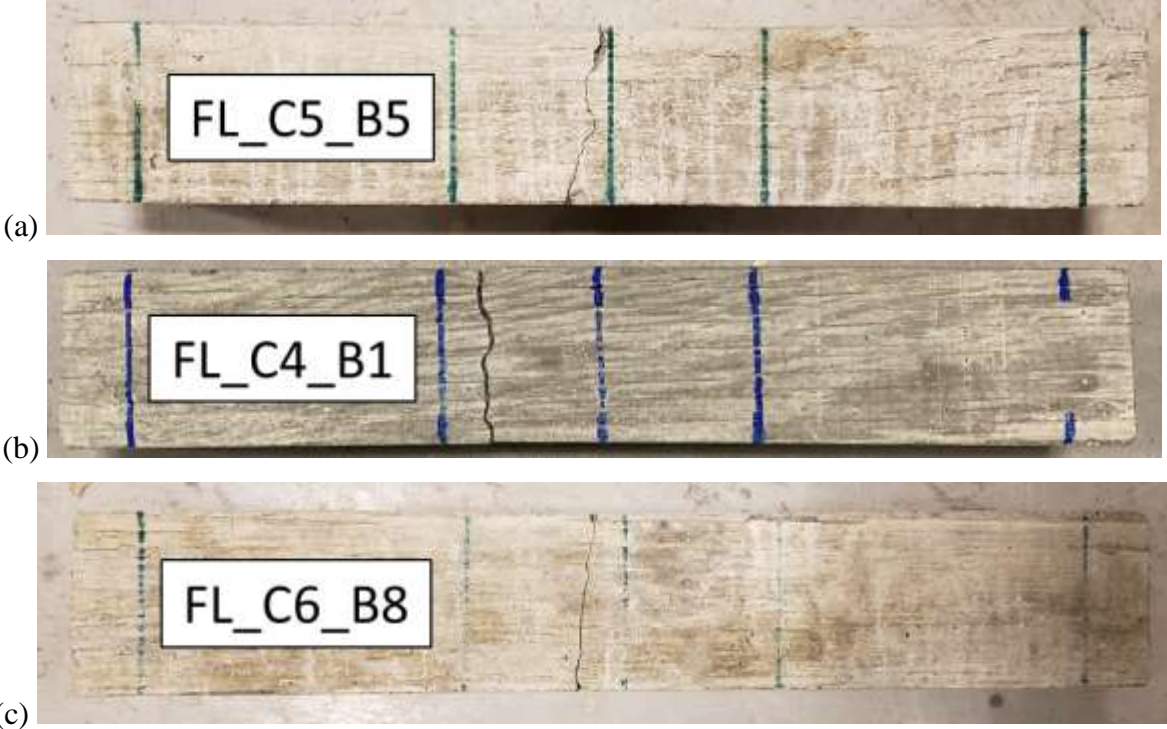
(d)

Figure 52: Failure cracks for (a) FL_C5_B5 (age = 4-day) (b) FL_C4_B1 (age = 3-day) (c) FL_C6_B8 (age = 17-day) (d) FL_C3_B12 (age = 20-day).

Figure 53-Figure 55 show the flexural strength gain curves for each cast. A similar trend in strength gain is observed for all casts. The mean flexural strength of the concrete was observed to be between 600 and 700 psi at 3 days. The mean flexural strength increased by 50 to 100 psi between days 3 and 6. After 7 days of moist curing, the flexural strength developed at a decreasing rate. For each cast, the flexural strength gain between 21 to 28 days was negligible. The flexural strength gain curves are best fit with a logarithmic or power function. The coefficients of determination for the fitted logarithmic and power curves were between 0.77 and 0.94, indicating a good to very good fit. Some variability was observed in the flexural strengths at early ages, especially for Casts 1 and 2. For all casts, this variability in the flexural strength decreased after 14 days. These observations are as expected, as concrete beams are anticipated to have a larger presence of defects at early ages. This contributes to a larger variation in the flexural strengths.

(a)

(b)

(c)
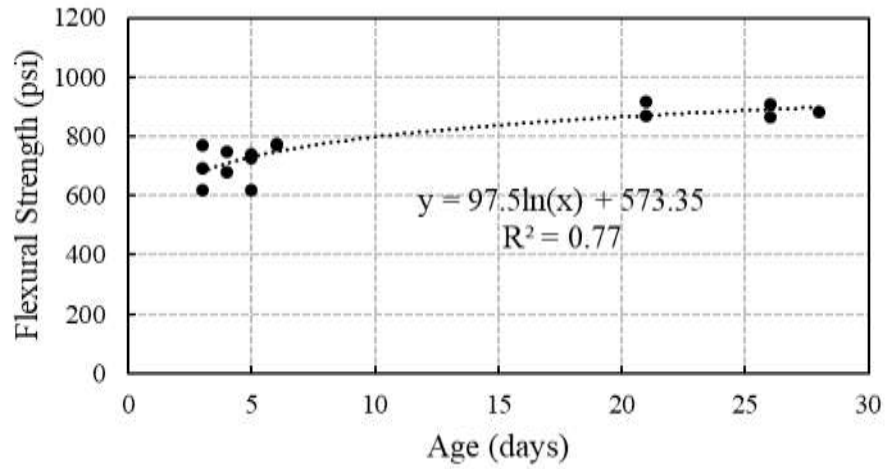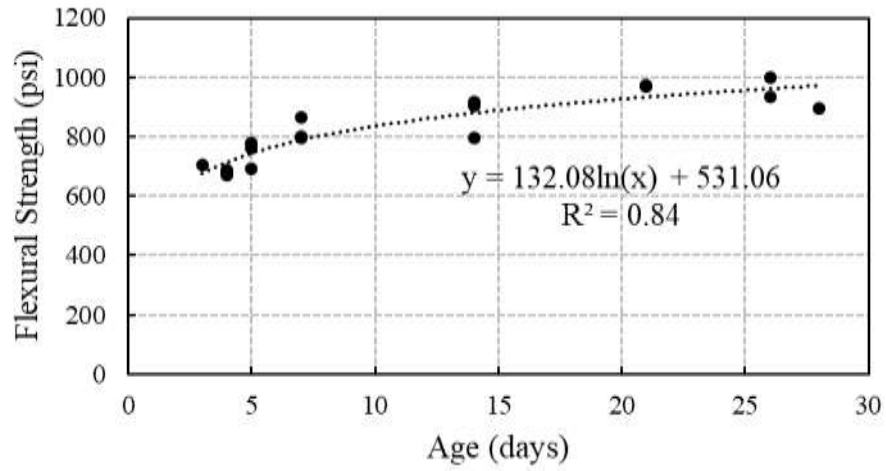
Figure 53: Flexural strength gain curves for (a) Cast 1 (b) Cast 2 and (c) Cast 3.

(a)

(b)

(c)
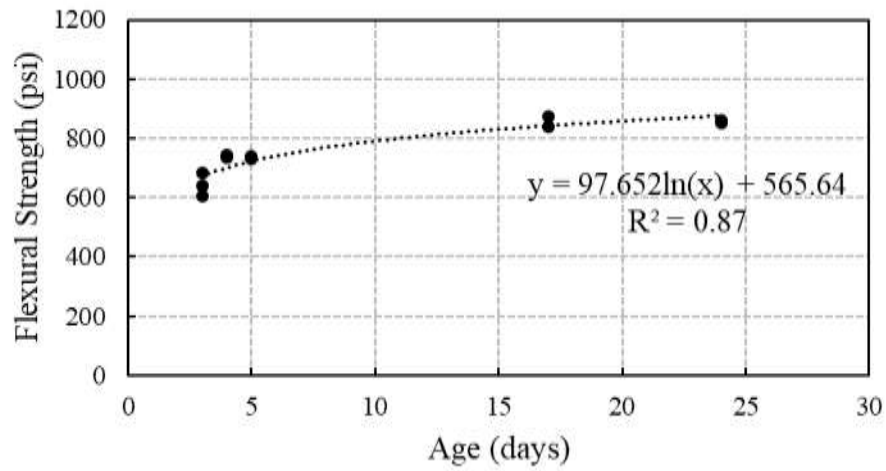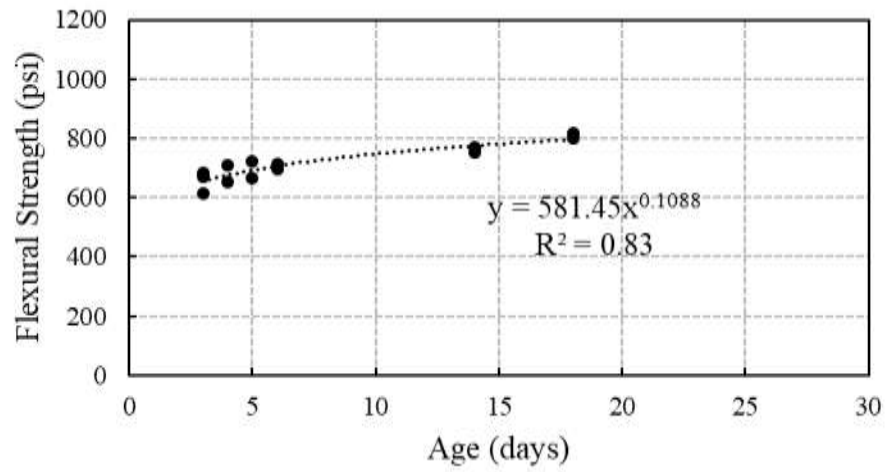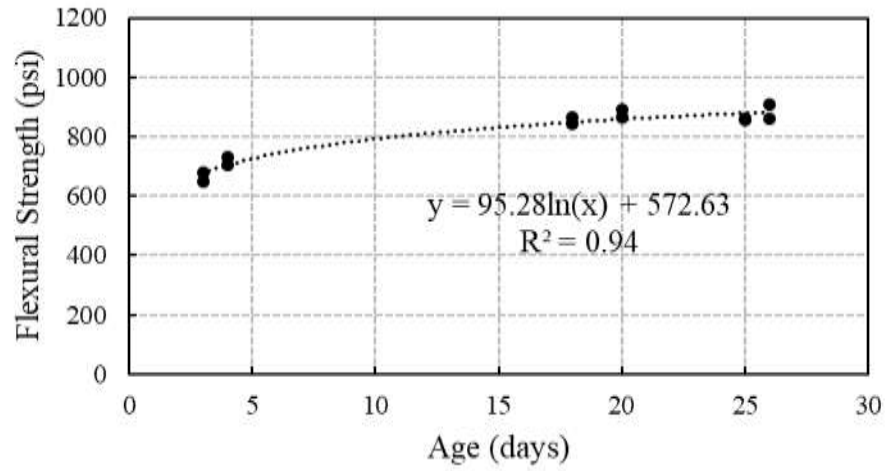
Figure 54: Flexural strength gain curves for (a) Cast 4 (b) Cast 5 and (c) Cast 6.

(a)

(b)

(c)
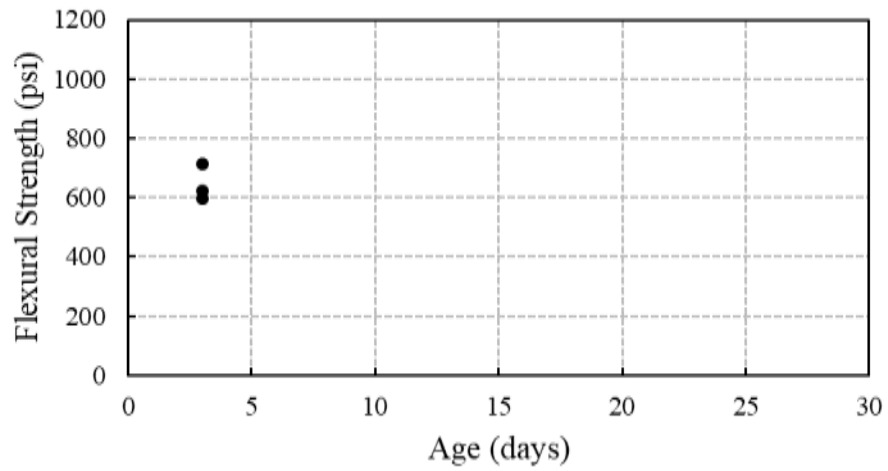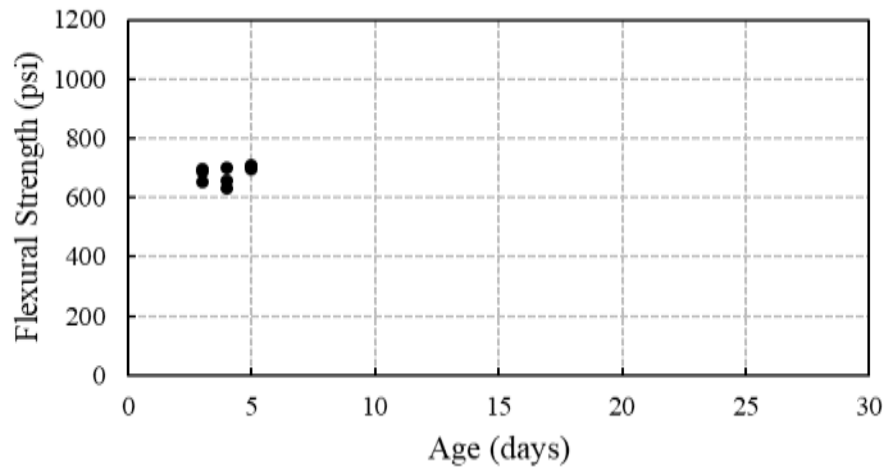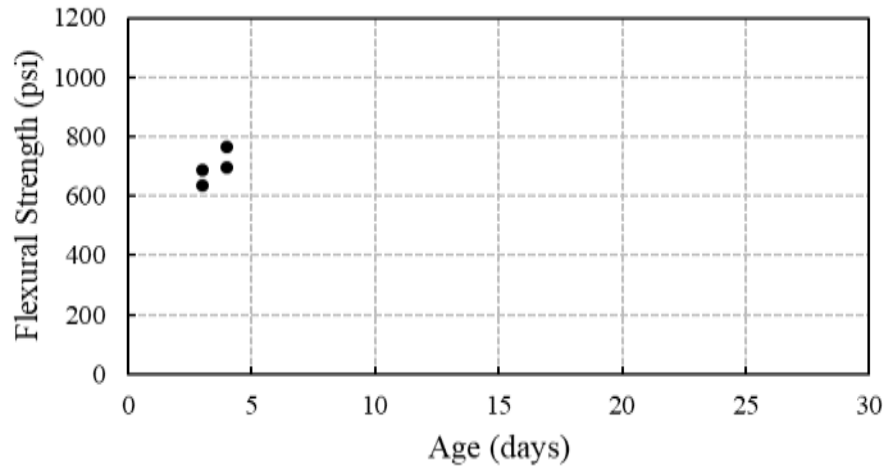
Figure 55: Flexural strength gain curves for (a) Cast 7 (b) Cast 8 and (c) Cast 9.

12.3 Constant Amplitude Testing

The fatigue life of concrete subjected to stress levels similar in magnitude to the stress that develops in a pavement due to superloads was evaluated. Three stress ratios (Section 12.2.1) were investigated for two different strengths (Section 12.2.2). A total of 28 constant amplitude fatigue tests were conducted using specimens from Casts 1-4, as shown in Table 18. The stress profiles used in the constant amplitude testing are provided in Figure 56.

Table 18: Number of constant amplitude tests for each cast.

Cast	New Pavement Strength	Old Pavement Strength
1	0	5
2	5	6
3	6	1
4	4	0
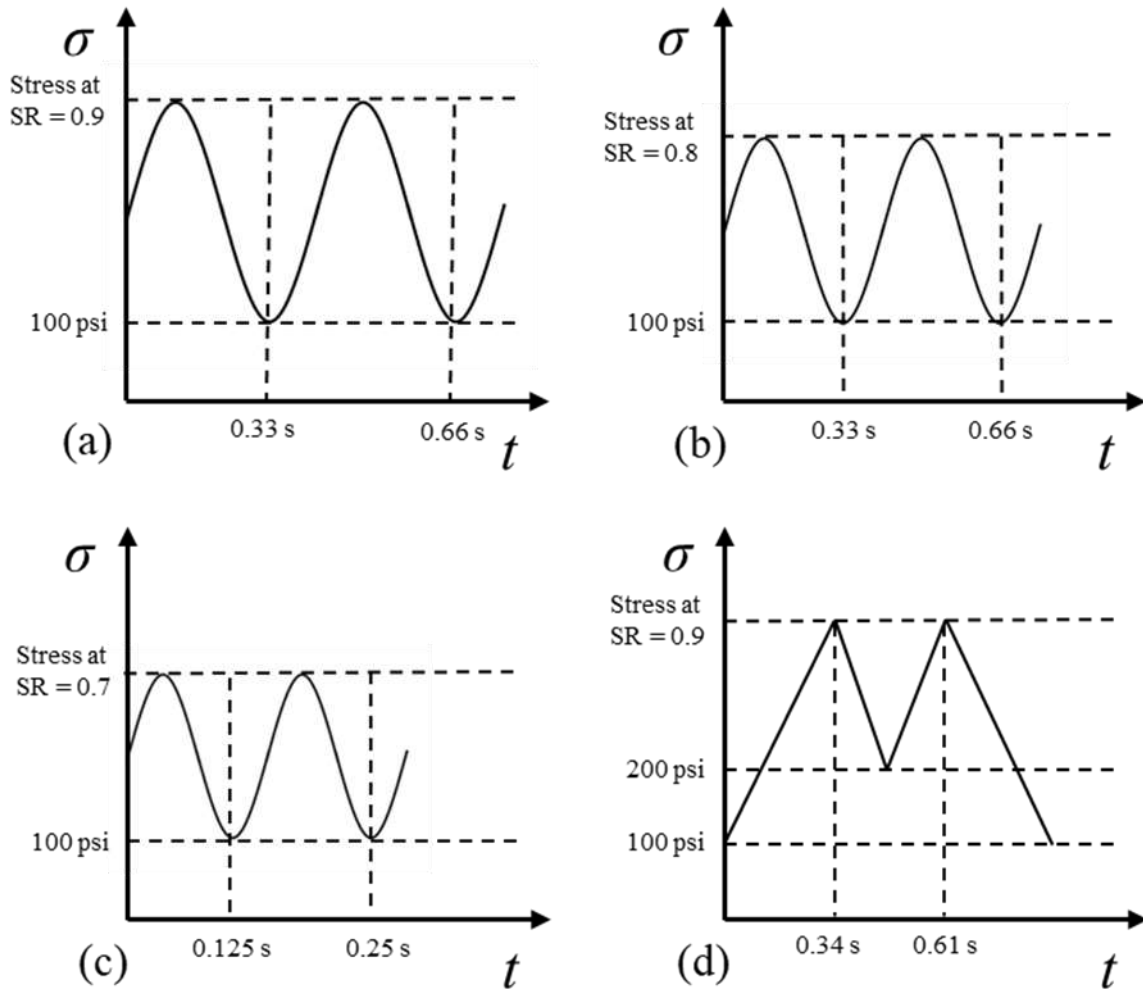
Figure 56: Stress profiles used in the constant amplitude testing (a) single axle at a stress ratio = 0.9 (b) single axle at a stress ratio of 0.8 (c) single axle at stress ratio = 0.7 and (d) tandem axle at a stress ratio of 0.9.

Constant amplitude fatigue testing was conducted on new pavement strength concrete beams at between 3 to 6 days after casting. The old pavement concrete beams with higher strengths were tested at between 14 to 28 days after casting. The number of tests performed in each test cell in the experimental design matrix for the new pavement strength was increased from 3 to 4 due to the high variability observed. A complete summary of the constant amplitude fatigue testing for all concrete beams is in Task 4 Appendix B (Table B1). The structural response data collected for each fatigue test is also included in Task 4 Appendix B (Figures B1-B28).

12.3.1 Fracture

The fracture behavior of concrete beams tested in constant amplitude fatigue was similar to the fracture behavior observed during flexural strength testing. Concrete beams tested after 3 to 7 days failed either mostly around the aggregate or through and around the aggregate. Concrete beams tested between 14 and 28 days failed either through and around the aggregate or mostly through the aggregate.

During the fatigue testing, no visual signs of cracking was observed until the crack developed at failure. The failure developed in the region between the two loading lines for each test performed. Figure 57 depicts examples of typical cracking at failure. Upon visual inspection, 16 of the 28 concrete beams tested in constant amplitude fatigue failed within 2 inches of the center of the beam. The remaining 12 concrete beams failed within the tension zone but beyond 2 inches from the center of the beam. The location of the failure crack is particularly important to interpret the bending strain measurements, as described in Section 13.3.5.

(a)

(b)

(c)
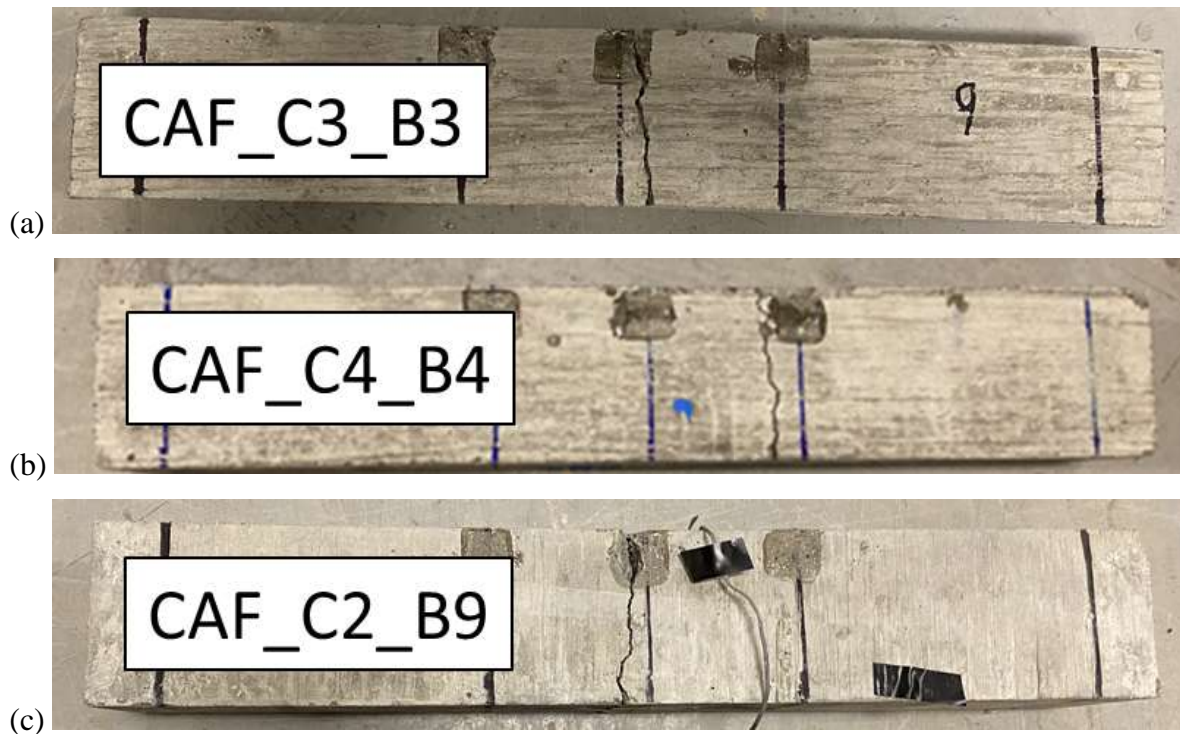
(d)

Figure 57: Failure cracks for (a) CAF_C3_B3 (age = 4-day) (b) CAF_C4_B4 (age = 4-day) (c) CAF_C2_B9 (age = 22-day) (d) CAF_C1_B3 (age = 27-day).

12.3.2 Fatigue Life

<u>S-N Curves</u>

To examine the effects of stress ratio on fatigue life, S-N curves were developed. Only the stress profiles resulting from a single axle load were initially considered. The S-N curves for new pavement strength and old pavement strength concrete are shown in Figure 58. As depicted in Figure Figure 58a, there was an outlier excluded from the relationship (CAF_C2_B3). Specimen CAF_C2_B3 had a fatigue life of 276 cycles at a stress ratio of 0.7. This break occurred at more than two orders of magnitudes of cycles earlier than anticipated based on the results for a similar study found in the literature (Chatti, et al., 2009). Upon visual inspection, the beam failed near an entrapped air void. The coefficient of determination was increased from 0.54 to 0.67 with the elimination of this erroneous point, which justified the exclusion.

(a)

(b)
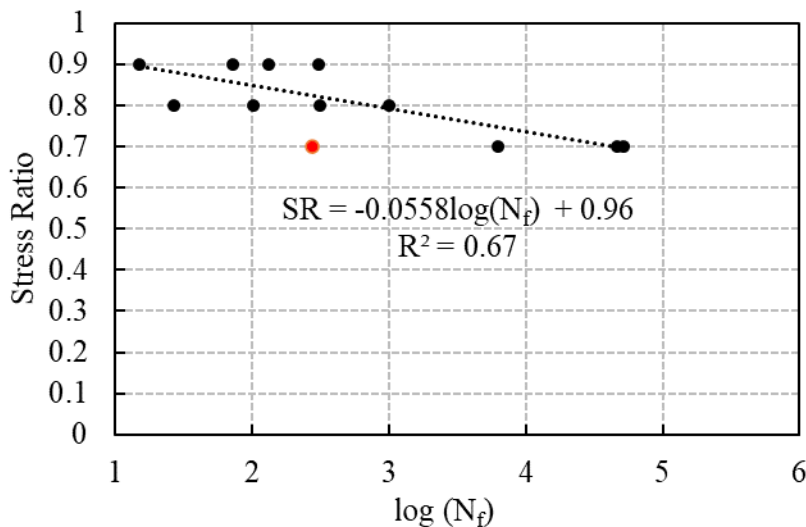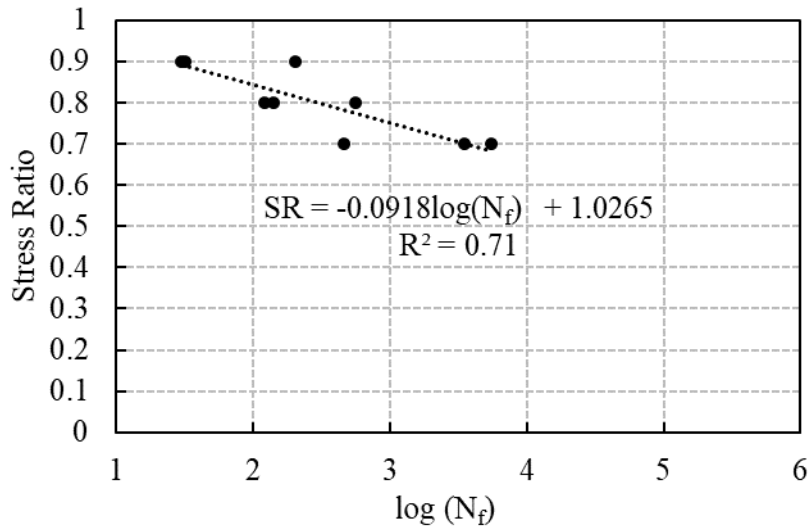
Figure 58: S-N curves for single axle fatigue testing (a) new pavement strength and (b) old pavement strength.

The old pavement S-N curve showed a reasonably strong coefficient of determination for only 9 data points. Three samples were tested for each stress ratio, except 0.9. A fourth test was performed at a stress ratio of 0.9 since one of the concrete beams failed after only 3 cycles and could not be added to the logarithmic curve fitting. Upon visual inspection, there were no obvious defects which contributed to the premature failure.

For concrete with new pavement strength, the number of single axle cycles to failure, N_f, is predicted by the respective S-N curve to be approximately $10^{4.5}$, 10^3, and 10^1 for stress ratios of 0.7, 0.8, and 0.9, respectively. For concrete with old pavement strength, the number of single axle cycles to failure is predicted by the respective S-N curve to be approximately $10^{3.5}$, $10^{2.5}$, and $10^{1.5}$ for stress ratios of 0.7, 0.8, and 0.9, respectively. The old pavement S-N curve appears to be slightly steeper than the new pavement S-N curve. A two-tailed t-test was performed to evaluate if the strength level is influential on the fatigue life of concrete from a given stress ratio. The results of this analysis are shown in Table 19. As shown in Table 19, a stress ratio of 0.7 applies a statistically different damage (with 90% confidence) to concrete with new pavement strength and old pavement strength.

Table 19: Comparison between cycles to failure for new pavement and old pavement strength testing.

Stress Ratio	0.7	0.8	0.9
Mean Cycles for New Pavement Strength	34,814	361	132
Mean Cycles for Old Pavement Strength	3,128	275	88
Standard Deviation for New Pavement Strength	24,925	444	127
Standard Deviation for Old Pavement Strength	2,518	250	99
Null Hypothesis	$\mu_1-\mu_2=0$	$\mu_1-\mu_2=0$	$\mu_1-\mu_2=0$
t-statistic	2.19	0.30	0.49
Degrees of Freedom	4	5	5
Significance	0.10	0.10	0.10
p-value	0.09	0.78	0.64

To assess how the difference affects the S-N curves, an evaluation was performed to determine if the difference in the two slopes is statistically significant. The results of this analysis are presented in Table 20. The difference in slopes between the two S-N curves is not observed to be statistically significant at a 95% level of confidence.

Table 20: Comparison of the difference in the two slopes of the S-N curves.

Flexural Strength	New Pavement	Old Pavement
Slope	-0.05581	-0.0918
Standard Error of Slope	0.0132	0.0221
Sample Size	11	9
Null Hypothesis	$S_1-S_2=0$	
t-statistic	1.40	
Degrees of Freedom	16	
Significance	0.05	
p-value	0.18	

Since the slopes were not statistically different, the data was combined into one S-N curve, as shown in Figure 59. The coefficient of determination was observed to decrease when all data was considered together. This further indicates the potential influence of flexural strength on the results of the constant amplitude testing. The perceived influence of flexural strength is

hypothesized to be a consequence of the stress range. Since the minimum stress was 100 psi for all constant amplitude tests, the beams with new pavement strength experienced a smaller stress range in each fatigue cycle than the beams with old pavement strength. To test this hypothesis, a SR-N curve (i.e., stress ratio range vs. number of cycles curve) was developed with all data consider together. As shown in Figure 60, the SR-N curve has a coefficient of determination comparable to those of the individual S-N curves. This finding indicates that stress range does likely affect the fatigue damage produced by a given stress ratio.
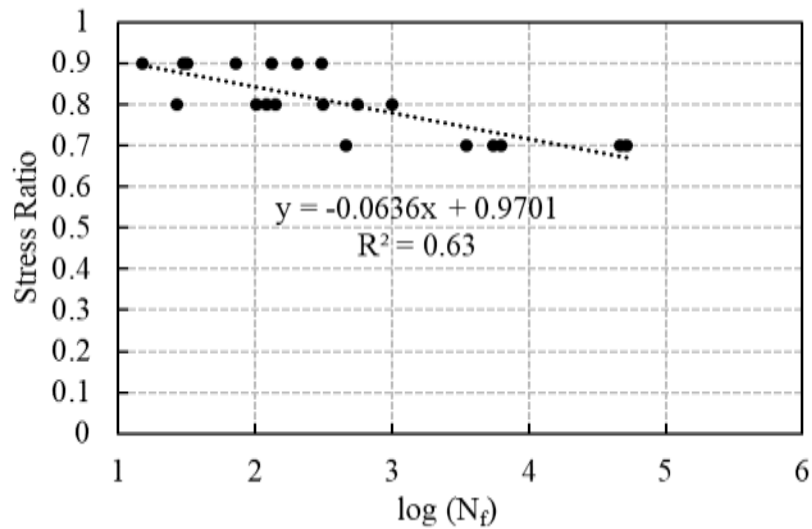
Figure 59: S-N curve with all data combined.
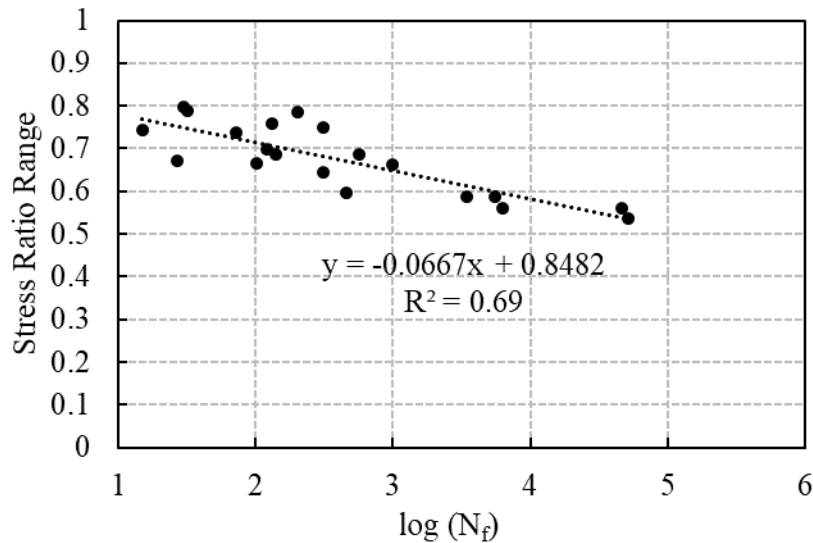
Figure 60: SR-N curve with all data combined.

The S-N curves were compared to others in the literature, as presented in Figure 61. The new pavement S-N curve has a similar slope to the Zero-Maintenance S-N curve (Darter, 1977), and the old pavement S-N curve has a similar slope to the PCA S-N curve (Packard and Tayabji 1985) and the Chatti et al. S-N curve (Chatti, et al., 2009). The Zero-Maintenance S-N curve and PCA S-N curve were both developed with beam fatigue data gathered from many studies. As such, these curves are representative of a range of beam parameters. For instance, the Zero-Maintenance S-N curve utilized fatigue data from 6-in by 6-in by 64-in and 4-in by 4-in by 20-in beams of flexural strengths between 500-900 psi (Ballinger, 1971; Raithby & Galloway, 1974). Collecting beam data from many studies creates a larger database to develop a relationship. However, several impactful factors may be different between studies, including:

- Fatigue beam size
- Flexural beam size
- Loading type
- Loading frequency
- Flexural strength
- Minimum load between consecutive fatigue cycles

The combinations of parameters represented in the data set used for the development of the Zero-Maintenance S-N curve yield a similar output to the new pavement S-N curve, and the combinations of parameters used in the data for the PCA S-N curve yield a similar output to the old pavement S-N curve. As shown in this study, it may be beneficial to account for stress range and the size effect in the prediction of fatigue damage.

The S-N curve that was developed by Chatti *et al.* was developed from fatigue testing of 4-in by 4-in by 24-in beams. Flexural testing of 4-in by 4-in by 12-in beams were used to establish the stress ratios for the fatigue testing. The flexural strengths of beams of this size were measured at between 600-800 psi, and all tests were conducted after 90 days of curing. Additionally, the Chatti *et al.* S-N curve was developed specifically for single axle load pulses. This combination of parameters yields a curve that aligns well with the old pavement S-N curve, meaning that the beams were most likely subjected to similar stress ranges, as well as the same beam size and a similar concrete strength.

132
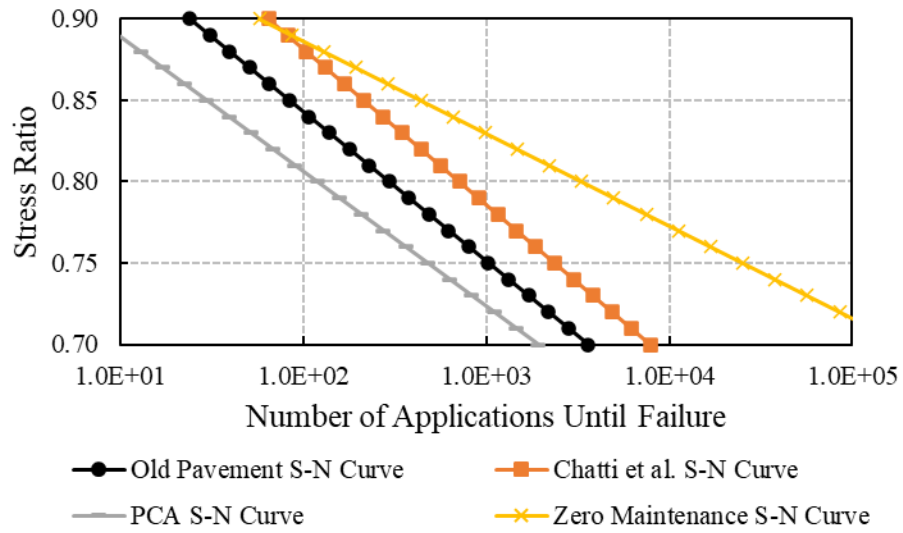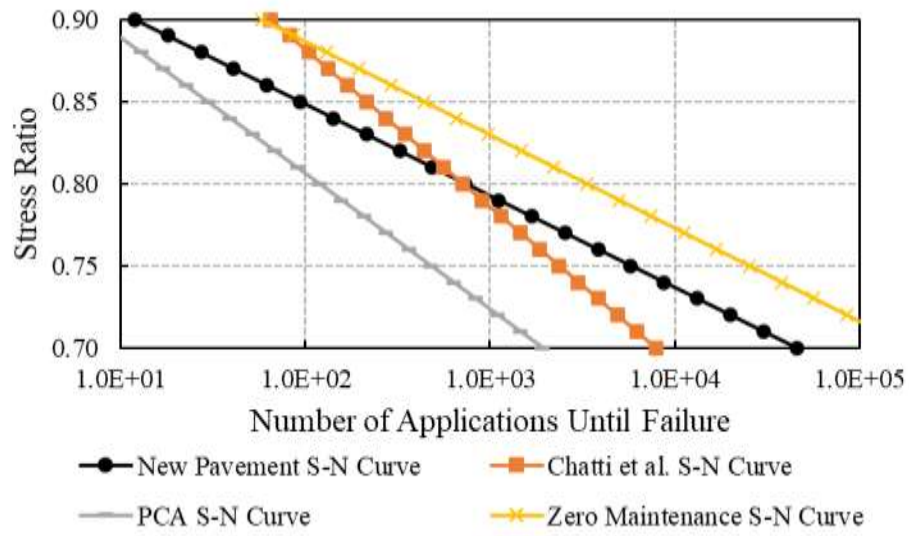
Figure 61: S-N curve comparisons for (a) new pavement strength and (b) old pavement strength.

Axle Type

The fatigue life of concrete beams subjected to single and tandem axle stress profiles at a stress ratio of 0.9 (Figure 56a-b) were compared to examine the effects of axle type. The results from these constant amplitude tests are given in Table 21. Upon initial observation, the results are on the same order of magnitude for each axle type. As shown in Table 22, a t-test was conducted to determine if there was a statistical difference between the two means. The effect of the minimum stress between peaks for tandem axles was shown to be insignificant with a 95% level of confidence for a stress ratio of 0.9, as indicated in the statistical tests.

Table 21: Number of cycles to failure for single and tandem axles at a stress ratio of 0.9.

Flexural Strength	Single Axle at SR = 0.9	Tandem Axle at SR = 0.9
New Pavement	$N_f = 15$ $N_f = 73$ $N_f = 131$ $N_f = 308$	$N_f = 12$ (23 peaks) $N_f = 110$ (220 peaks) $N_f = 137$ (273 peaks)
Old Pavement	$N_f = 3$ $N_f = 30$ $N_f = 32$ $N_f = 202$	$N_f = 7$ (13 peaks) $N_f = 11$ (22 peaks) $N_f = 51$ (101 peaks)

Table 22: Statistical significance of the difference between the mean of fatigue life for single axle and tandem axles at a stress ratio of 0.9.

Flexural Strength	New Pavement	Old Pavement
Average Single Axle Cycles to Failure	132	67
Average Tandem Axle Cycles to Failure	172	45
Standard Deviation of Single Axle Cycles to Failure	127	91
Standard Deviation of Single Axle Cycles to Failure	132	48
Null Hypothesis	$\mu_1-\mu_2=0$	$\mu_1-\mu_2=0$
t-statistic	0.41	-0.38
Degrees of Freedom	5	5
Significance	0.05	0.05
p-value	0.70	0.72

12.3.3 Deflection

The center deflection data measured with the LVDTs was utilized to evaluate the nonlinear progression of damage in the concrete. For each constant amplitude test, the maximum average center deflection and deflection difference were plotted as a function of the number of cycles. Deflection difference is defined as follows:

$$Deflection\ Difference\ (DD) = \delta_{i,max} - \delta_{i,min} \tag{49}$$

where,

DD = the deflection difference, mils

$\delta_{i,max}$ = the maximum average center deflection for cycle i, mils

$\delta_{i,min}$ = the minimum average center deflection for cycle i, mils

The maximum average center deflection and deflection difference vs. number of cycles plot for each constant amplitude fatigue test is included in the Task 4 Appendix B. Figure 62 shows example plots for fatigue tests of beams with new pavement strength. Figure 63 shows example plots for fatigue tests of beams with old pavement strength. As shown in these figures, the maximum average center deflection was observed to increase in three phases. In the first 10 to 15% of the fatigue life of the concrete, the maximum average center deflection increases at a decreasing rate. Then, up until about 70% to 80% of the fatigue life of the concrete, the maximum

average center deflection increases linearly. Lastly, in the final portion of each fatigue life, the maximum average center deflection accumulates at a significantly increasing rate.

(a)

(b)

(c)

(d)
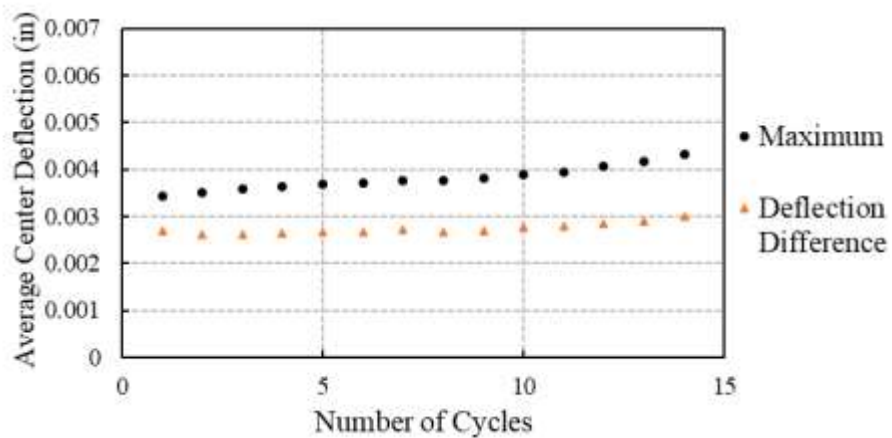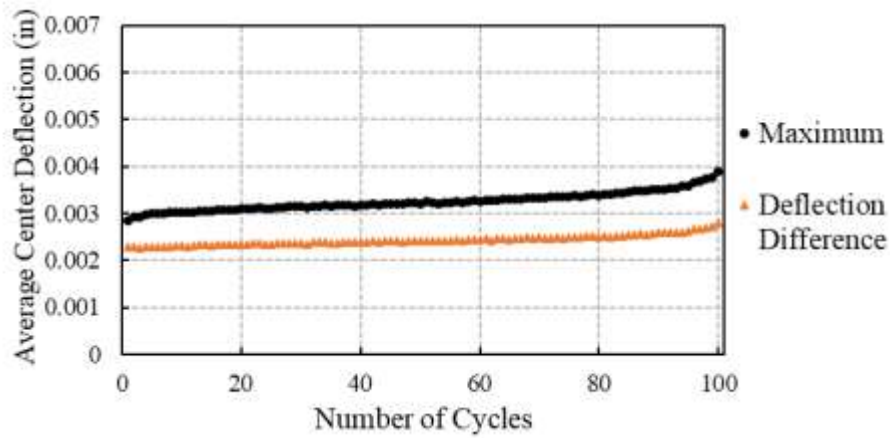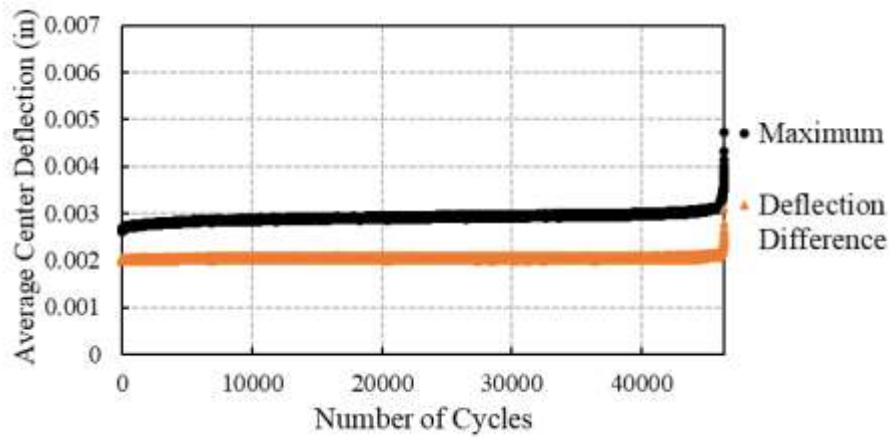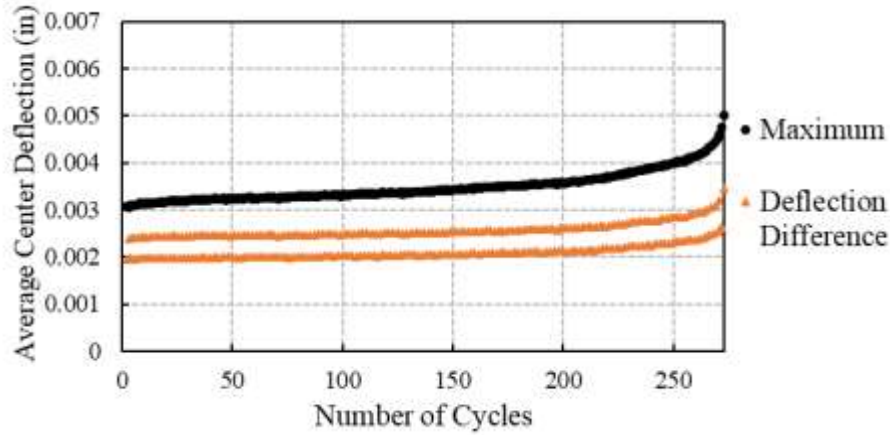
Note: Each tandem axle peak stress was considered a cycle.

Figure 62: Maximum average center deflection and deflection difference vs. number of cycles for (a) CAF_C4_B3 (single axle at SR = 0.7) (b) CAF_C2_B4 (single axle at SR = 0.8) (c) CAF_C3_B3 (single axle at SR = 0.9) and (d) CAF_C2_B2 (tandem axle at SR = 0.9).
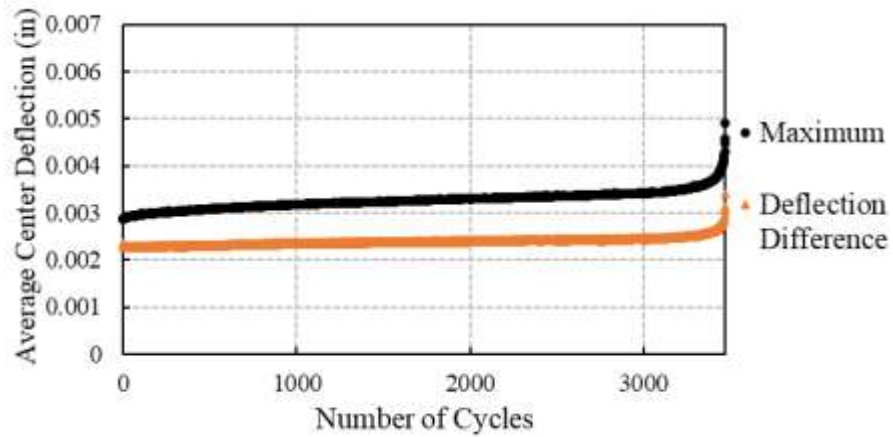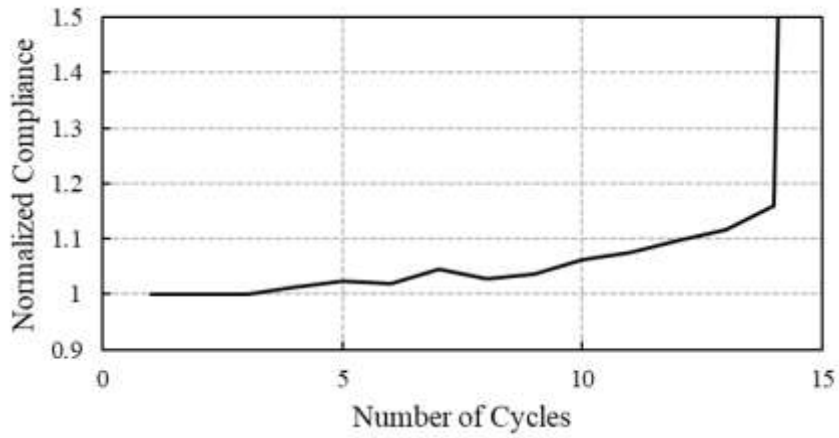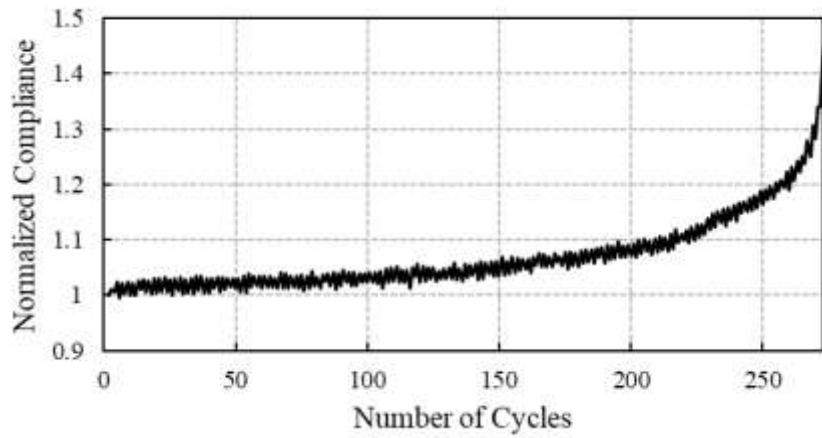

(a)
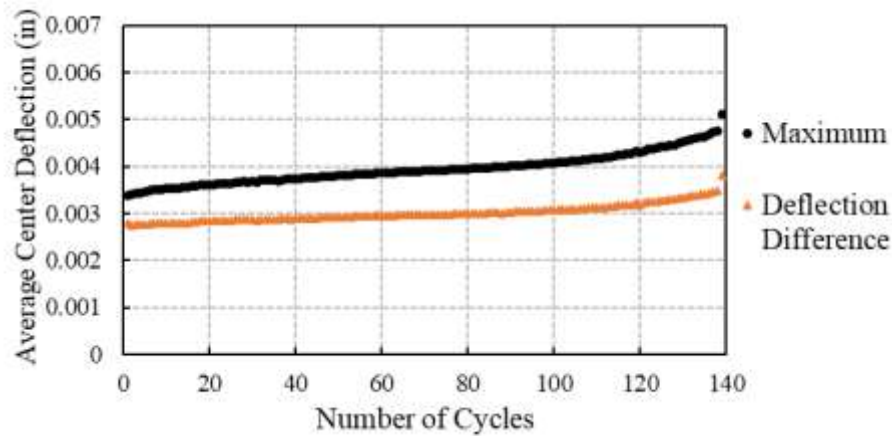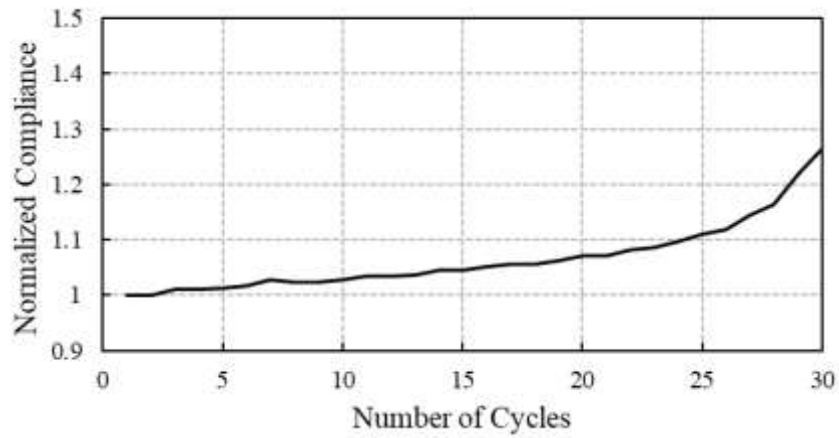

(b)
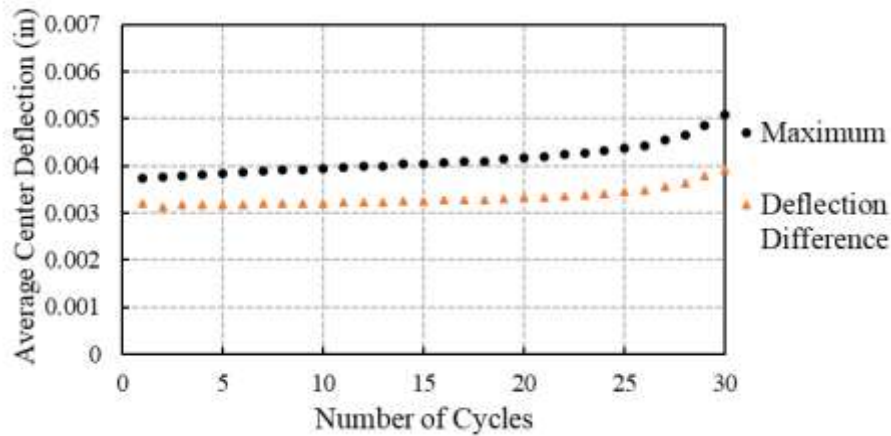
(c)
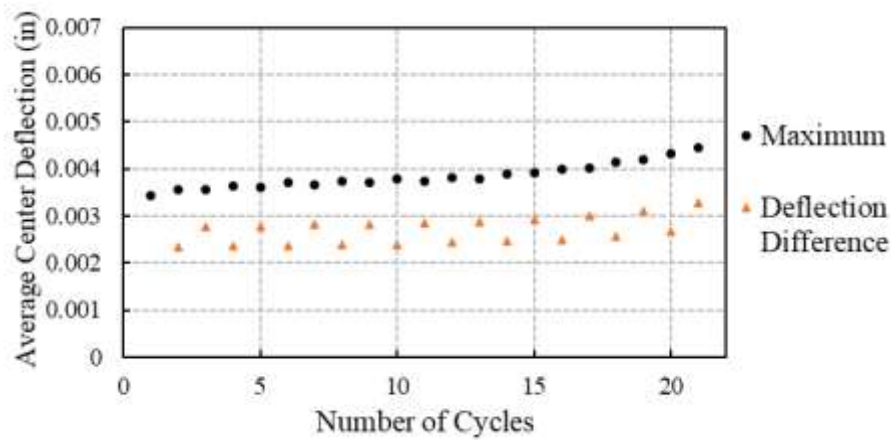
(d)

Figure 63: Maximum average center deflection and deflection difference vs. number of cycles for (a) CAF_C2_B6 (single axle at SR = 0.7) (b) CAF_C2_B7 (single axle at SR = 0.8) (c) CAF_C1_B3 (single axle at SR = 0.9) and (d) CAF_C2_B9 (tandem axle at SR = 0.9).

Deflection difference represents the loss of stiffness in the concrete. Deflection difference also increases nonlinearly, but does not clearly show a decreasing rate early in the fatigue life. The majority of the increase in deflection difference (i.e., stiffness loss) is observed to occur after 70% of the fatigue life has been consumed. This indicates that superload stresses are more damaging to the concrete when applied in the later portions of the fatigue life and less damaging when applied earlier in the fatigue life.

The maximum average center deflection and deflection difference increased with stress ratio. The deflection difference was also influenced by the stress range. Since the minimum stress was held constant at 100 psi, beams with new pavement strength had smaller deflection differences than beams with old pavement strength due to a smaller stress range.

138

12.3.4 Normalized Compliance

The compliance of each concrete beam was examined to further explore the nonlinear response of the concrete as fatigue damage increases. Using Equation 45, the deflection difference for a given fatigue cycle was divided by the difference in the maximum and minimum load recorded by the testing system for the fatigue cycle. The compliance for each fatigue cycle was normalized to the initial compliance to account for inherent differences (e.g., specimen size) between specimens.

The normalized compliance vs. number of cycles plot for each constant amplitude fatigue test is included in the Task 4 Appendix B. Figure 64 shows example plots for fatigue tests of beams with new pavement strength. Figure 65 shows example plots for fatigue tests of beams with old pavement strength.

(a)

(b)

(c)

(d)
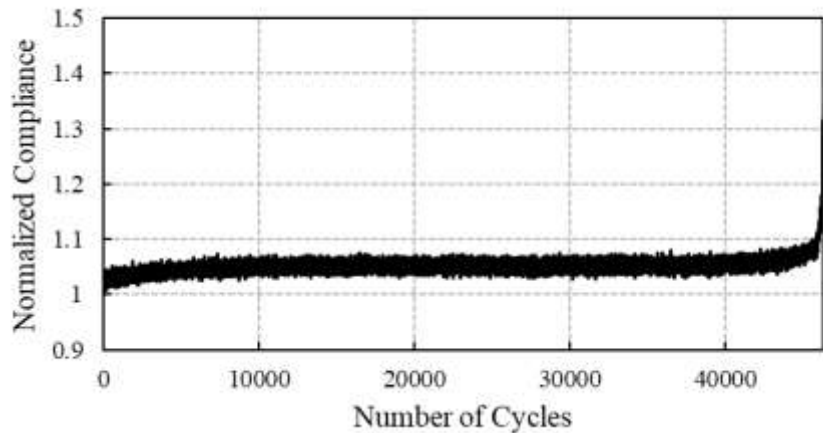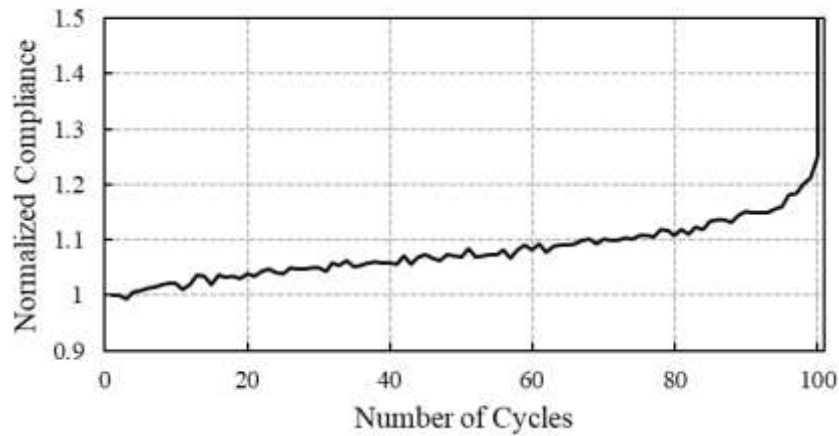
Note: Each tandem axle peak stress was considered a cycle.

Figure 64: Normalized compliance vs. number of cycles for (a) CAF_C4_B3 (single axle at SR = 0.7) (b) CAF_C2_B4 (single axle at SR = 0.8) (c) CAF_C3_B3 (single axle at SR = 0.9) and (d) CAF_C2_B2 (tandem axle at SR = 0.9).

(a)

(b)

(c)

(d)
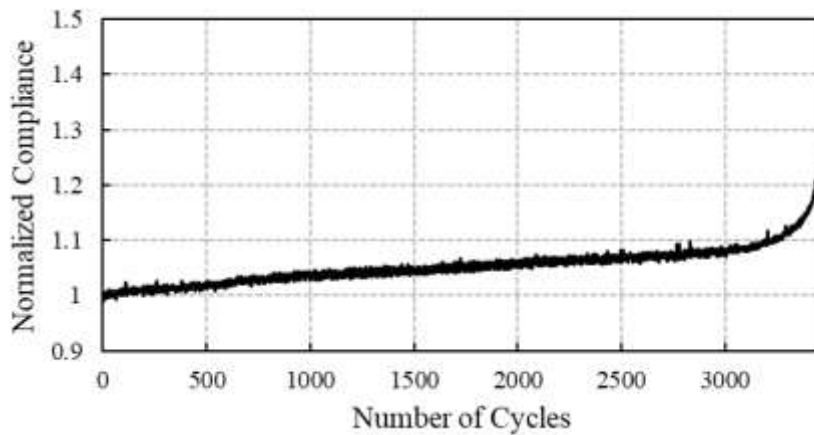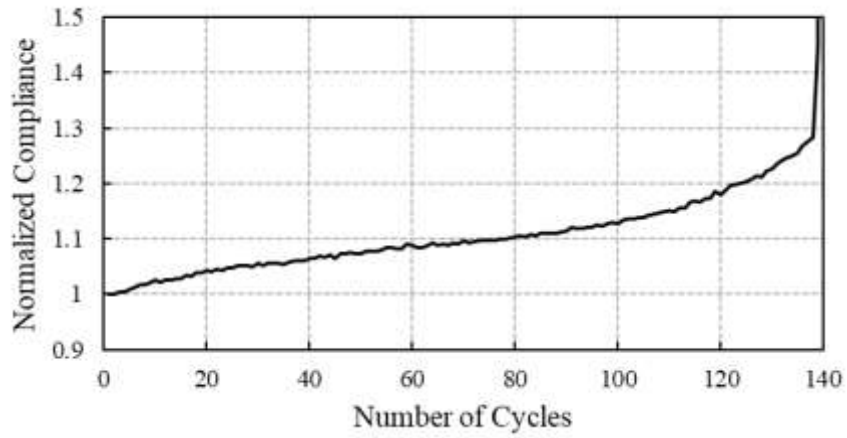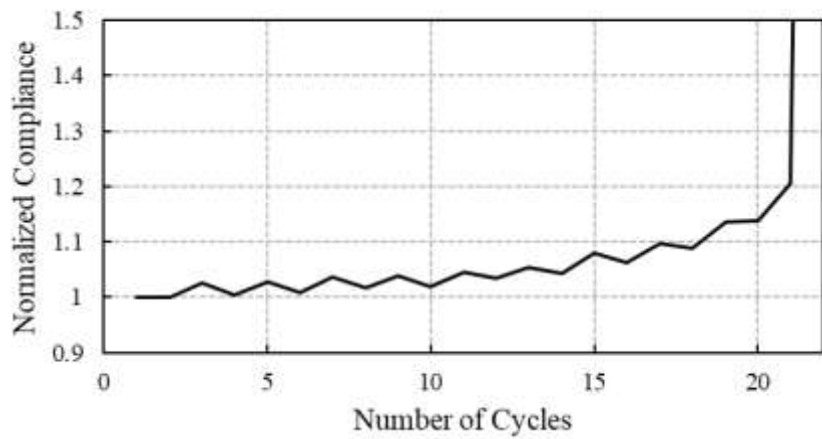
Note: Each tandem axle peak stress was considered a cycle.

Figure 65: Normalized compliance vs. number of cycles for (a) CAF_C2_B6 (single axle at SR = 0.7) (b) CAF_C2_B7 (single axle at SR = 0.8) (c) CAF_C1_B3 (single axle at SR = 0.9) and (d) CAF_C2_B9 (tandem axle at SR = 0.9).

As shown in these figures, the normalized compliance was observed to increase in three phases. In the first 10 to 15% of the fatigue life of the concrete, the normalized compliance increases at a decreasing rate. Then, up until about 70% to 80% of the fatigue life of the concrete, the normalized compliance increases linearly. Lastly, in the final portion of each fatigue life, the normalized compliance increases at a significantly increasing rate. The majority of normalized compliance increase (i.e., stiffness loss) is observed to occur after 70% of the fatigue life is consumed. This indicates that superload stresses are more damaging to the concrete when applied in the later portions of the fatigue life and less damaging when applied earlier in the fatigue life.

The normalized compliance increased similarly for each stress ratio and flexural strength since the load applied to the concrete is incorporated into the normalized compliance calculation. This observation was critical to the development of the normalized compliance-percent life consumed relationship that is described in Section 13.4.1.

12.3.5 Bending Strain

The bending strain measured with the strain gages was also utilized to evaluate the nonlinear progression of damage in the concrete. For each beam instrumented with strain gages, the maximum bending strain and strain difference were plotted as a function of the number of cycles. Strain difference is defined as follows (Equation 50):

$$Strain\ Difference\ (SD) = \varepsilon_{i,max} - \varepsilon_{i,min} \tag{50}$$

where,

SD = the strain difference

$\varepsilon_{i,max}$ = the maximum bending strain for cycle i

$\varepsilon_{i,min}$ = the minimum bending strain for cycle i.

The maximum bending strain and strain difference vs. number of cycles plot for each instrumented beam is included in the Task 4 Appendix B. Since the location of the failure cracks varied along the loaded region of the concrete beam, only some of the strain measurements captured the complete nonlinear progression of damage in the concrete. This was anticipated given that the loading span was seven inches with a four-inch-long gage placed at the center of the beam.
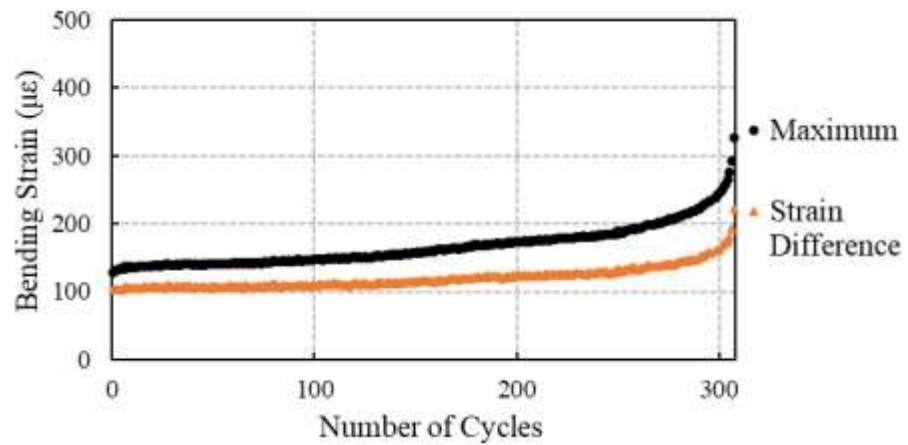
Figure 66b-d shows example plots for tests that captured nonlinear behavior of bending strain in the concrete.
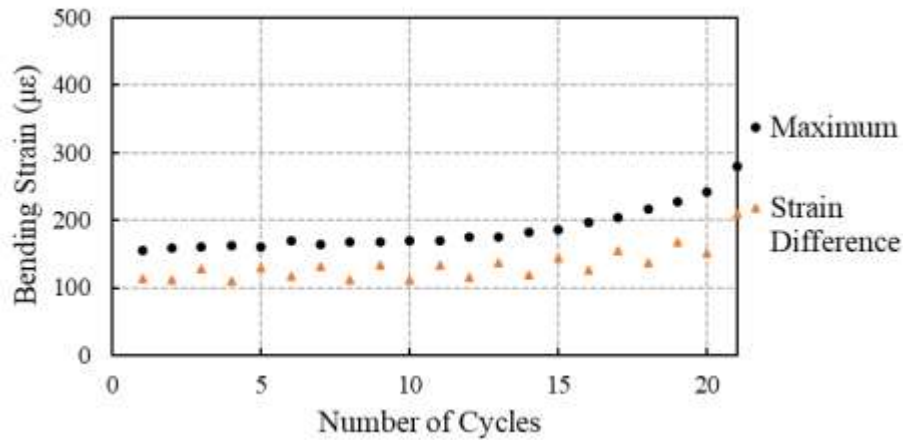

(a)

(b)

(c)

(d)
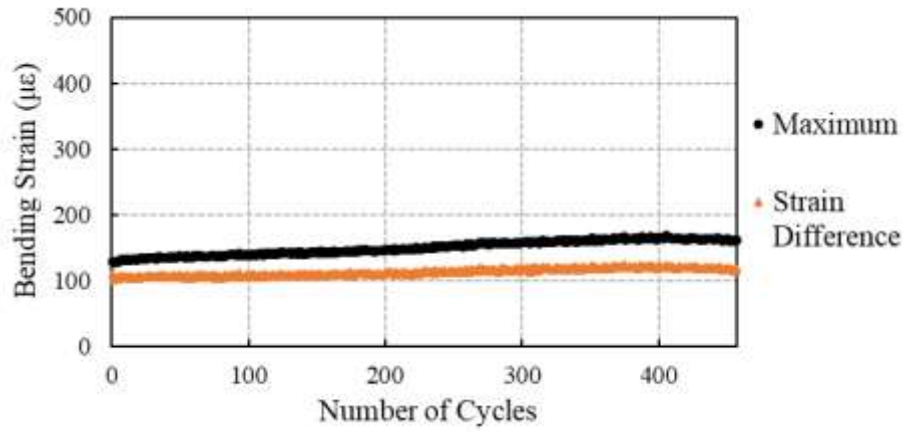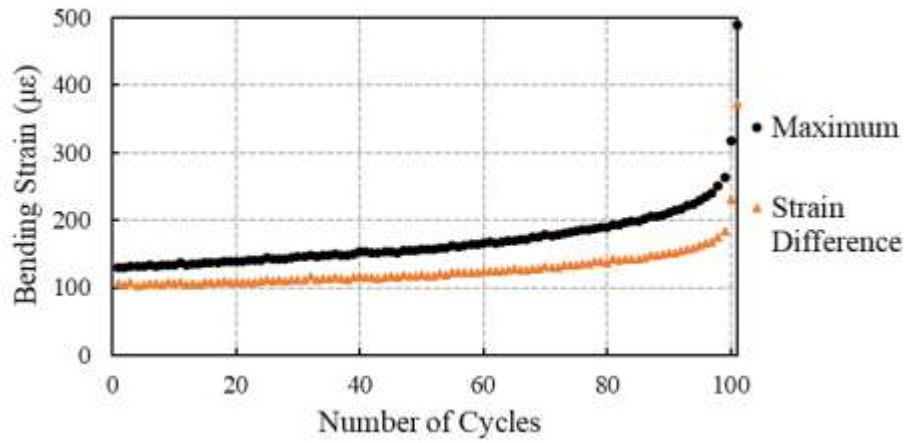
Note: Each tandem axle peak stress was considered a cycle.

Figure 66: Maximum bending strain and strain difference vs. number of cycles for (a) CAF_C1_B2 (single axle at SR = 0.7) (b) CAF_C2_B4 (single axle at SR = 0.8) (c) CAF_C4_B1 (single axle at SR = 0.9) and (d) CAF_C2_B9 (tandem axle at SR = 0.9).

As shown in Figure 66, the maximum bending strain was observed to increase in three phases. In the first 10 to 15% of the fatigue life of the concrete, the maximum bending strain increases at a decreasing rate. Then, up until about 70% to 80% of the fatigue life of the concrete, the maximum bending strain increases linearly. Lastly, in the final portion of the fatigue life, the maximum bending strain increases at a significantly increasing rate. Strain difference also increases nonlinearly but does not clearly show a decreasing rate early in the fatigue life. Figure 66a shows nonlinear bending strain behavior, but since the failure crack occurred near the left loading point, a sharp increase is not observed late in the fatigue life of the concrete. Both the maximum average bending strain and strain difference increased with stress ratio.

12.3.6 Summary and Conclusions

The results of the constant amplitude test program provide a basis to predict the fatigue damage induced by a superload with the traditional S-N curve and linear damage hypothesis approach. For concrete beams with new pavement strength, the number of single axle cycles to failure is predicted by the S-N curve to be about $10^{4.5}$, 10^3, and 10^1 for stress ratios of 0.7, 0.8, and 0.9, respectively. For concrete beams with old pavement strength, the number of single axle cycles to failure is predicted by the S-N curve to be about $10^{3.5}$, $10^{2.5}$, and $10^{1.5}$ for stress ratios of 0.7, 0.8, and 0.9,

144

respectively. The difference in the fatigue damage caused by a single axle and tandem axle stress profile at a stress ratio of 0.9 was not observed to be statistically significant.

The old pavement S-N curve was observed to be steeper, and this is hypothesized to be a consequence of a larger stress range. The two-tailed t-test indicated that a stress ratio of 0.7 caused different degrees of damage to concrete with new pavement and old pavement strength. The difference in the slopes between the two S-N curves were not found to be statistically significant. However, if one S-N curve was developed using the data for all the tests, the coefficient of determination decreased. The coefficient of determination did not decrease greatly when all the test data was used in the development of a SR-N curve. Thus, it was concluded that stress range likely affects the damage imposed by a stress ratio of 0.7.

The nonlinear progression of fatigue damage that developed in the concrete was examined through the collection of structural response data. The maximum average center deflection, deflection difference, normalized compliance, maximum bending strain, and strain difference all increased nonlinearly during cyclic loading. As indicated by the deflection and normalized compliance data, most of the stiffness loss occurred at an increasing rate after 70% of the fatigue life is consumed. This observation was further corroborated with the bending strains. These results suggest that as the fatigue damage in concrete increases, superload stresses become increasingly more impactful. Therefore, the traditional S-N curve and linear damage hypothesis approach for fatigue damage prediction in concrete pavements has limitations when used to assess the effects of the damage imposed by superloads.

The damaged concrete test program, described in Section 13.4, was developed based these observations and findings. The goal of this test program was to further explore and quantify how the damage state in the concrete at the time the stress resulting from the superload is applied affects the resulting fatigue damage.

12.4 Damaged Concrete Testing

The fatigue performance of damaged concrete subjected to stress levels similar in magnitude to the stress that develops in a pavement due to superloads was evaluated. One stress ratio was used to damage the concrete and two stress ratios were used to simulate a superload movement (Section 12.2.1). Two different strengths were investigated (Section 12.2.2). A total of 36 damaged concrete

fatigue tests were conducted using specimens from Casts 3-9, as shown in Table 23. The stress profiles used in the damaged concrete testing are provided in Figure 67-Figure 68.

Table 23: Number of constant amplitude tests for each cast.

Cast	New Pavement Strength	Old Pavement Strength
1	0	0
2	0	0
3	0	3
4	0	6
5	7	3
6	3	6
7	3	0
8	5	0
9	1	0
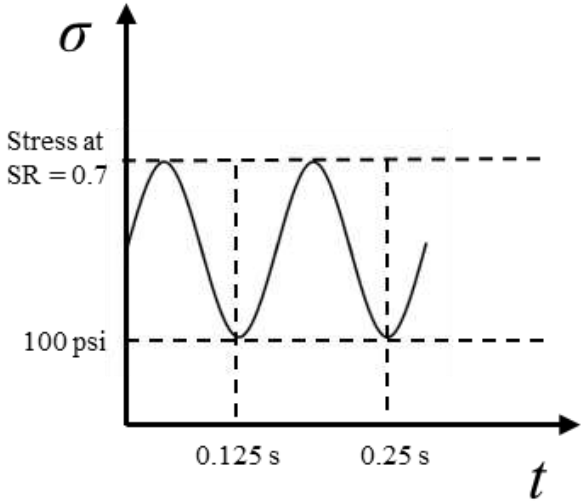
Figure 67: Stress profile used to damage the concrete before and after the overload.
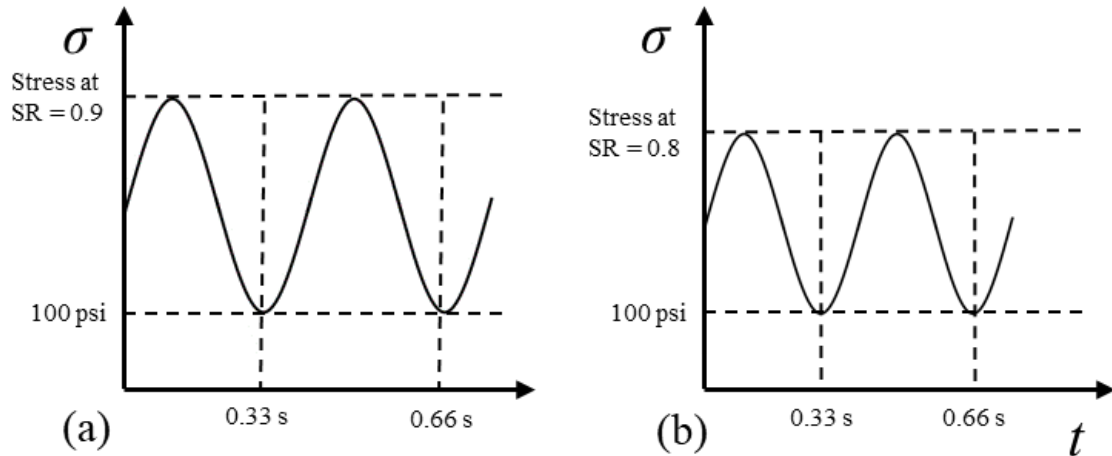
Figure 68: Stress profiles for (a) overload at a stress ratio of 0.9 (b) overload at a stress ratio of 0.8.

Damaged concrete testing was conducted on new pavement strength concrete beams at between 3 to 6 days after casting. The old pavement strength concrete beams were tested at between 14 to 28 days after casting. Three tests were performed in each test cell in the experimental design matrix. A complete summary of all concrete beams tested in the damaged concrete test program is in the Task 4 Appendix C (Table C1). The structural response data collected for each fatigue test is also included in the Task 4 Appendix C (Figures C1-C36).

12.4.1 Normalized Compliance-Percent Life Consumed Relationship

As mentioned in Section 12.2.3, concrete beams were fatigued to target damage states corresponding to 15%, 50%, and 85% life consumed using normalized compliance. Normalized compliance was chosen as the damage parameter for the damaged concrete test program since it depicts the nonlinearity of damage accumulation occurring in the concrete and follows similar behavior in each test.

The constant amplitude testing results were used to define the relationship between normalized compliance and percent life consumed. For each constant amplitude test involving a single axle stress profile, the normalized compliance was evaluated at 15%, 50%, and 85% life consumed, as shown in Figure 69. The mean and standard deviation at each percent life consumed for 19 specimens are listed in Table 24. There was a noticeable upward shift in the normalized compliance curves for specimens CAF_C2_B10 and CAF_C4_B2, so these were excluded from

147

the definition of the relationship. Upon further inspection, these curves were shifted upward because the initial compliance calculated was not indicative of the actual initial compliance of the beam.
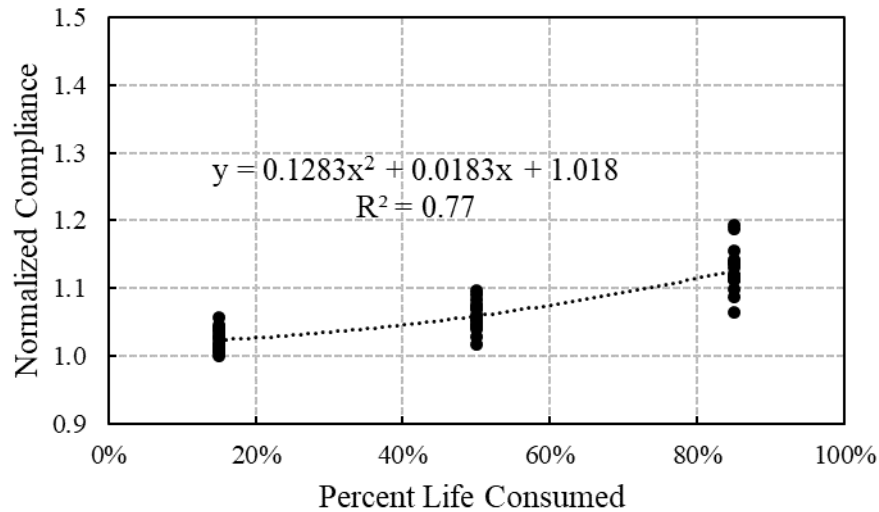

Figure 69: Normalized compliance evaluated at 15%, 50%, and 85% life consumed of 19 constant amplitude tests.

$$y = 0.1283x^2 + 0.0183x + 1.018$$
$$R^2 = 0.77$$

Table 24: Mean and standard deviation of normalized compliance evaluated at 15%, 50%, and 85% life consumed of 19 constant amplitude tests.

Percent Life Consumed	Mean Normalized Compliance	Standard Deviation
15%	1.024	0.015
50%	1.060	0.021
85%	1.123	0.055

As presented in Figure 69, a second order polynomial trendline fits the data well. The mean normalized compliances at 15%, 50%, and 85% life consumed were determined to be 1.024, 1.060, and 1.123, respectively. Moreover, it was observed that the normalized compliance for each test consistently increases by about 0.06 from 15% to 50% life consumed and 0.10 from 15% to 85% life consumed. Based on the results presented in Figure 69 and Table 24, target normalized compliances and the allowable ranges were determined for the damaged concrete testing. These are presented in Table 25. In addition to using these target values, the entire normalized compliance curve was monitored. This ensured that the rate of normalized

compliance increase at each target normalized compliance was representative of the anticipated rate for the respective percent life consumed.

Table 25: Target normalized compliances and allowable ranges for damaged concrete testing.

Percent Life Consumed	Target Normalized Compliance	Allowable Range
15%	1.030	1.02-1.04
50%	1.060	1.05-1.07
85%	1.130	1.11-1.15

12.4.2 Fracture

The fracture behavior of concrete beams tested in the damaged concrete fatigue testing was similar to the fracture behavior observed during flexural strength and constant amplitude testing. Concrete beams tested after 3 to 7 days failed either mostly around the aggregate or through and around the aggregate. Concrete beams tested between 14 and 28 days failed either through and around the aggregate or mostly through the aggregate.

During the fatigue testing, no visual signs of cracking was observed until the crack developed at failure. The failure developed in the region between the two loading lines for each test performed. Figure 70 depicts examples of typical failures. Upon visual inspection, 20 of the 36 concrete beams tested in damaged concrete fatigue failed within 2 inches of the center of the beam. The remaining 16 concrete beams failed within the tension zone but beyond 2 inches from the center of the beam. The location of the failure was particularly important when interpreting the bending strain measurements, as described in Section 13.4.6.

(a)

(b)

(c)

(d)
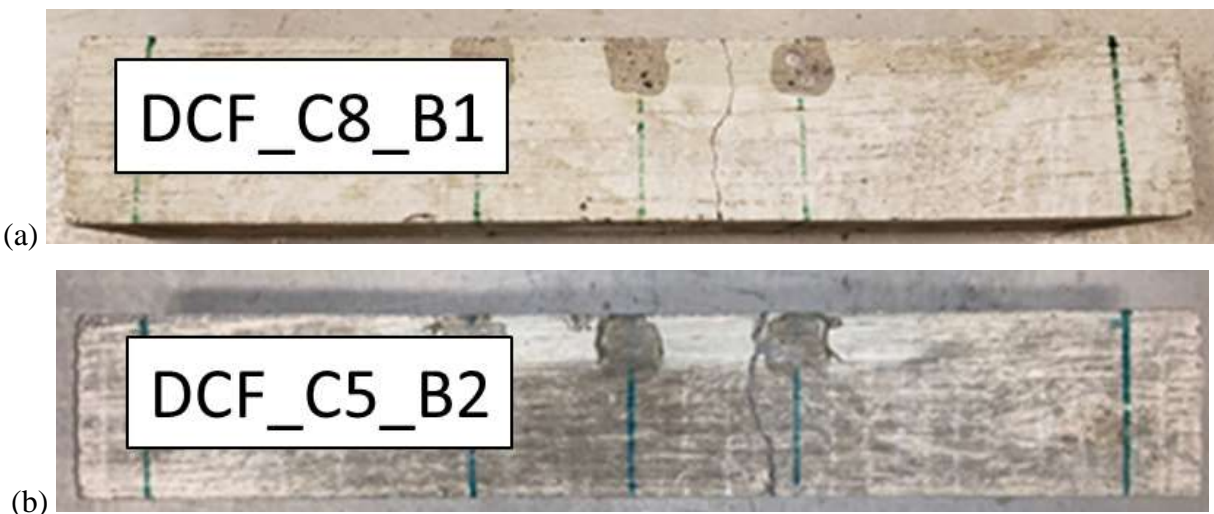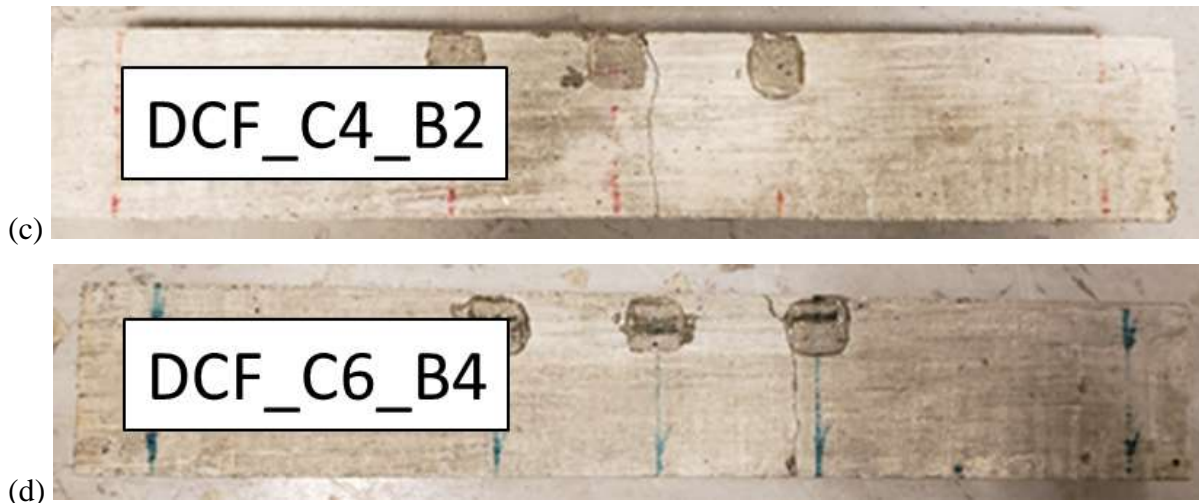
Figure 70: Failure cracks for (a) DCF _C8_B1 (age = 3-day) (b) DCF_C5_B2 (age = 4-day) (c) DCF_C4_B2 (age = 19-day) (d) DCF_C6_B4 (age = 17-day).

12.4.3 Fatigue Life

Table 26 provides the fatigue life for each of the damaged concrete specimens tested, and Figure 71 graphically shows the number of fatigue cycles to the target damage states representing 15%, 50%, and 85% life consumed. Several observations were found in the fatigue cycle data:

- While there is some overlap, beams with new pavement strength tended to require more fatigue cycles to reach the target damage states than beams with old pavement strength. This is potentially a result of the stress range effect

- As the target damage state increases, the number of cycles to failure after the overload decreases

- As the stress ratio of the overload increases, the number of cycles to failure after the overload is generally of the same order of magnitude

- Overloads applied at a target damage state of 85% life consumed with a stress ratio of 0.9 caused failure for several specimens during its application

Table 26: Fatigue life results of damaged concrete testing.

Specimen ID	Age at Testing (days)	Strength Condition	Target Damage State to Apply Overload	Applied Overload Stress Ratio	Number of Cycles to Target Damage State	Number of Cycles to Failure After Overload
DCF_C5_B2	4	New	15%	0.8	40,000	2,926

DCF_C5_B6	6	New	15%	0.8	1,000	6,059
DCF_C8_B3	4	New	15%	0.8	60,000	54,962
DCF_C5_B7	6	New	50%	0.8	27,000	4,022
DCF_C6_B2	5	New	50%	0.8	75,000	2,155
DCF_C8_B4	5	New	50%	0.8	16,998	2,138
DCF_C8_B2	4	New	85%	0.8	153,233	17
DCF_C5_B3	4	New	85%	0.8	40,000	407
DCF_C7_B3	4	New	85%	0.8	138,000	8,340
DCF_C5_B1	3	New	15%	0.9	58,000	15,528
DCF_C6_B1	4	New	15%	0.9	62,500	2,426
DCF_C6_B3	5	New	15%	0.9	84,000	11,808
DCF_C5_B5	5	New	50%	0.9	5,500	721
DCF_C7_B1	3	New	50%	0.9	87,000	954
DCF_C9_B1	3	New	50%	0.9	142,579	488,734
DCF_C5_B4	5	New	85%	0.9	61,049	225
DCF_C7_B2	3	New	85%	0.9	9,400	0
DCF_C8_B1	3	New	85%	0.9	227,306	0
DCF_C3_B1	21	Old	15%	0.8	6,500	5,979
DCF_C4_B6	26	Old	15%	0.8	37,000	11,988
DCF_C5_B10	19	Old	15%	0.8	24,000	41,021
DCF_C3_B3	25	Old	50%	0.8	3,000	1,000
DCF_C6_B4	17	Old	50%	0.8	6,000	7,612
DCF_C6_B9	25	Old	50%	0.8	6,200	1,179
DCF_C5_B8	14	Old	85%	0.8	45,563	8
DCF_C6_B5	18	Old	85%	0.8	43,700	7,354
DCF_C6_B7	24	Old	85%	0.8	7,110	191
DCF_C3_B2	25	Old	15%	0.9	500	5,449
DCF_C4_B3	19	Old	15%	0.9	9,000	10,197
DCF_C4_B4	20	Old	15%	0.9	50,000	22,520
DCF_C4_B1	18	Old	50%	0.9	7,500	280
DCF_C4_B2	19	Old	50%	0.9	25,000	1,788
DCF_C6_B6	24	Old	50%	0.9	44,000	9,501
DCF_C4_B5	21	Old	85%	0.9	4,300	0
DCF_C5_B9	18	Old	85%	0.9	32,878	117
DCF_C6_B8	25	Old	85%	0.9	66,490	0
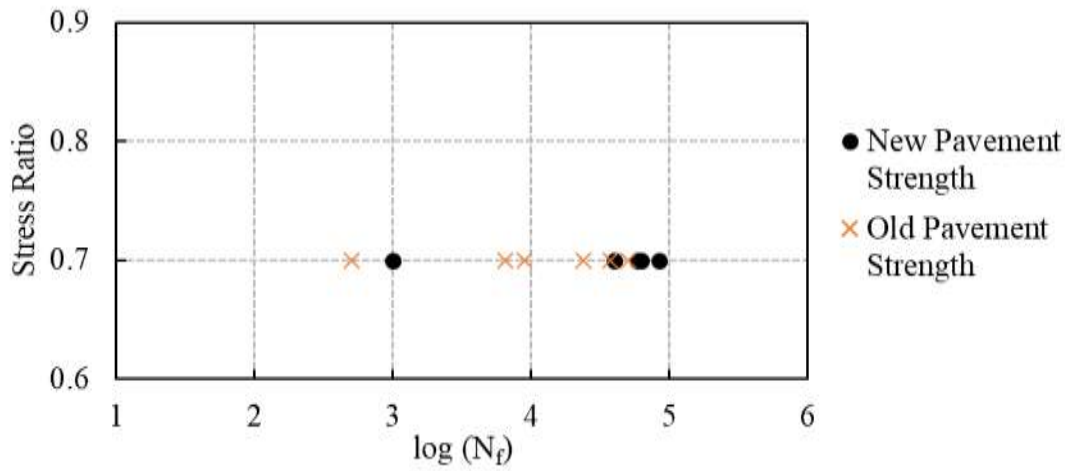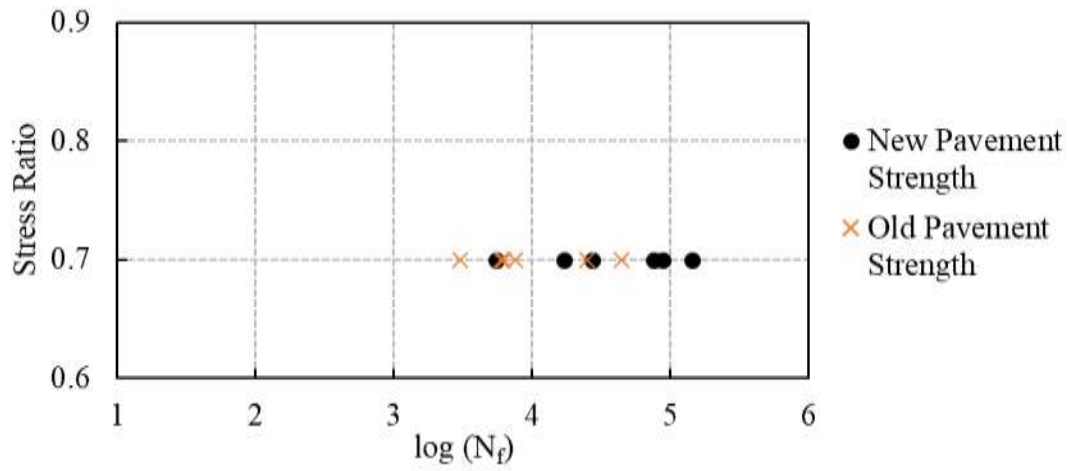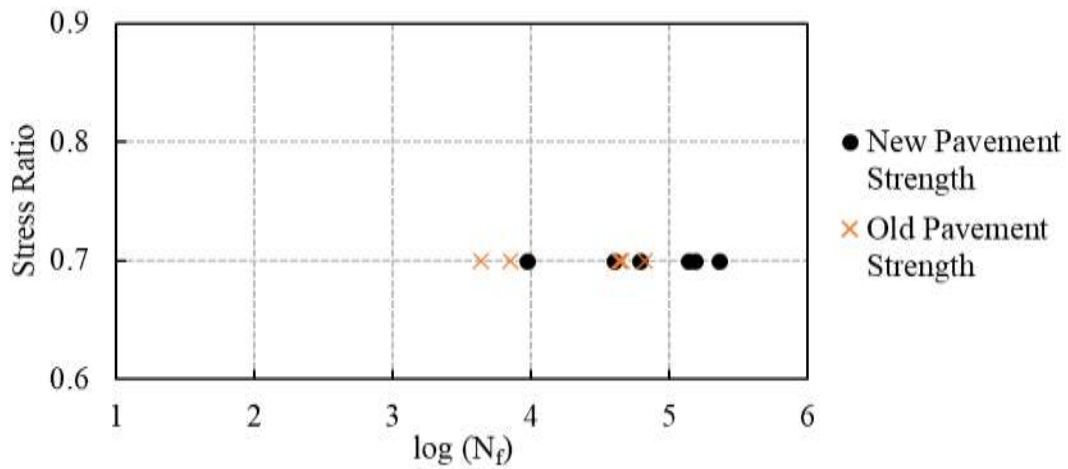
Figure 71: Number of fatigue cycles to target damage states representing (a) 15%, (b) 50%, and (c) 85% life consumed.

A two-tailed t-test was performed to evaluate if stress range is influential on the number of cycles to the target damage states. The results of this analysis are shown in Table 27. The two datasets were shown to be statistically different at a confidence level of 90% for each target damage state, indicating a potential influence of stress range.

Table 27: Two-tailed t-test for number of cycles to target damage state.

Target Damage State	15%	50%	85%
Mean Cycles for New Pavement Strength	50,917	59,013	104,831
Mean Cycles for Old Pavement Strength	21,167	15,283	35,008
Standard Deviation for New Pavement Strength	28,186	52,299	82,061
Standard Deviation for Old Pavement Strength	19,392	16,120	24,338
Null Hypothesis	$\mu_1-\mu_2=0$	$\mu_1-\mu_2=0$	$\mu_1-\mu_2=0$
t-statistic	2.13	1.96	2.00
Degrees of Freedom	10	10	10
Significance	0.10	0.10	0.10
p-value	0.06	0.08	0.07

12.4.4 Deflection

The center deflection data collected with the LVDTs was utilized to evaluate the nonlinear impact of an overload on the progression of damage in the concrete. Since each test was intermittently paused to check the normalized compliance in the concrete, the maximum average center deflection fluctuated slightly. However, the deflection difference of each fatigue cycle did not fluctuate because of these pauses. Therefore, for each damaged concrete test, the deflection difference was plotted as a function of the number of cycles, as shown in Appendix C. Since normalized compliance is just the deflection difference divided by the difference between the maximum and minimum load, normalized compliance and deflection difference follow the same behavior. Thus, the analysis and discussion of the damaged concrete tests is focused on normalized compliance.

12.4.5 Normalized Compliance

As stated in Section 13.4.1, normalized compliance was used to impose damage states representative of 15%, 50%, and 85% life consumed. As such, normalized compliance was considered the best measure of the damage imposed by an overload. The normalized compliance vs. number of cycles plot for each damaged concrete fatigue test is included in the Task 4 Appendix C. Figure 72 and Figure 73 show example plots for beams tested with new pavement strengths. Figure 74 and Figure 75 show example plots for beams tested with old pavement strength. Note that the overload is marked in red for all figures, and the target damage state is referred to as "D" in the figure captions.
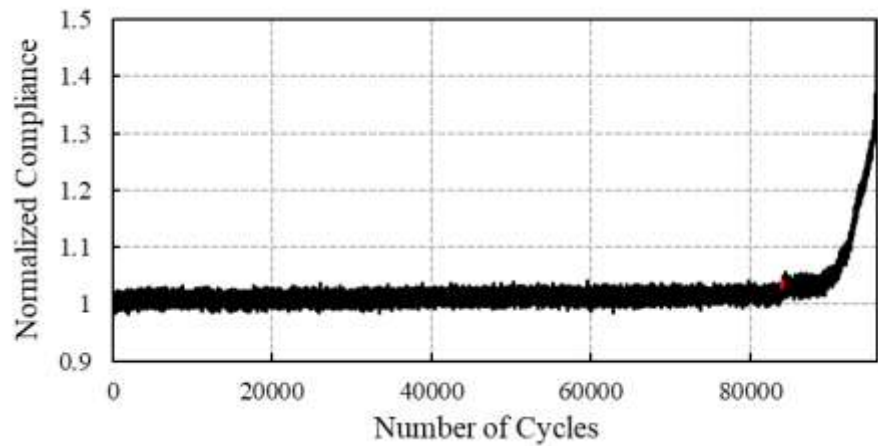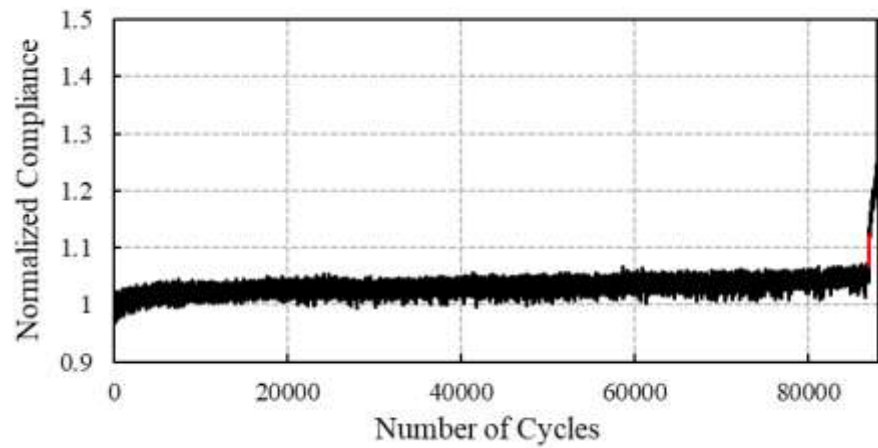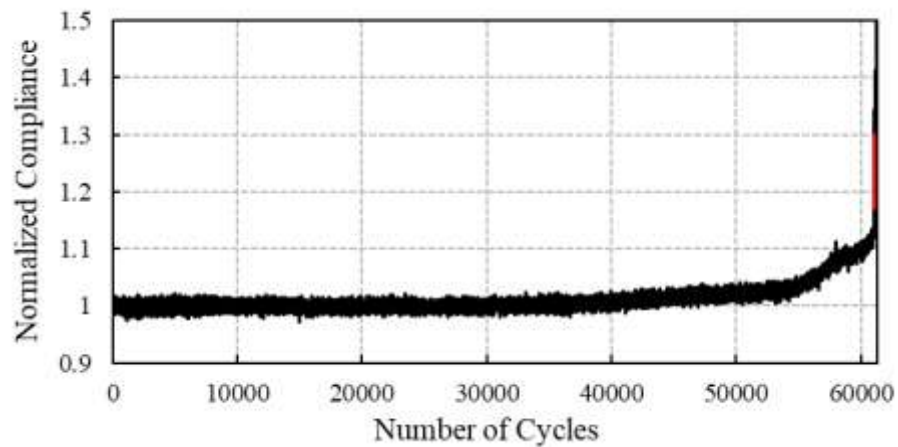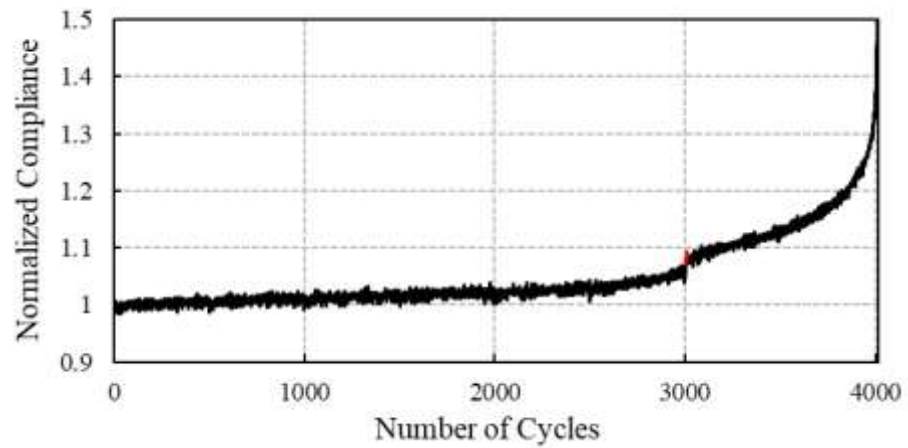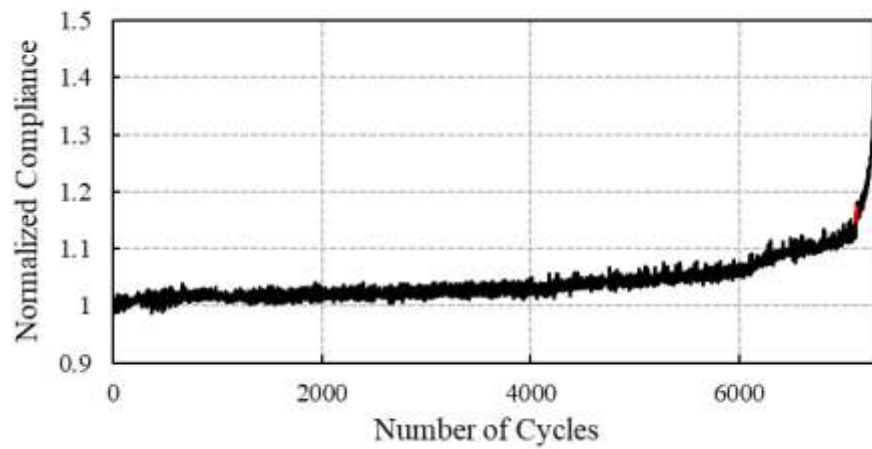
Figure 72: Normalized compliance vs. number of cycles for (a) DCF_C6_B3 (overload of SR = 0.9 at D = 15%) (b) DCF_C7_B1 (overload of SR = 0.9 at D = 50%) (c) DCF_C5_B4 (overload of SR = 0.9 at D = 85%).

155
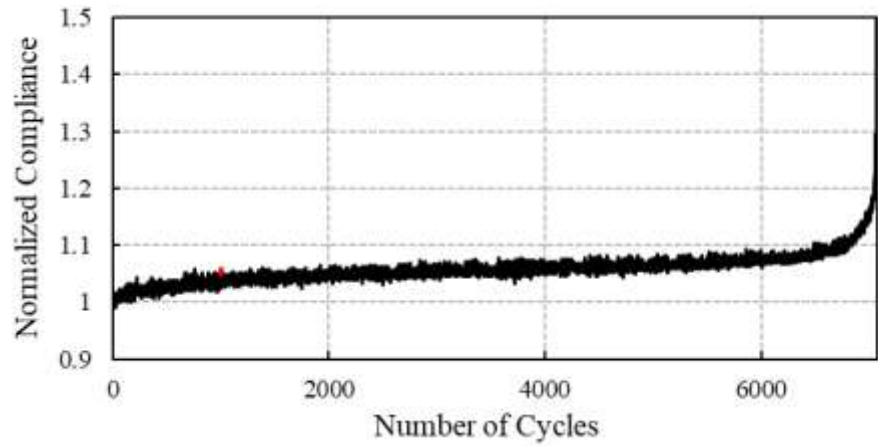
(a)
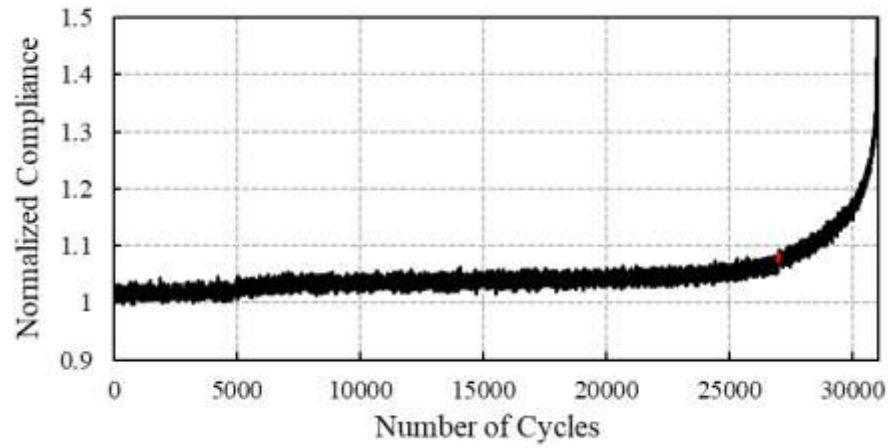
(b)
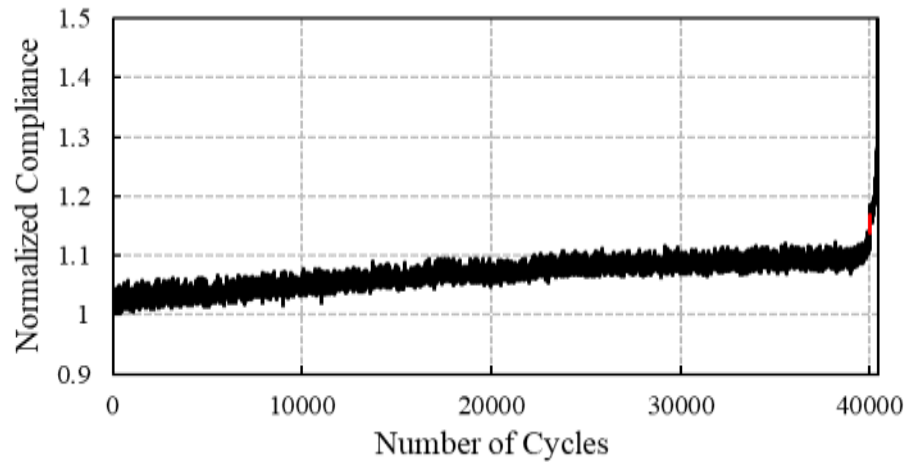
(c)

Figure 73: Normalized compliance vs. number of cycles for (a) DCF_C5_B6 (overload of SR = 0.8 at D = 15%) (b) DCF_C5_B7 (overload of SR = 0.8 at D = 50%) (c) DCF_C5_B3 (overload of SR = 0.8 at D = 85%).
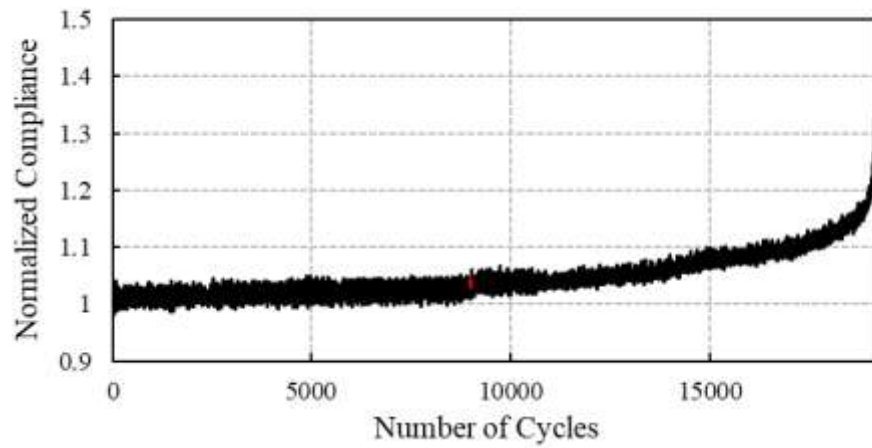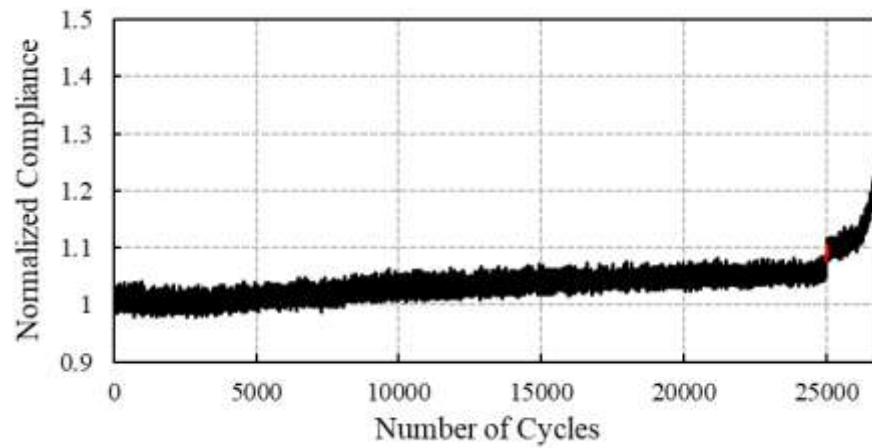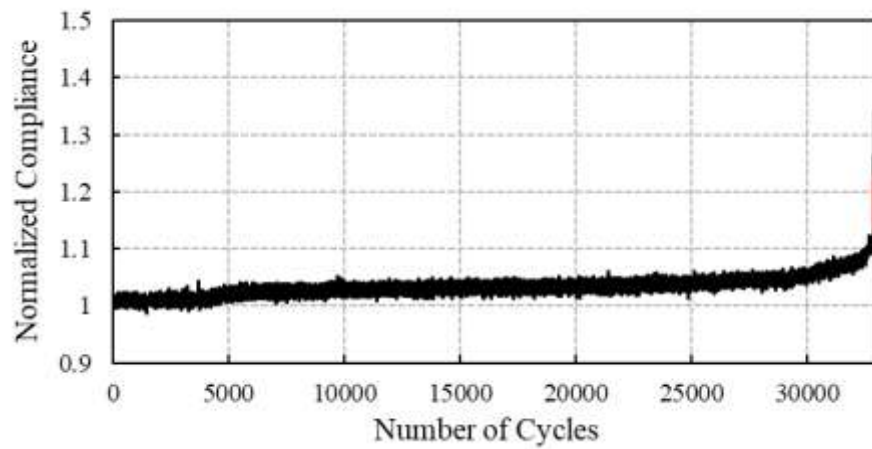
Figure 74: Normalized compliance vs. number of cycles for (a) DCF_C4_B3 (overload of SR = 0.9 at D = 15%) (b) DCF_C4_B2 (overload of SR = 0.9 at D = 50%) (c) DCF_C5_B9 (overload of SR = 0.9 at D = 85%).
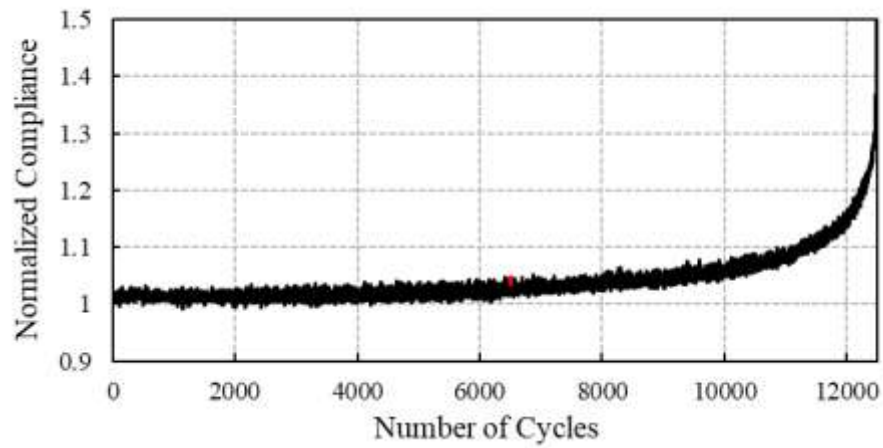
(a)

(b)

(c)

Figure 75: Normalized compliance vs. number of cycles for (a) DCF_C3_B1 (overload of SR = 0.8 at D = 15%) (b) DCF_C3_B3 (overload of SR = 0.8 at D = 50%) (c) DCF_C6_B7 (overload of SR = 0.8 at D = 85%).

158

As evident in Figure 72 through Figure 75, the target normalized compliance is achieved within the allowable range successfully. Moreover, the rate of increase in normalized compliance at each target was within expectations based on the results from the constant amplitude testing. At a target normalized compliance representing 15% life consumed, the normalized compliance increases linearly, signaling the end of the deceleration phase of damage development in the concrete. At a target normalized compliance representing 50% life consumed, the normalized compliance increases linearly with a slightly greater slope than at 15% life consumed. At a target normalized compliance representing 85% life consumed, the normalized compliance accelerates towards failure.

The immediate effects of overloads on the normalized compliance in the concrete were observed qualitatively in Figure 72 through Figure 75 and in the Task 4 Appendix C. In general, concrete with new pavement and old pavement strength showed very similar normalized compliance behavior due to overloads. Ten overload cycles at a stress ratio of 0.9 increased the normalized compliance in the concrete at each target damage state. However, the impact of the overload on the normalized compliance in the concrete became greater as the damage in the concrete increased. At the target damage state representing 15% life consumed, an overload at a stress ratio of 0.9 caused a slight, but noticeable, increase in normalized compliance, implying some loss in stiffness. At the target damage state representing 50% life consumed, the increase in normalized compliance due to the overload was observed to be more significant. Commonly, samples under these conditions were moved to the acceleration phase of the normalized compliance curve because of the overload, indicating a significant loss in stiffness. At the target damage state representing 85% life consumed, overloads critically increased the normalized compliance to at or near failure of the beam.

For overloads at a stress ratio of 0.8, the normalized compliance did not significantly increase when applied at the target damage state representing 15% life consumed. At 50% life consumed, the normalized compliance increased slightly more, but still not significantly. At 85% life consumed, the impact of an overload at a stress ratio of 0.8 varied. For some samples, the normalized compliance increased much more than at 15% and 50% life consumed. These samples were forced to near failure by the overload. For the other samples, the normalized compliance increased similarly to that observed at 15% and 50% life consumed.

To further investigate these qualitative observations, the average normalized compliance before the overload was quantitatively compared to the average normalized compliance after the overload for each specimen. The averages were taken over a two second span to account for variation in compliance inherent to cyclic loading. If the specimen failed during the overload, the average normalized compliance after the overload was assumed to be 1.65, as this was the average of the normalized compliances at failure for all damaged concrete tests. The results of this quantitative analysis are shown in Figure 76-Figure 78 and Table 28. As depicted in Figure 76 and Figure 77, overloads at a stress ratio of 0.9 clearly impact the normalized compliance more as the target damage state in the concrete increases. The same trend is present but not as clear for overloads at a stress ratio of 0.8 since the results at 85% life consumed vary. While there is some disparity in the results at 85% life consumed, a greater potential for a significant increase in normalized compliance and loss of stiffness in the concrete is observed at this target damage state.
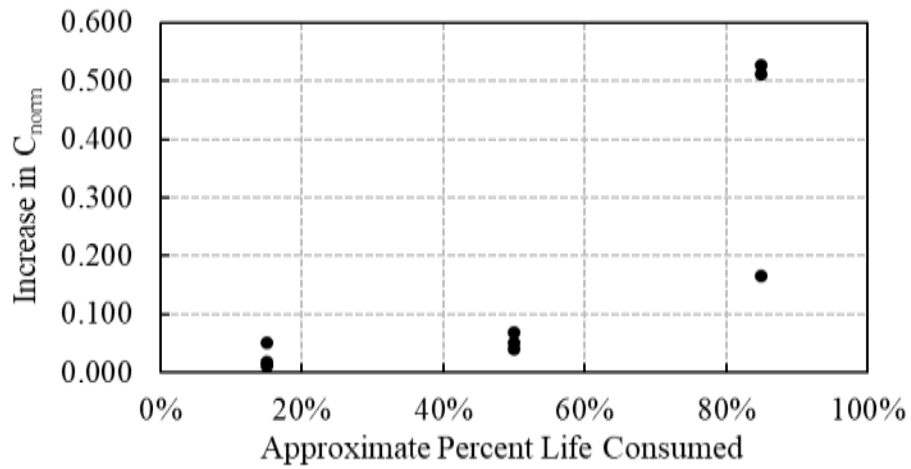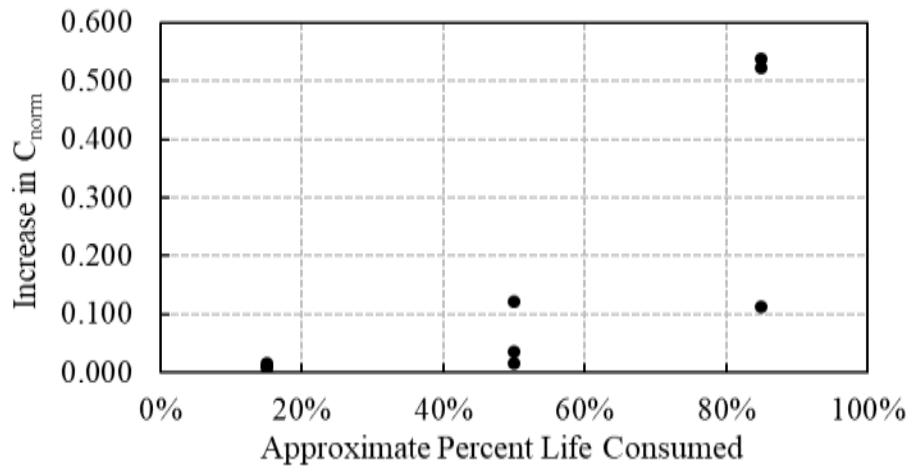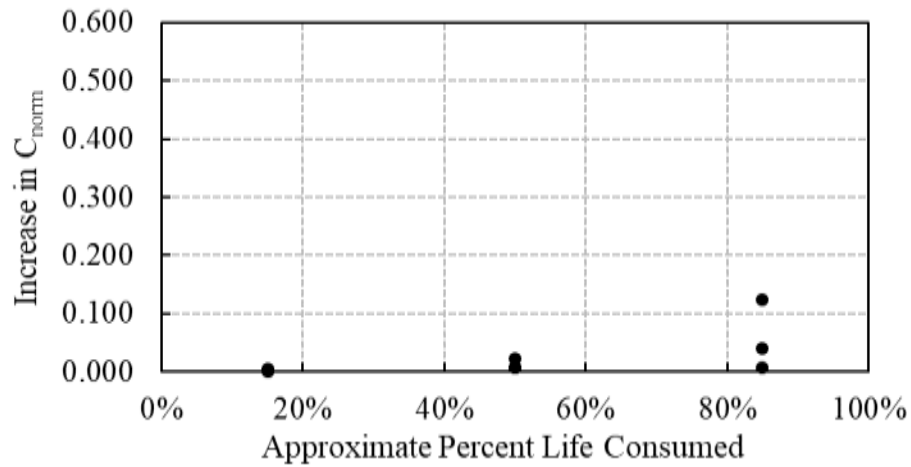
(a)
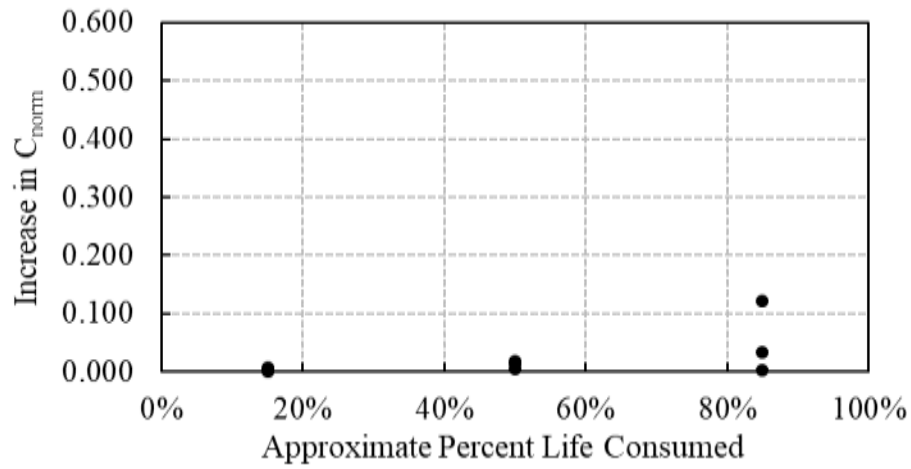
(b)

Figure 76: Increase in normalized compliance due to (a) overload of SR = 0.9 and (b) overload of SR = 0.8 for concrete with new pavement strength.

(a)

(b)

Figure 77: Increase in normalized compliance due to (a) overload of SR = 0.9 and (b) overload of SR = 0.8 for concrete with old pavement strength.
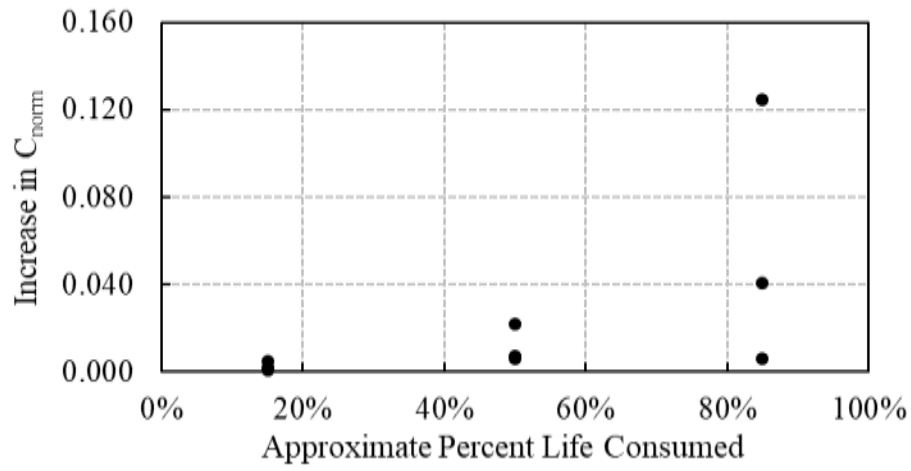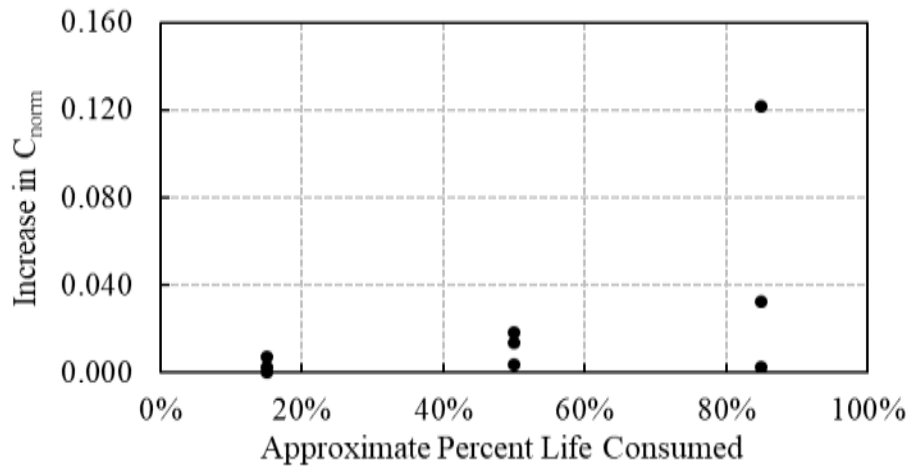
(a)

(b)

Figure 78: Zoomed increase in normalized compliance due to overload of SR = 0.8 for (a) new pavement strength and (b) old pavement strength.

In Table 28, statistics are presented for the increase in normalized compliance due to the overload. For each combination of strength condition and stress ratio, the mean and standard deviation of the increase in normalized compliance are observed to increase as the target damage state in the concrete increases. These results indicate that the impact of an overload stress is both greater and more variable as percent life consumed increases. This agrees with the constant amplitude test results, in which most of the normalized compliance increase (i.e., stiffness loss) is observed to occur after 70% of the fatigue life is consumed.

Table 28: Statistics of the increase in normalized compliance due to the overload.

| Strength	Stress Ratio	Target Damage State	Mean Normalized Compliance Increase	Standard Deviation
New	0.9	15%	0.027	0.021
		50%	0.053	0.014
		85%	0.402	0.204
Old	0.9	15%	0.011	0.004
		50%	0.058	0.057
		85%	0.390	0.241
New	0.8	15%	0.003	0.004
		50%	0.012	0.007
		85%	0.052	0.062
Old	0.8	15%	0.003	0.002
		50%	0.012	0.009
		85%	0.057	0.061

12.4.6 Bending Strain

The bending strain measured with the strain gages was utilized to corroborate the observations found in the normalized compliance data. For each damaged concrete test, the maximum bending strain was plotted as a function of the number of cycles, as shown in the Task 4 Appendix C.

The elastic bending strain resulting from a single axle stress pulse at a stress ratio of 0.7 typically was between 100-110 microstrain for concrete beams with new pavement strength and 110-120 microstrain for concrete beams with old pavement strength. Overloads at stress ratios of 0.8 and 0.9 were observed to increase the elastic bending strain by about 10 microstrain and 20 microstrain, respectively. This agrees well with the bending strain measurements in the constant amplitude testing.

For many of the specimens, the strain gages captured the increase in maximum bending strain occurring before the application of the overload. After the overload, only some samples failed through the strain gages. Figure 79 depicts the bending strain data for several damaged concrete tests involving an overload at a stress ratio of 0.9, and Figure 80 depicts the bending strain data for several damaged concrete tests involving an overload at a stress ratio of 0.8. The plots in Figure 79 are chosen to demonstrate the impact of an overload on the maximum bending strain in the concrete since the strain gages captured all three phases of strain accumulation. The overload in Figure 80a was not observed to significantly increase the maximum bending strain when applied after 15% of the life was consumed. However, as shown in Figure 80b-c, as percent life increased, the overload increasingly accumulated plastic bending strain in the concrete. These few examples corroborate the normalized compliance observations. Figure 80 shows damaged concrete tests that did not capture the fracture occurring at the end of the fatigue life of the beam. This was the case for most of the damaged concrete tests involving an overload at a stress ratio of 0.8.
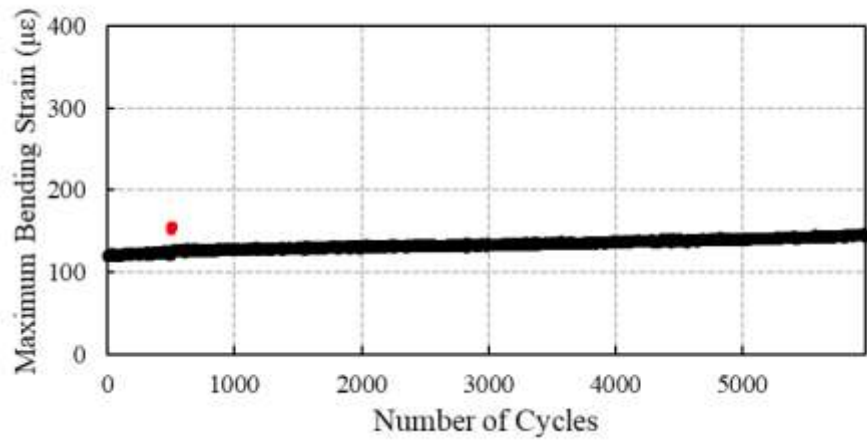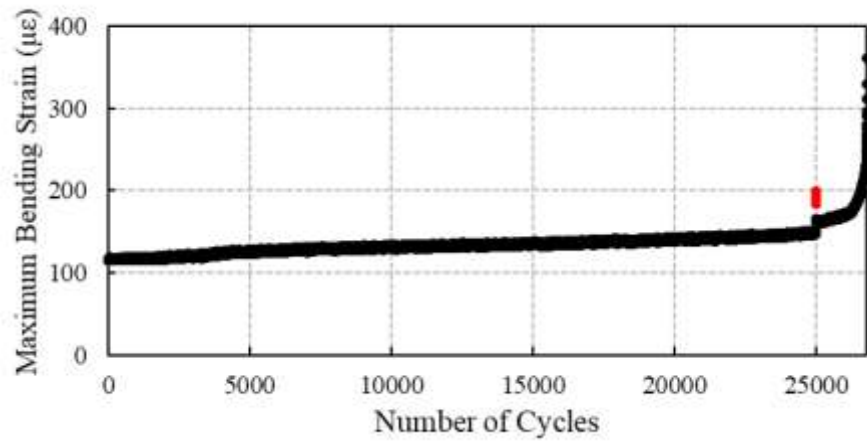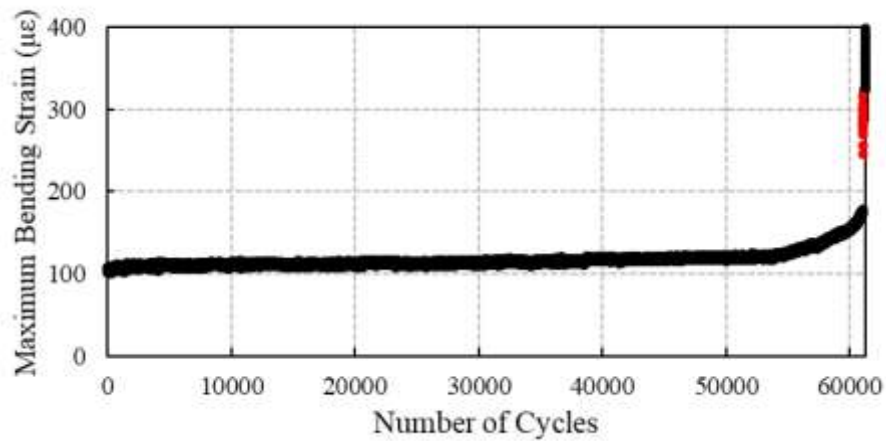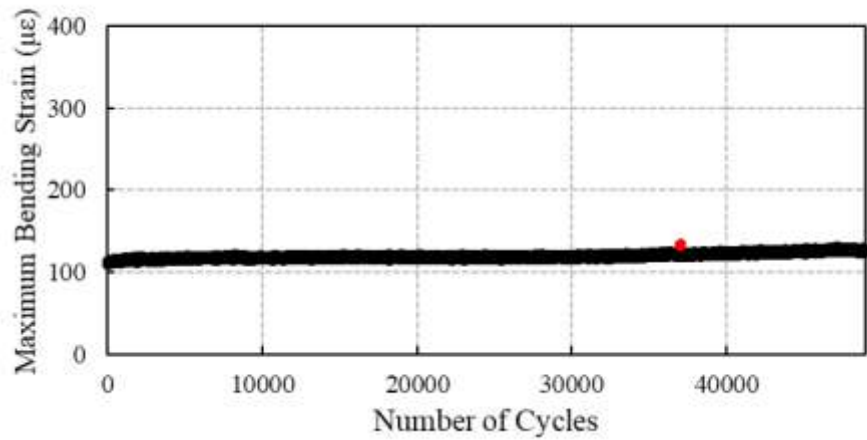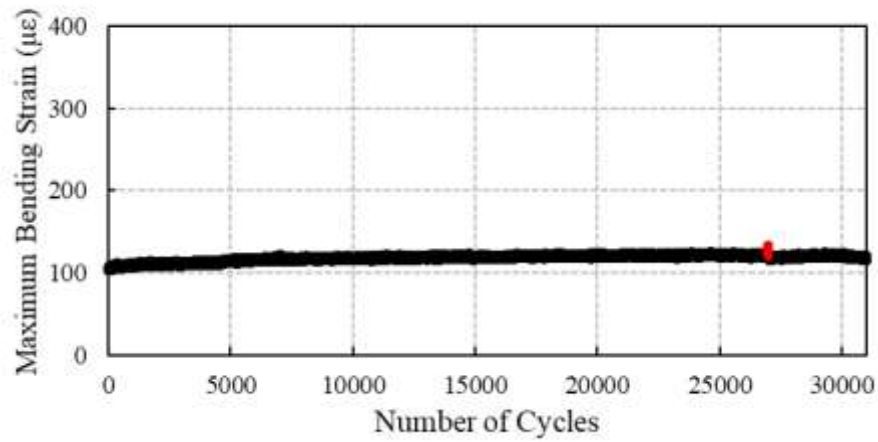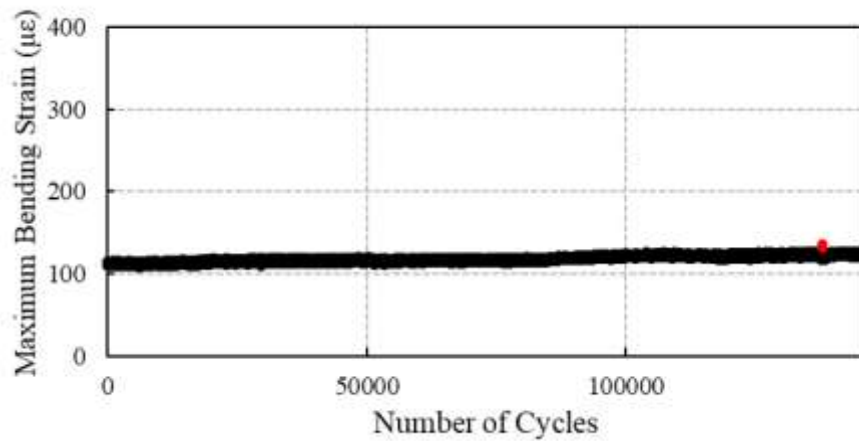
Figure 79: Maximum bending strain vs. number of cycles for (a) DCF_C3_B2 (overload of 0.9 at D = 15%) (b) DCF_C4_B2 (overload of 0.9 at D = 50%) and (c) DCF_C5_B4 (overload of 0.9 at D = 85%).

166

(a)

(b)

(c)

Figure 80: Maximum bending strain vs. number of cycles for (a) DCF_C4_B6 (overload of 0.8 at D = 15%) (b) DCF_C5_B7 (overload of 0.8 at D = 50%) and (c) DCF_C7_B3 (overload of 0.8 at D = 85%).

12.4.7 Summary of Fatigue Damage due to Superloads from Laboratory Testing

The damaged concrete test program quantified the effect of overloads on the fatigue life of concrete beams as a function of the percent life consumed in the concrete. The fatigue cycle data demonstrated that both overloads at a stress ratio of 0.8 and 0.9 impacted the fatigue life of the concrete and as the target damage state increases, the number of cycles to failure after the overload decreases. Additionally, the fatigue cycle data showed that more fatigue cycles are required to damage concrete with new pavement strength than concrete with old pavement strength. This was observed to be a consequence of the stress range effect.

The nonlinear progression of fatigue damage in concrete was examined through the collection of structural response data. The normalized compliance concept was an excellent parameter to not only impose target damage states in the concrete but also to evaluate the impact of overloads. Normalized compliance was successfully used to generate stiffnesses in the concrete representative of 15%, 50%, and 85% life consumed. By monitoring the normalized compliance during the application of an overload, the effect of percent life consumed on the damage imposed by an overload was elucidated. Overloads at a stress ratio of 0.9 were shown to clearly have a greater impact as percent life consumed increases. Moreover, overloads at a stress ratio of 0.8 were observed to have a greater potential for a significant impact as percent life consumed increases. The bending strain data corroborated the findings of the normalized compliance analysis.

The results of the damaged concrete testing have significant implications for superload damage analysis. These results show the limitations of using the traditional S-N curve and a linear damage hypothesis approach when predicting the damage resulting from a superload. For instance, consider the effects of ten overload cycles at a stress ratio of 0.8 on an older concrete pavement. This overload is predicted by the respective S-N curve to consume 3% of the fatigue life of the concrete. As indicated by the fatigue cycle and structural response data collected in the damaged concrete testing, the impact was observed to exceed this prediction as percent life consumed increased. A nonlinear damage model for fatigue damage accumulation from superload stresses would be beneficial so that the existing damage state in the concrete can be considered.

12.5 Conclusion of Fatigue Damage due to Superloads

This research provides insight for the fatigue damage analysis of superloads on JPCPs with 15-ft joint spacings. The superload stress analysis characterized the critical stresses caused by superloads on JPCPs and provided an initial estimate of the fatigue damage imposed by these stresses. The constant amplitude test program showed the nonlinear accumulation of fatigue damage resulting from superload stresses of several magnitudes. The damaged concrete test program demonstrated the effect of percent life consumed on the fatigue damage imposed by an overload.

Several conclusions were drawn from this coupled computational and laboratory investigation. From the superload stress analysis:

- Single and tandem axles on the trailer portion of superloads can impose high tensile stresses and fatigue damage in 8-in and 10-in concrete slabs when large positive temperature gradients are present

- Minor or insignificant fatigue damage occurs as a result of a superload on 8-in and 10-in concrete slabs with a zero or negative temperature gradient

- Superloads do not significantly decrease the fatigue life of 13-in concrete slabs regardless of the temperature gradient present at the time of loading

- Tied concrete shoulders greatly reduce the impact of superload stresses

- The predicted fatigue damage for superload stresses decreases by accounting for stress range

From the constant amplitude testing:

- For concrete beams with strengths similar to that of a newer pavement, the number of single axle cycles to failure is predicted to be about $10^{4.5}$, 10^3, 10^1 for stress ratios of 0.7, 0.8, and 0.9, respectively

- For concrete beams with strengths similar to that of an older pavement, the number of single axle cycles to failure is predicted to be about $10^{3.5}$, $10^{2.5}$, $10^{1.5}$ for stress ratios of 0.7, 0.8, and 0.9, respectively

- The fatigue damage caused by a single axle stress pulse at a stress ratio of 0.9 causes a similar amount of fatigue damage as a tandem axle stress pulse at a stress ratio of 0.9

- Midspan deflection, bending strain, and compliance increase nonlinearly during constant amplitude testing
- In constant amplitude testing, the majority of stiffness loss occurs at an increasing rate after 70% of the fatigue life of the concrete is consumed (as indicated by the deflection, normalized compliance, and bending strain data)
- As fatigue damage in concrete increases, superload stresses become more impactful
- The traditional S-N curve and linear damage hypothesis approach for fatigue damage prediction in JPCPs have limitations when being used to assess the damage due to a superload

From the damaged concrete testing:

- Overloads at a stress ratio of 0.8 and 0.9 impact the fatigue life of concrete
- Stress range affects the number of applications until failure for a stress ratio of 0.7
- Percent life consumed impacts the instantaneous fatigue damage imposed by an overload
- Overloads at a stress ratio of 0.9 clearly have a greater impact as percent life consumed increases
- Overloads at a stress ratio of 0.8 have a greater potential for a significant impact as percent life consumed increases
- Stiffness loss occurs at a greater rate after the application of an overload (stress ratio $\geq$ 0.7), even if the stiffness is not affected instantaneously
- The traditional S-N curve and linear damage hypothesis approach to predict fatigue damage for an overload stress can underestimate the damage of a superload

13.0 GUIDELINES FOR FLEXIBLE PAVAMENTS

Distresses that develop in Asphalt Concrete (AC) pavements are commonly correlated to strains. The location of the critical strain will vary based on the pavement structure and loading conditions but include the surface AC layer, the base/subbase layer, and the subgrade). As discussed previously, Layered Elastic Analysis (LEA) is commonly used in Mechanistic-Empirical pavement design procedures to evaluate these strains. In LEA, the strains depend not only on the load of each tire, but also their relative configuration. Superloads (SLs) have unique loads and configurations as compared to standard axles, and therefore require additional analysis to determine the magnitude and location of the critical strain(s), and the resulting impact on pavement damage.

This section discusses the development of a method to analyze the damage caused by SLs in Pennsylvania, as obtained from permits received by PennDOT and discussed in previous sections. The section is broadly divided into two parts:
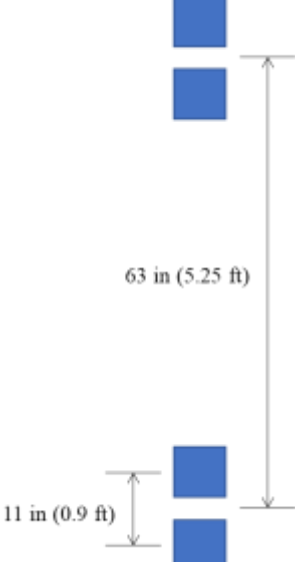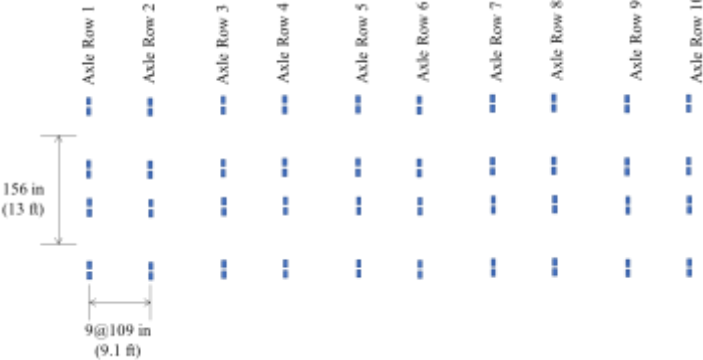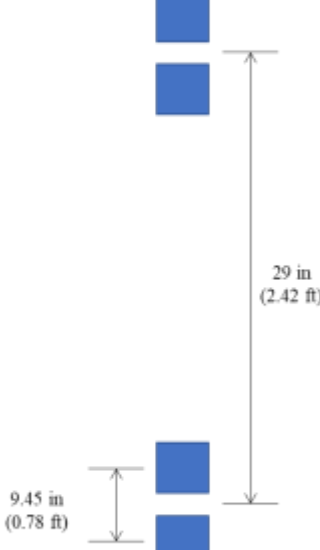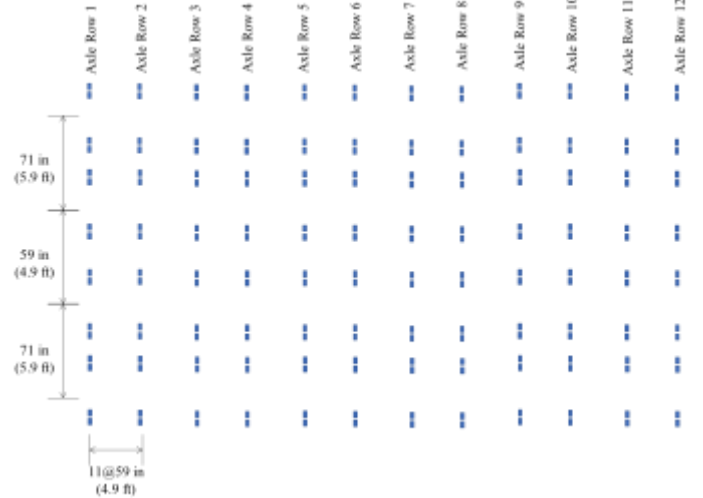
1) Analysis of existing SLs to identify configurations that produce similar strain magnitudes and locations
2) Development of a predictive model for the analysis of future SLs

In all the cases discussed in this section, it may be noted that the SL is assumed to be adjacent to the outer edge of the pavement, which corresponds to the critical configuration for stresses and strains.

13.1 Analysis of Existing SLs

From permits previously submitted to PennDOT, five SLs were identified that are representative of the various SL configurations in Pennsylvania. These five configurations are shown in Table 29.

Table 29: Axle configurations of representative SLs in Pennsylvania

Name	Configuration of each axle	Trailer configuration
SL1	63 in (5.25 ft); 11 in (0.9 ft)	Axle Row 1 – Axle Row 10; 156 in (13 ft); 9@109 in (9.1 ft)
SL2	29 in (2.42 ft); 9.45 in (0.78 ft)	Axle Row 1 – Axle Row 12; 71 in (5.9 ft); 59 in (4.9 ft); 71 in (5.9 ft); 11@59 in (4.9 ft)

SL3		
SL4		
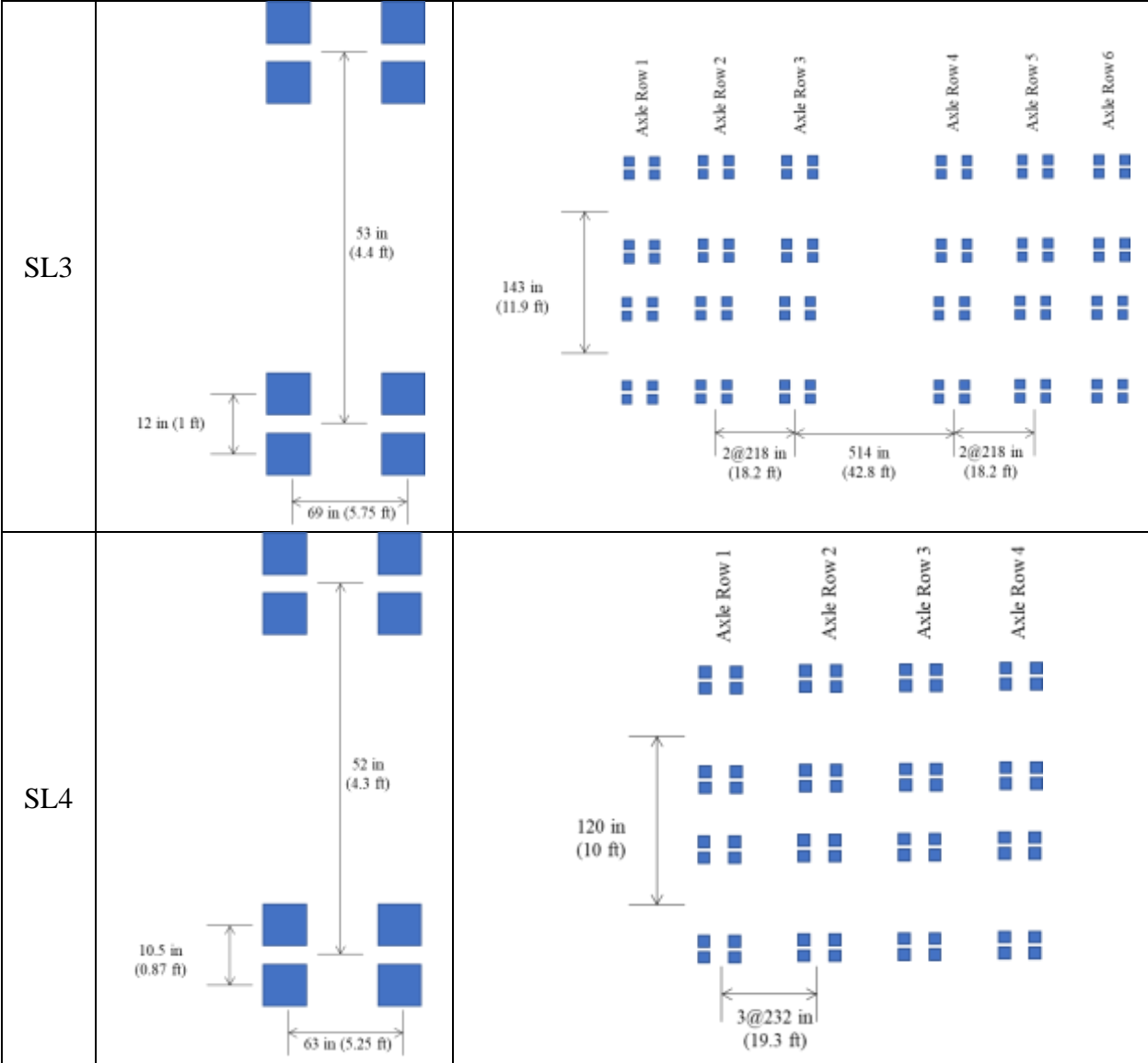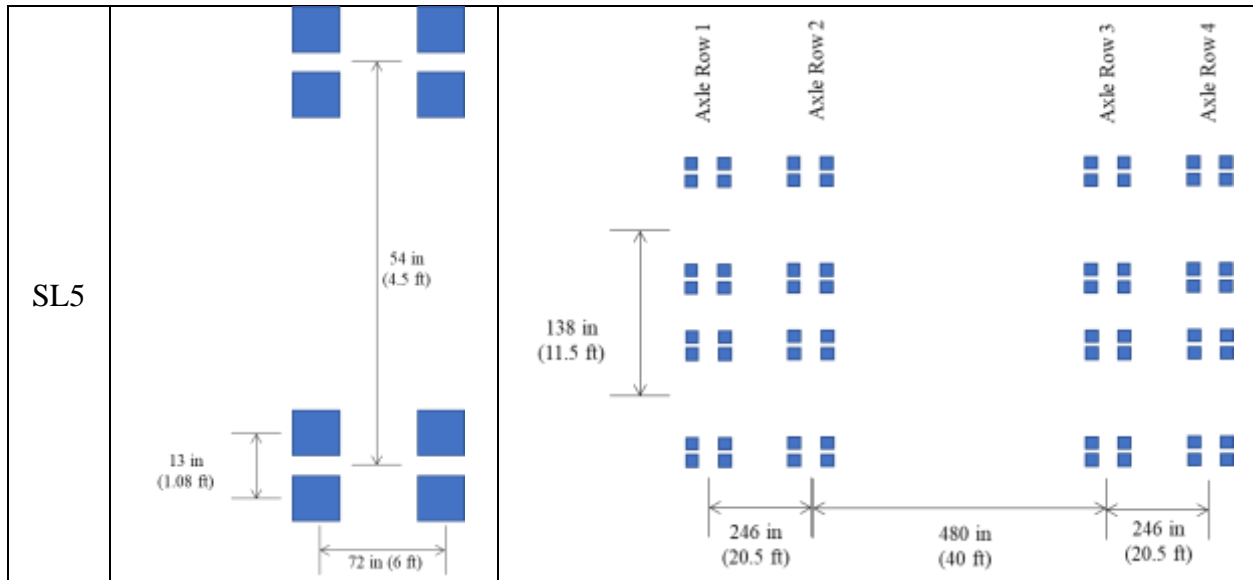
Based on the route reported in the permits for these SLs as well as the recommended elastic moduli of AC, base/subbase, and subgrade from PennDOT Publication 242 (Pennsylvania Department of Transportation, 2019), three pavement structures were identified based on the level of risk they would be subjected to by a single pass of the SL truck. These are summarized in Table 30. The Low risk structure has a relatively thick AC and base layer (the base and subbase are grouped into a single layer for simplicity) with a relatively high elastic modulus, and is expected to suffer minimal damage due to a single pass of an SL truck. On the other hand, the High risk structure has relatively thin layers with relatively low elastic moduli, and is expected to suffer significant damage. The Medium risk structure is in between these two extremes. Changes in modulus can be expected to occur with changes in the temperature of the AC or changes in the moisture content of the base layer.

Table 30: Pavement structures identified for analysis

Layer	Low risk	Medium risk	High risk
AC	Thickness = 18 in Modulus = 2.5×10^6 psi	Thickness = 10 in Modulus = 1×10^6 psi	Thickness = 3 in Modulus = 3×10^5 psi
Base (including subbase)	Thickness = 24 in Modulus = 39000 psi	Thickness = 16 in Modulus = 23000 psi	Thickness = 7 in Modulus = 10000 psi
Subgrade (SG)	Modulus = 8000 psi	Modulus = 8000 psi	Modulus = 8000 psi

It may be noted that for all three structures, the subgrade modulus was kept at a low 8000 psi. This corresponds to a clayey soil that is typically observed in Pennsylvania. Soils with a modulus lower than this value typically need to be improved before pavement construction.

13.1.1 Analysis of SL1

The configuration of SL1 was shown in Table 29. Each single axle consists of four tires carrying 4508 lb at a pressure of 100 psi each, with 20 single axles arranged along 10 axle rows. The first step in analyzing this configuration is to identify the nucleus of the SL. The nucleus of an SL is a repeating unit of the SL that represents the entire truck, such that the analysis of the entire SL truck can be reduced to analyzing a series of nuclei (Hajj, et al., 2018). Identifying the nucleus of an SL is as much an art as a science however, a general rule of thumb is that tires and/or axles separated by a spacing below a threshold of 60 in (5 ft) do not generally influence each other and therefore this threshold forms the basis of identifying the nucleus of any SL.

In the SL1 configuration, each row of axles is separated by a spacing of 9 ft 1 in, well above the threshold of influence. Therefore, each axle row can be analyzed separately. Furthermore, within each axle row, each axle is separated by a distance of 13 ft, which is again well above the threshold. Therefore, the only tires that are below or reasonably close to the threshold are contained within each axle and hence, the nucleus of SL1 is each single axle. It may be noted that this single axle has a different configuration (in terms of tire spacing) than a standard axle.

Next, each pavement structure is analyzed for loading with the nucleus using the layered elastic analysis program MnLayer (Khazanovich & Wang, 2007), assuming full bond between the layers. The strains at the bottom of the AC (horizontal and vertical), bottom of the base (vertical), and top of the subgrade (vertical) are evaluated at the points depicted by a red "X" in Figure 81. The results are shown in Figure 82.
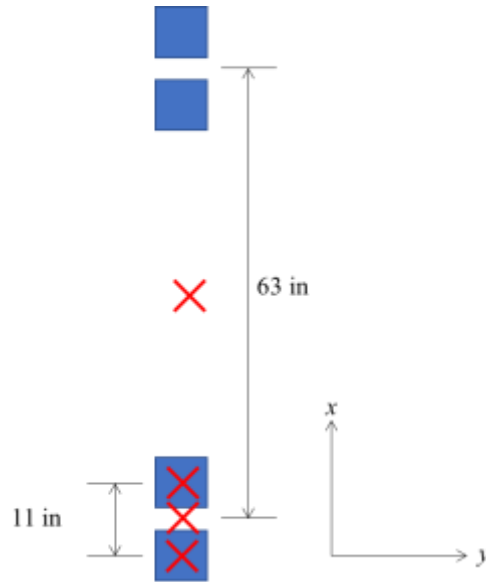
Figure 81: Analysis points in the nucleus of SL1

The maximum horizontal strain at the bottom of the AC was highest approximately below the inner tire for the High risk case, and in between the two closest tires for the Medium and Low risk cases, with the magnitude of the strain corresponding with the level of risk (highest for High risk, lowest for Low risk). The maximum value of these strains can then be used to evaluate the damage caused by one pass of the SL truck, consisting of 10 repetitions of the nucleus. Damage can be quantified using two measures: fatigue life consumed, and total rutting.

The number of allowable repetitions of the nucleus for fatigue N_f can be evaluated using the model from Pavement ME (National Cooperative Highway Research Program Report 1-37A, 2004) discussed previously and reproduced below:

$$N_f = 0.00432C \left(\frac{1}{\varepsilon_t}\right)^{3.291} \left(\frac{1}{E}\right)^{0.854} \tag{51}$$

$$C = 10^M \tag{52}$$

$$M = 4.84 \left(\frac{V_b}{V_a + V_b} - 0.69\right) \tag{53}$$

Where,

V_a = air voids in asphalt mixture by volume, %

V_b = effective asphalt binder content by volume, %

ε_t = maximum tensile strain at the bottom of the AC layer, in/in

E = the modulus of the AC layer, psi

In the present study, it was assumed that $V_a = 7.07\%, V_b = 9.47\%$, which are typical values recommended by PennDOT (Brink, Wilke, Darter, & Von Quintus, 2020).
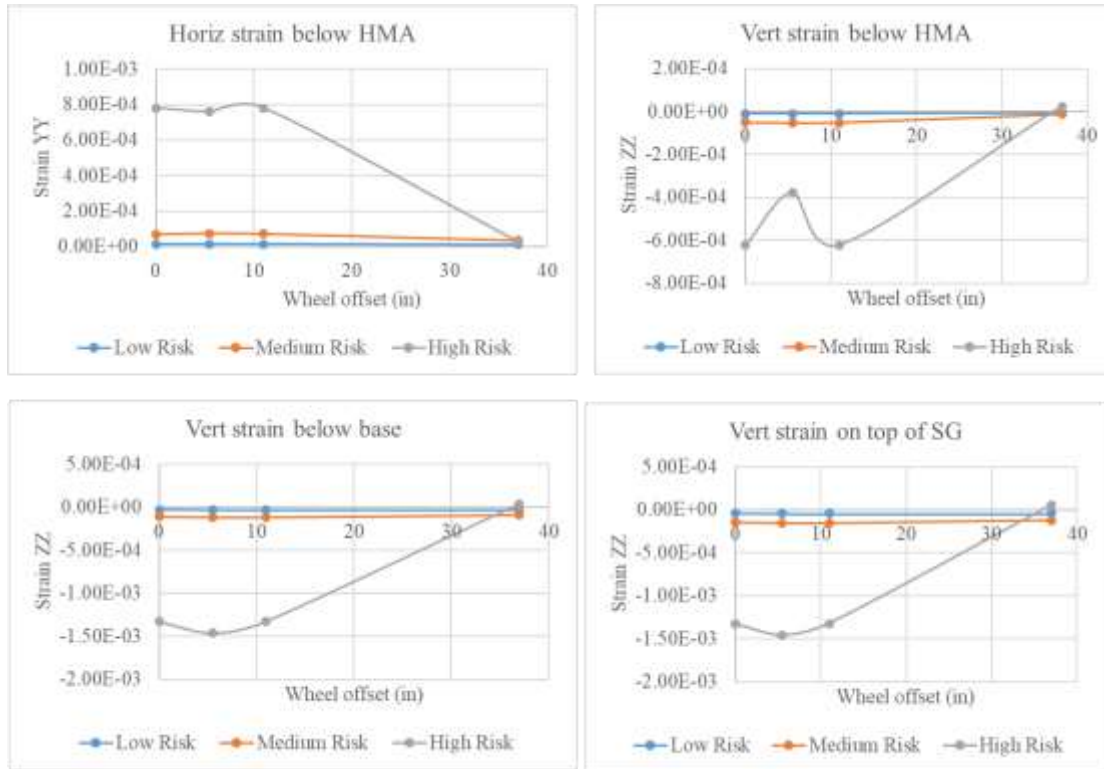

Figure 82: Horizontal and vertical strains under the nucleus of SL1

The percentage of fatigue life consumed can be evaluated as:

$$D(\%) = \frac{n}{N_f} \times 100 \tag{54}$$

where,

n = the number of repetitions of the nucleus over a point.

For SL1, any given point experiences ten repetitions of the nucleus for one pass of the SL, and therefore, $n = 10$. The percentage of fatigue life consumed for each pavement structure

177

after one repetition of the SL is shown in Figure 83. For the Low and Medium risk structures, there is negligible damage from one pass of the SL. However, for the High risk structure, one pass consumes about 2.4% of the fatigue life.
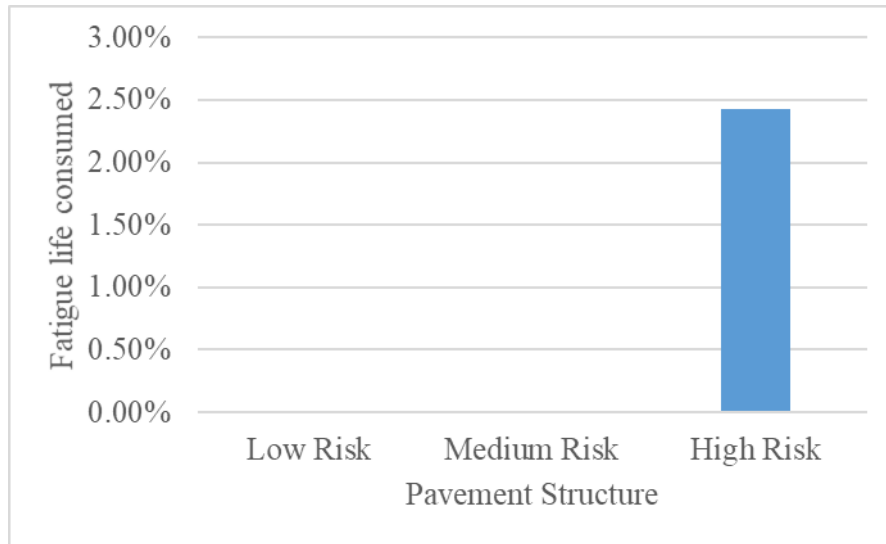

Figure 83: Percentage of fatigue life consumed by one pass of SL1

The maximum vertical strains at each point are in between the two closest tires for the base and SG, indicating the interaction between them, and underneath the inner tire for the AC. The total rutting depth (RD) was evaluated using the Pavement ME models for AC and unbound layers (National Cooperative Highway Research Program Report 1-37A, 2004), as described below:

AC rutting:

$$RD_{AC} = \varepsilon_r 10^{-3.15552} T^{1.734} N^{0.39937} h_{AC} \tag{55}$$

where,

T = mid-depth temperature of the AC layer, °F

h_{AC} = the thickness of the AC layer, in

ε_r = the resilient strain, in/in

The resilient strain is calculated using the following equation:

$$\varepsilon_r = \frac{1}{E}\left(\sigma_z - \mu(\sigma_x + \sigma_y)\right) \tag{56}$$

where,

σ_z = vertical stress at mid-depth of the AC layer, psi

σ_x = horizontal stresses at mid-depth of the AC layer, psi

σ_y = horizontal stresses at mid-depth of the AC layer, psi

μ = Poisson ratio of the AC (assumed to be 0.3 always)

Base rutting

$$RD_{GB} = \beta_{GB}\left(\frac{\varepsilon_0}{\varepsilon_r}\right) e_v^{\left(-\frac{\rho}{n}\right)^{\beta}} \varepsilon_v h \tag{57}$$

SG rutting

$$RD_{GB} = \beta_{SG}\left(\frac{\varepsilon_0}{\varepsilon_r}\right) e_v^{\left(-\frac{\rho}{n}\right)^{\beta}} \varepsilon_v h \tag{58}$$

Where the constants $\varepsilon_0, \varepsilon_r, \rho, \beta, \beta_{GB}, \beta_{SG}$ are specified by the model and ε_v is the vertical strain at the mid-depth of the corresponding layer.

The total rutting is then evaluated as:

$$RD = RD_{AC} + RD_{GB} + RD_{SG} \tag{59}$$

The rutting can then be scaled to RD_p for a user-specified reliability p (selected as 85% in the present study) using the following model:

$$RD_p = RD + \left(\sqrt{Se_{RDAC}^2 + Se_{RDGB}^2 + Se_{RDSG}^2}\right) Z_p \tag{60}$$

Where,

Se_i = standard error of rutting, in

$Se_{RDAC} = 0.1587(RD_{AC}^{0.4579})$

$Se_{RDGB} = 0.1169(RD_{GB}^{0.5303})$

$$Se_{RDSG} = 0.1724(RD_{SG}^{0.5516})$$

Z_p = standard normal variate

This is calculated for each pavement structure and shown in Figure 84. For the Low and Medium risk structures, negligible rutting is predicted to develop with one pass of the SL. However, for the High risk structure, a significantly higher rutting was predicted.
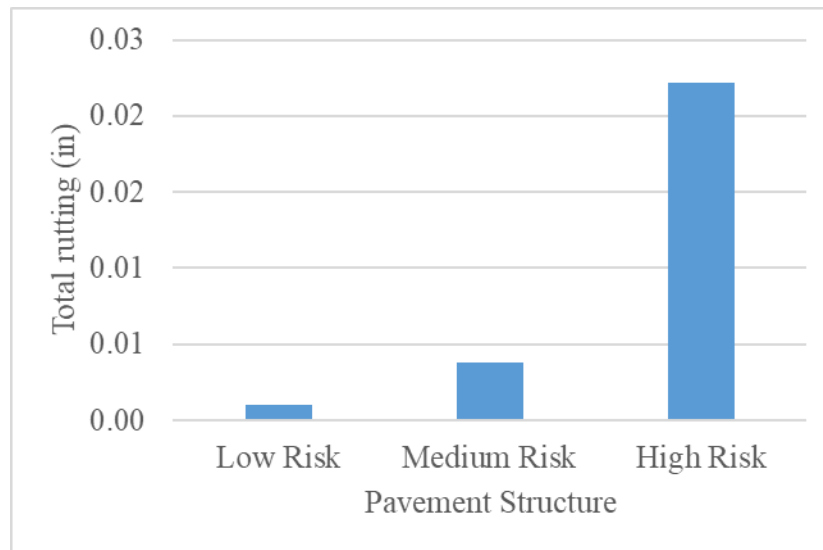

Figure 84: Predicted rutting for one pass of SL1

13.1.2 Analysis of SL2

SL2 consists of a series of 48 single axles along twelve rows, with each tire having a load of 4508 lbs at a pressure of 100 psi. Along the direction of travel, each row is separated by a spacing of 4.9 ft, which is just below the threshold of interaction. Therefore, either a single row or two rows may be part of the nucleus of SL2. Within each axle row, there are four single axles. The closest spacing between any two adjacent single axles is 59 in, which is also just below the threshold. Therefore, two nuclei are possible: a Single nucleus consisting of two single axles spaced 59 in apart, and a tandem nucleus consisting of two groups of single axles. These, along with the points at which the strains are evaluated, are shown in
Figure 85.

For the Single nucleus, the strains evaluated are shown in Figure 86. The maximum horizontal strain at the bottom of the AC was observed in between closely spaced tires due to the

interaction between them. On the other hand, the maximum vertical strain at the bottom of the AC was directly below the tires. At the bottom of the base and top of the subgrade, the vertical strains were in between closely spaced tires, again showing the interaction between them.
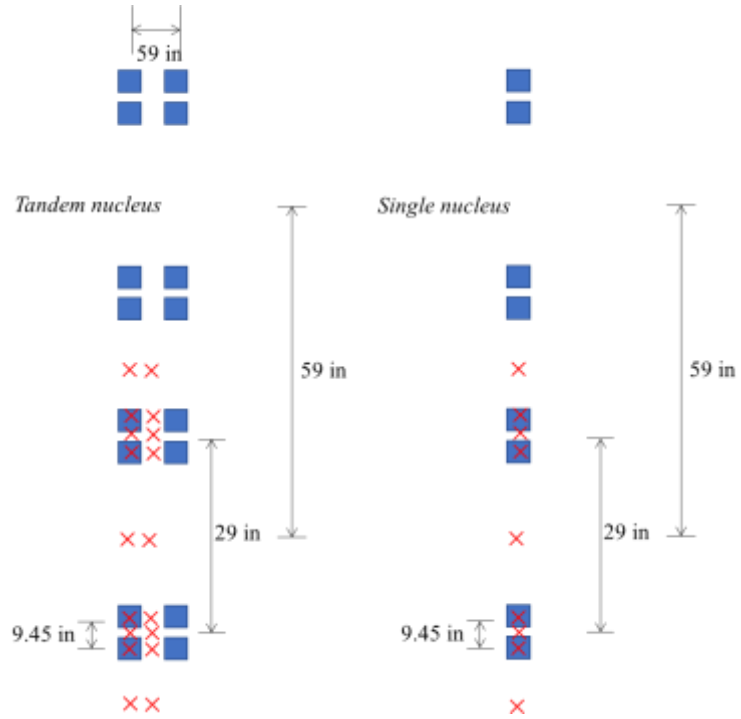

Figure 85: Nuclei of SL2 and corresponding analysis points depicted by the red "X"
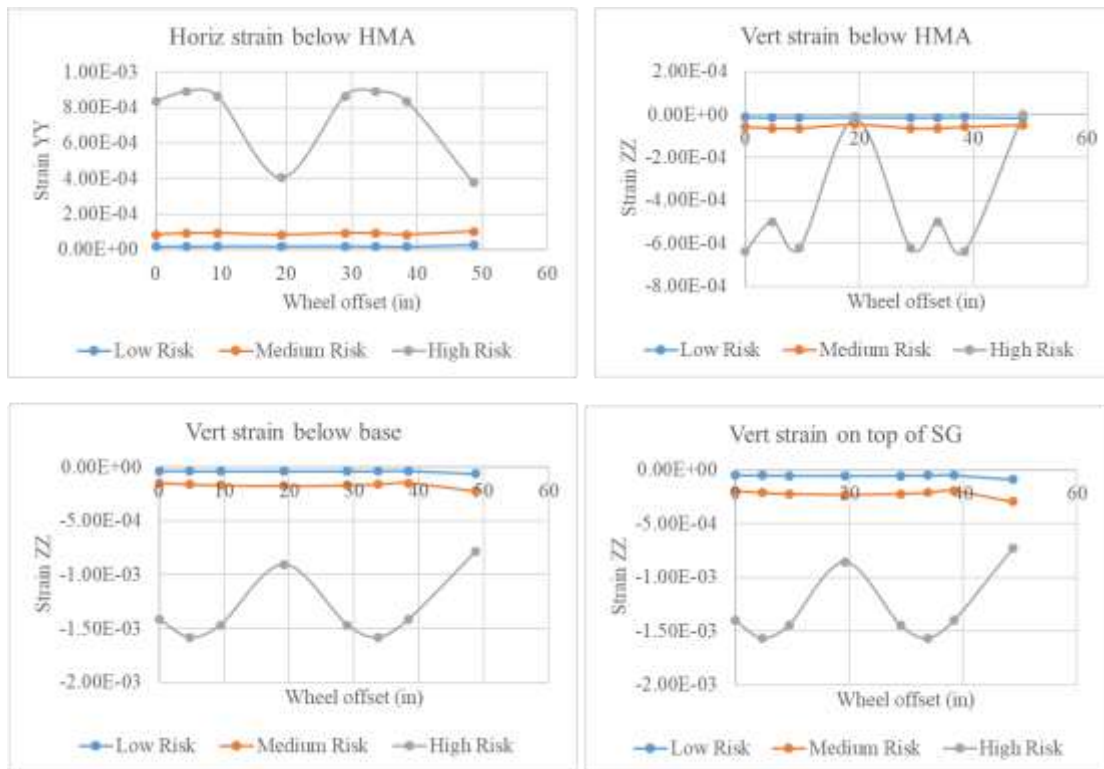
Figure 86: Horizontal and vertical strains under the Single nucleus of SL2

For the Tandem nucleus, the strains evaluated along one of the axles is shown in Figure 87. The strains are similar to the Single nucleus, showing that there is little interaction with the adjacent axle row. This can be confirmed by looking at the strains in between the axle rows, as shown in Figure 88. The strains are a full order of magnitude smaller than the corresponding strains along an axle, and moreover, some of the strains are reversed in their direction and thus do not contribute to fatigue cracking or rutting entirely.
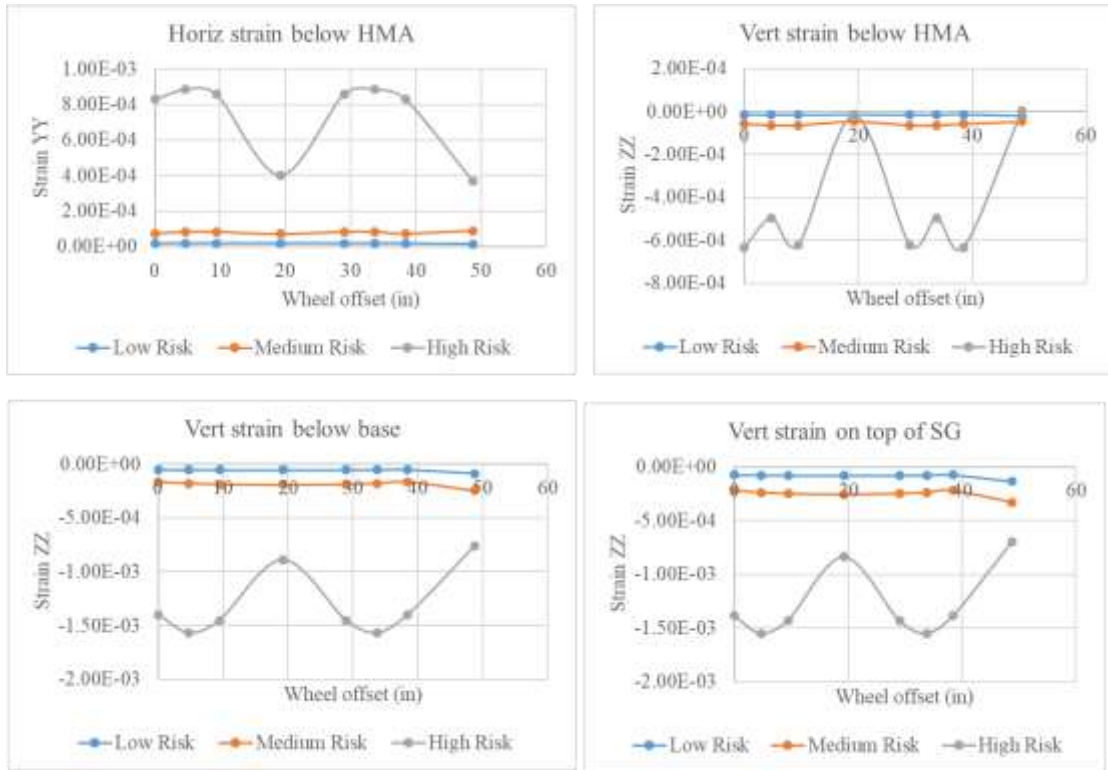
Figure 87: Horizontal and vertical strains under an axle of the Tandem nucleus of SL2
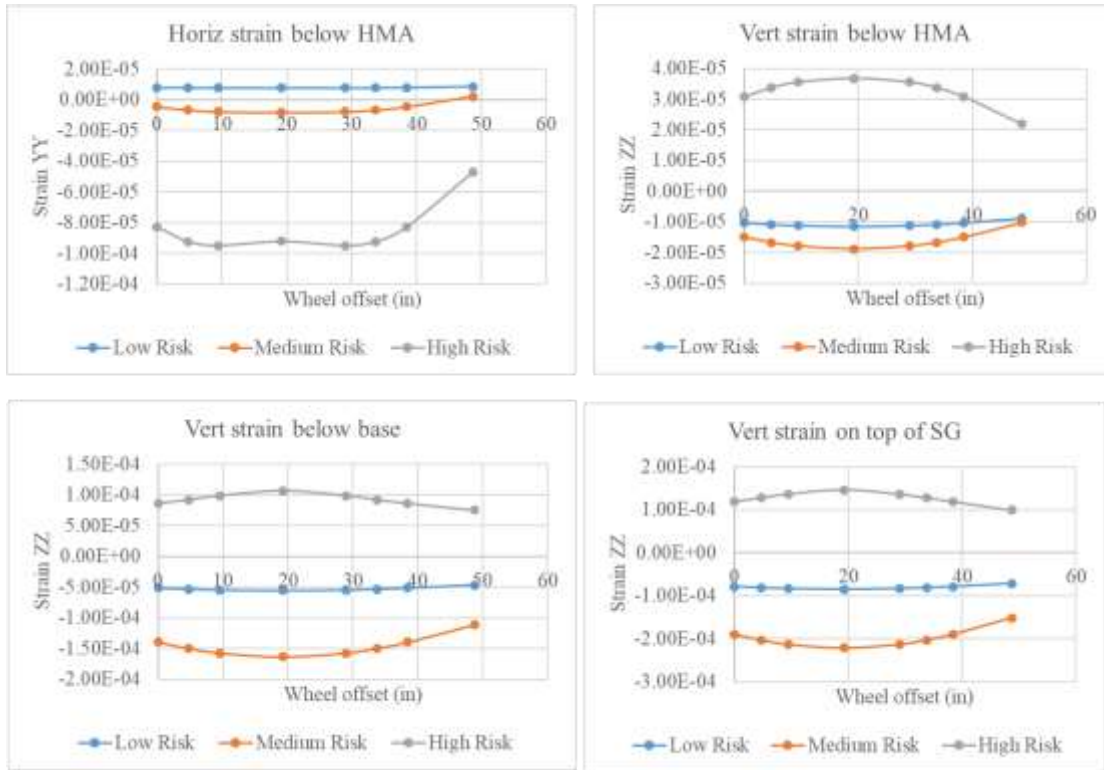
Figure 88: Horizontal and vertical strains in between the axles of the Tandem nucleus of SL2

Based on the above results, it can be concluded that the Single nucleus is sufficient to analyze SL2, with any point on the pavement experiencing 12 repetitions of the nucleus. Using the strains obtained from the Single nucleus and the models described in SL1, the percentage of fatigue life consumed by a single pass of SL2 as well as the total rutting at the top of the subgrade are shown in Figure 89 and Figure 90 respectively.
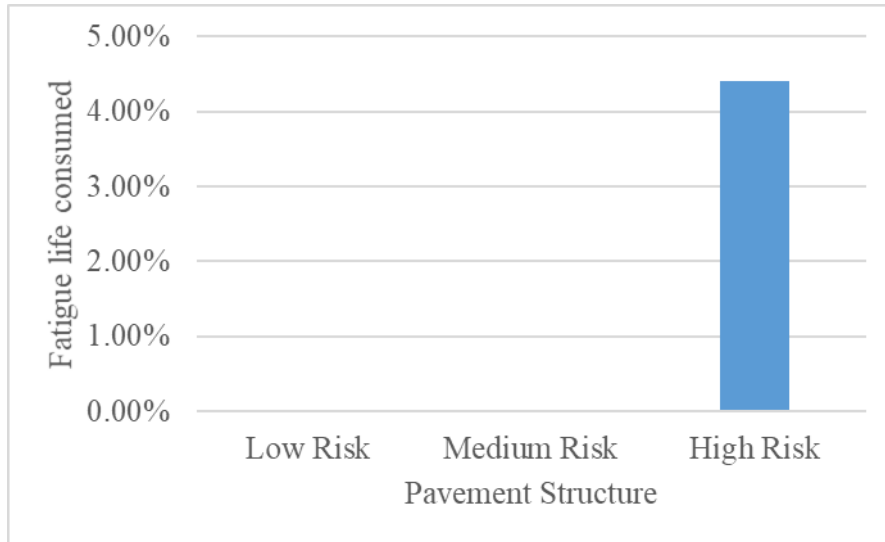
Figure 89: Percentage of fatigue life consumed by one pass of SL2
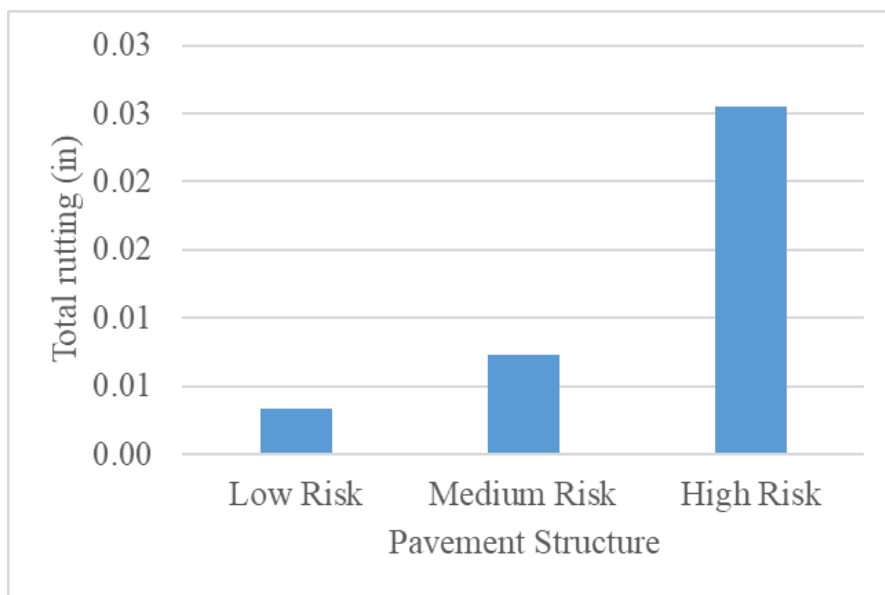

Figure 90: Predicted rutting for one pass of SL2

Like SL1, the Low and Medium risk pavements did not consume significant portion of the fatigue life. The High risk pavement however did consume about 4.5% of its fatigue life with one pass of the SL. For rutting, the Low and Medium risk pavements did not show significant rutting, while the High risk pavement showed a small amount.

13.1.3 Analysis of SL3

SL3 consists of a series of 12 tandem axles along six rows, with each tire having a load of 4656 lb at a pressure of 100 psi. Each tandem axle consists of two axles. The first step is to identify the nucleus of the SL. Each axle row is separated by 18.2 ft - 42.8 ft, well above the threshold, so they can be analyzed separately. Within each axle row, each tandem axle is separated by 11.9 ft, again above the threshold. Thus, the entire SL reduces to the analysis of a single tandem axle.

Within each tandem axle, the individual axles are separated by a spacing of 5.75 ft. While this is above the threshold for interaction, it is just barely so. Hence, the nucleus could be either a single axle or a tandem axle. Both are examined here, with the Single nucleus and Tandem nucleus shown in Figure 91, along with the points at which the strains were evaluated depicted by a red "X".
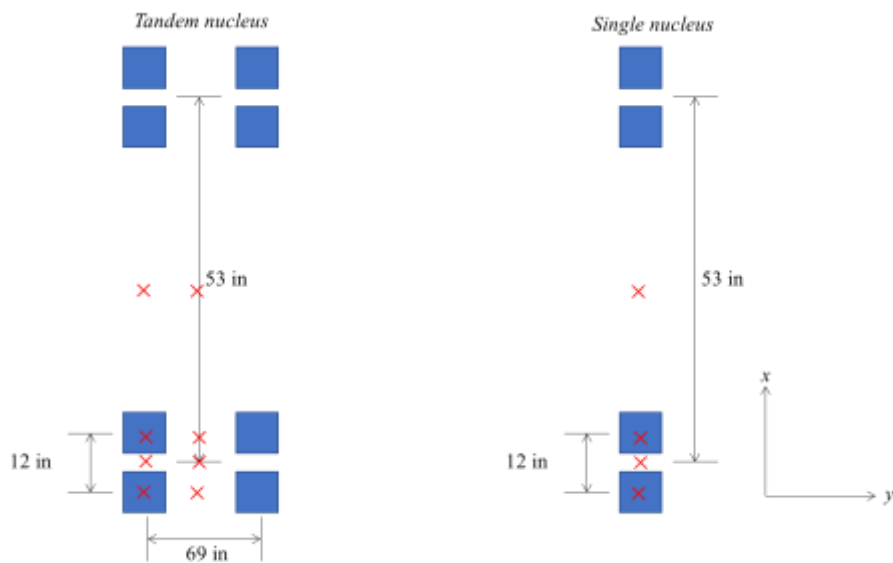

Figure 91: Tandem and Single nuclei of SL3

For the Single nucleus, the strains evaluated are shown in Figure 92. The maximum horizontal and vertical strain below the AC was approximately underneath the inner tire, while the maximum vertical strain below the base and on top of the subgrade was in between the nearest tires.
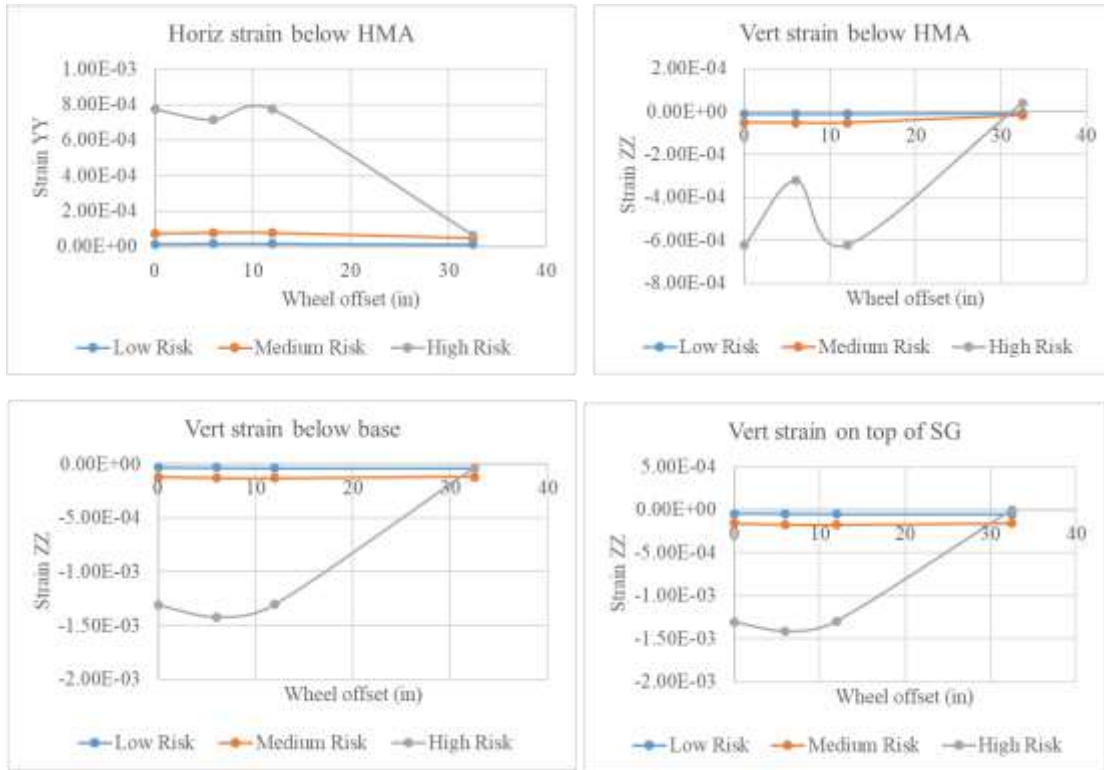
Figure 92: Horizontal and vertical strains under an axle of the Single nucleus of SL3

For the Tandem nucleus, strains along a single axle are in Figure 93. Once again, there is very little difference between these results and that from the Single nucleus. This shows little interaction between the tires. This can be confirmed by examining the strains in between the axles of the Tandem axle nucleus, shown in Figure 94.
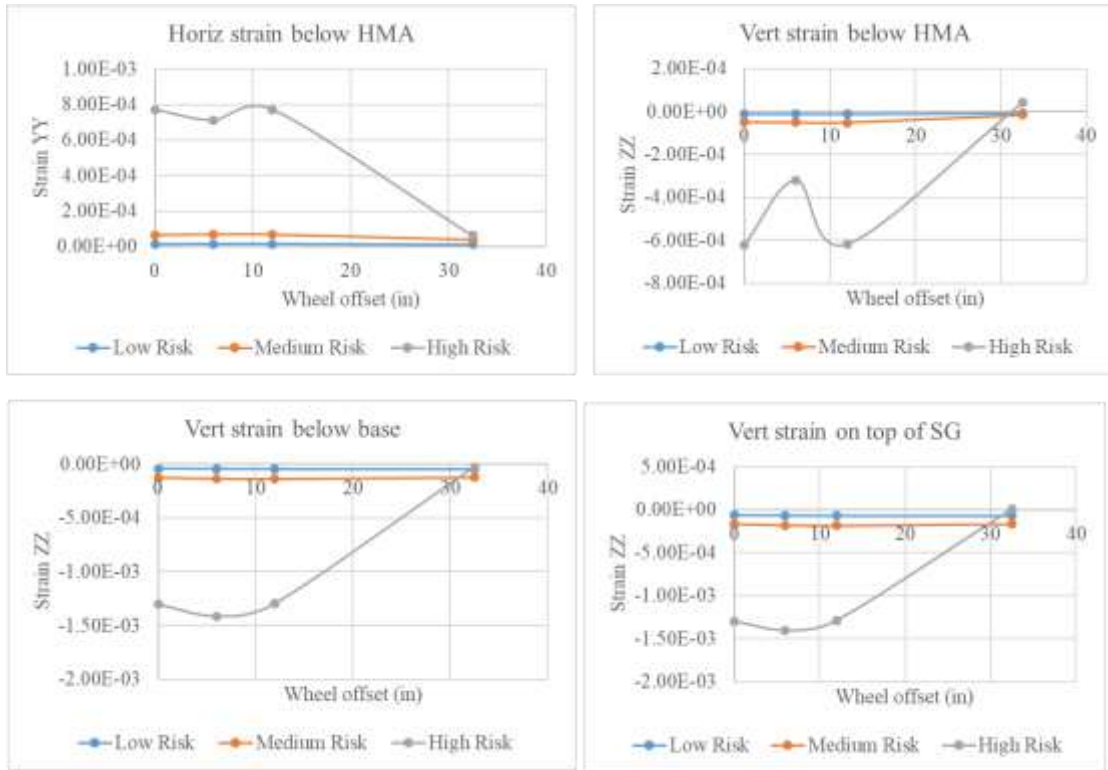
Figure 93: Horizontal and vertical strains under an axle of the Tandem nucleus of SL3
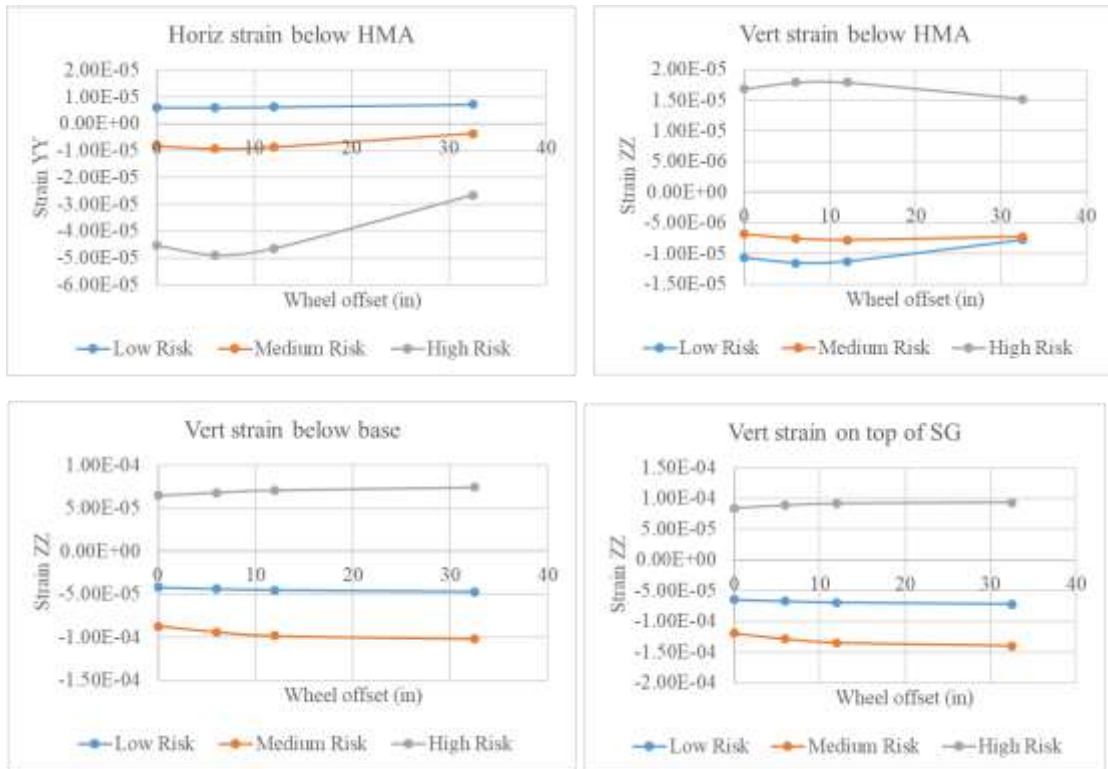
Figure 94: Horizontal and vertical strains in between the axles of the Tandem nucleus of SL3

In this case, the strains are a full order of magnitude less than the corresponding strains along the axle, and in some cases the sign is also reversed (i.e., tensile strain becomes compressive and vice versa). This again reinforces the fact that there is little interaction between the axles. From the above discussion, it can be concluded that there is no considerable interaction between the two axles for the tandem axle configuration. Therefore, the nucleus is a single axle, and a point on the pavement experiences 12 repetitions of the nucleus. Using this information, the percent fatigue life consumed and total rutting at the top of the subgrade were determined and are shown in Figure 95 and Figure 96 respectively.
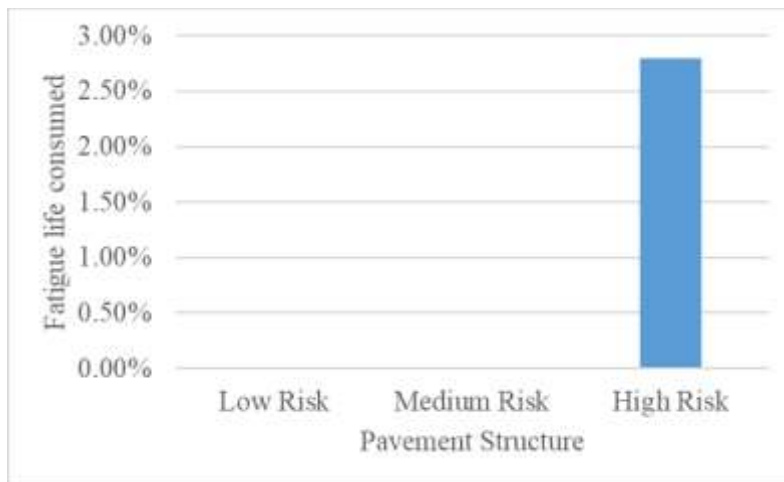
Figure 95: Percentage of fatigue life consumed by one pass of SL3
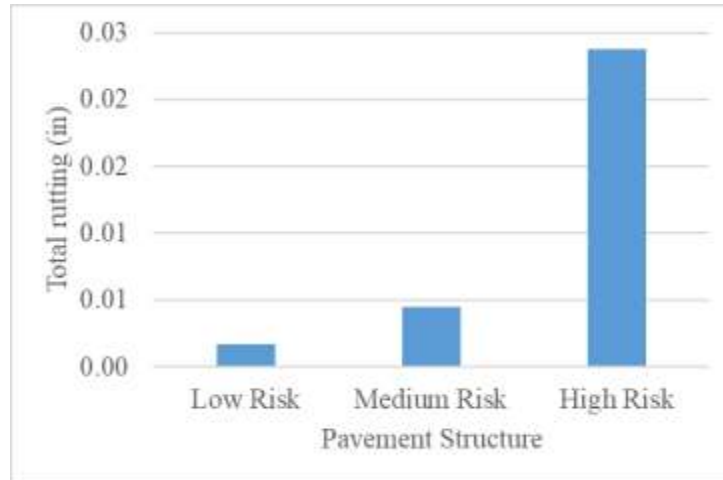
Figure 96: Predicted rutting for one pass of SL3

Like the previous SLs, only the High risk pavement had a considerable part of its fatigue life consumed. Predicted rutting was negligible for the Low and Medium risk pavements, and small for the High risk pavement.

13.1.4 Analysis of SL4

SL4 consists of a series of 8 tandem axles along 4 rows, with each tire having a load of 5,782 lbs at a pressure of 100 psi. Each tandem axle consists of two axles. Each axle row is separated by 19.3 ft, well above the threshold, so they can be analyzed separately. Within each axle row, each tandem axle is separated by 10 ft, again above the threshold. Thus, the entire SL reduces to the analysis of a single tandem axle, just like SL3.

Within each tandem axle, the individual axles are separated by a spacing of 5.25 ft. While this is above the threshold for interaction, it is just barely so. Hence, the nucleus could be either a single axle or a tandem axle. Both are examined here, with the Single nucleus and Tandem nucleus shown in Figure 97, along with the points at which the strains were evaluated depicted by a red "X".
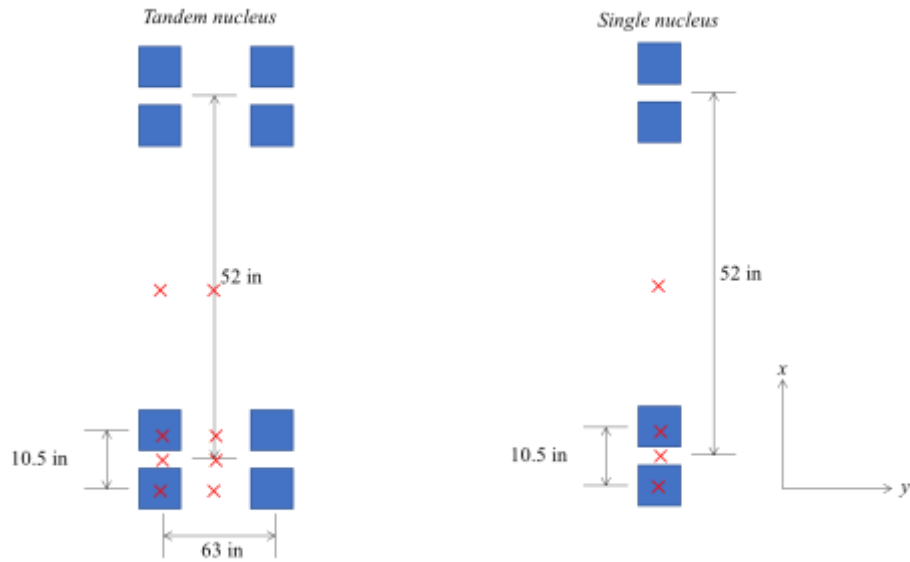
Figure 97: Tandem and Single nuclei of SL4

For the Single nucleus, the strains are shown in Figure 98, while for the Tandem nucleus, in Figure 99. Once again, the two sets of strains are nearly identical to each other, indicating only minor interaction between the axles. This can be confirmed by looking at the strains in between the axles in the Tandem nucleus, as shown in Figure 100.

The strains in this case were an order of magnitude lower than along one of the single axles, and in some cases had a reversed direction. This shows that the critical strains are not in between the axles. It can thus be concluded that the analysis of a single axle as the nucleus is sufficient for this case, and any point on the pavement experiences 8 repetitions of the nucleus.

Figure 98: Horizontal and vertical strains under an axle of the Single nucleus of SL4

Figure 99: Horizontal and vertical strains under an axle of the Tandem nucleus of SL4

Figure 100: Horizontal and vertical strains in between the axles of the Tandem nucleus of SL4

For one pass of SL4, the percentage of fatigue life consumed and total rutting at the top of the subgrade are shown in Figure 101 and Figure 102, respectively. Similar to the other cases, a considerable fatigue life was consumed only for the High risk pavement. The Low and Medium risk pavements showed a negligible amount of rutting, while it was small for the High risk pavement.

Figure 101: Percentage of fatigue life consumed by one pass of SL4
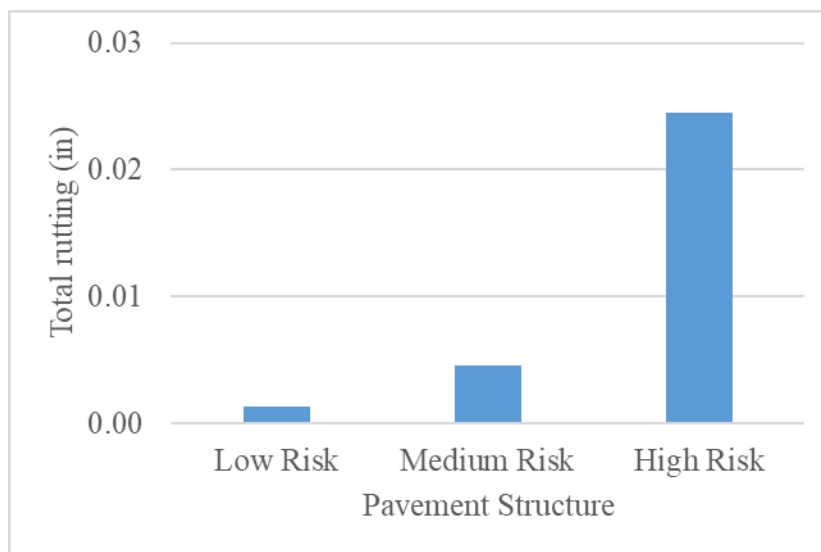
Figure 102: Total rutting after one pass of SL4

13.1.5. Analysis of SL5

SL5 consists of a series of 8 tandem axles along 4 rows, with each tire having a load of 5563 lb at a pressure of 100 psi. Each tandem axle consists of two axles. Each axle row is separated by 20.5 ft - 40.0 ft, well above the threshold, so they can be analyzed separately. Within each axle row, each tandem axle is separated by 11.5 ft, which is again above the threshold. Thus, the entire SL reduces to the analysis of a single tandem axle.

Within each tandem axle, the individual axles are separated by a spacing of 6 ft. While this is above the threshold for interaction, it is just above by 1 ft. Hence, the nucleus could be either a

single axle or a tandem axle. Both are examined here, with the Single nucleus and Tandem nucleus shown in Figure 103, along with the points at which the strains were evaluated depicted by a red "X".

For the Single nucleus, the strains were evaluated and shown in Figure 104, while for the Tandem nucleus, they are shown in Figure 105. The results are similar, indicating that there is little interaction between the axles. The strains between the adjacent single axles within a tandem axle is shown in Figure 106. Like the other SLs, the strains are a full order of magnitude lower, and the direction also reverses in some cases. Therefore, the effect of adjacent axles can be ignored. The Single nucleus is then the nucleus for the entire SL, and any point on the pavement experiences 8 repetitions of it.
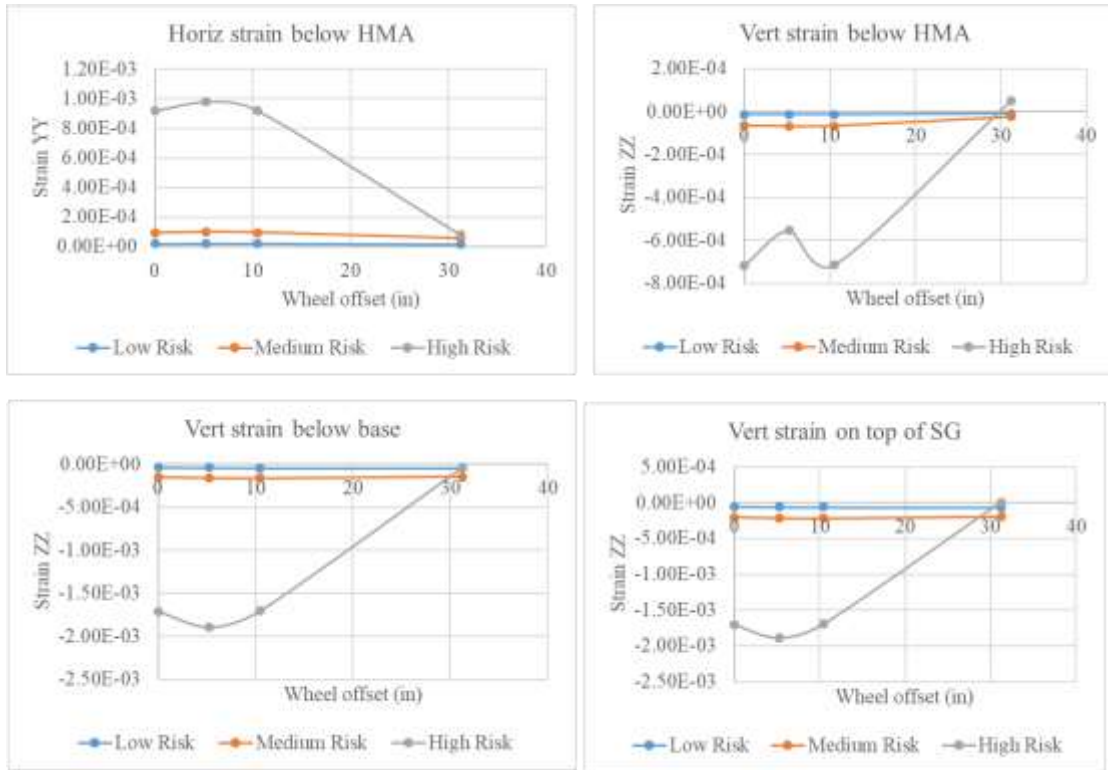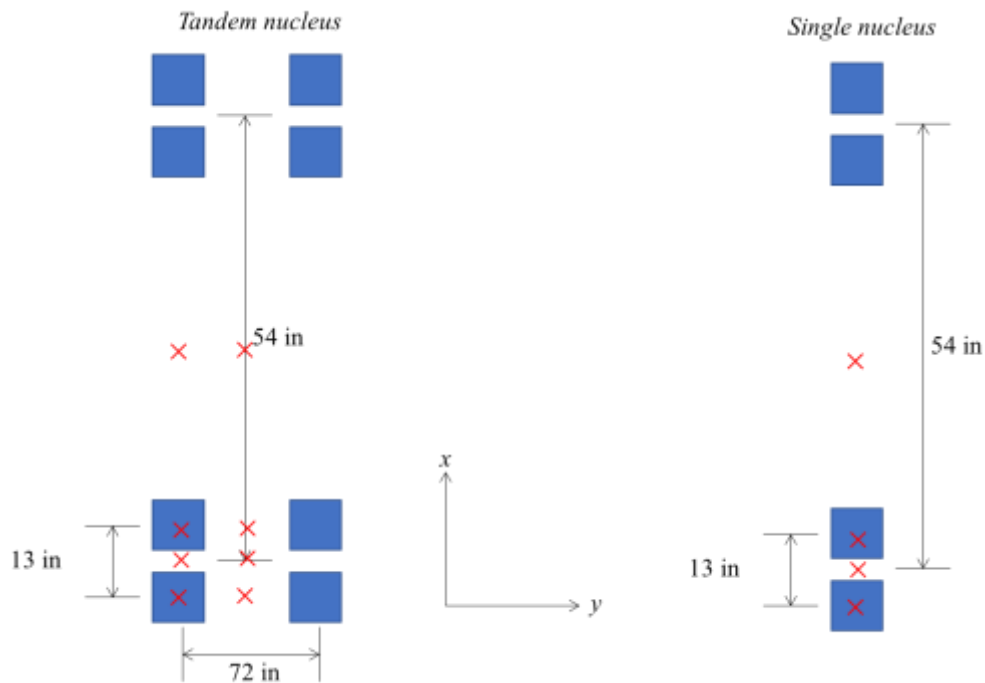

Figure 103: Tandem and Single nuclei of SL5
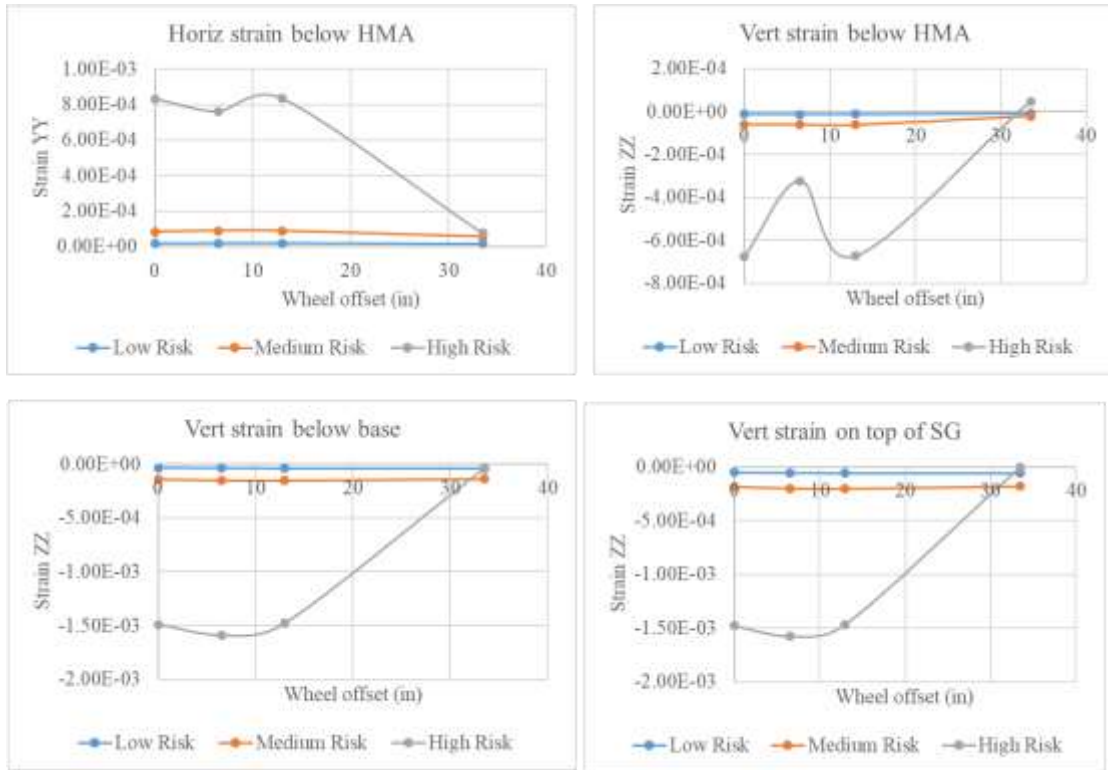
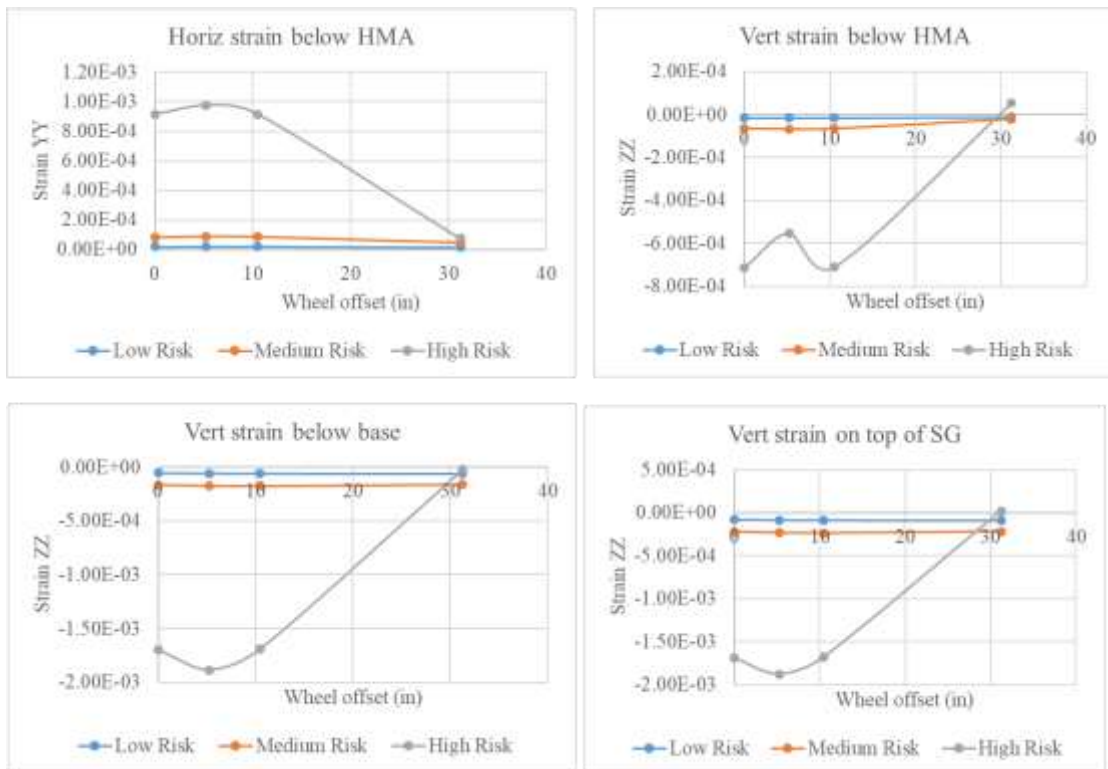Figure 104: Horizontal and vertical strains under an axle of the Single nucleus of SL5
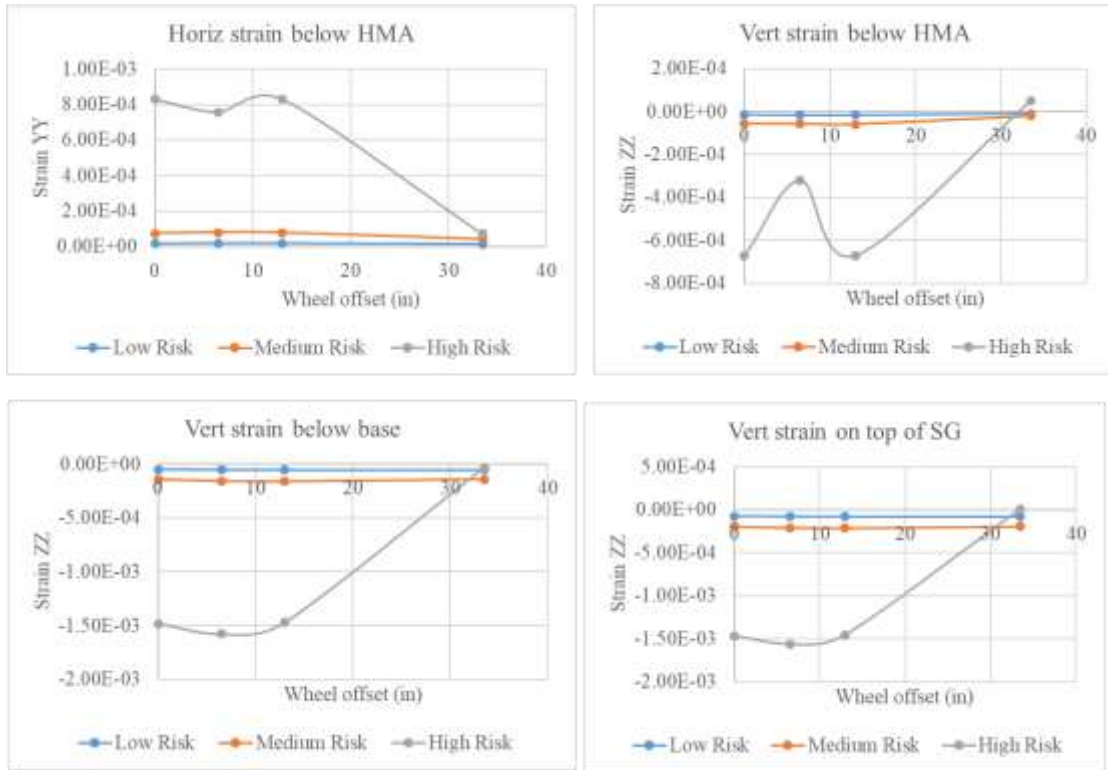
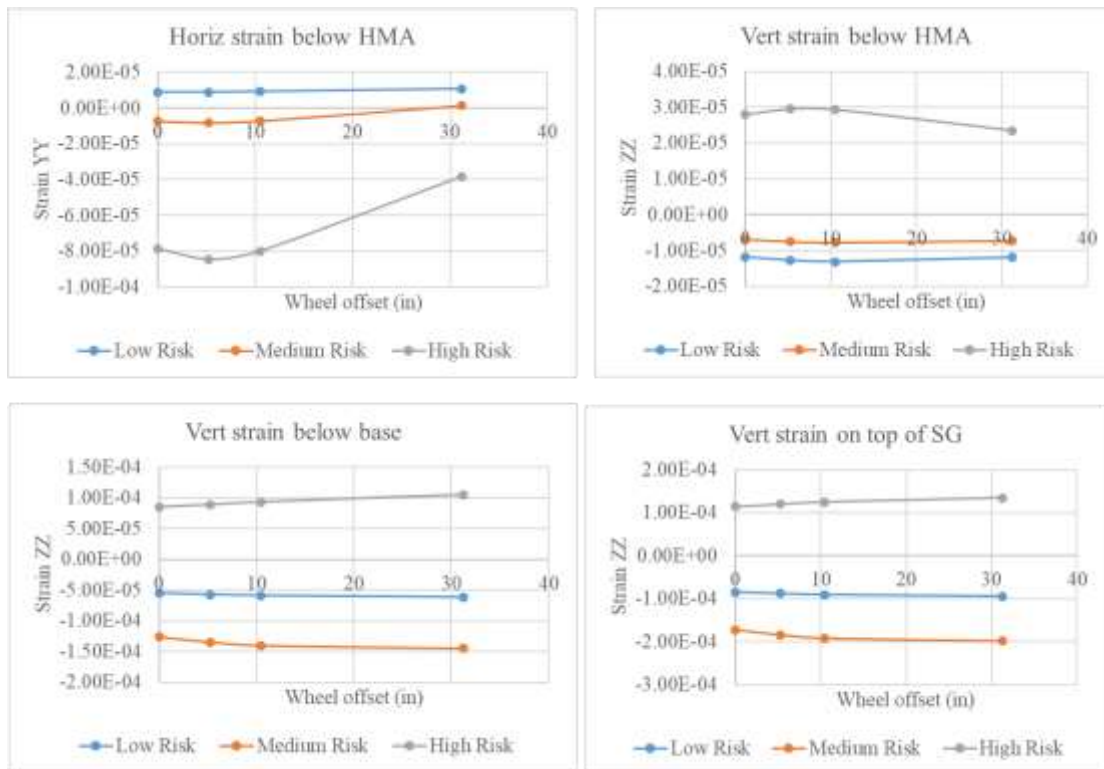Figure 105: Horizontal and vertical strains under an axle of the Tandem nucleus of SL5
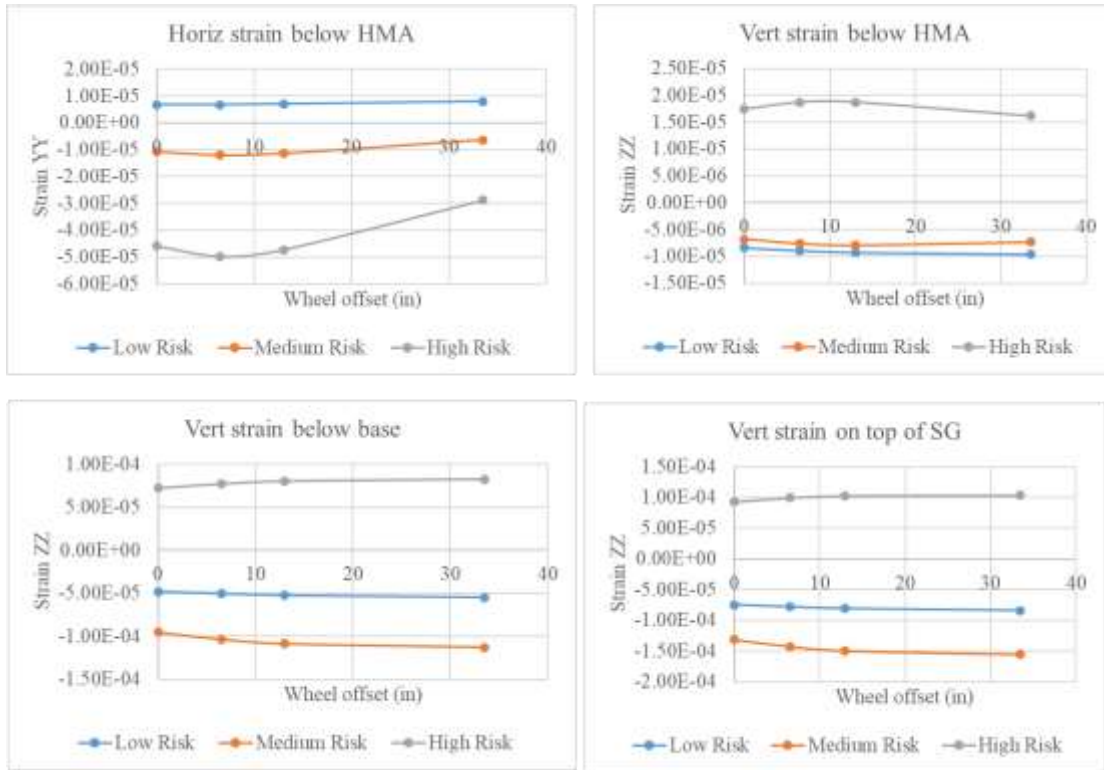
Figure 106: Horizontal and vertical strains in between the axles of the Tandem nucleus of SL5

Based on the preceding analysis, the fatigue life consumed and the total rutting are shown in Figure 107 and Figure 108 respectively.

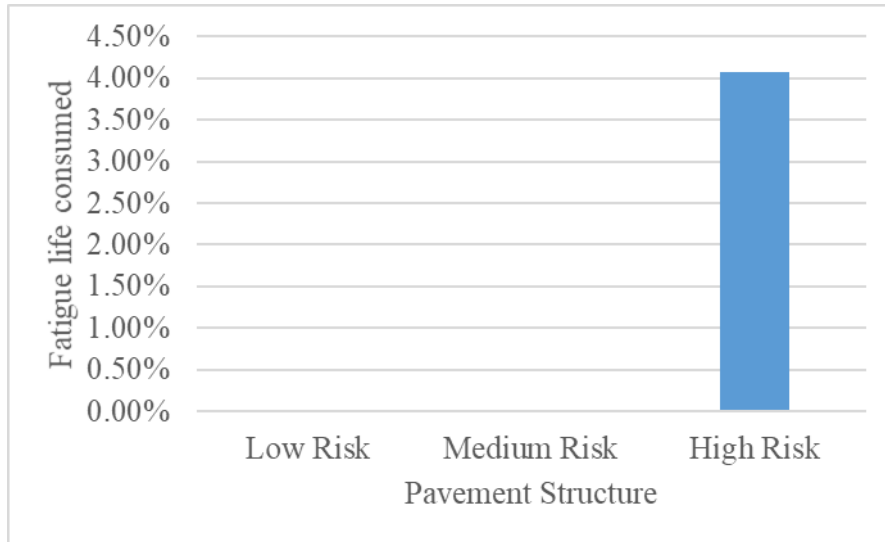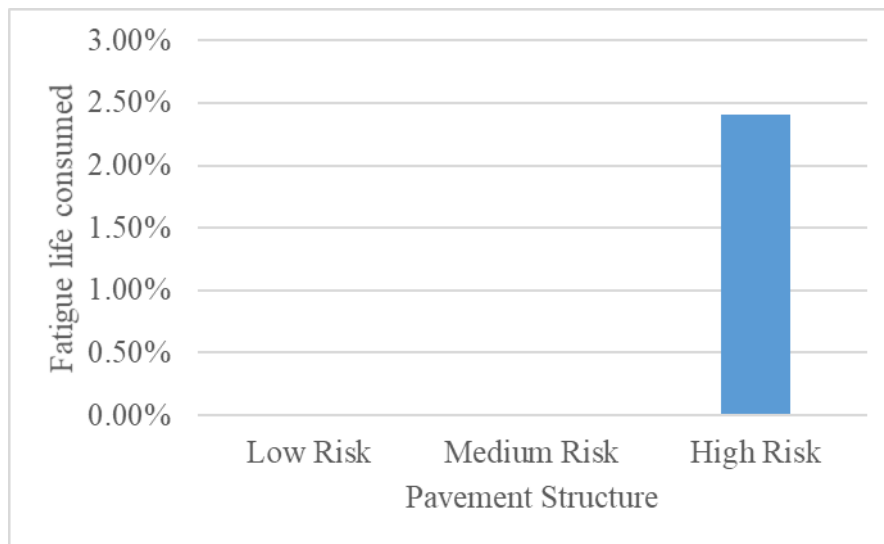
Figure 107: Percentage of fatigue life consumed by one pass of SL5
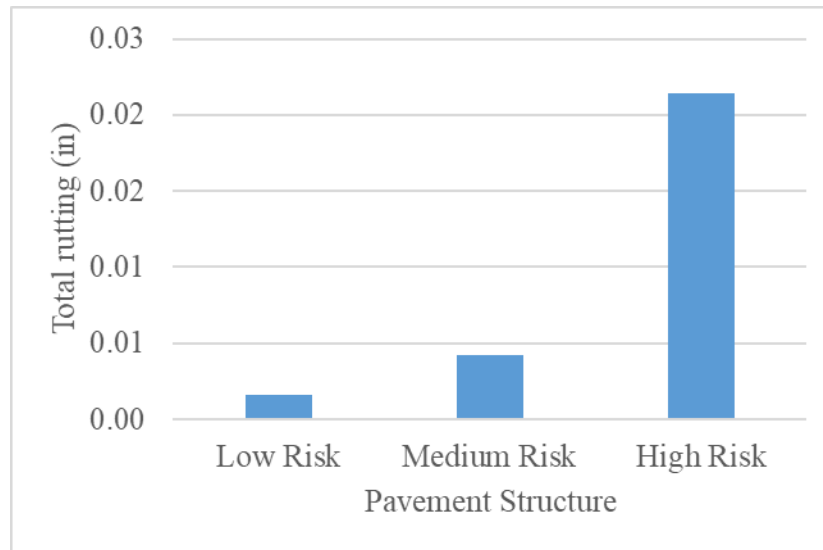
Figure 108: Total rutting after one pass of SL5

Once again, only the High risk pavement case showed a considerable consumption of fatigue life. Both the Low and Medium risk pavements had a negligible amount of rutting predicted, while the High risk case showed a small amount.

For SL1 – SL5, an additional analysis was performed to check whether shear failure at the top of the subgrade occurs in the subgrade due to a pass of each SL. The details of the model are discussed in the following sections, but for all cases discussed above, no risk of shear failure was found.

13.1.6 Summary of findings
From the analysis of typical SLs in Pennsylvania, the following conclusions can be drawn:
1. The nucleus of SLs in Pennsylvania can be assumed to be just a single axle, as all the axles are spaced sufficiently far apart as to be effectively independent of each other.
2. Fatigue damage is not a significant concern except for particularly thin AC pavements or pavements with weak base/subbase (such as during the late spring).
3. Similar to fatigue damage, rutting is not a concern except for particularly poor pavement structures.
4. Shear failure at the top of the subgrade is not of concern for the typical SLs in Pennsylvania

13.2 Development of a Predictive Tool

While the preceding analysis was for existing SLs reported to PennDOT, for analyzing future permits, there is a need to develop a convenient tool. While a layered elastic analysis program could be used to analyze any general SL, for the typical SLs in Pennsylvania, a convenient Excel-based tool was developed instead. The development of this tool and a description on how to use it is discussed in this section.

13.2.1 Tool development

As established in the previous section, the nucleus of typical SLs in Pennsylvania consists of a single axle. The axle shown in Figure 109 was found to be representative for the SLs in Pennsylvania, as discussed in Task 4 of this project. The total axle load varied from 18 kips to as high as 25 kips. This axle configuration was used in the development of the response prediction model for AC pavements.

63 in

10.5 in
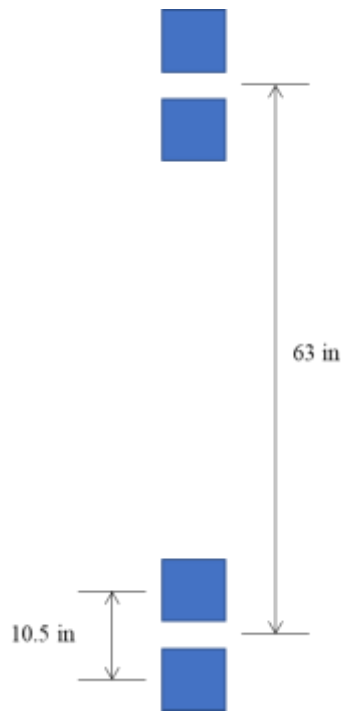
Figure 109: Representative single axle for SLs in Pennsylvania

To develop the predictive model, a factorial analysis with the parameters shown in Table 31 was run using MnLayer based on Layered Elastic Analysis (LEA) theory. All the cases correspond to the axle placed along the outer edge of the pavement, which is the critical configutation.

Table 31: Factorial analysis parameters and values

Parameter and units	Values
Axle load (lb)	18,000, 22,000, 25,000
AC thickness (in)	3, 4, 5, 6, 8, 10, 12, 18
AC modulus (psi)	2e5, 3e5, 5e5, 8e5, 1e6, 3e6
Base thickness (in)	7, 12, 18
Base modulus (psi)	1e4, 2e4, 3e4, 4e4, 5e4
SG modulus (psi)	8e3

From LEA, the outputs shown in Table 32 are obtained for each case in the factorial analysis. The outputs used for fatigue and rutting using the Pavement ME models discussed previously as indicated. Additionally, stresses at the top of the subgrade, which are used to check for instantaneous shear failure, are also obtained from the MnLayer outputs.

Table 32: Outputs from LEA and goodness of fit

Output parameter	Units	Symbol	R^2 adj	Used to calculate
Horizontal strain at the bottom of AC	No units	StrainYYHMABottom	0.834	Fatigue
Vertical strain at mid-depth of AC	No units	StrainZZHMAMid	0.498	AC Rutting
Vertical strain at mid-depth of base	No units	StrainZZBaseMid	0.893	Base Rutting
Vertical strain at top of SG	No units	StrainZZSGTop	0.925	SG Rutting
Horizontal stress at mid-depth of AC	psi	StressXXHMAMid	0.753	AC Rutting
Horizontal stress at mid-depth of AC	psi	StressYYHMAMid	0.937	AC Rutting
Vertical stress at mid-depth of AC	psi	StressZZHMAMid	0.962	AC Rutting
Horizontal stress at top of SG	psi	StressXXSGTop	0.945	Shear failure
Horizontal stress at top of SG	psi	StressYYSGTop	0.872	Shear failure
Vertical stress at top of SG	psi	StressZZSGTop	0.931	Shear failure

Based on the factorial analysis, a predictive model for each of these outputs was developed using stepwise regression, incorporating linear, quadratic, and interaction terms. The predicted values from these regression models are compared to the values obtained from LEA are shown in

Figure 110. In general, the goodness of fit (R^2 adj, indicated in Table 32) are very good, except for the stresses and strains evaluated at the mid-depth of the AC layer. However, these mid-depth values are used to evaluate rutting, which is very low in the AC layer and therefore, the lower goodness of fit does not greatly affect the results.
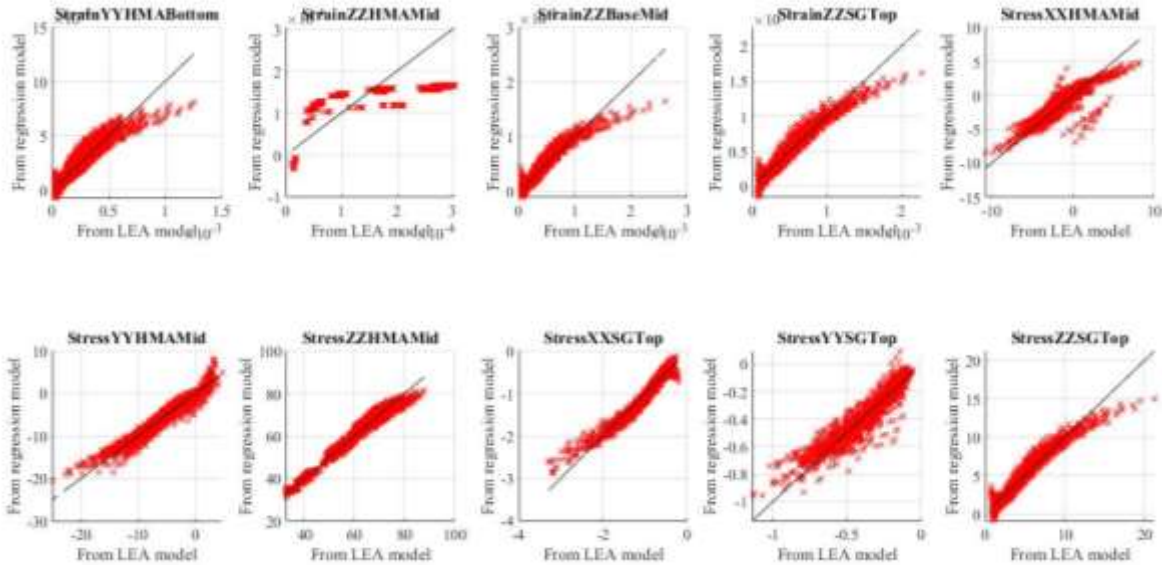
Figure 110: Predicted vs calculated outputs for the AC predictive tool (stresses reported in psi)

13.2.2 Tool description

The Excel-based predictive tool requires a set of user inputs shown in Figure 111. The first set of inputs are the same as the regression models i.e., axle load (in lb), AC and base layer thicknesses (in), and AC and base layer elastic moduli (in psi). Based on the factorial analysis, the axle load must be between 18,000 and 25,000 lb, AC thickness between 3 and 18 in, AC modulus between 3e5 and 3e6 psi, base thickness between 7 and 18 in, and base modulus between 1e4 and 5e4 psi. If any of the inputs are outside of this range, then a warning is provided to the user, otherwise "Value OK" is indicated by the tool.

Inputs		
Superload:		
Axle load	23126 lbs	Value OK
# of axle rows	8	
Pavement Structure:		
AC thickness	8 in	Value OK
AC modulus	3.00E+05 psi	Value OK
Mid-depth AC temperature	100 ºF	
Air voids in AC	7.07 %	
Effective binder content	9.47 %	
Base thickness	10 in	Value OK
Base modulus	3.00E+04 psi	Value OK
Subgrade c	20 psi	
Subgrade phi	20 degrees	
Depth of ground water table	10 ft	
Rutting reliability	85 %	

Figure 111: User inputs in the Excel-based predictive tool

An additional set of inputs is also required to evaluate rutting and fatigue. This includes the number of axle rows (nuclei) that cross a given point on the pavement surface, the mid-depth AC temperature (in °F, which can be a rough estimate based on the season), air voids and effective binder content in the AC mixture, desired reliability of the rutting prediction (typically 85%), and depth of the groundwater table (in ft, a rough estimate is adequate).

The tool provides guidance for adjusting the modulus of the AC layer if fatigue cracking is present, based on the model used in Pavement ME. This can be found in the "damaged AC modulus calculator" section of the inputs, as shown in Figure 112. These are just suggested values – the user is responsible for providing the desired values in the actual input section.

Damaged AC modulus calculator		
Undamaged AC modulus	3.00E+05	psi
Damaged AC modulus for Adequate AC pavement (0-8% fatigue (or aligator) c	2.85E+05	psi
Damaged AC modulus for Marginal AC pavement (8-20% fatigue (or aligator)cr	2.63E+05	psi

Figure 112: Damaged AC modulus calculator section of the tool

In addition to fatigue and rutting, literature shows that shear failure at the top of the subgrade may also be of interest when SLs pass over flexible pavements. Therefore, to evaluate this, a Mohr-Coulomb shear failure criteria was adopted based on the following equations:

$$\sigma_{1cr} = \sigma_3 \tan^2\left(45 + \frac{\phi}{2}\right) + 2c \tan\left(45 + \frac{\phi}{2}\right) \tag{61}$$

$$\frac{\sigma_1}{\sigma_{1cr}} < 1 \tag{62}$$

where,

σ_1 and σ_3 = the principal stresses obtained from the horizontal and vertical stresses at the top of the subgrade, psi

σ_{1cr} = the critical stress from Mohr-Coulomb theory, psi

c = cohesive strength of the soil, psi

ϕ = angle of internal friction of the soil, degrees

The tool requires the user to provide the c, ϕ values for the soil. A rough estimate of these values based on the material type is also provided in the tool in case this information is unknown, as shown in Figure 113.

Typical c, phi values of subgrade materials		
Material	c (psi)	phi (º)
Rock	1500	30
Sand	0	35
Gravel	0	35
Silt	12	34
Clay	20	20
Loose sand	0	33
Medium sand	0	40
Dense sand	0	40
Gravel with some sand	0	42

Figure 113: Typical c, ϕ values for various soils (adapted from (Das, 2011))

Once the user provides all the necessary inputs, the Messages box provides the next steps, as shown in Figure 114. Typically, the user is directed to see the results in the Results tab of the spreadsheet. However, if the thickness of the AC layer is greater than 10 in, then typically the effect of one pass of any SL is negligible, and the user is directed to ignore the Results tab; no further action is required.

Messages
See Results tab for calculated distresses

Figure 114: Messages box in the tool

In the Results tab, the following is displayed, as shown in Figure 115:

1. The fatigue damage caused by one pass of the SL, expressed as an equivalent number of ESALs to the next multiple of five. The rounding off of the ESALs was done to account for the error in the prediction model and also because ESALs are generally reported as a whole number.
2. Total predicted rutting after one pass of the SL.
3. A binary warning (yes or no) as to whether shear failure is predicted to occur.

The tool also contains an additional set of tabs that perform the intermediate calculations however, these are hidden to prevent users from accidentally modifying the predictive model. They can be unhidden, if necessary, though it is not recommended to do so without first contacting the research team.

After **one pass** of the Superload:		
Fatigue damage is approx. equivalent to	30	ESALs
Total rutting =	0.0094	in
Shear failure?	No	

Figure 115: Example results displayed by the tool

The predictive tool thus synthesizes the knowledge gained from the analysis of typical SLs in Pennsylvania and the predictive model developed based on LEA to enable the user to perform a quick estimate of the damage that could be caused by a future SL. Detailed examples on using the tool for a new SL permit is discussed in the companion User's Guide submitted with this report.

14.0 GUIDELINES FOR CONSIDERING RIGID PAVEMENTS: FATIGUE DAMAGE

14.1 Introduction

In Section 10, an analysis of five representative SLs and their effect on JPCP sections was presented. The concept of a critical stress pulse was introduced, which shows the stress history in the JPCP section when the SL moves over it. Using this stress pulse, the percentage of fatigue life consumed was evaluated, and it was found that under certain conditions, such as a positive temperature gradient and untied shoulders, the fatigue damage on the JPCP could be significant. In this report, a general model for the effect of SLs on JPCP sections was developed and converted into an Excel-based tool that can be used to estimate the fatigue damage caused by any SL.

14.2 Model Framework

From the SLs analyzed in Section 10, three broad categories of SLs in PA were identified. Only the trailers were analyzed as they cause the vast majority of the damage. Each SL was categorized into one of the following groups:

a) Continuous: This consists of twelve rows of axles, each row consisting of four individual single axles. Each row is separated by 5 ft, while the spacing between single axles within an axle row is shown in Figure 116.

b) Single: This consists of ten rows of axles, each row consisting of two individual single axles. Each row is separated by 9 ft, while the spacing between single axles within an axle row is shown in Figure 117.

c) Tandem: This consists of six rows of axles, with each row consisting of two tandem axles spaced 6 ft apart. The spacing between each row of tandem axles varies, while the spacing within each tandem axle is shown in Figure 118.

Similar to the work described in Section 10, the stress pulse from a pass of each of these SL truck categories could be evaluated using the finite element analysis program ISLAB (Khazanovich, et al., 2000). In order to develop a model to predict fatigue damage, the first step was to establish a factorial analysis to evaluate the critical stress over a range of expected conditions. The factorial analysis adopted in the present study is shown in Table 33. It may be

noted that axle spacing varies only for the Tandem SL, while the axle load is assumed to be evenly distributed among all the tires of the axle.
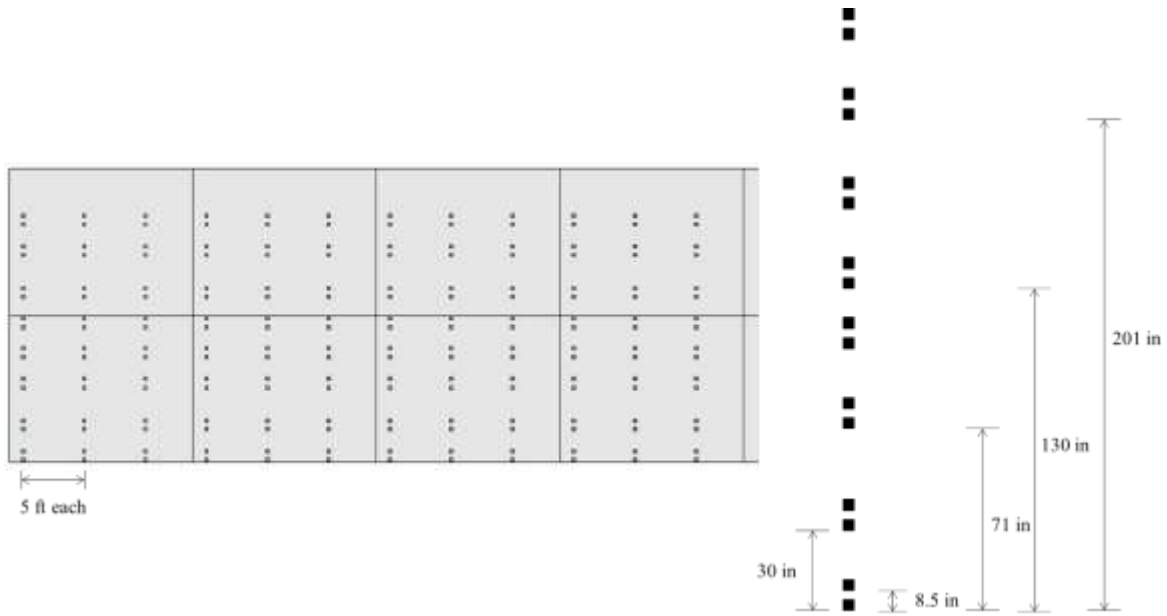

Figure 116: Continuous SL configuration, each slab is 15 ft x 15 ft
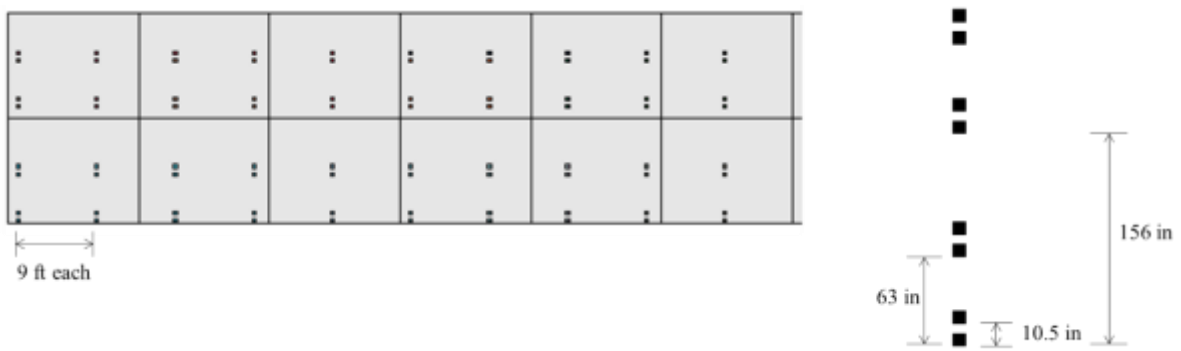

Figure 117: Single SL configuration, each slab is 15 ft x 15 ft
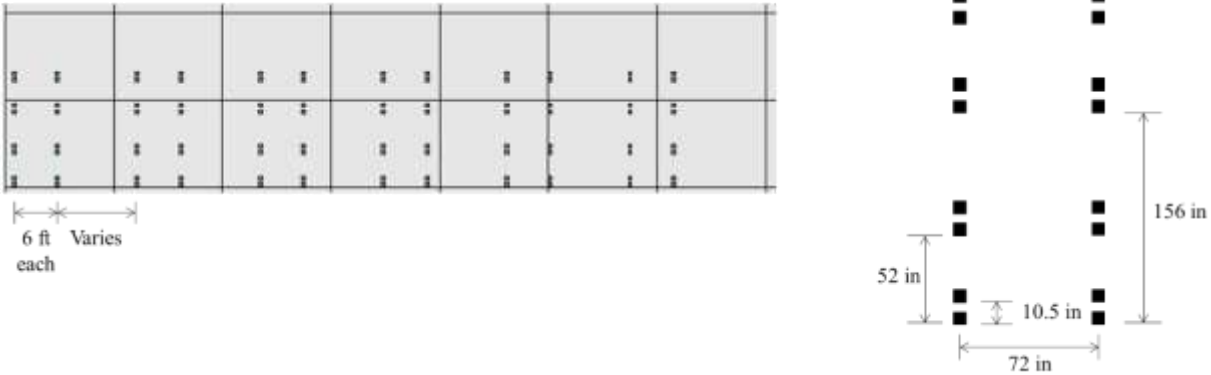
Figure 118: Tandem SL configuration, each slab is 15 ft x 15 ft

Table 33: Factorial analysis of SLs

SL category	Parameter	Units	Values in factorial analysis
Continuous, Single, and Tandem	Load Transfer Efficiency (LTE) of shoulders	%	0 (untied shoulders), 90 (tied shoulders)
Continuous, Single, and Tandem	PCC thickness	inches	8, 10, 13
Continuous, Single, and Tandem	Subgrade k-value	psi/in	100, 200, 350
Continuous, Single, and Tandem	Coefficient of thermal expansion	$\mu\varepsilon/°F$	4.5, 5.25, 6.0
Continuous, Single, and Tandem	Equivalent linear temperature gradient	°F/in	-3.0, -1.5, -1.0, -0.5, 0.0, 0.5, 1.0, 1.5, 3.0
Tandem	Axle spacing	feet	11, 13, 15
Continuous and Single	Axle load	kip	18, 22, 25
Tandem	Axle load	Kip	36, 43, 50

For each of the configurations shown in Table 33, fifteen stress analyses were performed using ISLAB by moving the SL 15 in along the roadway in 1-in increments. The results were used to define the corresponding critical stress pulse (for the maximum and minimum stresses in the slab) resulting from the SL. The analysis of these stress pulses and the development of a predictive model are discussed below.

14.3 Analysis of Stress Pulses

For each case in the factorial analysis, the stress pulse of the SL movement was developed. A stress pulse shows the history of the stress within the central 2 ft of the slab along the outer edge as the SL travels over it. While this can theoretically be constructed for any stress, for the present study,

two types of stress pulses were constructed, corresponding to the minimum and maximum stress within this region for each position of the SL as it traverses along the roadway. In this manner, two stress pulses were developed for each of the three SL types: one corresponding to the maximum mid-slab stress history, and the other to the minimum. An example stress pulse for Continuous, Single, and Tandem SLs is shown in Figure 119, Figure 120 and Figure 121, respectively.
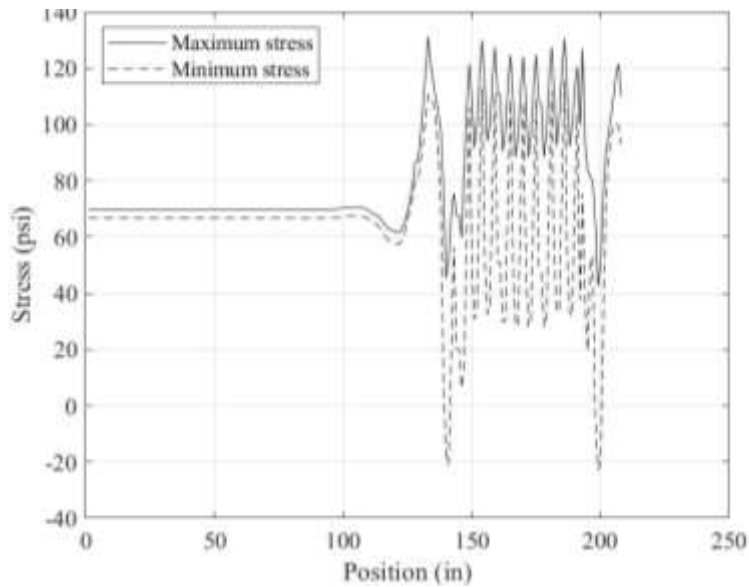

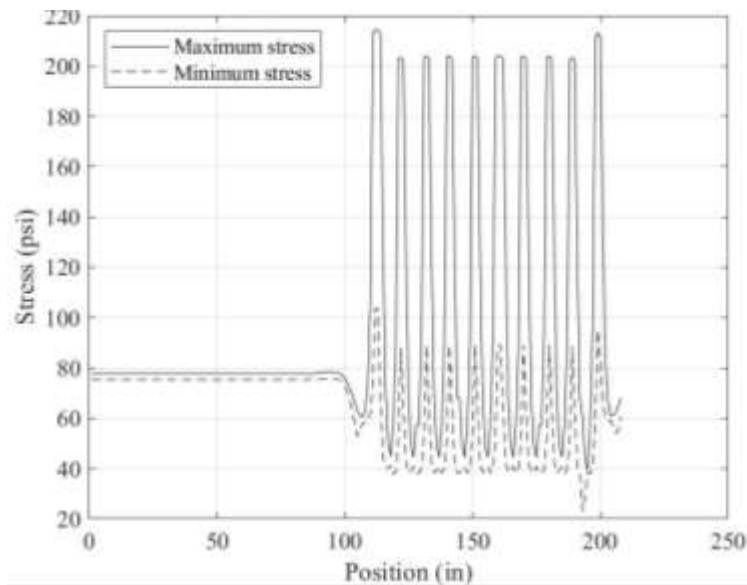Figure 119: Example stress pulse for a Continuous SL

Figure 120: Example stress pulse for a Single SL
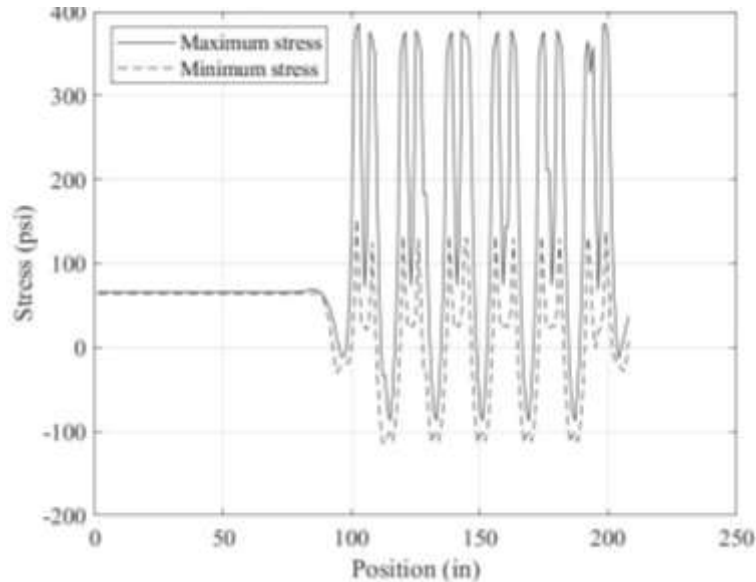
Figure 121: Example stress pulse for a Tandem SL

Several observations can be made regarding these stress pulses. First, for the Continuous SL, the magnitude of the stress is relatively small as compared to Single and Tandem SLs, and this was found to be generally true across all cases in the factorial analysis. Second, for the Single and Tandem SLs, the stress that developed as a result of the outermost axles (called the "end axles") was slightly different from that which developed from the inner axles (called the "mid axles"). Finally, each axle pulse consisted of a series of peak stresses corresponding to the maximum stress developed as each axle passed over the critical point in the JPCP. These peak stresses are key in analyzing the fatigue damage caused by one pass of the SL.

It may be recalled that fatigue damage is not a function of only stress, but the ratio of stress to strength, called the SR. Strength is typically measured in terms of the MOR. In PA, the typical 28-day pavement design MOR is 650 psi. Using this as a reference value, the strength development was estimated using the model incorporated into Pavement ME to estimate the early-age strength development for a mixture with a 28-day compressive strength of 650 psi (National Cooperative Highway Research Program Report 1-37A, 2004). This is shown in Figure 122. The concrete reaches an MOR of 700 psi in about 5 months, and it may generally be assumed that SLs will be driven only across JPCP pavements in PA that are older than that. Considering variability in strength, it was decided to use an MOR of 700 psi uniformly for the rest of the analysis for evaluating the SR for each stress level.

210
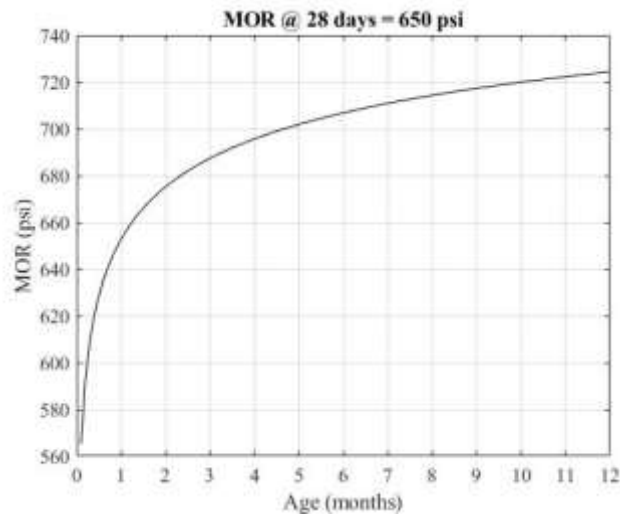
Figure 122: Development of concrete strength for a mix with 28-day MOR = 650 psi

It was determined that the SR for the Continuous SLs was always very low (less than 0.40). At such low SRs, it is generally understood that fatigue damage is not a concern and that an infinite number of load applications can be applied at these stress levels without concern. Therefore, Continuous SLs were removed from further consideration. For the Single and Tandem SLs, however, it was found that the SR could be higher (above 0.70) under certain conditions, for which a predictive model would have to be developed.

As a last step before developing a predictive model, the peak stresses generated by the end and mid axles from each stress pulse was evaluated. Since the factorial analysis was very large, this information was extracted using an automated algorithm implemented in MATLAB. An example of peak stresses identified for the Single and Tandem SLs is shown in Figure 123 and Figure 124, respectively. The algorithm generally does well, however some misidentified peaks are possible, especially for the mid axle peaks. To filter out these outliers, the median of the of the mid axle peaks was evaluated for each case, which is a more robust measure than the average. For the end axle peaks, the average was evaluated for each case. The focus of this investigation uses the maximum stress pulses depicted in the graphs above and not the minimum stress pulses. The minimum stress pulse was used to determine the minimum stress to be considered in the fatigue laboratory study and to ensure that large stress reversals did not occur.

211

In this way, a database was developed for each of the cases in the factorial analysis, containing the predicted mid and end axle peak stresses. This database was then used to develop a predictive model, as discussed below.
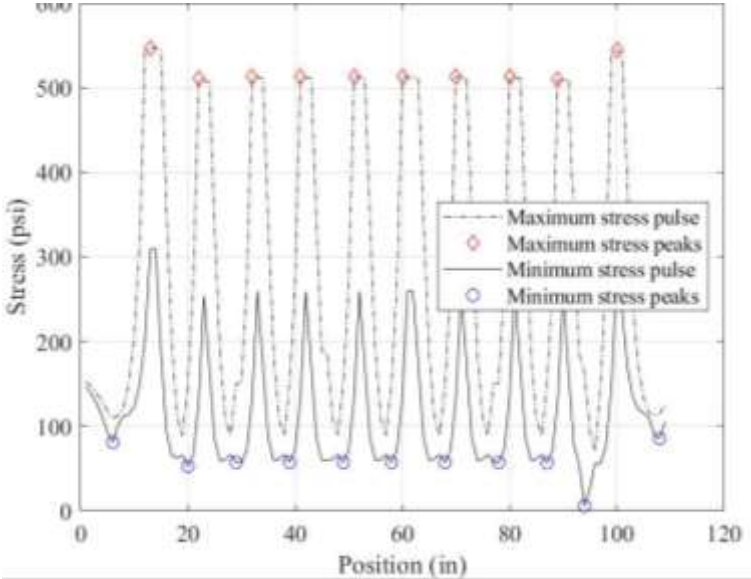
Figure 123: Example of peak stresses evaluated from a stress pulse from a Single SL
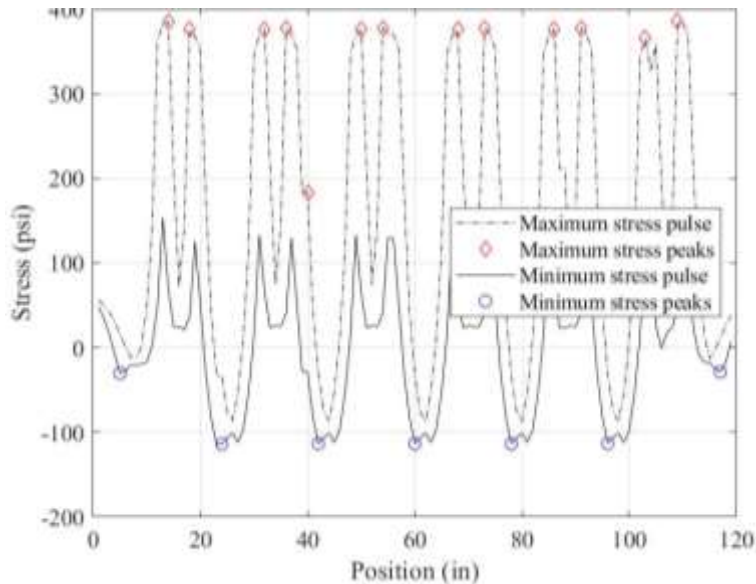
Figure 124: Example of peak stresses evaluated from a stress pulse from a Tandem SL

14.4 Model Development

A predictive model was developed that would relate seven predictors to the peak mid axle stress. These predictors are shown in Table 33: LTE, PCC thickness, temperature gradient, subgrade k-value, CTE, axle load, and axle spacing (axle spacing varied only for the Tandem SL). The predictive model chosen in this case is an Artificial Neural Network (ANN). In all, four ANNs were developed:

a) Single SL: an ANN to predict the maximum mid axle stress for a positive and a separate ANN for the negative temperature gradient condition. Separate ANNs were required since the position of the maximum stress for a positive gradient is at the bottom of the slab and at the top of the slab for a negative gradient.

b) Tandem SL: an ANN to predict the maximum mid axle stress for a positive and a separate ANN for the negative temperature gradient condition.

All the cases correspond to the axle placed adjacent to the outer edge of the pavement, which is the critical condition. Each ANN was trained using a 75/25 training/testing split using Bayesian regularization, meaning that 25% of the original dataset was randomly selected and not included for training the model. This data was used instead for model validation, as discussed below. It was found that an ANN with two hidden layers of eight neurons each gave the best overall

213

fit, while reducing the potential for overfitting. The goodness of fit (R^2 adj) on the training dataset is summarized in Table 34.

Table 34: Goodness of fit of ANNs within the training dataset

SL category	Sign of the Temperature Gradient	R^2 adj
Single	Positive	0.99
Single	Negative	0.99
Tandem	Positive	0.99
Tandem	Negative	0.99

14.4.1 Model Validation

Each of the four ANNs were validated using the 25% of the dataset not used in the training. Each of the four models were used to generate predicted results, which were then compared to the simulated results from ISLAB. Since the cases used for validation were not used to train the model, this analysis also evaluates the ability of each model to predict outside of the training set. The results for the validation are shown in Figure 125. These show that each model is performing adequately.
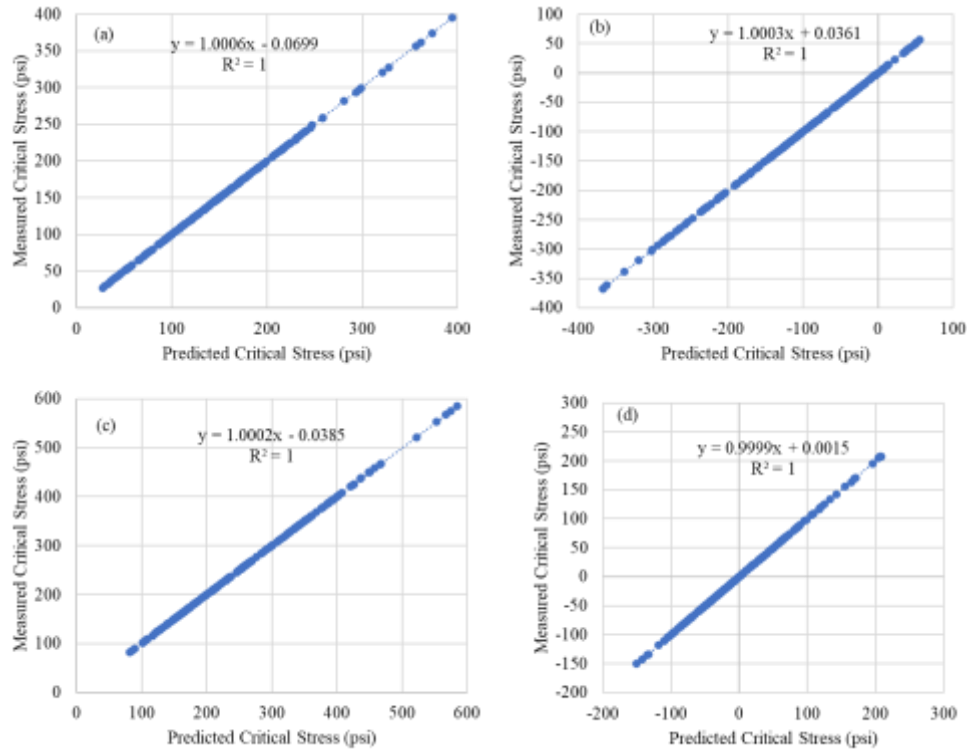
Figure 125: Model validation with testing dataset for Single SL with (a) negative and (b) positive temperature gradients, and for Tandem SL with (c) negative and (d) positive temperature gradients

14.4.2 Model Sensitivity

A sensitivity analysis was performed on each model to evaluate its ability to predict stress for cases outside of the training dataset. For example, each model was trained using PCC thicknesses of 8, 10, and 13 in, however, a well-performing model should be able to adequately predict stresses for 9 in pavements. An extensive sensitivity analysis on each input parameter was performed. To do so, one parameter was varied at small increments while all other parameters in the model was held constant. The predicted stresses were then evaluated to ensure the change in the predicted stress appeared adequate. This analysis also ensures that the model is not overly sensitive to a single parameter, which may not reflect the correct physical behavior.

The sensitivity plots are shown in Figure 126 and Figure 127. All four models displayed adequate prediction performance. If there was poor performance, it would be seen in non-physical discontinuities or spikes in predicted critical stresses, which is not seen in this case.
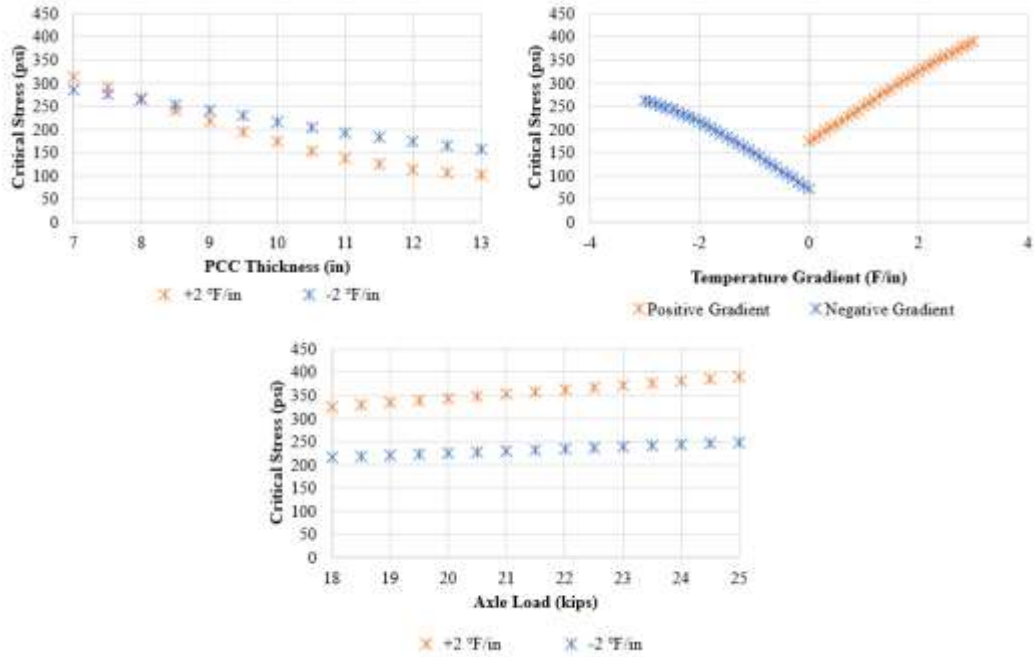
Figure 126: Example plots from the sensitivity analysis for Single SL for (a) PCC thickness, (b) temperature gradient for a 10-in thick slab, and (c) axle load for a 10-in thick
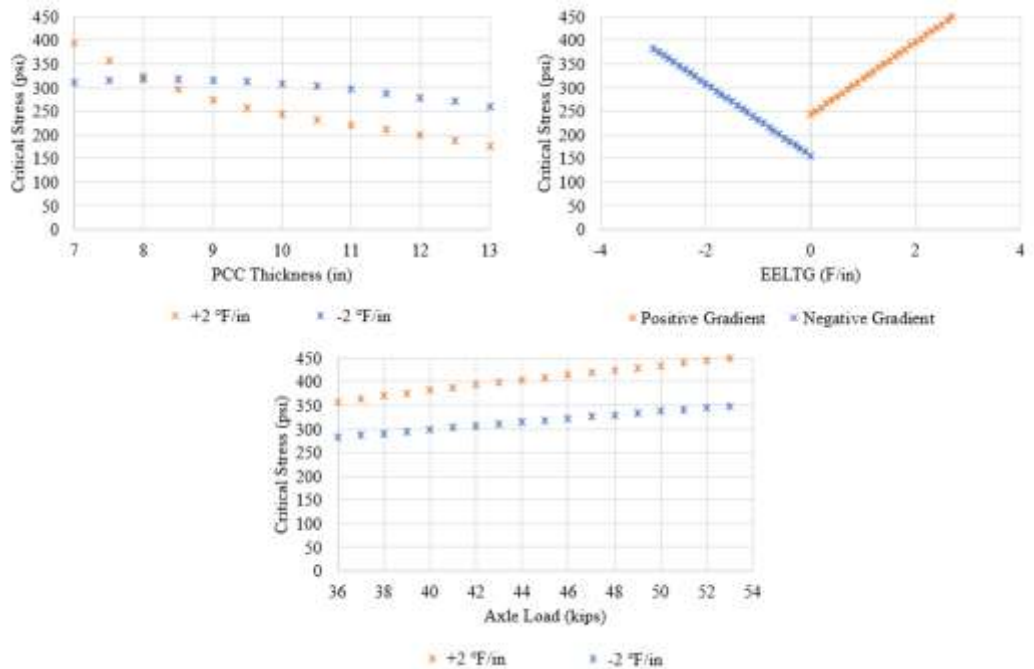
Figure 127: Example plots from the sensitivity analysis for the Tandem SL for (a) PCC thickness, (b) temperature gradient for a 10-in thick, and (c) axle load for a 10-in thick

14.4.3 End axle stresses

Using the ANNs, the mid axle stresses for each case can be predicted very accurately. In order to account for the slight variation in stress caused by the outermost or "end" axle, the difference between the mid and end axle stress was evaluated. It was found that on average, the end axle stress is higher than the mid axle stress by 5% for the Single SLs, and lower by 13% for Tandem SLs. This simple average was used to correct for end axle stresses, while developing guidelines and a predictive tool, as discussed below.

14.5 Guidelines for SLs

Using the ANNs discussed above as well as an MOR of 700 psi, the SR of each of the cases was evaluated. Most of the SRs were less than 0.40, indicating that fatigue damage from a single pass of the SL truck was not of concern. However, for a few cases, the SR exceeded 0.70, which might contribute to quantifiable damage. For those cases, the distribution of the values of the predictors are shown in Figure 128 and Figure 129 for Single and Tandem SLs, respectively. It may be noted that additional factorial points for the temperature gradient were added to obtain a finer distribution using the corresponding ANN. These values were verified by randomly comparing them with values from additional runs of ISLAB, and showed excellent agreement to within 1% in each case.

Figure 128: Frequency distribution of predictors for cases of Single SL where SR exceeded 0.70: a) LTE b) PCC thickness c) axle load d) subgrade k-value e) CTE and f) temperature gradient

Figure 129: Frequency distribution of predictors for cases of Tandem SL where SR exceeded 0.70: a) LTE b) PCC thickness c) axle load d) subgrade k-value e) CTE f) temperature gradient and g) axle spacing

From these results, the following conditions were identified as scenarios that might have a SR greater than 0.70:
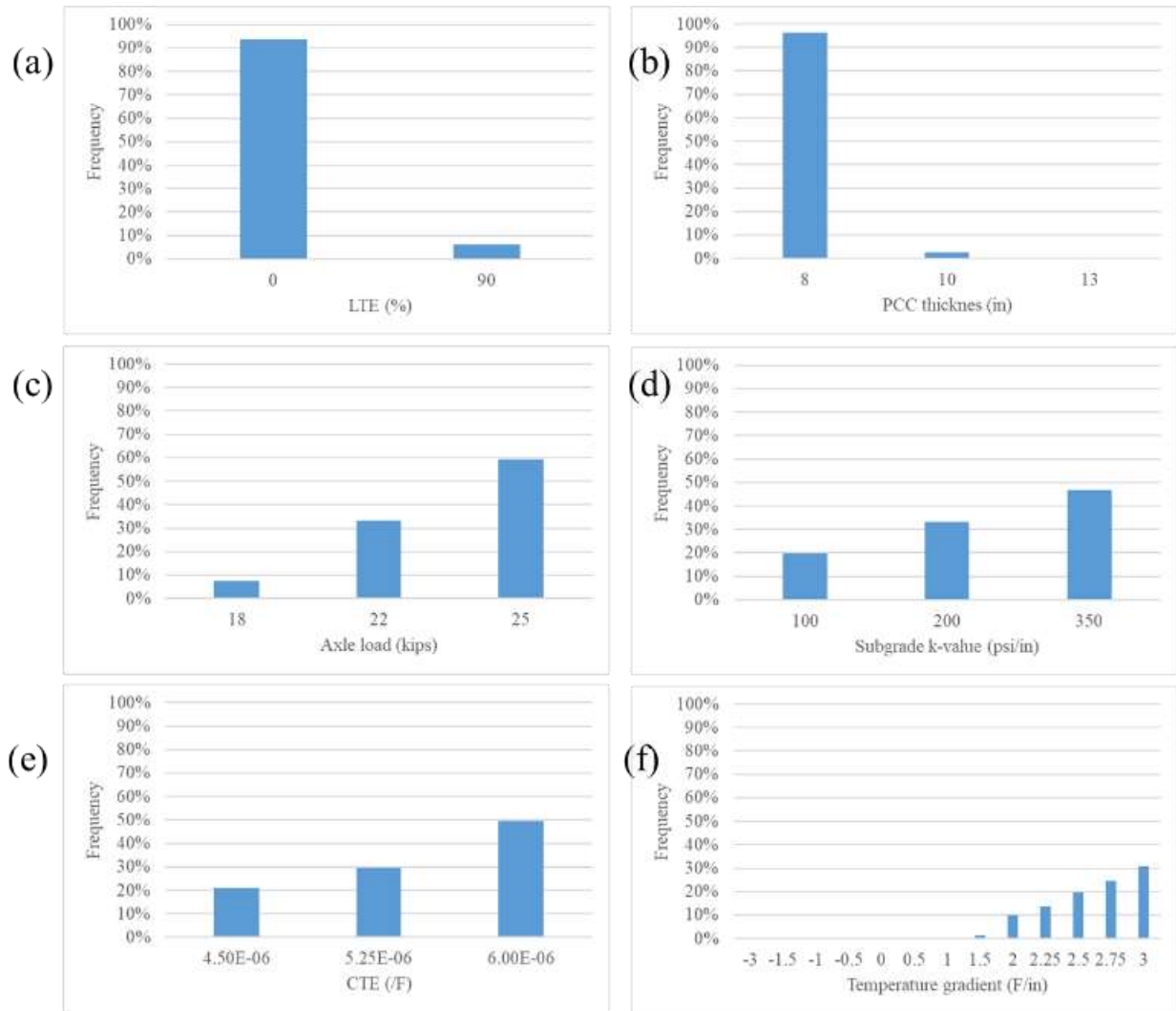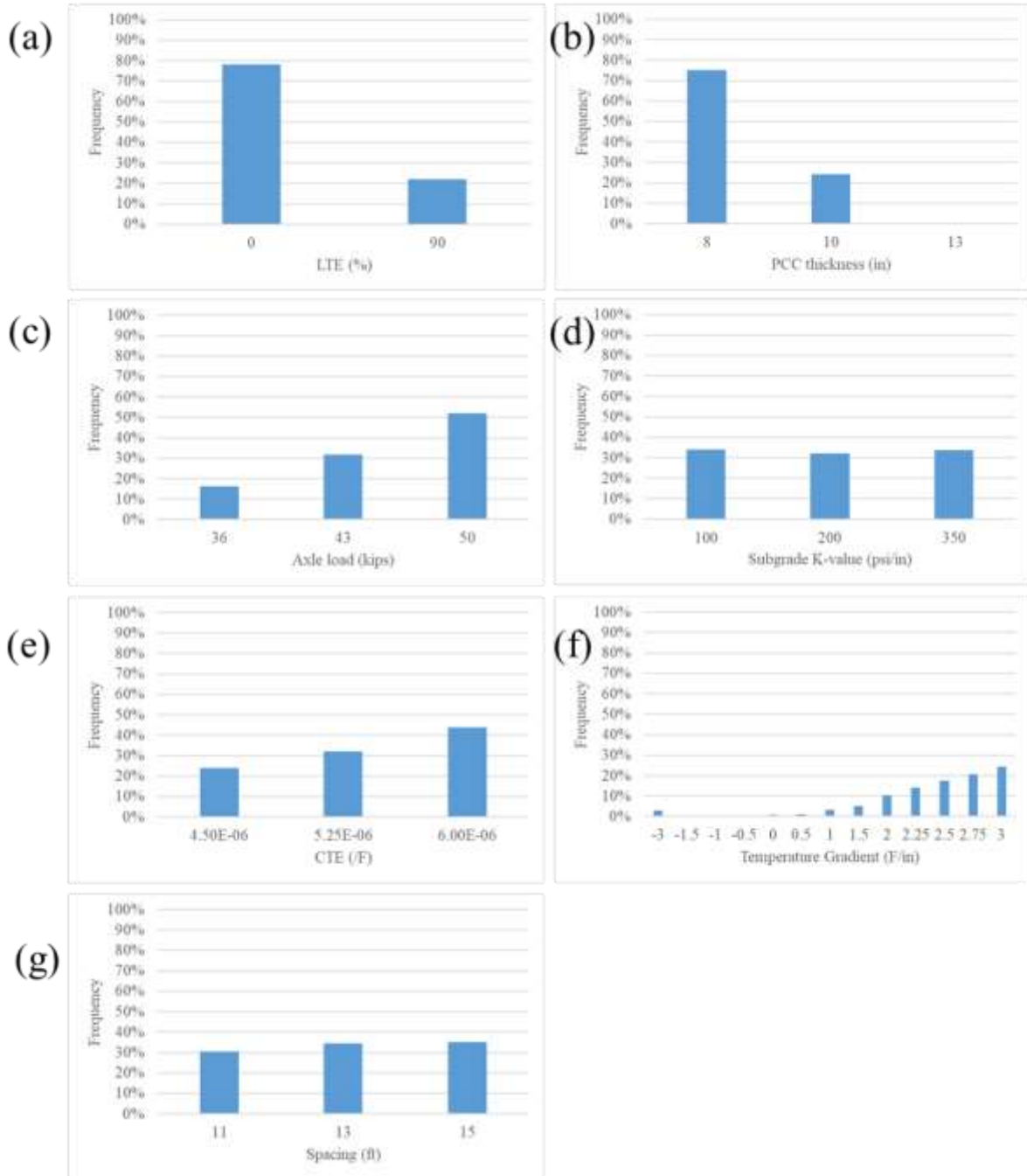
a) For Single SL: asphalt shoulders, PCC thickness of less than 10 in, axle load of 22 kips or greater, and temperature gradient greater than 2.5 °F/in.

b) For Tandem SL: asphalt shoulders, PCC thickness of less than 10 in, axle load of 36 kips or greater, and temperature gradient greater than 2.5 °F/in

All of the above information can be obtained from the SL permit submitted to PennDOT as well as information about the pavement structure along the desired route, except for the temperature gradient. The temperature gradient depends on the location, time, and pavement structure and is generally not known beforehand, although in general, peak positive gradients develop in the afternoon when the top of the slab is much warmer than the bottom. To develop a general guideline for peak positive temperature gradients in PA, the Enhanced Integrated Climatic Model (EICM) (Larson & Dempsey, Enhanced integrated climatic model Version 2.0, 1997) was used. The EICM is a one-dimensional analysis program that is part of Pavement ME, and which calculates the temperature profile for a given pavement at a given location using weather data corresponding to that location. The EICM was used to estimate the temperature profile that develops throughout the depth of an 8-in slab for each hour over a one-year period of time. This was performed for five locations spread across Pennsylvania (Pittsburgh, Erie, Scranton, Philadelphia, and Harrisburg). Using this data, the monthly probability of a temperature gradient exceeding 2.5 °F/in was evaluated, as shown in Table 35. It can be seen that April-August (spring and summer) are the main months of concern. During these months, the 11 am – 3 pm time frame was generally found to have the greatest probability of these high positive gradients. These high gradients only typically manifest for 15-30 minutes as the temperature profile changes over time.

Table 35: Monthly probability of temperature gradient exceeding 2.5 °F/in in PA for an 8-in JPCP

Month	Probability of temperature gradient exceeding 2.5 °F/in in PA
Jan	0.46%
Feb	0.18%
Mar	1.10%
Apr	8.50%
May	7.28%

Jun	10.11%
Jul	5.51%
Aug	4.65%
Sep	3.72%
Oct	1.81%
Nov	0.33%
Dec	0.00%

For any new SL permit, the pavement structure, axle configuration and loading, and time of the year and day can be compared to the preceding guidelines. If any of these conditions are within the critical conditions when SR may exceed 0.70, further analysis using the tool discussed in the next section is recommended. If not, no further action is necessary, as one pass of the SL would not pose a risk of significant fatigue damage to the JPCP.

14.6 Fatigue Damage Prediction Tool

In the preceding section, guidelines for when the SR may exceed 0.70 during a single pass of a SL truck (Single or Tandem) were presented. In these cases, fatigue damage is of significant concern and needs to be quantified. For this, the ANNs presented previously were programmed into a simple Excel tool (only for the positive temperature gradients, since negative gradients are never of concern). This tool – one each for Single and Tandem SLs – can be used to quantify the relative damage from one pass of the SL truck to one pass of a standard 18-kip single axle. The tool is described below.

14.6.1 User Inputs

The user inputs for Single and Tandem SLs in the tool are shown in Figure 130 and Figure 131, respectively, and can be found in the User Inputs tab of the respective spreadsheet. These inputs are the same as the predictors in Table 33, with the Tandem SL having one additional predictor (axle spacing) as compared to the Single SL. Additionally, the user also needs to specify the number of axle rows, which can be obtained from the drawings submitted as part of the permitting process, as well as the total number of SL trucks under consideration.

Inputs		
Superload:		
Axle load	22.931 kips	Value OK
Number of rows of single axles in SL	10	Value OK
Number of superload trucks	100	Value OK
Pavement Structure:		
PCC thickness	7 in	Value OK
Concrete thermal coef of expansion	5.50E-06 /F	Value OK
Temperature gradient in slab	2.5 F/in	Value OK
Transverse joint LTE	90 %	Value OK
Subgrade k-value	200 psi/in	Value OK

Figure 130: User inputs and typical values for predictive tool for Single SLs

Inputs		
Superload:		
Axle load	46.252 kips	Value OK
Number of rows of tandem axles in SL	4	Value OK
Spacing between tandem axles	14.08333 ft	Value OK
Number of superload trucks	100	Value OK
Pavement Structure:		
PCC thickness	7 in	Value OK
Concrete thermal coef of expansion	5.5E-06 /F	Value OK
Temperature gradient	2.5 F/in	Value OK
Transverse joint LTE	90 %	Value OK
Subgrade k-value	200 psi/in	Value OK

Figure 131: User inputs and typical values for predictive tool for Tandem SLs

The User Inputs tab also contain comments and value checks to ensure that the inputs are within the following range, over which the ANNs have been trained and tested:

a) LTE between 0 and 100%

b) PCC thickness between 7 and 14 in

c) Temperature gradient greater than 0 °F/in

d) k-value between 100 and 350 psi/in

e) Axle load between 36 and 50 kips for Tandem SLs and 18 and 25 kips for Single SLs

f) CTE between 4.5 and 6.0 $\mu\varepsilon/°F$

g) For Tandem SLs, axle spacing between 11 and 15 ft

h) The number of axle rows must be at least 3

Using these user inputs, the tool evaluates the predicted mid and end axle stresses using the corresponding ANN. Using a fixed MOR of 700 psi, SR is then computed and converted into an allowable number of load repetitions, N_f, using the Pavement ME model shown below (National Cooperative Highway Research Program Report 1-37A, 2004), which was also discussed previously in the literature review:

$$\log N_f = 2.0 \, SR^{-1.22} + 0.4371 \tag{63}$$

This is then converted into a fatigue damage FD as follows:

$$FD = \sum_{mid \; axles} \frac{n_{mid}}{N_f} + \sum_{end \; axles} \frac{n_{end}}{N_f} \tag{64}$$

where,

n = the number of mid or end axles as indicated by the subscript.

The outputs are reported in the Results tab, an example of which is shown in Figure 132. Two outputs are reported: the allowable number of axle repetitions for the SL truck before failure (defined as 50% fatigue cracking), percentage of fatigue life consumed, which is the ratio of the SL truck repetitions to the allowable number of repetitions.

For this superload truck:	
Allowable number of truck repetitions	2.57E+03
Actual number of truck repetitions	1.0E+02
Fatigue life consumed	3.9%

Figure 132: Example results in the Results tab of the tool

Thus, using this tool, a quantitative measure of damage can be obtained, and an appropriate permitting cost applied for the SL trucks for the critical conditions defined above.

14.7 Conclusion

In this report, three broad categories of SLs for which permits were pulled in Pennsylvania – Continuous, Single, and Tandem – were evaluated within a large factorial analysis using the finite element analysis program, ISLAB. It was found that the Continuous SLs are generally not a concern with respect to fatigue damage, but under certain conditions, the Single and Tandem SLs may be of concern. These might be of concern for thin (less than 10 in) PCC slabs, high axle loads as compared to standard axles, and temperature gradients that exceed 2.5 °F/in. Gradients of this magnitude can develop in the afternoon during the spring and summer months.

For these cases of concern, ANNs were developed to predict the stresses caused by one pass of a SL truck. This model was implemented into an Excel-based tool, which reports the allowable number of passes of the SL truck and the fatigue life consumed by a user-defined number of passes of the truck. This tool – one each for Single and Tandem SLs – can be used to quantify fatigue damage caused by these SLs.

15.0 GUIDELINES FOR CONCRETE PAVEMENTS CONSIDERING DAMAGE AT DOWELED JOINTS

15.1 Introduction

Repeated applications of heavy vehicle loads on rigid pavements with doweled joints have the potential to damage the concrete surrounding the dowel bar. This causes a reduction in the stiffness of the doweled joint. Due to the high loads and unique axle configurations, superloads (SLs) have the potential to induce significant damage with a relatively small number of vehicle passes. Below an evaluation of typical SL vehicles found in Pennsylvania was performed for the purpose of developing guidelines on the critical conditions under which significant dowel damage may be induced.

There are two main components within this section. The first portion is focused on establishing the stresses generated from a single application of a SL vehicle using a full-factorial finite element analysis. The second characterizes the implications of these stresses on the potential damage that could contribute to the development of faulting under repeated loading.

15.2 Analysis of Single Load Application

The concrete surrounding the dowel bar can become damaged when vehicle loads induce significant bearing stress, $\sigma_{bearing}$. These bearing stresses also depend on the load transferred across the shoulders (if any) and through aggregate interlock across the transverse joints. To evaluate the potential for damage to occur due to a single application of a SL vehicle, the critical bearing stresses generated by SL vehicles on a JPCP were evaluated and compared to a failure criteria established in the literature as well as criteria established based on the results of a laboratory study. First, a full factorial analysis was designed, which considers important pavement design features and SL configurations. A series of finite element analyses were performed to populate a database of critical bearing stresses based on this full factorial design. Lastly, these critical stresses were compared to failure criteria to identify critical conditions when damage in the vicinity of the dowel might occur.

15.2.1 Bearing Stress Calculation

A number of important design factors were considered for populating the database of dowel bearing stress. These included pavement thickness, shoulder type (tied or untied), dowel diameter,

presence or absence of aggregate interlock, modulus of subgrade reaction (k-value), modulus of dowel support (κ), concrete elastic modulus, axle type, axle load, and equivalent linear temperature gradient. The values considered for each factor is presented in Table 36.

Table 36: Range of parameters incorporated in the finite element analysis.

Parameter	Values
Truck Type	Standard 18-kip single axle, Superload
Axle Type	Single, Tandem
Axle Load (kip)	18, 22, 25 (Single)
	36, 43, 50 (Tandem)
PCC Thickness (in)	6, 8, 10, 13
Dowel Diameter (in)	1, 1.25, 1.5
Modulus of Dowel Reaction, κ (ksi/in)	500, 1500, 2000
Temp Gradient (F/in)	-3, -1.5, 0, 1.5, 3
k-value (psi/in)	100, 200, 350
Concrete Modulus (x10^6 psi)	4, 5, 6
Shoulder Load Transfer Efficiency (LTE) (%)	0 (untied), 90 (tied)
LTE by aggregate interlock across transverse joint (%)	0 (no interlock), 90 (interlock)

A finite element analysis was performed to calculate the critical bearing stress for each combination of the factors presented in Table 36. The concrete pavement-specific finite element software EverFE (Davids, 2003) was used to perform the analysis. EverFE was used selected because the software allows users to design unique axle configurations for static analyses. Additionally, dowels are explicitly modeled as separate elements interacting with the concrete slab through a spring interaction with a stiffness κ, and as a result the bearing stresses can be directly evaluated (Davids, 2003). Figure 133 depicts how the dowel interaction is modeled using EverFE, including springs with stiffness κ between the dowel and surrounding concrete.

For each case considered, a six-slab finite element model was analyzed as part of a JPCP, as shown in Figure 134. Each slab size was 12 x 15 ft, and they are discretized into 6 x 6 in elements in the horizontal direction and with two elements through the depth in the vertical direction. The slabs were assumed to be placed directly on a spring foundation, with the stiffness being specified using a modulus of subgrade reaction, or k-value. Figure 133 depicts how EverFE models the subgrade as a bed of springs (Winkler foundation) with a stiffness equal to k-value. To incorporate

tied shoulders, an additional row of slabs was added with 90% LTE across the longitudinal joint. For the transverse joint, aggregate interlock can be achieved by specifying a traction modulus k_{SB}, which was selected to achieve 90% LTE in the present study. This is generally achieved when the weighted average temperature of the pavement exceeds about 85°F, while below that, aggregate LTE can be assumed to be 0%. Both conditions were examined in this study.
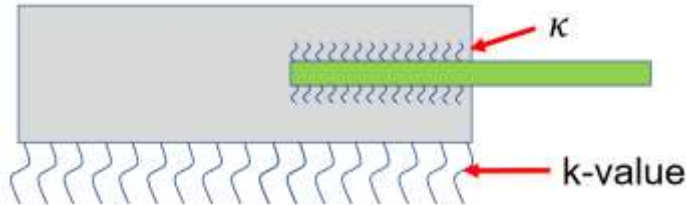

Figure 133: Cross-section graphic of a doweled pavement being modeled using κ and k-value for the dowel-concrete interaction and subgrade stiffness, respectively.

The outermost dowel in the driving lane is considered the critical dowel. Figure 134 indicates the critical dowel using a red arrow.
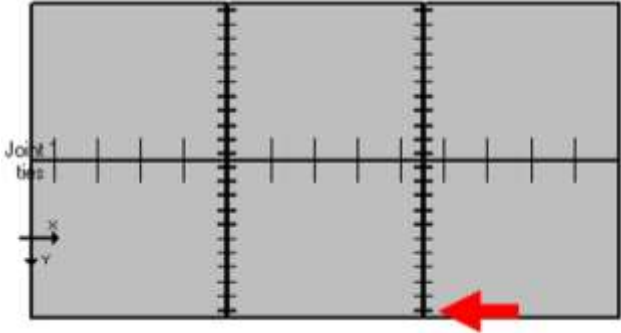

Figure 134: Six-slab model, with the critical dowel identified with red arrows.

Vehicle loads were modeled by placing the wheels of the axles adjacent to the transverse joint, with the outermost wheel being positioned directly above the critical dowel to simulate the position when the bearing stresses would be the highest for that dowel. A preliminary analysis indicated that axle loads placed greater than 40 in away from the critical dowel do not contribute to the bearing stress. The longitudinal spacing between the SL single axles is 9 ft (108 in), and so only one axle needed to be modeled at the joint. Transverse axle width and tire dimensions were

determined using the SL permits submitted to PennDOT. Figure 135 shows an example of a single and tandem axle SL, with the critical dowel identified in each case. Note that the axle is placed adjacent to the outer edge of the pavement, which is the critical condition.
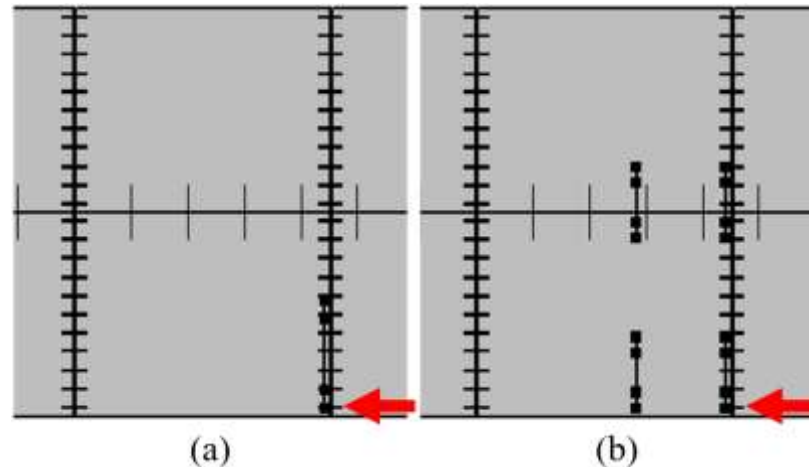

Figure 135: Layout of (a) single axle and (b) tandem axle SLs, with the critical dowel identified with red arrows.

Using the above factorial design and axle configurations, the critical bearing stresses were evaluated for each case. However, some cases that represented unrealistic designs – such as 6 in slabs with 1.5 in dowels, or 13 in slabs with 1 in dowels – were excluded from the final database and the following analysis. Consequently, the final set of cases evaluated had a higher fraction of slabs that were 8 in or 10 in thick, and 1.25 in diameter dowels.

15.2.2 Results

The database generated through the finite element analysis was used to evaluate the effect each parameter shown in Table 36 has on the magnitude of bearing stress between the dowel and the surrounding concrete. A cumulative probability density function (CDF) plot was generated for the resulting stresses separated by level of each factor.

Figure 136 shows the bearing stress distribution as a function of the κ used in the finite element analysis. It can be seen that κ effects the critical bearing stress, with average bearing stresses for each κ shown in Table 37. In general, bearing stress increases with κ and is always higher when the contribution of aggregate interlock is not considered. However, κ is not a well-established parameter, and a commonly used value of 1,500 ksi/in was selected based on the

literature (Friberg, 1938) (Marcus H. , 1951). Therefore, the remainder of the analysis of the results will focus on stresses for a κ equal to 1,500 ksi/in.
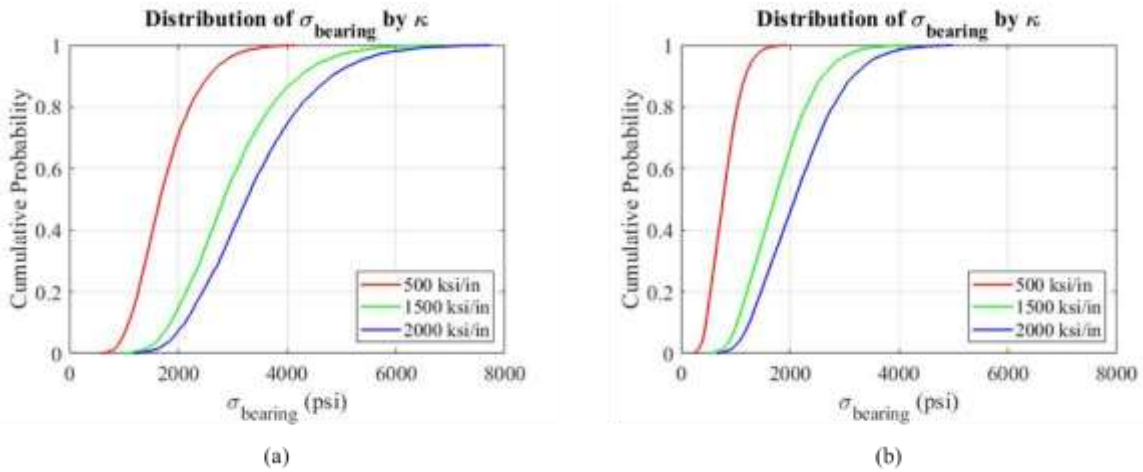

Figure 136: Cumulative distribution of bearing stress as a function of κ with (a) no aggregate interlock and (b) aggregate interlock.

Table 37: Average bearing stress for each κ considered in the finite element analysis.

κ, ksi/in	Average bearing stress, psi	
	No aggregate interlock	Aggregate interlock (LTE=90%)
500	2,070	960
1500	3,483	1,910
2000	3,902	2,080

The effect of dowel diameter was considered for only cases with κ is equal to 1,500 ksi/in, as shown in Figure 137. Increases in dowel diameter cause decreases in bearing stress. For example, 10% of cases with a dowel diameter equal to 1.0 in have bearing stresses greater than 5,000 psi without aggregate interlock, the same is true for less than 4% of cases when the dowel diameter is 1.25 in and less than 3% of the cases when the dowel diameter is 1.5 in. However, when the joints are locked and the load is transferred through aggregate interlock than the effect of dowel diameter is diminished.
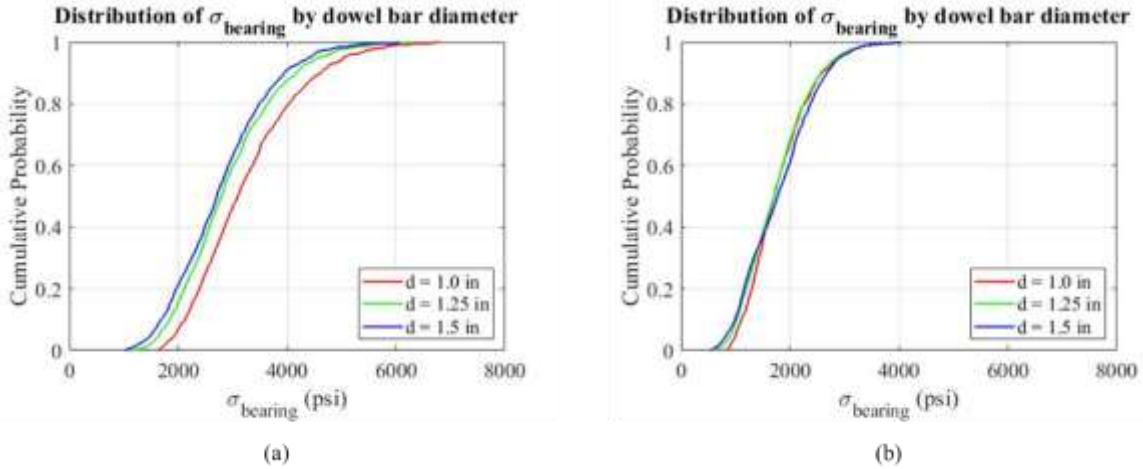
Figure 137: Cumulative distribution of bearing stress as a function of dowel diameter, d with (a) no aggregate interlock and (b) aggregate interlock (LTE=90%).

To examine the effect of pavement thickness h_{PCC} on bearing stress for each dowel diameter, Figure 138 through Figure 140 depict the CDF plots for bearing stress as a function of slab thickness for 1, 1.25, and 1.5 in dowels, respectively. While thinner pavement structures appear to result in lower bearing stress for 6 and 8 in pavements with 1 and 1.25-in diameter dowels, there appears to be no significant effect of pavement thickness on bearing stress for the thicker pavements. Increasing the amount of load transferred through aggregate interlock also reduces bearing stresses, as would be assumed.
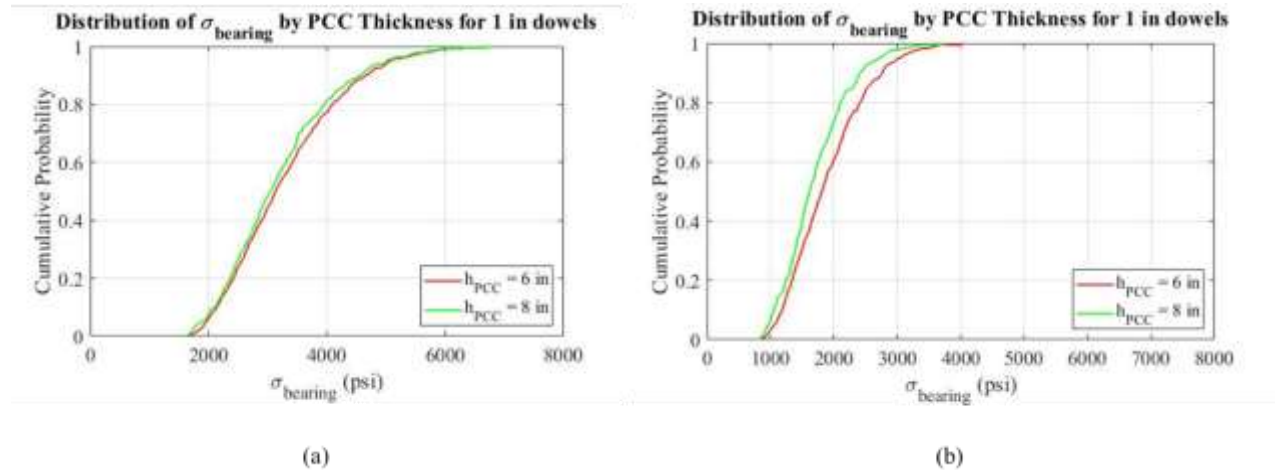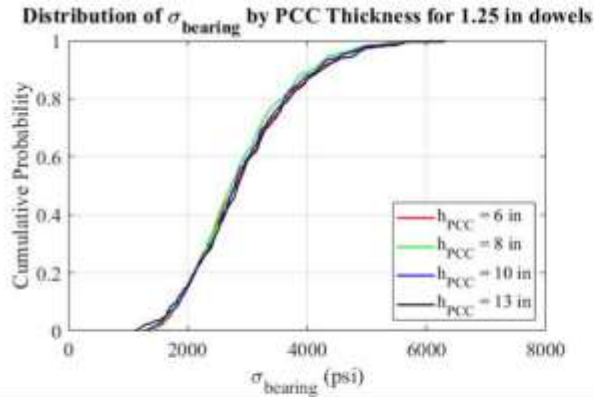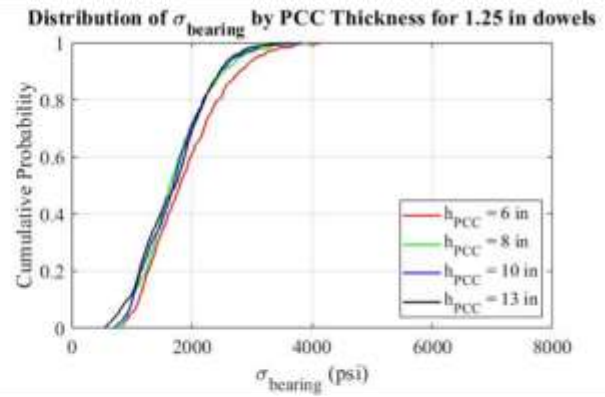

Figure 138: Cumulative distribution of bearing stress for 1 in diameter dowel as a function of pavement thickness with (a) no aggregate interlock and (b) aggregate interlock (LTE=90%).

Figure 139: Cumulative distribution of bearing stress for a 1.25 in diameter dowel as a function of pavement thickness with (a) no aggregate interlock and (b) aggregate interlock (LTE=90%).
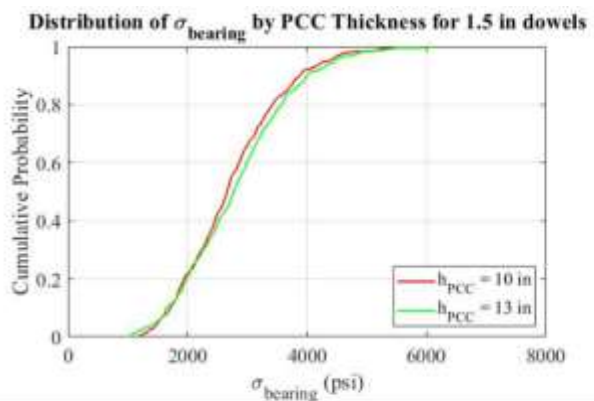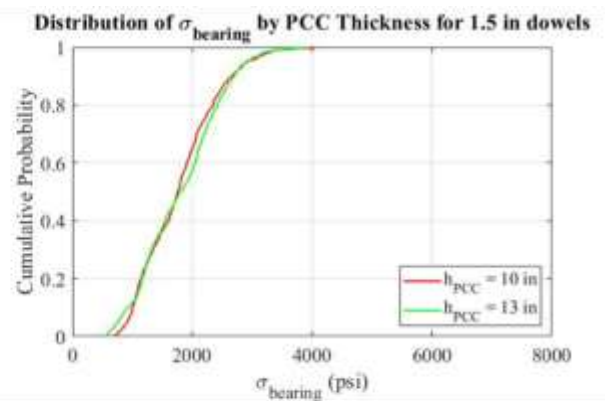
Figure 140: Cumulative distribution of bearing stress for a 1 in diameter dowel as a function of pavement thickness with (a) no aggregate interlock and (b) aggregate interlock (LTE=90%).

The CDF plot of bearing stress separated by equivalent linear temperature gradients is shown in Figure 141. High positive temperature gradients are shown to result in higher overall bearing stresses. This occurs because a positive temperature gradient causes the top surface of the slab to expand, resulting in a downward slab curvature. This curvature causes the top of the dowel to be pressed into the surrounding concrete, resulting in a higher bearing stress when subjected to vehicle loads.

231
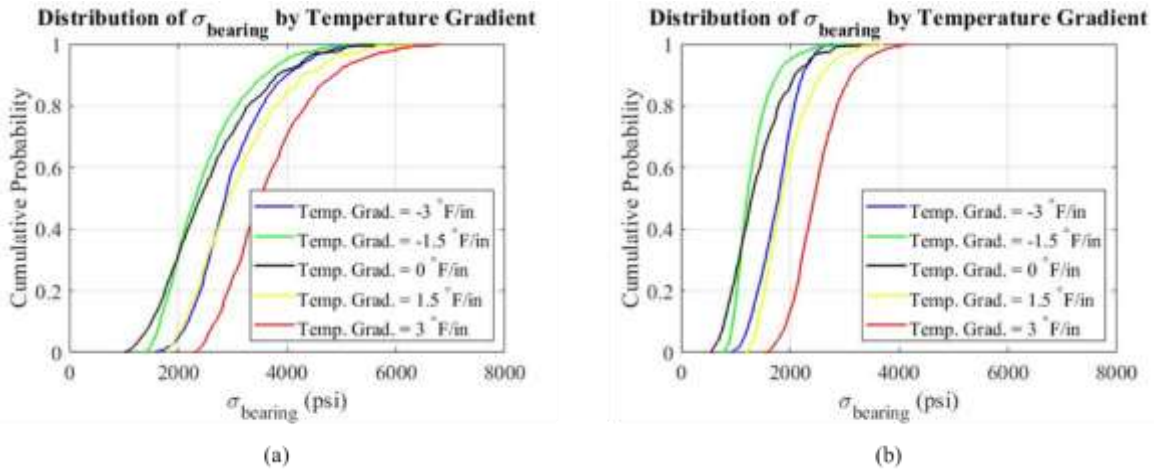
Figure 141: Cumulative distribution of bearing stress as a function of temperature gradient (Temp. Grad.) with (a) no aggregate interlock and (b) aggregate interlock (LTE=90%).

Figure 142 and Figure 143 show the CDF plots for bearing stress for the single axle and tandem axle SL, respectively, for a range of axle loads with and without load transfer through aggregate interlock. As expected, the cases with higher axle loads have higher bearing stresses. Additionally, cases with tandem axles have higher bearing stresses overall compared to cases with single axles, which can be seen by comparing 50th percentile bearing stresses for the highest magnitude of loading for each case from Figure 142 and Figure 143. For the 25-kip single axle SL, this is approximately 3,500 psi, whereas for the SL tandem axle with 50 kips, it is approximately 4,500 psi, both without aggregate interlock load transfer. When aggregate interlock load transfer is considered, the bearing stresses are still higher for higher loads, but the magnitude is smaller.
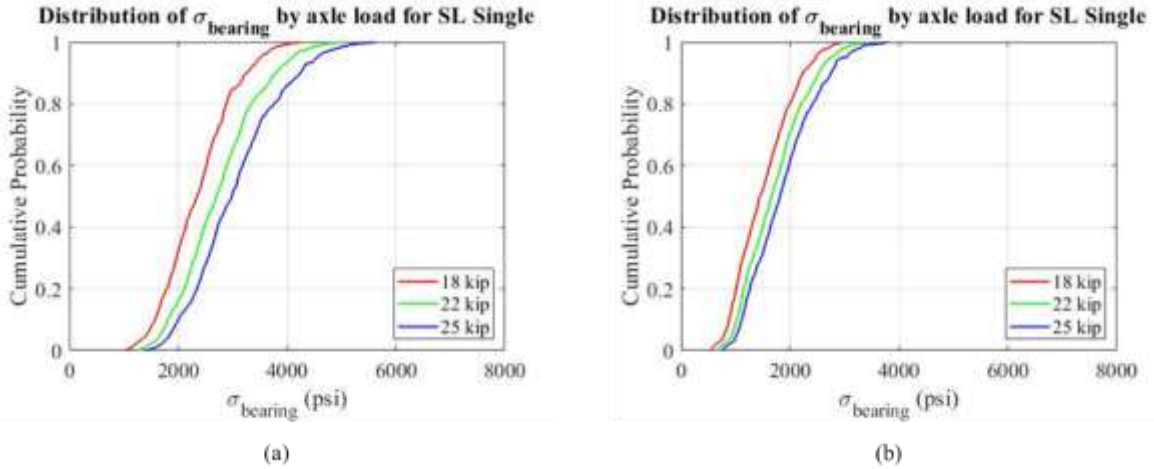
Figure 142: Cumulative distribution of SL single axle bearing stress as a function of axle load with (a) no aggregate interlock and (b) aggregate interlock (LTE=90%).
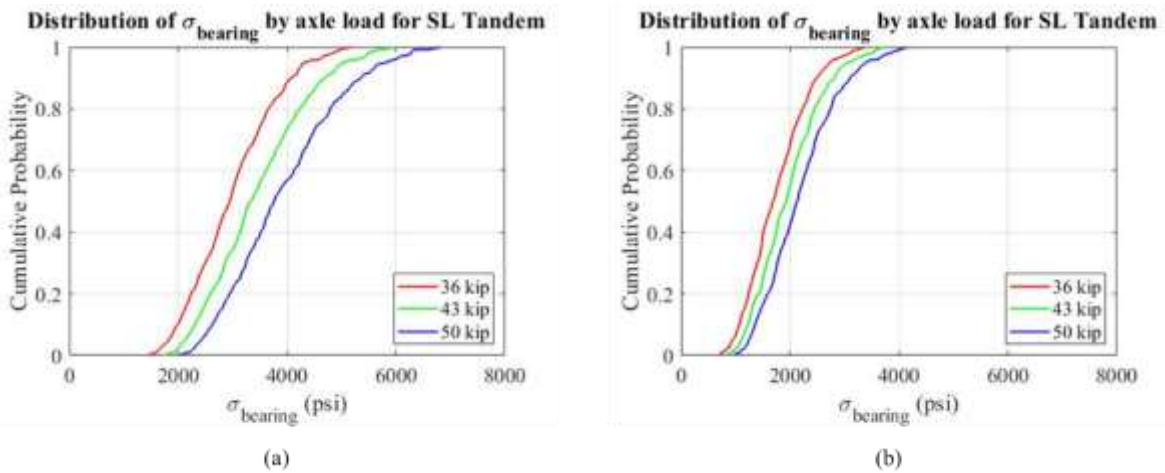
Figure 143: Cumulative distribution of SL tandem axle bearing stress as a function of axle load with (a) no aggregate interlock and (b) aggregate interlock (LTE=90%).

15.2.3 Failure Criteria

The critical bearing stresses determined through the finite element analysis were evaluated to assess the potential for damage to the concrete surrounding the dowel. For each dowel diameter, the allowable bearing stress was calculated using Equation 62, which was developed by ACI (Subcomittee III, 1956).

$$\sigma_{allow} = \frac{(4-d)}{3} f_c' \tag{65}$$

where,

233

σ_{allow} is the allowable bearing stress, psi,

d is the diameter of the dowel, in., and

f_c' is the compressive strength of the concrete, psi.

Assuming a typical concrete modulus of rupture of 700 psi, which corresponds to a compressive strength of 5,430 psi, the allowable bearing stresses were calculated as a function of dowel diameter. Table 38 presents the allowable bearing stress for each diameter.

Table 38: Allowable bearing stress calculated using Equation 1 for each dowel diameter considered.

Dowel diameter, in	Allowable bearing stress, psi
1	5,429
1.25	4,977
1.5	4,524

Based on the allowable bearing stress calculated in Equation 1, the results from the finite element analysis were evaluated to estimate the probability of a case exceeding the failure criteria. Figure 144 shows the distribution of bearing stress by dowel diameter with $\sigma_{allowable}$ for each dowel diameter identified with vertical lines. As shown, the majority of the cases for each dowel diameter do not exceed $\sigma_{allowable}$, with approximately 95%, 96%, and 94% of cases being under $\sigma_{allowable}$ for 1, 1.25, and 1.5 in diameter dowels, respectively, when load transfer through aggregate interlock was not considered. When load transfer through aggregate interlock was considered, none of the cases exceeds their respective thresholds.

Figure 144: Cumulative distribution of bearing stress as a function of dowel diameter, d, with $\sigma_{allowable}$ of each dowel diameter identified iwith the vertical lines with (a) no aggregate interlock and (b) aggregate interlock (LTE=90%).

Furthermore, the effect of tied and untied shoulders can also be examined with respect to the failure criteria. Figure 145 shows the distribution of bearing stresses by dowel diameter and shoulder type. It can be seen that none of the tied shoulder cases ever exceed the corresponding threshold. It can thus be established that the critical case for high bearing stresses is when there are untied shoulders and no load transfer occurs through aggregate interlock.
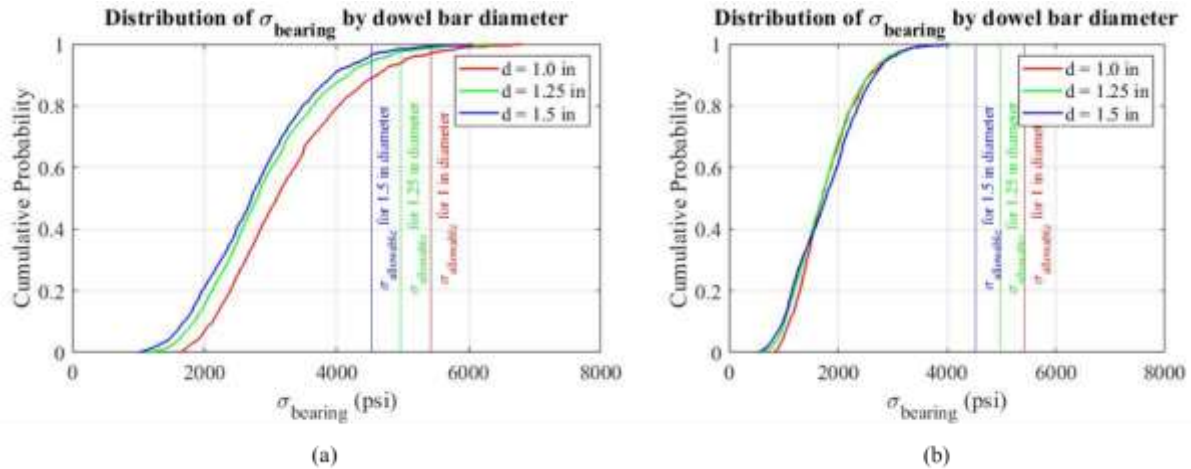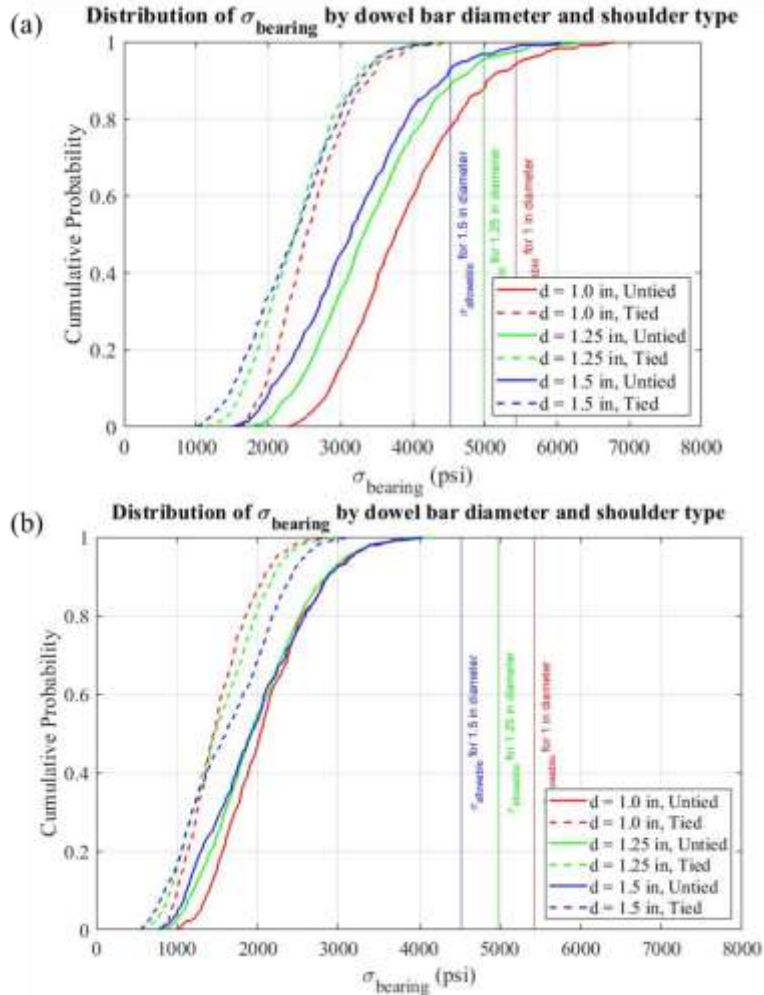
Figure 145: Cumulative distribution of bearing stress as a function of dowel diameter, d, and shoulder type with $\sigma_{allowable}$ of each dowel diameter identified iwith the vertical lines with (a) no aggregate interlock and (b) aggregate interlock (LTE=90%).

There are a limited number of cases that exceed $\sigma_{allowable}$, however, it is not well established how bearing stress magnitudes that exceed the $\sigma_{allowable}$ affect dowel performance. The laboratory study, described below, was performed to identify how repeated load applications cause an increase in the looseness of the dowel, which can then be related to performance.

15.3 Analysis of Repeated Load Applications

The accelerated load study for repeated applications of a SL and an 18-kip single axle was previously discussed in Section 9. Beam specimens were subjected to a high number of repeated load cycles, and looseness was measured at frequent intervals to quantify the effect key factors

have on the development of dowel looseness. Of the parameters examined, it was determined that vehicle load and concrete strength were critical parameters, which have an impact on the development of looseness. Results indicate that single load applications for these load magnitudes were not found to cause measurable increases in looseness.

15.3.1 Laboratory Results

All laboratory results were presented in Section 9. Select results are presented in the following section to illustrate the effect of key parameters on the development of looseness. The looseness measurements at 1,000 cycles were subtracted from the looseness measurements at subsequent intervals to eliminate the effect of the initial seating load.

The effect of the magnitude of the applied load is shown in Figure 146 and Figure 147 for 8- and 10-in beams, respectively. The strength of the concrete at the time of testing is provide in the legend, adjacent to the load magnitude applied to the dowel (Low load, LL; Medium load, ML; and High load (HL). In both cases, specimens tested with a HL, representative of a critical SL tandem axle application, display greater looseness over 2,000,000 load cycles when compared to specimens tested with a ML or LL load. The rate of the development of looseness is greater for the HL specimen when compared to the ML and LL specimens in the early load cycles (below 100,000). The earlier cycles of loading were the most critical, and the results indicate that the HL specimens accumulate more damage in this phase. It should be noted that all measured looseness was less than the 10 mils that has been historically considered critical and many load applications were required to generate looseness.
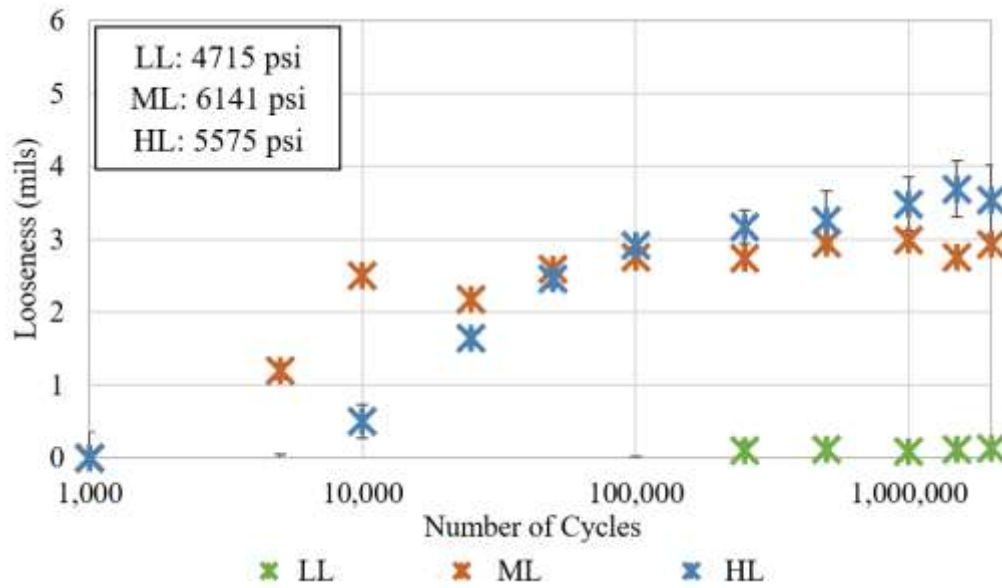
Figure 146: Effect of load magnitude on looseness development for 8 in beams and concrete compressive strength for each loading level indicated on the top left.
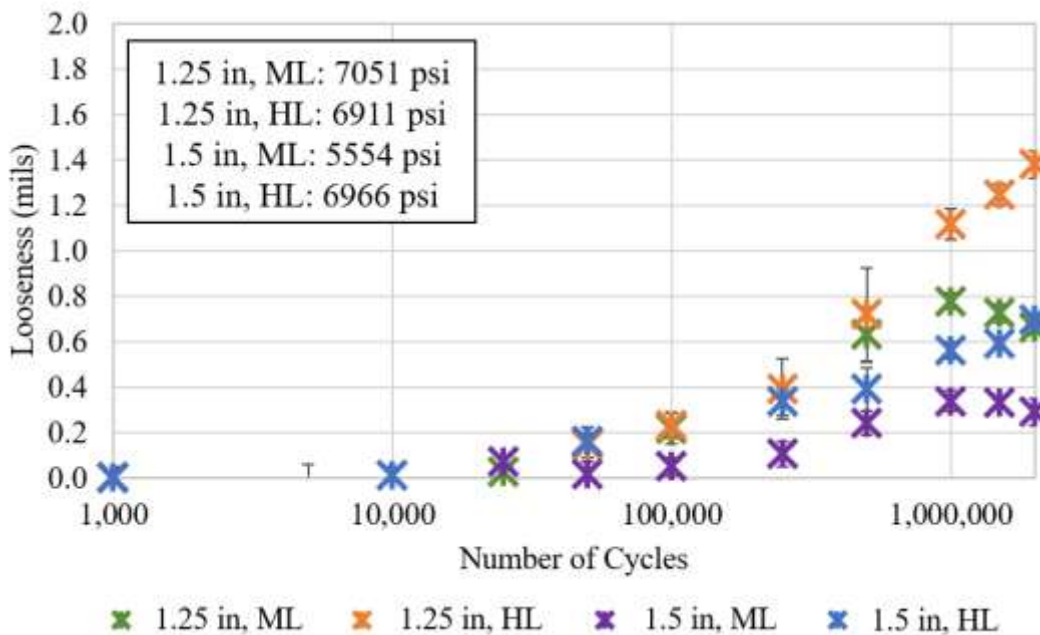
Figure 147: Effect of load magnitude on looseness development for 10 in beams with concrete compressive strength for each loading level indicated on the top left. (*NOTE: y-axis scale was changed to enhance the visibility of the effect of the parameters.*)

Concrete strength was identified as a significant factor in the development of looseness for the smaller diameter dowels and the 1.5-in diameter dowels with lower strength concrete. Strength

238

was classified as low, medium, or high based on the criteria shown in Table 39. As shown in Figure 148, 8-in beams were tested with 1.25 in dowels and a ML, and the only parameter which varied was the strength of the concrete. The effect of the concrete strength was significant, as the low strength specimen developed nearly twice as much looseness as the medium strength specimen after 250,000 load applications. The high strength specimen generated negligible looseness after 250,000 load applications.

Table 39: Range of concrete strengths evaluated in laboratory study.

Strength level	Concrete compressive strength (f'_c) range, psi
Low	$f'_c < 5000$
Medium	$5000 < f'_c < 6000$
High	$f'_c > 6000$
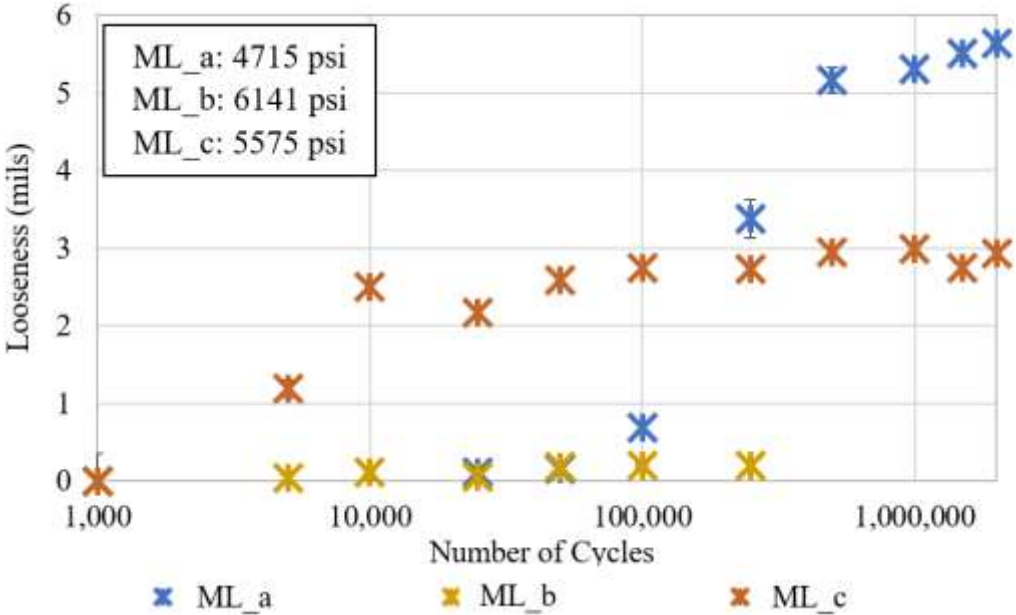
Figure 148: Effect of concrete strength on looseness development for 8 in. beams with 1.25-in diameter dowels.

15.3.2 Estimating Looseness Using Deflection

Looseness was measured in the lab by evaluating the change in deflection at the joint with increase in load. The relationships between maximum looseness and the commonly measured DD and LTE are shown in Figure 149 and Figure 150. Looseness is strongly correlated to DD, indicating that DD could be used to estimate the level of damage of the concrete around the dowel at a given

point. Looseness is similarly correlated to LTE; however, the correlation is much weaker at low LTEs.
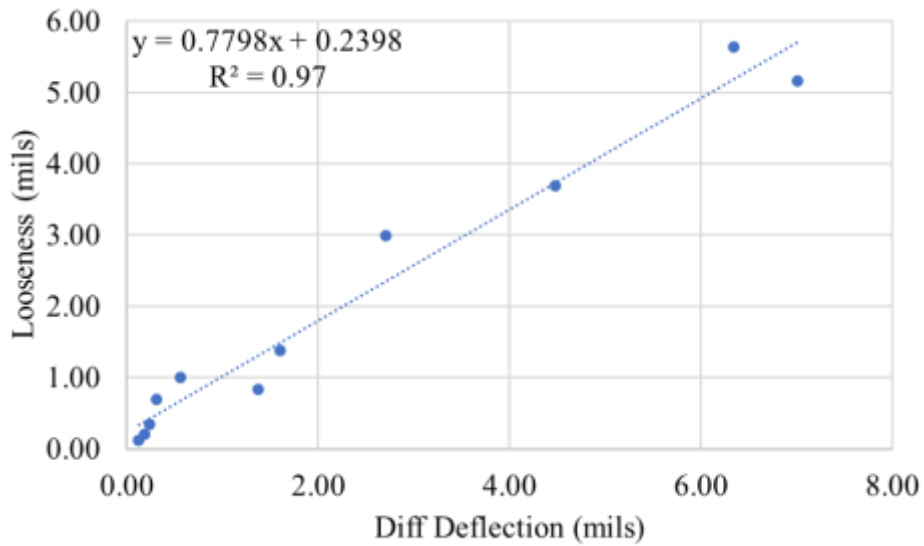
Figure 149: Looseness as a function of differential deflection.
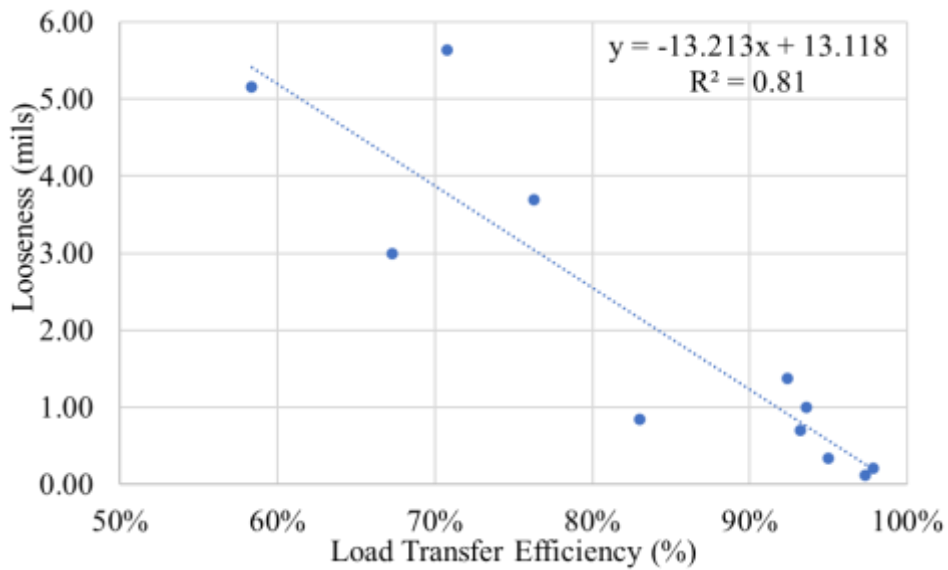
Figure 150: Looseness as a function of load transfer efficiency.

15.3.3 Summary

The laboratory results indicate that a low number of additional load applications (less than 1,000) result in minimal increase in looseness. The results from the laboratory indicate three critical

240

factors for the development of damage in the concrete surrounding the dowel over a high number of repeated loads:

a) Load magnitude: low loads (representative of an 18-kip single axle) were shown to generate minimal looseness over 2,000,000 load cycles. High loads (representative of a critical tandem SL) generated measurably higher looseness compared to both low and medium loads (representative of a standard tandem axle). Therefore, SLs with a higher axle load as compared to a standard axle have the potential to generate greater damage.

b) Concrete strength: High strength specimens ($f_c' > 6000$ psi) showed minimal looseness development over 250,000 load cycles compared to both medium ($5000 < f_c' < 6000$) and low strength mixes ($f_c' < 5000$ psi). Thus, lower strength concrete pavements (SL applied early in the pavement life) are more susceptible to greater damage under repeated SL applications.

c) Dowel diameter: Specimens 1.5-in diameter dowels generated lower looseness compared to specimens with 1.25-in diameter dowels with comparable strengths and loads over 2,000,000 cycles. Specimens with 1.25-in diameter dowels generated lower looseness compared to specimens with 1-in diameter dowels with comparable strengths and loads over 2,000,000 cycles. Therefore, larger diameter dowels are more effective at mitigating looseness, as was expected.

Looseness was correlated to DD and LTE, and it was observed that DD has a strong correlation to looseness at all ranges of looseness and can thus be used as a measure of looseness. Whereas LTE can be used as a predictor for looseness when LTE is high (typically for relatively new pavements) however, the correlation is weak at LTE values below 90% and should not be used in that case.

15.4 Analysis of Laboratory Bearing Stresses

A series of finite element models were used to quantify bearing stresses generated for the different cases investigated in the laboratory. The models were evaluated with various stiffness values of κ set for the interaction between the dowel and surrounding concrete.

The ABAQUS^{TM} model previously used to inform the laboratory setup was implemented in this analysis. A mesh convergence was performed to ensure the mesh was sufficiently fine for evaluating differential deflections between the loaded and unloaded faces of the joint and bearing stresses along the length of the dowel. An example model is shown in Figure 151.
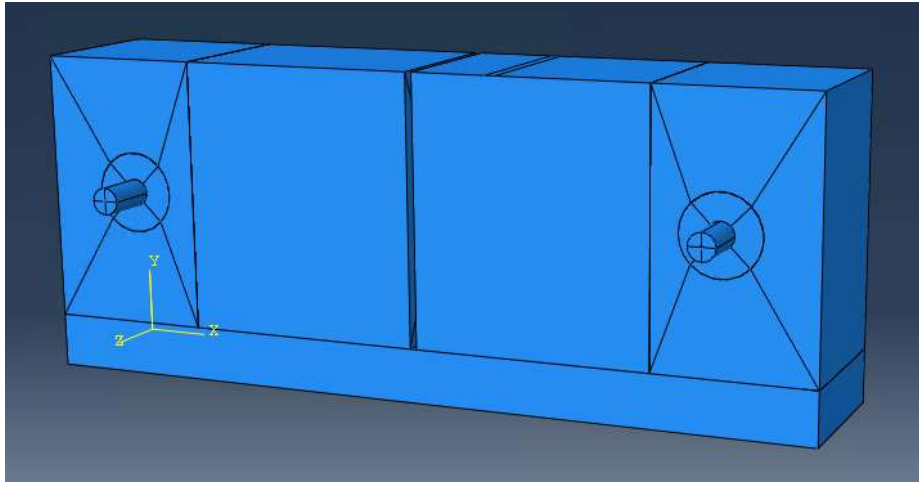
Figure 151: Beam model for a 10-in specimen

The following cases were evaluated with the beam model: 10-in beams with 1.25- and 1.5-in diameter dowels, and 8-in beams with 1.25-in diameter dowels. Each beam was evaluated with a medium load (ML) and high load (HL), which matched the loads used in the laboratory investigation. These loads were investigated because they showed appreciable damage (in the form of looseness). Table 40 shows the six models evaluated and their corresponding IDs.

Table 40: Models and corresponding parameters evaluated in the finite element analysis

Model ID	Beam Height, in	Dowel diameter, in	Load level
8B_125D_ML	8	1.25	Medium
8B_125D_HL	8	1.25	High
10B_125D_ML	10	1.5	Medium
10B_125D_HL	10	1.5	High
10B_150D_ML	10	1.5	Medium
10B_150D_HL	10	1.5	High

The spring interaction (κ) was specified between the dowel and the surrounding concrete. In the laboratory, κ is not directly known, so each finite element model was evaluated with various κ values ranging from 500 ksi/in to 3,500 ksi/in. The differential deflections and bearing stresses

were then identified for each finite element analysis. Figure 152 and Figure 153 show the differential deflections and maximum bearings stresses as functions of κ, respectively.
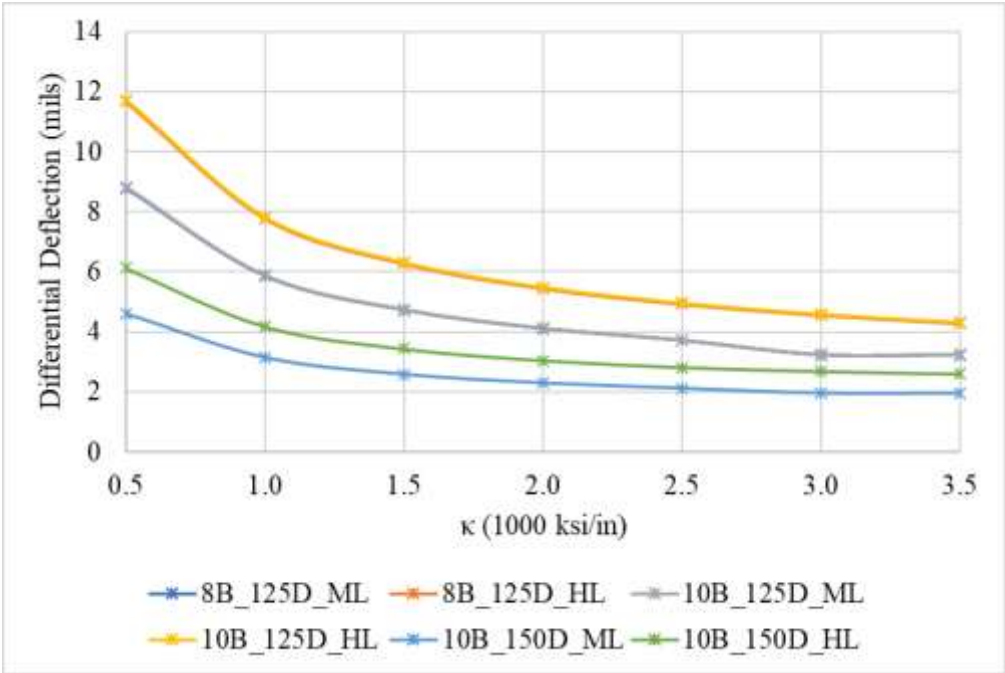
Figure 152: Finite element results for each beam case considered showing differential deflection as a function of κ
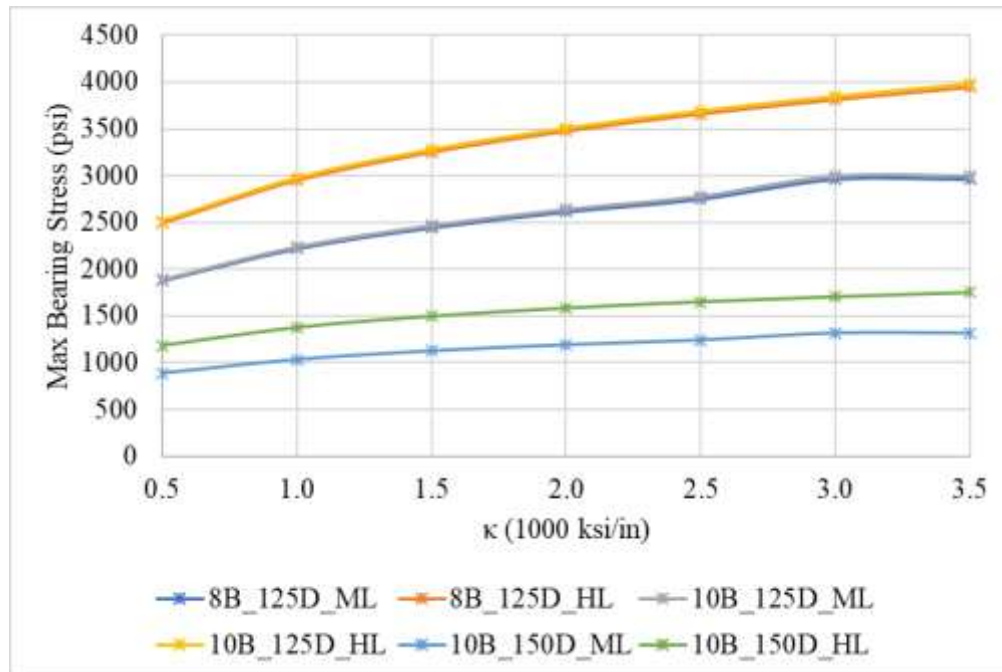
Figure 153: Finite element results for each beam case considered showing bearing stress as a function of κ

It can be seen that dowel diameter has a significant effect on the maximum bearing stress on the dowel. For the 10-in beam models, 1.5-in dowels showed a decrease in bearing stress of approximately 55% compared to the 1.25-in dowels, regardless of κ. These results also indicate the effect of applied load on bearing stress, as analyses with a high load generated bearing stresses approximately 33% greater than those with a medium load.

The finite element analysis shows that an increase in κ results in an increase in bearing stress and a decrease in differential deflection. κ is not directly measurable in a pavement structure, however, a value of 1,500 ksi is considered typical for a well-performing pavement structure. Maximum bearing stresses for the models evaluated at κ equal to 1,500 ksi are presented in Table 41.

Table 41: Maximum bearing stresses for each analysis when κ = 1,500 ksi

Model ID	Maximum bearing stress, psi
8B_125D_ML	2445
8B_125D_HL	3252
10B_125D_ML	2467

244

10B_125D_HL	3280
10B_150D_ML	1126
10B_150D_HL	1497

As shown in Table 38, the allowable bearing stresses for dowels with 1.25-in and 1.5-in diameters are equal to 4,977 and 4,524 psi, respectively. The bearing stresses generated in the laboratory investigation for typical load levels are far below the allowable bearing stress threshold, which indicates that there is low risk for failure at the joint with single passes of a SL vehicle. The corresponding dowel looseness results support the claim that single SL applications do not cause measurable damage, as increases in looseness is only achieved by thousands of load applications.

15.5 Guidelines
A finite element analysis was performed to identify critical cases, which result in high bearing stress between the dowel and surrounding concrete. Of the scenarios which resulted in high bearing stress, the following conditions were observed to be critical:

a) High positive temperature gradients;
b) Smaller diameter dowels; and
c) High vehicle loading.

Upon analysis of these results, it was observed that the majority of these cases were below an allowable bearing stress threshold. The laboratory study was performed to quantify the increase in looseness that develops with repeated load applications. The laboratory results indicated that the following conditions resulted in the development in a greater amount of looseness:

a) High load magnitude;
b) Low concrete strength; and
c) Low dowel diameter.

Although several specimens did exhibit significant increases in looseness due to repeated load applications, in no case did a single application of a load result in a measurable increase in

looseness. In order to observe any increase in looseness, at least 1,000 repetitions of the SL would need to be applied to the pavement structure when a critical range of conditions are present.

BIBLIOGRAPHY

AASHTO. (1993). *AASHTO Guide for Design of Pavement Structures, 1993.* Washington, DC: AASHTO.

AASHTO. (2008). Mechanistic-Empirical Pavement Design Guide, Interim Edition: A Manual of Practice. Washington, DC.: AASHTO.

Aas-Jakobsen, K. (1970). *Fatigue of concrete beams and columns.* Division of Concrete Structures, Norwegian Institute of Technology, University of Trondheim.

ABAQUS. (2011). ABAQUS Theory Manual (6.11).

ACI. (2008). *Guide for the Design and Construction of Concrete Parking Lots.* Farmington Hills, MI: American Concrete Institute Committee 330.

ACI Committee 325, S. I. (1956). Structural Design Considerations for Pavement Joints. *Journal of The American Concrete Institute, 53*, 1-28.

Adams, T., Perry, E., Schwartz, A., Gollnik, B., Kang, M., Bittner, J., & Wagner, S. (2013). *Aligning Oversize/Overweight Fees with Agency Costs: Critical Issues.* Madison, WI: Wisconsin Dot.

Ali, H. A., & Tayabji, S. D. (2000). Using transverse profile data to compute plastic deformation parameters for asphalt concrete pavements. *Transportation Research Record, 1716(1)*, 89-97.

Alland, K. (2018). *Analyzing Falling Weight Deflectometer Data on Curled and Warped Concrete Slabs.* Pittsburgh, PA: University of Pittsburgh.

Allen, D., & Deen, R. (1986). A computerized analysis of rutting behavior of flexible pavement. *Transportation Research Record, 1095*, 1 - 10.

Alliche, A. (2004). Damage model for fatigue loading of concrete. *International Journal of Fatigue, 26(9)*, 915-921.

Applied Research Associates (ARA), I. (2004). *Guide for Mechanistic–Empirical Design of New and Rehabilitated Pavement Structures.* Washington, D.C.: Transportation Research Board of the National Academies.

Asphalt Institute. (1982). *Research and Development of the Asphalt Institute's Thickness Design Manual.* Lexington, KY: Asphalt Institute.

Bai, Y., Schrock, S. D., Mulinazzi, T. E., Hou, W., Liu, C., & Firman, U. (2010). *Estimating highway pavement damage costs attributed to truck traffic.* Lincoln, NE: Mid-America Transportation Center.

Baladi, G. (1989). Fatigue life and permanent deformation characteristics of asphalt concrete mixes. *Transportation Research Record, 1227*, 75-86.

Ballinger, C. A. (1971). Cumulative fatigue damage characteristics of plain concrete. *Highway Research Record, 370*, 48-60.

Batioja-Alvarez, D. D., Kazemi, S. F., Hajj, E. Y., Siddharthan, R. V., & Hand, A. J. (2018). Probabilistic Mechanistic-Based Pavement Damage Costs for Multitrip Overweight Vehicles. *Journal of Transportation Engineering, Part B: Pavements, 144(2)*.

Bonnaure, F., Gravois, A., & Udron, J. (1980). A new method for predicting the fatigue life of bituminous mixes. *Association of Asphalt Paving Technologists Proceedings*, (pp. 499-529).

Brink, W., Wilke, P., Darter, M., & Von Quintus, H. L. (2020). *PennDOT Pavement ME Design User Input Guide.* Harrisburg, PA: Pennsylvania Department of Transportation.

Buch, N., & Zollinger, D. (1996). Development of dowel looseness prediction model for jointed concrete pavements. *Transportation Research Record, 1525*, 21-27.

Burmister, D. M. (1945). The general theory of stresses and displacements in layered systems. I. *Journal of applied physics, 16(2)*, 89-94.

C192/C192M-21, A. (2019). *Standard Practice for Making and Curing Concrete Test Specimens in the Laboratory.* West Conshohocken, PA: ASTM International.

C39/C39M-21, A. (2021). *Standard Test Method for Compressive Strength of Cylindrical Concrete Specimens.* West Conshohocken, PA: ASTM International.

C469/C469M-14, A. (2014). *Standard Test Method for Static Modulus of Elasticity and Poisson's Ratio of Concrete in Compression.* West Conshohocken, PA: ASTM International.

C617/C617M-15, A. (2015). *Standard Practice for Capping Cylindrical concrete Specimens.* West Conshohocken, PA: ASTM International.

Campbell, S., Swearingen, K. C., Honefanger, J. G., Keller, T., Ray, D., Humphrey, D., . . . Varner, S. (2009). Impacts of Permitted Trucking on Ohio's Transportation System and Economy.

Chatti, K., Manik, A., Salama, H., Brake, N., Haider, S. W., Mohtar, C. E., & Lee, H. S. (2009). *Effect of Michigan Multi-axle Trucks on Pavement Distress (Volume III).* East Lansing, Michigan: Michigan Department of Transportation.

Chen, D. H., Fernando, E., & Murphy, M. (1996). Application of falling weight deflectometer data for analysis of superheavy loads. *Transportation research record, 1540*, 83-90.

Chen, X., Lambert, J. R., Tsai, C., & Zhang, Z. (2013). Evaluation of Super Heavy Load Movement on Flexible Pavements. *International Journal of Pavement Engineering*, 440–448.

Ciolko, A., Nussbaum, P., & Colley, B. (1979). *Load Transfer of Dowel Bars and Star Lugs.* Skokie, Illinois: Construction Technology Laboratories.

Claessen, A. I., Edwards, J. M., Sommer, P., & Uge, P. (1977). Asphalt Pavement Design--The Shell Method. *Proceedings of 4th International Conference on Structural Design of Asphalt Pavements (Volume I)* . Ann Arbor, Michigan.

Cornelissen, H. A. (1984). Fatigue failure of concrete in tension. *HERON, 29(4)*, 1-68.

Correia, J. P., & Branco, F. A. (2006). New methodology: Permit checking of vehicular overloads. *Journal of Bridge Engineering, 11*(3), 274-281.

Darter, M. I. (1977). *Design of a Zero-maintenance Plain Jointed Concrete Pavement, Volume One-Development of Design Procedures.* Washington, D.C.: Federal Highway Administration.

Das, B. M. (2011). *Geotechnical Engineering Handbook.* Ft Lauderdale, FL: J Ross Publishing, Inc.

Davids, W. (2003). EverFE Theory Manual, Version 2.24.

De Jong, D. L., Peutz, M. G., & Korswagen, A. R. (1979). *Computer program BISAR, layered systems under normal and tangential surface loads.* External Rep. No. AMSR, 6.

Domenichini, L., & Marchionna, A. (1981). Influence of stress range on plain concrete pavement fatigue design. Proceedings of the 2nd International Conference on Concrete Pavement Design. (pp. 55-65). West Lafayette, Indiana: Purdue University.

FHWA. (2000). *Addendum to the 1997 federal highway cost allocation study final report.* Washington. D.C.

FHWA, & DOT. (2016). *Pavement Comparative Analysis Technical Report.*

FHWA, & DOT. (2018). US Code of Federal Regulations, Title 23, Part 658.17. Federal Register.

FHWA; DOT. (1998). *Final Report on the Federal Highway Cost Allocation Study. Federal Highway Cost Allocation Study, 1997.* Washington. D.C.

Finn, F., Saraf, C., Kulkarni, R., Nair, K., Smith, W., & Abdullah, A. (1977). The use of distress prediction subsystems for the design of pavement structures. *Proceedings of 4th International Conference on Structural Design of Asphalt Pavements (Volume I).* Ann Arbor, MI.

Fiorillo, G., & Ghosn, M. (2014). Procedure for Statistical Categorization of Overweight Vehicles in a WIM Database. *Journal of Transportation Engineering*.

Friberg, B. (1938). Design of Dowels in Transverse Joints of Concrete Pavements. *64*(9).

Gaedicke, C., Roesler, J., & Shah, S. (2009). Fatigue crack growth prediction in concrete slabs. *International Journal of Fatigue, 31(8-9)*, 1309-1317.

Ghosn, M., Fiorillo, G., Gayovyy, V., Getso, T., Ahmed, S., & Parker, N. (2015). *Effects of Overweight Vehicles on New York State DOT Infrastructure.*

Hajj, E. Y., Siddharthan, R. V., Nabizadeh, H., Elfass, S., Nimeri, M., Kazemi, F. S., . . . Piratheepan, M. (2018). *Analysis Procedures for Evaluating Superheavy Load Movement on Flexible Pavements, Volume I: Final Report.* Reno, NV: University of Nevada.

Harichandran, R. S., Yeh, M. S., & Baladi, G. Y. (1990). MICH-PAVE: A nonlinear finite element program for analysis of flexible pavements. *Transportation Research Record, 1286*, 123-131.

Hayhoe, G. F. (2002). *LEAF: A new layered elastic computational program for FAA pavement design and evaluation procedures.* Washington, D.C.: Federal Aviation Administration.

Hiller, J. E., & Roesler, J. R. (2005). Determination of critical concrete pavement fatigue damage locations using influence lines. *Journal of Transportation Engineering, 131(8)*, 599-607.

Hilsdorf, H. K., & Kesler, C. E. (1966). Fatigue strength of concrete under varying flexural stresses. *ACI Journal, 63(10)*, 1059-1075.

Holmen, J. O. (1982). Fatigue of concrete by constant and variable amplitude loading. *ACI Journal, SP75*, 71-110.

Hsu, T. T. (1981). Fatigue of plain concrete. *ACI Journal Proceedings, 78(4)*, 292-305.

Huang, Y. H. (2004). Pavement analysis and design.

Inc, A. (2013). *ABAQUS Software Version 6.13: User's Manual.* Providence, RI.

Khazanovich, L. (2018). *Quantifying the Effects of Implements of Husbandry on Pavements.* Washington, D.C.: National Cooperative Highway Research Board.

Khazanovich, L., & Wang, Q. (2007). MnLayer: high-performance layered elastic analysis program. *Transportation Research Record, 2037*, 63-75.

Khazanovich, L., Yu, H. T., Rao, S., Galasova, K., Shats, E., & Jones, R. (2000). *ISLAB 2000: finite element analysis program for rigid and composite pavements: user's guide.* Urbana, IL: ERES Consultant.

Kolluru, S. V., O'Neil, E. F., Popovics, J. S., & Shah, S. P. (2000). Crack propagation in flexural fatigue of concrete. *Journal of Engineering Mechanics, 126(9)*, 891-898.

Larson, G., & Dempsey, B. (2003). *Enhanced Integrated Climatic Model Version 3.0 (EICM).* Urbana, IL: University of Illinois.

Larson, G., & Dempsey, B. J. (1997). *Enhanced integrated climatic model Version 2.0.* Urbana, IL: University of Illinois at Urbana-Champaign.

Leahy, R. (1989). *Permanent Deformation Characterization of Asphalt Mixtures.* College Park, MD: University of Maryland.

Lytton, R. L. (1993). *Development and validation of performance prediction models and specifications for asphalt binders and paving mixes.* Washington, D.C.: Strategic Highway Research Program.

Marcus, H. (1951). Load Carrying Capacity of Dowels at Transverse Pavement Joints. *48*.

Miao, T. J., & Chan, T. H. (2002). Bridge Live Load Models from WIM Data. *Engineering Structures, 24(8)*, 1071–1084.

Miner, M. A. (1945). Cumulative damage in fatigue. *Journal of Applied Mechanics, 12*, 149–164.

Minnesota Department of Transportation. (2012, July). MnPAVE User's Guide.

Mohammadi, J., & Shah, N. (1992). Statistical Evaluation of Truck Overloads. *Journal of Transportation Engineering, 118(5)*, 651–665.

Murdock, J. W., & Kesler, C. E. (1958). Effect of range of stress on fatigue strength of plain concrete beams. *ACI Journal Proceedings, 55(8)*, 221-231.

Nassiri, S., & Vandenbossche, J. M. (2012). Establishing built-in temperature gradient for jointed plain concrete pavements in Pennsylvania. *International Journal of Pavement Research and Technology, 5(4)*, 245.

National Cooperative Highway Research Program Report 1-37A. (2004). *Guide for Mechanistic-Empirical Design of New and Rehabilitated Pavement Structures.* Washington, DC: Transportation Research Board.

OBrien, E. J., Enright, B., & Getachew, A. (2010). Importance of the Tail in Truck Weight Modeling for Bridge Assessment. *Journal of Bridge Engineering, 15(2)*, 210–213.

Oh, B. H. (1986). Fatigue analysis of plain concrete in flexure. *Journal of Structural Engineering, 112(2)*, 273-288.

Oh, B. H. (1991a). Cumulative damage theory of concrete under variable-amplitude fatigue loadings. *ACI Materials Journal, 88(1)*, 41-48.

Packard, R. G. (1995). *Thickness design for concrete highway and street pavements.* Skokie, IL: Portland Cement Association.

Packard, R. G., & Tayabji, S. D. (1985). New PCA thickness design procedure for concrete highway and street pavements. *Third International Conference on Concrete Pavement Design and Rehabilitation.* West Lafayette, IN: Purdue University.

Papagiannakis, A. T. (2015). *NCHRP Synthesis 476: Practices for Permitting Superheavy Load Movements on Highway Pavements.* Washington, D.C.: National Cooperative Highway Research Program.

Pennsylvania Department of Transportation. (2019). *Publication 242: Pavement Policy Manual.* Harrisburg, PA: Pennsylvania Department of Transportation.

Pennsylvania Department of Transportation. (2020b). *Pavement Policy Manual (Publication 242/2020).* Harrisburg, PA: Pennsylvania Department of Transportation.

Pennsylvania Department of Transportation,. (2020a). *Materials Specifications (Publication 408/2020).* Harrisburg, PA: Pennsylvania Department of Transportation.

Raad, L., & Figueroa, J. L. (1980). Load response of transportation support systems. *Journal of Transportation Engineering, 106(1)*, 111-128.

Raithby, K. D. (1979). Flexural fatigue behaviour of plain concrete. *Fatigue of Engineering Materials and Structures, 2*, 269-278.

Raithby, K. D., & Galloway, J. W. (1974). Effects of moisture condition age, and rate of loading on fatigue of plain concrete. *ACI Special Publications, 41*, 15-35.

Rodriguez, M., Sinha, K., Labi, S., Tine, G., & Dutta, R. (2005). Procedures for the Estimation of Pavement and Bridge Preservation Costs for Fiscal Planning and Programming. *Joint Transportation Research Program.*

Roesler, J. R. (1998). *Fatigue of Concrete Beams and Slabs.* Urbana, IL: University of Illinois.

Roesler, J. R. (2006). Fatigue resistance of concrete pavements. *6th International DUT– Workshop on Fundamental Modelling of Design and Performance of Concrete Pavements.* Belgium.

Roesler, J. R., & Barenberg, E. J. (1999). Fatigue and static testing of concrete slabs. *Transportation Research Record, 1684(1)*, 71-80.

Sachs, S., Vandenbossche, J. M., & Snyder, M. B. (2015). Calibration of national rigid pavement performance models for the pavement mechanistic–empirical design guide. *Transportation Research Record, 2524(1)*, 59-67.

Sain, T., & Kishen, J. C. (2008). Probabilistic assessment of fatigue crack growth in concrete. *International Journal of Fatigue, 30(12)*, 2156-2164.

Shi, X. P., Fwa, T. F., & Tan, S. A. (1993). Flexural fatigue strength of plain concrete. *ACI Materials Journal, 90(5)*, 435-440.

Simpson, A. L., Rauhut, J. B., Jordahl, P. R., Owusu-Antwi, E. B., Darter, M. I., & Ahmad, R. (1994). *Early Analysis of LTPP General Pavement Studies Data, Volume 3: Sensitivity Analyses for Selected Pavement Distresses.* Washington, D.C.: Strategic Highway Research Program.

Subcomittee III, C. 3. (1956). Structural Design Considerations for Pavement Joints. *Journal of the American Concrete Institute, 53*, 1-28.

Tanquist, B. (2012). *MnPAVE User's Guide.* St. Paul, MN: Minnesota Department of Transportation.

Teller, L. W., & Cashell, H. D. (1959). Performance of Doweled Joints Under Repetitive Loading. *Highway Research Board Bulletin, (217)*, 8–49.

Tepfers, R. (1979). Tensile fatigue strength of plain concrete. *ACI Journal, 76(8)*, 919-934.

Titus-Glover, L., Owusu-Antwi, E. B., & M.I, a. D. (1999). *Design and Construction of PCC Pavements, Volume III: Improved PCC Performance.* Washington, D.C.: Federal Highway Administration.

Tseng, K. H., & Lytton, R. L. (1989). Prediction of permanent deformation in flexible pavement materials. In *Implication of aggregates in the design, construction, and performance of flexible pavements.* ASTM International.

Uzan, J. (1994). Advanced backcalculation techniques. In *Nondestructive Testing of Pavements and Backcalculation of Moduli: Second Volume.* ASTM International.

Van Cauwelaert, F. J., Alexander, D. R., White, T. D., & Barker, W. R. (1989). Multilayer elastic program for backcalculating layer moduli in pavement evaluation. In *Nondestructive testing of pavements and backcalculation of moduli.* ASTM International.

Vega, I. M., Bhatti, M. A., & Nixon, W. A. (1995). A Non-linear Fatigue Damage Model for Concrete in Tension. *International Journal of Damage Mechanics, 4(4)*, 362-379.

Wu, C. L., Mack, J. W., Okamoto, P. A., & Packard, R. G. (1993). Prediction of Faulting of Joints in Concrete Pavements. *Proceedings of the Fifth International Conference on Concrete Pavement Design and Rehabilitation.* West Lafayette, IN: Purdue University.

Yu, H. T., Khazanovich, L., Rao, S. P., Darter, M. I., & Von Quintus, H. (1998). *Guidelines for Subsurface Drainage Based on Performance, Appendices.* National Cooperative Highway Research Program.

Yu, H., Darter, M., Smith, K., Jiang, J., & and Khazanovich, L. (1996). *Performance of Concrete Pavements Volume III - Improving Concrete Pavement Performance. Final Report, Contract DTFH61-91-C-00053.* McLean, VA: Federal Highway Administration.

Zhang, B., Phillips, D. V., & Wu, K. (1996). Effects of loading frequency and stress reversal on fatigue life of plain concrete. *Magazine of concrete research, 48(177)*, 361-375.